Copyright

by

Matthew Thomas Raiford

2014

The Dissertation Committee for Matthew Thomas Raiford Certifies that this is the approved version of the following dissertation:

Creating More Effective Functional Materials: Altering the Electronics of Conducting Metallopolymers for Different Applications

Committee:

Bradley J. Holliday, Supervisor

Eric V. Anslyn

Benny D. Freeman

Simon M. Humphrey

Richard A. Jones

Creating More Effective Functional Materials: Altering the Electronics of Conducting Metallopolymers for Different Applications

by

Matthew Thomas Raiford, B.S.

Dissertation

Presented to the Faculty of the Graduate School of

The University of Texas at Austin

in Partial Fulfillment

of the Requirements

for the Degree of

Doctor of Philosophy

The University of Texas at Austin

May 2014

Dedication

To Jen,

For all the love and patience, you are wonderful. You made this possible.

To Mom,

Thank you for the endless support.

To Dad,

Thank you for always being the man I strive to be.

Acknowledgements

I would like to thank Prof. Bradley J. Holliday, my advisor, for all of the amazing guidance, support, and help these past five years. His mentorship has benefitted my research and professional development, and my success in graduate school would have not been possible without it. I would like to also thank the members of my committee: Dr. Eric Anslyn, Dr. Benny Freeman, Dr. Simon Humphrey, and Dr. Richard Jones for their illuminating discussions and helpful guidance with my research. Specifically, I acknowledge the help of Dr. Simon Humphrey with NP alloy characterization and phosphine chemistry and Dr. Eric Anslyn for helping me understand binding constants in macromolecular sensors.

I would also like to thank my co-workers, Kory Mueller, Dr. Travis Hesterberg, Leander Cinninger, and Lauren Mitchell for their friendship, discussion, and suggestions. Aside from the research, they are what made the day-to-day work truly enjoyable.

I am very blessed to have such a wonderful family, who has supported me so well these past five years. To my wife, I love you and thank you for sacrificing so much, you have been wonderful. To my parents, thank you for always being there, and for lending a hand no questions asked.

Creating More Effective Functional Materials: Altering the Electronics of Conducting Metallopolymers for Different Applications

Matthew Thomas Raiford, Ph.D.

The University of Texas at Austin, 2014

Supervisor: Bradley J. Holliday

Conducting metallopolymers possess attractive electronic properties for use in sensors, photoelectronic devices, catalysts, and other applications. Modification of the conducting polymer backbone, through chemical or electrochemical methods, enables control of catalytic, electronic, and optical properties of the metal *via* inductive modulation of the electron density. Understanding in detail the relationship between the metal and polymer backbone could lead to more effective metallopolymer materials. We hope to study this relationship by probing the band gaps, excited state energy levels, catalytic activity, and sensor function in four metallopolymer systems.

Devices with sub-stochiometric ratios of Cu_2ZnSnS_4 NPs (CZTS: $(Cu_2Sn)_{1-x}Zn_{1/x}S)(0\geq x\geq 0.75)$) grown in Cu(II) conducting metallopolymers were produced to study band gap tuning in hybrid materials. The valence and conductance bands of CZTS (x = 0.60) aligned with the HOMO/LUMO of the Cu(II) metallopolymer. Changing the alignment facilitated charge transfer in the hybrid material, leading to photovoltaic materials with efficiencies of ~0.1%.

Chemoresistive ionophore sensors were developed by incorporating selective binding groups, such as thiourea, into conducting polymer backbones. Thiourea monomers and polymers showed high selectivity for Pb(II) ions over many competitive ions. XPS experiments demonstrated that reversible chelation of Pb(II) ions could be achieved through a simple uptake/rinse process. The conductivity of the thiourea polymer increased fifty-fold, from 7.75×10^{-2} S/cm^2 to 3.5 S/cm^2, after Pb(II) exposure. Sensitivity measurements indicated the sensors have limits of detection near 10^{-10} M.

Highly conjugated ligands were synthesized to explore effective sensitization of visible and near-IR emitting lanthanides. (3,4-ethylenedioxy)thiophene was appended to dipyridophenazine and dipyridoquinoxaline to introduce a group that could be easily electropolymerized. These bi-functional ligands emitted from π-π^* and an inter-ligand charge transfer excited states, and therefore, two distinct triplet states were observed. These separate energy pathways allowed for efficient sensitization of both visible (Tb(III), Eu(III), Dy(III)) and near-IR emitting (Nd(III), Yb(III), Er(III)) ions.

Finally, we explored the oxidation of a rhodium-containing conducting metallopolymer and the subsequent effect on the activity of the metal center. Oxidation of the backbone led to ancillary ligand attenuation, allowing for control of the catalytically active species in the conducting metallopolymer. Rh(I,III) monomer and metallopolymer catalytic studies showed potential for new heterogenous/homogeneous hybrid catalysts.

Table of Contents

List of Tables xiii

List of Figures xv

List of Schemes xxv

Chapter 1: Modification of Conducting Metallopolymers and Polymers *via* Chemical and Electrochemical Doping 1

Introduction: Conducting Polymers 1

From Conducting Polymers to Conducting Metallopolymers 4

Optimizing performance in conducting polymer systems 6

Photovoltaic (OPV) Device Optimization 6

Metallopolymer and Hybrid Light Emitting Materials 11

Metallopolymer and Hybrid Sensors: Ultra-Sensitive Recognition 21

Hybrid Conducting Polymer Catalysts 26

Scope of thesis 33

Chapter 2: Composition Effects on the Photodiode Behavior of $(Cu_2Sn)_{x/3}Zn_{1-x}S$ ($0 \leq x \leq 0.75$) NPs in a Cu(II) Conducting Metallopolymer 36

Introduction 36

Cu-based Hybrid Materials 41

Tunable CZTS NPs 47

Experimental 49

General Methods 49

Synthesis 49

Synthesis of the ligand 49

NP Growth 51

Transmission Electron Microscopy 51

Film thickness and Conductivity Measurements 52

Crystal Structure Determination 52

Electrochemistry 53

Results and Discussion 55

Characterization of Cu(II) Metallopolymer 55
Cu(II) Metallopolymer Studies 56
CZTS and $(Cu_2Sn)_{x/3}Zn_{1-x}S$ NP Growth and Characterization 59
Nanoparticle Growth Process 59
TEM/EDX Characterization 60
XPS Surface Analysis of the Hybrid Materials 63
Spectroelectrochemistry of the Hybrid Films 65
PVDevice Fabrication and Composition Effects on Performance 69
Device Prototype Scheme 69
J-V Curve Analysis 70
Conclusions 72

Chapter 3: Electropolymerizable Mono- and Bisaroylthiourea Monomers as Highly Sensitive and Selective Amperiometric Heavy Metal Cation Sensors 73
Introduction 73
Ion Selective Electrodes 73
Choosing an Ionophore 76
Mono- and Bis- (Thiourea)benzene Pb(II) Ionophores 77
Experimental 80
General Methods. 80
Film Thickness and Conductivity Measurements. 80
Electrochemistry. 81
Crystal Structure Determination. 81
Synthesis 82
Synthesis of the Ionophores 82
Results and Discussion 95
Electropolymerizable Mono- and Bis(aroylthiourea)benzene 95
Crystal Structures of the Ionophores 98
Selectivity Measurements of the Aroylthioureabenzenes 101
Selectivity of the Bis(thiourea)s 101
Selectivity of the Mono(thiourea)s 105

Electropolymerization of the Thiourea Ionophores 106
Chemical Stability and Detection of Heavy Metals by the Polymers 108
Selective Adsoprtion Process of the Ionophoric Films.....109
Selectivity and LODs of the Conducting Polymers.....112
Selectivity of the Ionophoric Polymers.....112
LODs for the Ionophoric Polymers.....114
Probing the Effect of Pb(II)-Doping on Redox Conductivity.....116
Mechanism of the Conductivity Enhancement 119
Other Electropolymerizable Ionophores for ISEs.....123
Conclusions.....126
Chapter 4: Highly Conjugated Dual Emissive Ligands: Pathway to Effective Antennas for Both Visible and Near-IR Emitting Ln(III) Ions.....127
Introduction.....127
Background 127
Ln(III) Sensitization.....128
Pathways to Broadly Usable Antenna Ligands.....130
Experimental 134
General Methods 134
Synthesis 134
Synthesis of the Ligands 134
Synthesis of the Ln(III) Complexes.....135
UV-Vis and Luminescent Measurements 139
Electochemistry.....139
Results and Discussion 140
Synthesis of Dual Emissive Ligands.....140
UV-Vis and Near-IR Photophysical Properties of **L1** and **L2**.....142
Photophysics of **L1** 142
Triplet Energy Level of the Bound **L1** 145
Photophysics of **L2** 146
Triplet Energy Level of the Bound **L2** 147

Blue Emission from Tm(III)(β-diketonate)$_3$ Complexes 149
Highly Luminescent Dy(III)(β-diketonate)$_3$(**L2**) Complexes 149
Highly Luminescent Tb(III)(β-diketonate)$_3$(**L1**) Complexes.....152
Tb(III)(β-diketonate)$_3$(L2) and Eu(III)(β-diketonate)$_3$(**L1**, **L2**) Complexes: Ineffective Sensitization 154
Sensitization of the NIR Emitting Ln(III) ions 156
Electropolymerization of Ln(III) Complexes to Form Ln(III) Metallopolymers 158
Dy(III) Metallopolymers.....158
Luminescent Tb(III) Metallopolymers 160
Luminescent Yb(III) Metallopolymers 162
Conclusion 165

Chapter 5: Using Novel Electropolymerizable Redox-Active Pincer Ligands for Catalytic Rh(I,III) Complexes and Metallopolymers 167
Introduction.....167
Experimental 171
General Methods 171
Electochemistry.....171
Synthesis 172
Synthesis of the Ligands 172
Synthesis of the Rh(I,III) Complexes 174
Results and Discussion 177
Initial Pathways to Redox-Active Electropolymerizable Ligands.....177
Producing an Electropolymerizable Redox-Active Ligand 179
Rh(I,III) Metallation Routes 180
Electropolymerization of the Rh(III) Monomer 181
Spectroelectrochemistry of poly-**5**.....182
Catalysis of the Monomers and Metallopolymers 184
Catalysis using **1** and **5** 184
Catalysis using poly-**5**.....187
Other Potential Catalytic Metallopolymers 189

Conclusions.....194
Crystal Tables 195
References.....199

List of Tables

Table 1. Crystal data and structure refinement for **1**.....53

Table 2. Selected Bond Lengths (Å) and Angles (°) for the **1**. 54

Table 3. Atomic ratios of the elements found from TEM/EDX experiments. Paranthetical values are theoretical values using the NP formual and metallopolymer composition.....60

Table 4. A representative absorbance vs. band gap for the $(Cu_2Sn)_{x/3}Zn_{1-x}S(0\leq x\leq 0.75)$ (a) 0.15, (b) table of optical band gaps. Method adapted from literature.[132,133] 68

Table 5. Selected bond (º) and the hydrogen bonding parameters for **5** derived from the single-crystal X-ray structure. 99

Table 6. The binding constants and association energies for **5** and **7a** with various metal ions. 103

Table 7. The binding constants and association energies for **6** and **8a** with various metal ions. 104

Table 8. The binding constants and association energies for **7b** and **8b** with various metal ions. 105

Table 9. Selectivity coefficients of the different polymer ionophores versus log (K_{Pb}^{amp}).....113

Table 11. Redox conductivities of each polymer before and after Pb(II) exposure. 118

Table 12. Photophysical data for the chromophores, **L1** and **L2**. 144

Table 13. Summary of photophysical data for the Dy(III) complexes.....152

Table 14. Photophysical data for the Tb(III) complexes for ligands **L1** and **L2**. 153

Table 15. Photophysical data for the Eu(III) complexes. 155

Table 16. Photophysical data for the Yb(III) complexes. 157

Table 17. Summary of catalytic data for different hydrogenation reactions using complexes **1** and **5**. 186

List of Figures

Figure 1. Structures of conjugated conducting polymer systems discussed. 2

Figure 2. Examples of thiophene-based oligomers utilized for photoelectronic devices.[4-9] 3

Figure 3. Scheme illustrating the three Wolf types of metallopolymers and examples of each type of metallopolymer. (top) Type I Wolf-type metallopolymer consists of a conducting polymer backbone covalently linked to the metal center.[21-23] (middle) Type II Wolf-type metallopolymer include metal centers in direct contact with the polymer backbone.[19] (top) Similar to Type II, Type III metallopolymers include the metal centers as part of the structure.[13] 5

Figure 4. Several literature examples of Type II/III conducting metallopolymer OPV materials. Many literature examples incorporate fluorene, benzothienyl, thienyl, and other highly conjugated OPV materials. 11

Figure 5. Selected luminescent metallopolymers from the literature.[48-51] 13

Figure 6. *In-situ* polymerization of the CdSe NPs yields highly luminescent hybrid polymers. The drop cast polymers are transparent in ambient light conditions. Edited and reprinted with permission from ref 60. Copyright 2007 Elsevier. 18

Figure 7. Examples of conducting polymers used as ultra-senstive fluorometric and amperiometric sensor materials.[68-71] 22

Figure 8. Modified deacetylated chitosan allowed for ordered coordination of the Au NPs, leading to a biocompatible caffeic acid sensor. 26

Figure 9. Examples of metallopolymer catalysts in the literature.[77-81] 27

Figure 10. Hybrid materials have been utilized for many useful applications. State of the art devices have been produced using a broad variety of polymers with well known NPs, like CdSe, PbS, ZnO, FeO, Fe_2O_3, and many others. 37

Figure 11. TEM images of NP growth processes discussed herein. NP aggregation and size inconsistencies are dominant in SILAR and solvothermal methods. 41

Figure 12. ORTEP single crystal representation for the Cu(II) salpen monomer, **1**.....54

Figure 13. (a) Electrochemical deposition of poly-**1** onto ITO-coated glass electrode. (inset) the linear dependence of current vs. number of scans. (b) Current vs. Scan rate for poly-**1**. (inset) the linear dependence of the current vs. scan rate. 58

Figure 14. TEM image showing CZTS NPs grown in the Cu(II) metallopolymer film. Increasing growth cycles resulted in larger NP diameter. Size distribution studies were performed after four and six growth cycles. 61

Figure 15. Selected TEM micrographs for the $(Cu_2Sn)_{x/3}Zn_{1-x}S$ ratios x = 0.15, 0.30, 0.45, 0.6, 0.75.....62

Figure 16. XPS surface analysis spectra and the binding energies found for Cu, Sn, and S. The table compares experimental values to literature values.[117-127] 63

Figure 17. PXRD of the $(Cu_2Sn)_{x/3}Zn_{1-x}S$ NP/ metallopolymer film. 64

Figure 18. The relationship between the electronic energy levels CZTS NPs to the Cu(II) metallopolymer can be changed based on NP composition. a) The energy alignment shown characterizes both the polymer and CZTS NPs acting as p-type materials b) Composition modification changes the VB and CB of the $(Cu_2Sn)_{x/3}Zn_{1-x}S$ creating a p-n heterojunction and E_g = ~1.2-1.3 eV. The dotted line represents the literature range of values for $(Cu_2Sn)_{x/3}Zn_{1-x}S$ for the energy levels, from -3.30 eV to -6.07 eV.....66

Figure 19. a) The spectroelectrochemistry of CZTS NP/poly-**1** hybrid where x = 0.75, b) The spectroelectrochemistry of CZTS NP/poly-**1** hybrid where x = 0.60. Literature methods were used to find optical band gap of the $(Cu_2Sn)_{x/3}Zn_{1-x}S$ (x = 0.60, 0.75) NPs.[132] The optical band gap of the increases as the materials become more Zn-rich in NP composition.....67

Figure 20. The *J-V* curves for (a) x = 0.30, (b) x = 0.45, (c) x = 0.60, (d) x = 0.75.....70

Figure 21. The *J-V* curve for the hybrid films where x = 0.60. Photodiode behavior was present exclusively for this ratio.....71

Figure 22. Graphical representation of a multi-component ion selective electrode used in a potentiometric sensors. 74

Figure 23. Several structures of Pb(II) ionophores present in the literature. Structure 2, EDTA, is included for comparison of the current medical standard for heavy metal chelation therapy.....76

Figure 24. The proposed structure and setup of a conducting polymeric Pb(II) sensor. 79

Figure 25. The crystal structure for structure **5**. ORTEP ellipsoids shown with a 50% probability level. Hydrogens were omitted from the structure for clarity.....98

Figure 26. The crystal structure and hydrogen bonding parameters for structures **7b** and **8b**. 100

Figure 27. Representative Job's plot analysis (right) of the furanyl *bis*(thiourea) benzenes **5** and **7a** with metal ions showing a 1:1 host to guest speciation. A sample Benesi-Hildebrand plot (left) for ionophore **5** with Pb(II) ions. 102

Figure 28. Representative Job's plot analysis (right) of the furanyl *bis*(thiourea) benzenes **6** and **8a** with metal ions showing a 1:1 host to guest speciation. A sample Benesi-Hildebrand plot (left) for ionophore **6** with Pb(II) ions. 103

Figure 29. Representative Job's plot analysis of the furanyl mono(thiourea) benzenes **7b**and **8b** with metal ions showing a 1:1 host to guest speciation. 105

Figure 30. (A) Electropolymerization of **poly-5** using 20 cycles of film growth under oxidative current. (inset) The film growth dependence showing linear growth of the polymer over the growth cycles. (B) Cyclic voltammagrams at scan rates of 10-500 mV/s in monomer-free solution. (inset) linearity of scan rate for oxidative (black trace) and reductive (red trace) scans.....107

Figure 31. (A) Electropolymerization of **poly-7a** using 20 cycles of film growth under oxidative current. (inset) The film growth dependence showing linear growth of the polymer over the growth cycles. (B) Cyclic voltammagrams at scan rates of 10-500 mV/s in monomer-free solution. (inset) linearity of scan rate for oxidative (black trace) and reductive (red trace) scans. 107

Figure 32. (A) Electropolymerization of poly-**7b** using 20 cycles of film growth under oxidative current. (inset) The film growth dependence showing linear growth of the polymer over the growth cycles. (B) Cyclic voltammagrams at scan rates of 10-500 mV/s in monomer-free solution. (inset) linearity of scan rate for oxidative (black trace) and reductive (red trace) scans. 108

Figure 33. Cyclic voltammagrams of poly-**5** in the presence of Pb(II) ions (left) in 1 M KNO_3 solution. Cyclic voltammagrams of poly-**7a** in the presence of Pb(II) ions (right) in 1 M KNO_3 solution. 109

Figure 34. XPS spectra for poly- **5** after Pb(II) exposure and after EDTA exposure (left, bottom). Comparative spectra of the S^{2p} and Pb^{4f} peaks in the samples (right). 110

Figure 35. Distribution of selectivity coefficients for different ions versus log (K_{Pb}^{amp}) 113

Figure 36. (A) The maximum current versus the log of each Pb^{2+} concentration (10^{-11} to 10^{-3} M) for poly-**5**. The onset of Nernstian response was used to find the limit of detection. (B) The maximum current versus the log of each Pb^{2+} concentration (10^{-11} to 10^{-3} M) for poly-**5**. The onset of nernstian response was used to find the limit of detection. 114

Figure 37. (left) Cyclic voltammogram of poly-**5** (black trace) and the *in situ* conductivity measurements for poly-**5** (red trace) and poly-**5** after Pb(II) ion exposure (blue trace). (right) Cyclic voltammogram of poly-**6** (black trace) and the *in situ* conductivity measurements for poly-**6** (red trace) and poly-**6** after Pb(II) ion exposure (blue trace). 117

Figure 38. Depiction of the increase in charge production and flow from the ionic strength of the Pb(II) ions. 119

Figure 39. (left) Comparison of the oxidative and reductive scan rate vs. current in the mono(thiourea) poly - **8b** before and after Pb(II) exposure. (right) Comparison of the oxidative and reductive scan rate vs. current in the bisthiourea poly - **5** before and after Pb(II) exposure. 120

Figure 40. UV-Vis spectroelectrochemistry of poly-**5**.....122

Figure 41. Scheme and crystal structure of the reaction of lead(II) acetate with monomer **8b**. 123

Figure 42. (Left) Electropolymerization of poly-**12** from 20 cycles of film growth under oxidative current. (inset) The film growth dependence showing linear growth of the polymer over the growth cycles. (Right) Cyclic voltammagrams at scan rates of 10-500 mV/s in monomer-free solution. (inset) linearity of scan rate for oxidative (black trace) and reductive (red trace) scans.....124

Figure 43. Crystal structure of **L2.**.....142

Figure 44. (top) Absorption and photophysical spectra for $EDOT_2dppz$ (**L1**) (bottom) NIR emission and excitation for **L1**.....143

Figure 45. Emission and excitation spectra of $(hfac)_3Gd$-**L1** at 77 K in 2-MeTHF.....145

Figure 46. Near-IR emission and excitation spectra of $(hfac)_3Gd$-**L1** at 77 K in 2-MeTHF. The dotted traces represent the emission and excitation at room temperature. 145

Figure 47. Absorption and photophysical spectra for $EDOT_2dpq$ (**L2**).....146

Figure 48. NIR emission and excitation spectra for **L2**. 147

Figure 49. Emission and excitation spectra of $(tta)_3Gd$-**L2** at 77 K in 2-MeTHF. 148

Figure 50. Near-IR emission and excitation spectra of $(tta)_3Gd$-**L2** at 77 K in 2-MeTHF. The dotted trace are spectra taken at room temperature in 2-MeTHF. 148

Figure 51. Excited state energy levels for visible and nIR-emitting Ln(III) ions. The lines represent the energy levels of the **L1** (purple) and **L2** (red). 150

Figure 52. Representative emission, excitation, and absorption spectra of the ($EDOT_2$dppz) Dy(III)$(tta)_3$.....151

Figure 53. Photophysical spectra of the $(hfac)_3$Tb(**L1**) complex (top left). Absorption spectra for the Tb(**L1**) complexes (top right). Excitation spectra for the Tb(**L1**) complexes (bottom left). Emission spectra for the Tb(**L1**) complexes (bottom right). 153

Figure 54. Absorption spectra for the Tb(**L2**) complexes (top left). Excitation spectra for the Tb(**L2**) complexes (top right). Emission spectra for the Tb(**L2**) complexes (center). 154

Figure 55. Energy level alignment of the triplet energy levels of **L1**, **L2**, and ancillary ligands to the Eu(III) excited state (left). Photophysical characterization of a selected Eu(III) complex, $(hfac)_3$Eu(**L2**) (right). 156

Figure 56. Excitation and emission spectra for the $(dbm)_3$Yb(**L1**) complex.....157

Figure 57. Film growth of poly-**Dy(L1)** over 20 scans at -0.5 V to +1.5V (top). Scan rate dependence of poly-**Dy(L2)** at -0.5 V to +1.5V from 10-500 mV/s in monomer-free solution (bottom). 159

Figure 58. Pictures of the Ln(III) metallopolymer films after electropolymerization. Absorption spectra of the Ln(III) metallopolymers.....160

Figure 59. Film growth of poly-**Tb(L1)** over 20 scans at -0.5 V to +1.5V (top left). Scan rate dependence of poly-**Tb(L1)** at -0.5 V to +1.5V from 10-500 mV/s in monomer-free solution (top right). Film growth of poly-**Tb(L2)** over 20 scans at -0.5 V to +1.5V (bottom left). Scan rate dependence of poly-**Tb(L2)** at -0.5 V to +1.5V from 10-500 mV/s in monomer-free solution (bottom right). 162

Figure 60. Film growth of poly-**Yb(L1)** over 20 scans at -0.5 V to +1.5V. (Inset) Linear growth of oxidative (black) and reductive (red) peaks (left). Scan rate scans from 10-500 mV/s of poly-**Yb(L1)** in monomer free solution (right). (Inset) Linear scan rate dependence of oxidative (black) and reductive (red) peaks.....164

Figure 61. XPS spectra of poly-$(dbm)_3$Yb**L1**. 164

Figure 62. Photophysics of poly-$(dbm)_3$Yb**L1** and comparison of Yb(III) monomer and metallopolymer emission. 165

Figure 63. A depiction of the dual excitation pathways present in these ligand systems. 166

Figure. 64 (A)ATR-IR transmission spectra of ligand **3** and complex **4**. (B) Carbonyl IR bands present in complexes **3b** and **5**.....177

Figure 65. UV-vis-NIR spectroelectrochemistry spectra of poly - **5**. Bipolaron formation was observed as a broad peak at ~1250 nm. 182

Figure 66. (A) Electropolymerization of **5** from 20 cycles of film growth under oxidative current (top). The film growth dependence showing linear growth of the polymer over the growth cycles (top inset). (B) Cyclic voltammagrams at scan rates of 10-500 mV/s in monomer free solution (bottom). Scan rate vs. current for oxidative (black trace) and reductive (red trace) scans(bottom inset). 183

Figure 67. A comparison of the conversion rate of hydrogenation of cyclohexanone to cyclohexanol by the electrochemically oxidized poly-5 (red) and neutral poly-5 (black).....189

Figure 68. The compounds **L1**-**L4** (from left to right)**.** 192

Figure 69. The photophysics for TerThdppz **L3** (right) and Terthdpq **L4** (left). 193

Figure 70. The polymerization and scan rate dependence studies of poly-Pd**L2**. 193

List of Schemes

Scheme 1. The device layout scheme and electroluminescent organic components PFO and $Ir(MDQ)_2(acac)$.[61-65] 19

Scheme 2. The flow of electron-hole pairs in a hybrid inorganic-organic PV device. 36

Scheme 3. The scheme outlines the approach taken to produce an array of different NPs in a conducting metallopolymer matrix. Wolf type II and type III metallopolymers were used as a seeded growth platform. 39

Scheme 4. The energy level diagram and device schematic of the P3OT-capped $CuInSe_2/TiO_2$ device. Edited and reprinted with permission from ref 107. Copyright 2011 Elsevier. 43

Scheme 5. The energy levels and charge carrier transport in the $CuInSe_2$/P3HT. (a) CISe NP weight ratio of 1:19, and (b) a CISe NP weight ratio of 6:1.[112] 45

Scheme 6. The relationship between CZTS NPs to the Cu(II) metallopolymer can be changed based on NP composition. The energy alignment shown characterizes both the polymer and CZTS acting as *p*-type materials.....48

Scheme 7. The synthetic scheme for the electropolymerizable ligand and electropolymerizable Cu(II) complex. 55

Scheme 8. The synthetic route to form the Cu(II) salpen metal complex (**1**) from the salpen ligand (**L**). A single crystal was isolated from DCM/hexanes and the structure solved, an ORTEP diagram with a labeling scheme showing a 50% probability level. Hydrogen atoms have been omitted for clarity. 56

Scheme 9. The scheme for electropolymerization, seeding, and NP growth process used to grow CZTS NPs in Cu(II) metallopolymer. 59

Scheme 10. The method utilized to construct the $(Cu_2Sn)_{x/3}Zn_{1-x}S$ NP/Cu(II) metallopolymer hybrid devices. 69

Scheme 11. Synthetic scheme for the electropolymerizable ionophoric monomers. 96

Scheme 12. Schematic of the M^{2+} electrochemical adsorption/removal process used to test the polymers capacity to reversibly interact with the cations and be recycled. 111

Scheme 13. Scheme outlining the electropolymerization and Pb(II) absorption process. 118

Scheme 14. Planarization of the thiourea polymers in the presence of Pb(II) ions. 121

Scheme 15. Synthetic scheme to produce compounds **9 – 13.** 123

Scheme 16. Synthetic pathway used to produce the electropolymerizable phen$(MeOH)_2$ (**15**). 124

Scheme 17. Graphical representation of the possible energy pathways in sensitization of the Ln(III) excited state. 129

Scheme 18. The charge transfer centered triplet state allows for effective sensitization of near-IR emitting Ln(III) ions. 133

Scheme 19. Synthetic scheme of the ligand **L1** and **L2** and Ln(III) complexes.141

Scheme 21. Synthetic scheme of the model complexes **1** and **2**. 168

Scheme 22. Synthetic scheme for the electropolymerizable materials **3** - **7**. 170

Scheme 23. The different synthetic pathways explored to produce complex **5**. 179

Scheme 24. Electrochemical polymerization of **5** to poly-5. 181

Scheme 25. Selective hydrogenation of crotonaldehyde to crotyl alcohol by complexes **1** and **5**.....184

Scheme 26. Graphical representation of the facilitated activation in the Rh(III) metallopolymer catalysts. 188

Scheme 27. The synthetic scheme for a electropolymerizable Rh[NCN] complex.....190

Scheme 28. Synthetic scheme for electropolymerizable ligands **L1-4**. 191

Scheme 29. The synthetic scheme to produce Pd-**L1-4** and poly-Pd-**L1-4**. 192

Chapter 1: Modification of Conducting Metallopolymers and Polymers *via* Chemical and Electrochemical Doping

INTRODUCTION: CONDUCTING POLYMERS

Inorganic semiconductors, such as silicon and germanium, have played a vital role in light-emitting diodes, photovoltaic devices, and other electronic devices. In semiconductors the conduction and valence band are close enough that excitation can promote an electron. Excitation can occur from thermal, optical, electrical, chemical, and electrochemical means, leading to movement and diffusion of electrons throughout the material. Due to high conductivity upon doping, band gap tuning capabilities, and thermoelectric behavior, vast amounts of research have focused on improving performance and processability. Unfortunately, the processes used to produce semiconductors are highly energy intensive, like in the Siemens process, which uses tetrachlorosilane at 1100 ºC to produce crystalline Si. Furthermore, useful semiconductors, such as CdSe and InP, are manufactured from toxic and expensive precursor materials. Organic polymeric semiconductors have proven to be great alternatives to conventional inorganic semiconductors. The discovery of organic semiconductors has resulted in highly processable, flexible interfaces for electronics produced *via* low temperature processes from more abundant and less toxic precursors.

In 1977, Shirakawa, MacDiarmid, and Heeger proved that chemical oxidation of polyacetylene by exposure to chlorine, bromine, or iodine vapor could produce polymers with metal-like conductivities.[1] The modified polyacetylene possessed a conductivity of 10^{-5} S m^{-1}, which was much higher than any other polymeric material (10^{-11} S m^{-1}) at that time. The conjugation in the systems combined with a redox reaction with iodine or

AsF_5 allowed for charge carriers to be produced in the form of holes, leading to the highly conductive polymeric cations.[2,3] Charge carrier generation is typically driven by a doping process in metal semiconductors, and similarly "doping" occurs in organic materials using chemical or electrochemical redox conditions.

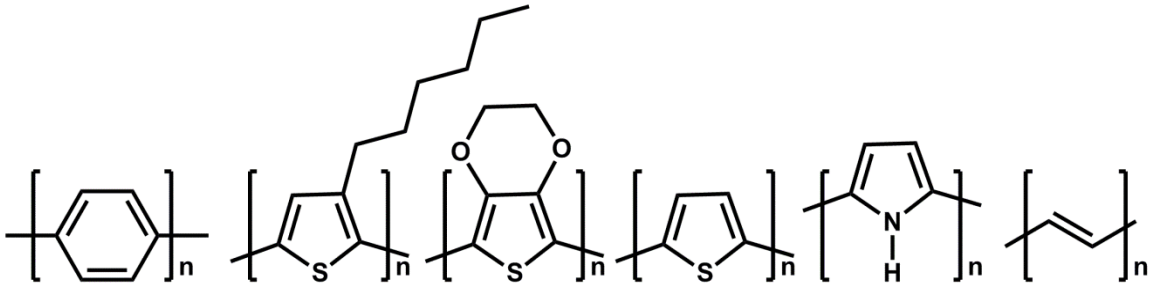

Figure 1. Structures of conjugated conducting polymer systems discussed.

Since this seminal work, a wide variety of different polymer semiconductors, as shown in Figure 1, have been discovered.[4] Research in conducting polymers has expanded to many different molecules and highly effective materials have been developed for many different applications. The thiophene-based polymers pictured above have demonstrated especially high conductivities in the 10^{-2} – 10^{2} S cm^{-1} regime. Poly-3,4-ethylenedioxythiophene (PEDOT) and regioregular poly-3-hexylthiophene (P3HT), in particular, serve as exceptional active and hole transport layers in optoelectronic devices. Thiophene molecules and oligomers are easily modified and polymerized, and materials produced from this class of conducting polymers have demonstrated incredible performance in a wide array of applications.

Over the past few decades, conducting oligomer and metal-containing polymer systems have also been studied due to high redox conductivities and attractive electronic

behavior. Specifically, oligomeric and polymeric thiophene systems and metal-containing polythiophene systems have shown great promise for use in photonics, optical devices, photovoltaics, light emitting diodes, sensors, and catalytic platforms. Figure 2 outlines some of the oligomeric thiophene materials developed for various applications.[4-9]

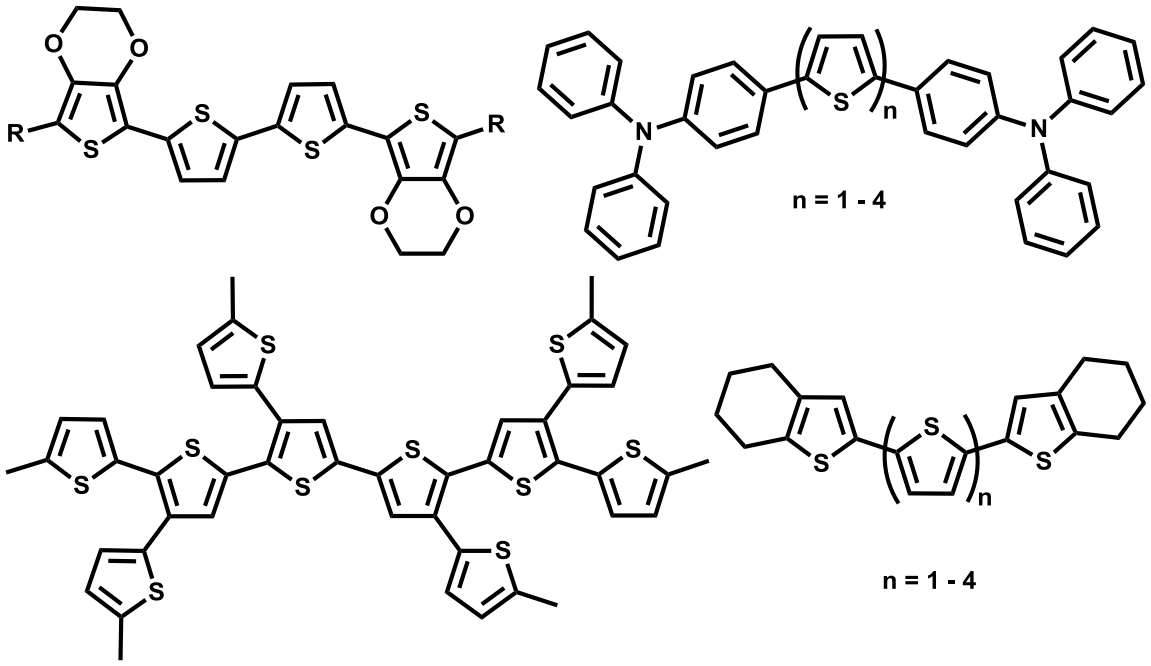

Figure 2. Examples of thiophene-based oligomers utilized for photoelectronic devices.[4-9]

Typical highly conjugated conducting polymers, like poly(thiophene)s, benefit from inter- and intra-molecular energy transfer processes. Not only does conductivity increase in these organic materials by chemical or electrochemical doping, but intra-molcular π-stacking between polymer chains also contributes to increases in conductivity. This "hopping" mechanism between polymer chains has garnered special interest and oligothiophenes serve as suitable models for studying the electron transfer processes at a more manageable scale.

FROM CONDUCTING POLYMERS TO CONDUCTING METALLOPOLYMERS

Effective materials for catalysis, photoelectronic devices, sensors, and electrochromic applications have been produced by incorporating metal centers into conducting polymers. These utilize not only the processability of polymers, but combine the functionality of metals and the conductivity of the polymers together to form new useful materials. Preliminary research producing metallopolymers focused on producing materials that were soluble and possessed high molecular weight.[10] Major advances in synthesis have allowed for much easier production of useful metallopolymers. Over the last 20 years, research on metallopolymers has shifted from synthesis to application. Metal-containing polymers have been produced from numerous polymer motifs and thiophene-based conducting metallopolymers have shown great potential as functional materials.[10-17]

The conductive poly(thiophene) matrix provides highly conjugated backbones with strong electron delocalization. The electron delocalization in the system facilitates good electronic communication with included metal centers, and has resulted in hybrid materials with more attractive catalytic activity, redox behavior, conductivity, and other important material properties. Metal incorporation can be differentiated into several types, and can be directly related to level of electronic communication present in the metallopolymer. Wolf *et al.* has classified metallopolymers into three different types, as depicted in Figure 3.[18,19] Type I metallopolymers covalently link the metal containing component to the conducting polymer backbone, and electronic communication in these systems is minimal. Type II and III metallopolymers benefit from a good electronic interface between the metal and conducting polymer backbone. In these two systems

electron transfer mechanisms are synergistic. For instance, redox matching of the metal center to the conducting backbone in these systems results in unusually high redox conductivity.[20]

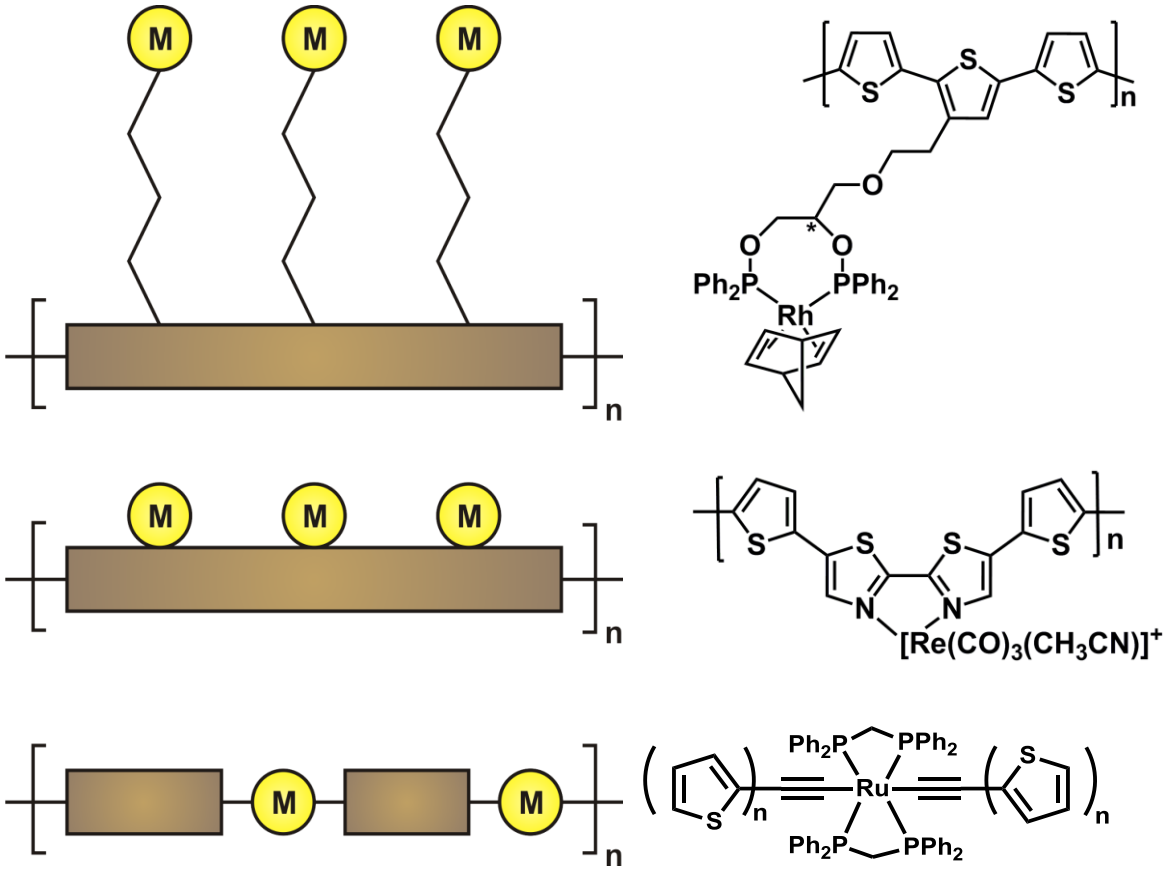

Figure 3. Scheme illustrating the three Wolf types of metallopolymers and examples of each type of metallopolymer. (top) Type I Wolf-type metallopolymer consists of a conducting polymer backbone covalently linked to the metal center.[21-23] (middle) Type II Wolf-type metallopolymer include metal centers in direct contact with the polymer backbone.[19] (top) Similar to Type II, Type III metallopolymers include the metal centers as part of the structure.[13]

OPTIMIZING PERFORMANCE IN CONDUCTING POLYMER SYSTEMS

Conducting metallopolymer systems can serve as functional materials for sensors, polymer light-emitting diodes (PLED)s, optoelectronic materials, and in a few cases as catalytic platforms. Design of these useful materials requires that each component in the target monomer be considered and designed to best suit the desired application. Small changes in the monomer, the electropolymerizable groups, sterics, ancillary ligands, and many other factors can lead to drastic difference in benchmark data like quantum yields, selectivity coefficients, or power conversion efficiencies. The following sections will focus on functional materials produced from conducting polymers and metallopolymers and some important considerations to take into account when designing these systems. [24-27]

Photovoltaic (OPV) Device Optimization

A prime example of optimizing the performance in conducting polymer/NP (NP) hybrid PV materials was studied by Alivisatos *et al.* Seminal work by the Alivisatos' group reported the fabrication of CdSe/poly(3-hexylthiophene) (P3HT) films by mixing pyridine treated NPs with P3HT in a mixture of 4 volume% to 12 volume% pyridine in chloroform to give a uniform film of dispersed NPs in a spin casted film. The amount of pyridine (Py) present is critical to the mixture, too much pyridine results in precipitation of the polymer, and not enough pyridine results in precipitation of the NPs, both resulting in phase separation. AFM was used to study the topology of the films cast from different Py concentrations, yielding rough films at low concentrations, and increase in

smoothness with an increase in Py concentration. External quantum efficiency (EQE) measurements reveal a decrease in EQE as the surface roughness increases, confirming that large-scale surface separation negatively affects PV performance. Heating of the samples results in the removal of Py from the films, allowing for the nanorods to pack closer together, bringing the two materials in closer contact of each other.[28-32] Later in 2003, Alivasatos and coworkers reported that use of CdSe nanorods (NR)s, measuring 7 nm by 60 nm in size. Nanorods act as more efficient electron transport materials when compared to NPs due to the main diffusion mechanism being band conduction as opposed to hopping, which occurs in the smaller NPs.[28,31] The shape of the NPs were further studied resulting in hybrid devices made of hyperbranched NPs blended with P3HT. The use of hyperbranched NPs yields a hybrid material in which the inorganic component is dispersed throughout the polymer, resulting in large distributed interfacial surface area between the two materials. The hyperbranched materials span the thickness of the film, forming a direct pathway for electron transport to the anode. Devices were prepared by spin casting a mixture of the two materials and the V_{OC} was measured at 0.6 V. The V_{OC} increases steadily with an increase in the concentration of NPs present in the film. The hyberbranched NP devices had a PCE of 2.2% under AM1.5.[32,33]

Nanocomposite thin films of electron-rich PEDOT and 3,4-propylenedioxythiophene-capped CdSe nanocrystals, tethered to ITO electrodes were produced for photovoltaic and electrocatalytic applications.[36] Synthesis of the material began with kinetic-controlled electropolymerization of ultra-thin layers (10 nm) of PEDOT onto the ITO electrodes, followed by a chemisorbed monolayer of 10-((3-methyl-3,4-dihydro-2*H*-thieno[3,4-*b*][1,4]dioxepin-3-yl)-methoxy)-10-oxo-decanoic acid

(ProDOT-CA). ProDOT-CA-capped-CdS NPs were then cross linked onto the monolayer through electropolymerization produced the desired tethered material. This particular hybrid material utilizes a unique pathway for wiring of the light-harvesting CdS NPs to the electron donor, PEDOT, and the ITO electrode. SEM and AFM imaging, as well as XPS experiments, showed the formation of the capped CdS-NPs cross-linked onto ProDOT-CA-PEDOT/ITO films. Background-corrected photoelectrochemical responses of CdS/ProDOT-CA-PEDOT/ITO composite films and control ProDOT-CA-PEDOT/ITO copolymer films were conducted. Photocurrents corresponding to NP-sensitized reduction of C_{60} by the CdS/ProDOT-CA-PEDOT/ITO film began at ca. -0.4 V (vs Fc/Fc^{+}), more positive when compared to the $E°$ for $C_{60}/C_{60}^{-\bullet}$ (ca. -1.0 V vs Fc/Fc^{+}), and increased exponentially with increasing negative potential (Tafel-like behavior). These potentials are sufficient to fully reduce (de-dope) PEDOT and allow electron injection into photoexcited CdSe-NPs. Copolymer of ProDOT-CA-PEDOT/ITO showed much smaller photocurrents, even though it has been recently demonstrated that photoinduced charge injection from a ProDOT polymer to C_{60} is possible.[35] This material shows promise as an efficient PV material, but optimization of ProDOT-CA length, nanoparticle size/type, and type of electron donor should be explored to allow for most desired optoelectrical behavior.[36]

Beyond conducting polymer/NP hybrid nanocomposites, highly absorbing metallopolymer systems have also been used in photovoltaic devices.[37] Many literature examples incorporate fluorene, benzothienyl, thienyl, and other highly conjugated OPV materials into metallopolymers. There have been several examples of conducting platinyne metallopolymers acting as OPV materials in the literature. Shown below in

Figure 4, are two examples of metallopolymers produced utilizing platinyne to initiate polymerization.[37-39] The best performance came from platinyne materials utilizing oligothienyl-2,7-fluorene spacer groups. Efficiencies of ~ 2.9% were achieved and the performance was primarily contributed to preferential arrangement of staggered platinum centers in the polymer. In other systems the degree of planarization directly impacted absorption and conductivity, but lead to little overall improvement in performance.

In other work, a Zn-porphyrin platinyne metallopolymer absorbed more of the solar spectrum leading to devices with PCE = 1.04%, V_{OC} = 0.77 V, J_{sc} = 3.42 mA cm^{-2}, FF = 0.39.[40] When compared to a thiazole-based platinyne metallopolymer, there was no overall improvement in device performance due to little improvement in the visible spectrum absorption. Similarly, platinyne metallopolymers with different conjugated fluorine, benzo*bis*(thiadiazole), and quinoxaline-type spacers were utilized in OPV devices. The best performance came from materials with a fluorene-benzo*bis*(thiadiazole)-fluorene spacer copolymerized with benzo*bis*(thiadiazole) which gave V_{OC} = 0.66 V, J_{SC} = 4.95 mA cm^{-2} and FF = 0.31 and PCE = 1.02%. Devices produced from blends of PCBM ([6,6]phenyl-C_{61}-butyric acid Me ester) and Pt(II) oligothienyl-phenothiazine metallopolymers gave PCE = 2.24%. Multi-dimensional and linear polymers were created using these blends, with the multidimensionality leading to the highest performing devices. Absorption and hole mobility were much higher in the non-linear polymers.[41-42]

Other systems utilizing metallopolymers have demonstrated very effective photovoltaic behavior. Recent work by Cao and coworkers featured Hg(I) poly(fluorene) ethylene diamine (PFEN) metallopolymers as a cathode interlayer.[46] Inclusion of this

material in the devices leads to a three-fold increase of the PCE from 3.08 to 9.00%. This material showcases the properties of metallopolymers, with the band gap, film formation, and absorption profile of the metallopolymer beneficial to the device performance. The Hg-PFEN cathode layer amine functionalization first lowered the work function of the ITO and greatly increased the electron extraction in the films. Also, the large band gap (3.92 eV) of the Hg-fluorene metallopolymers helped gather excitions along the interface of the layers. Finally, the metallopolymer absorption was not in the near-IR or visible region which minimizes the optical loss *via* interlayer absorption and therefore provides optimal light harvesting conditions for the active layer. Utilizing these properties in the device produced one of the highest PCEs reported in an organic single-junction device to date.

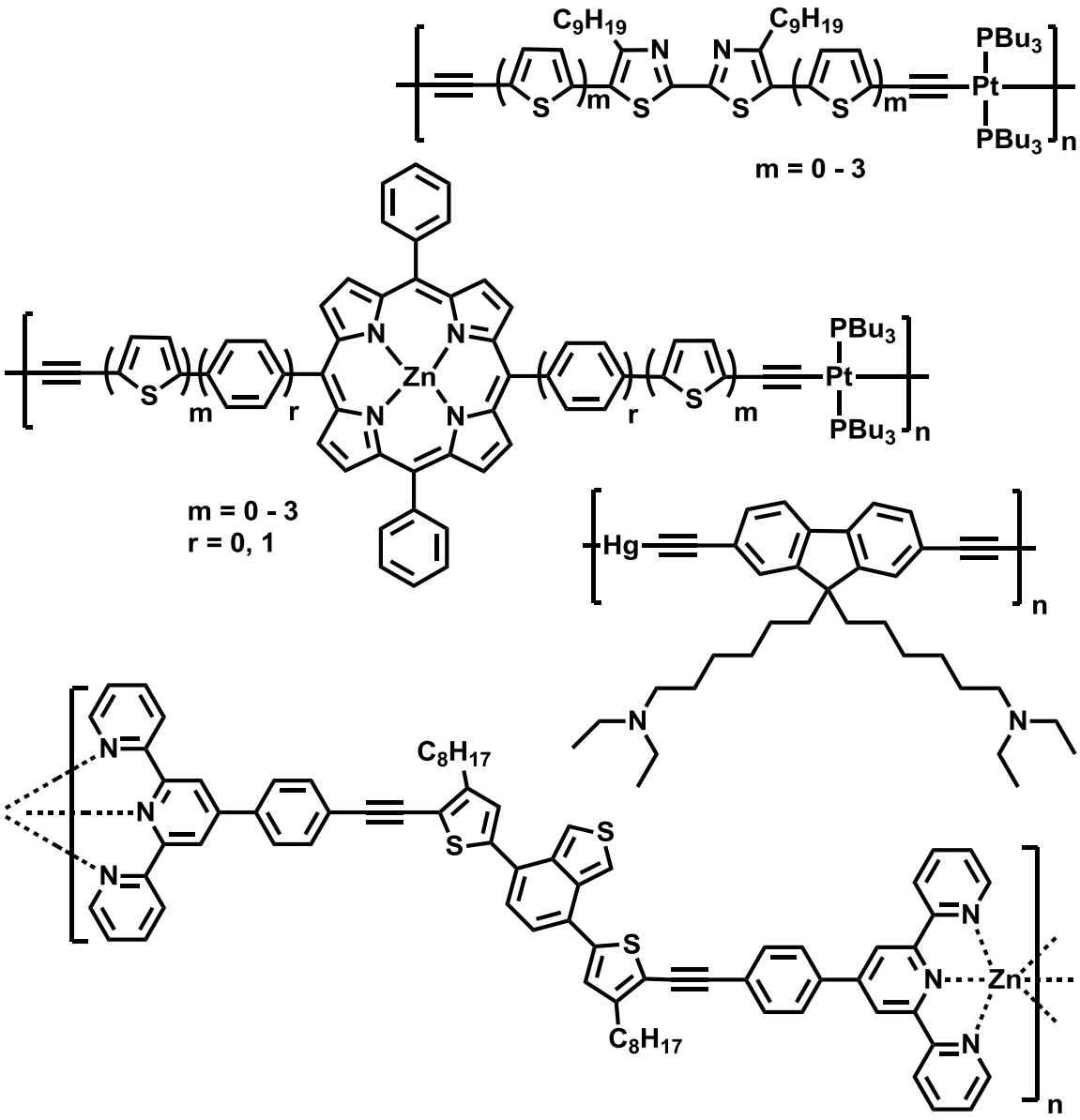

Figure 4. Several literature examples of Type II/III conducting metallopolymer OPV materials. Many literature examples incorporate fluorene, benzothienyl, thienyl, and other highly conjugated OPV materials.

Metallopolymer and Hybrid Light Emitting Materials

Luminescent metal complexes have led to efficient phosphors for use in light emitting diodes (LED)s and bio-imaging. Effective materials have been produced from

transition metal and lanthanide metal ions, leading to phosphors emitting at every color in the visible spectrum. Typical organic chromophores harvest only 25% of excited electrons in the singlet state, unlike the possible 100% conversion capable in metal-based phosphors. Nonradiative decay processes typically prevail over proper transfer to the triplet state, with the majority of energy relaxing as heat or ligand-based fluorescence. Inclusion of a metal in a chromophore increases the spin-orbit coupling based on the heavy atom effect. The increase in spin-orbit coupling increases the probability of triplet conversion to 100%, in turn facilitating long lifetimes and more efficient phosphorescence. This has a resulted in a host of new luminescent technologies based on transition metal and lanthanide complexes. The pure, sharp color emission and long luminescent lifetimes of lanthanide ions (Dy^{3+}, Eu^{3+}, Pr^{3+}, Sm^{3+}, and Tb^{3+}) make them effective materials for not only LEDs, but bio-imaging as well.

Transition metal and lanthanide-based metallopolymers utilize the advantages of both highly luminescent metal phosphors and the processability of polymers. Furthermore, covalent incorporation of the metal complex in the polymer facilitates homogeneity in organic-inorganic polymer devices, negating phase segregation problems common in metal phosphor/organic blend-based active layers. Other systems have been developed from NP/conducting polymer hybrids leading to robust and stable active layers with tunable emission color.

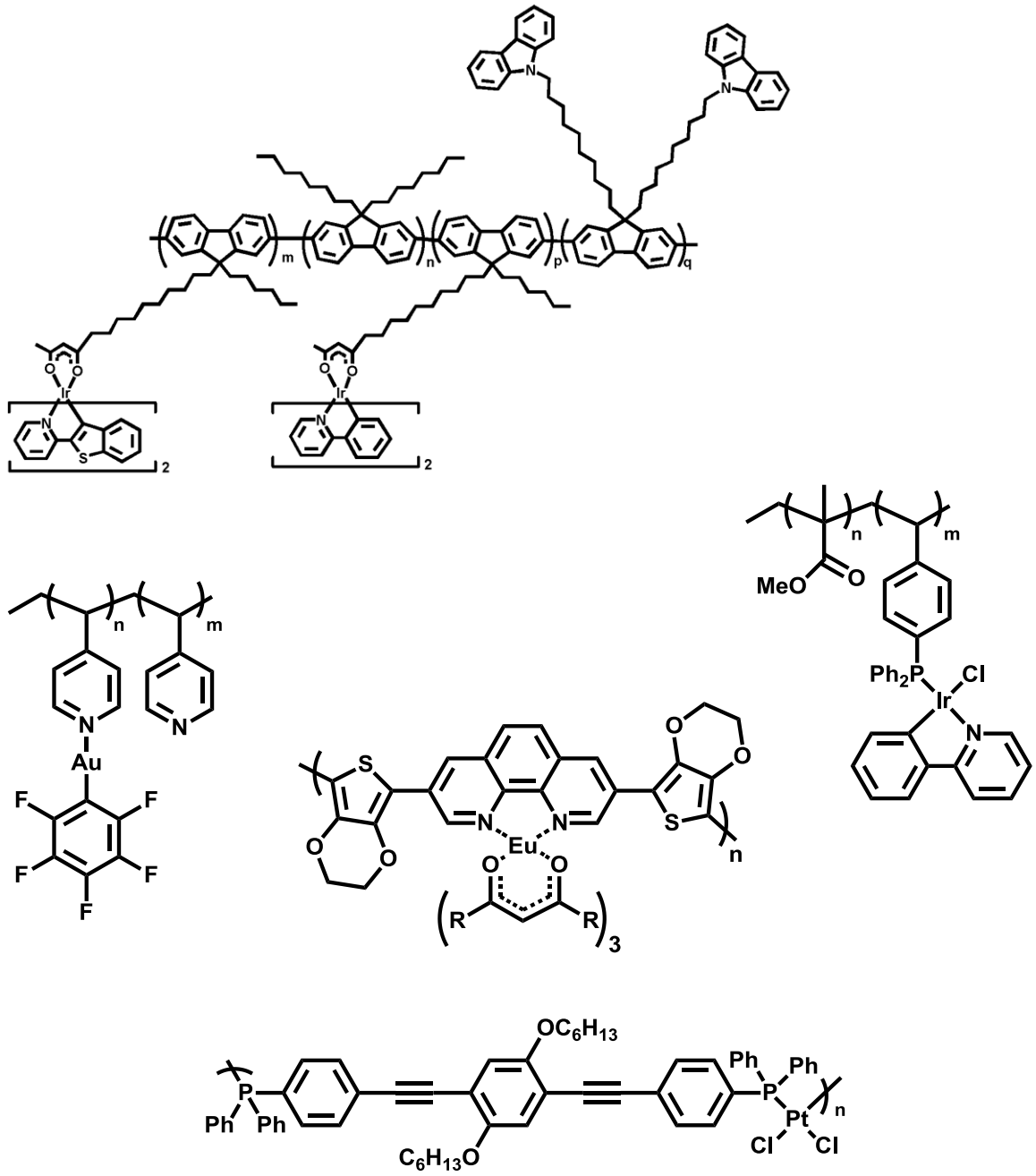

Figure 5. Selected luminescent metallopolymers from the literature.[48-51]

Numerous metallopolymers, as shown in Figure 5, have been developed exhibiting excellent photophysical properties and quantum yields. Rawashdeh-Omary *et al.* utilized poly(4-vinyl)pyridine polymers with pentahalo gold(I) to produce highly

luminescent metallopolymers.[48] This particular example utilized commercially available polymer backbones with little inherent luminescence to produce Au(I) metallopolymers with quantum yields between 28 and 63%. There are several key attributes associated with the energy transfer and photophysics of these materials that make these materials attractive as luminescent metallopolymers. Au(I) metallopolymers had not only high Φ_{RT}, but the T_1 excitions provided sutiable energy levels for energy transfer into red and blue color centers. Also the short triplet lifetimes in the μs regime both decrease the probability of triplet-triplet annihilation and rapid on/off switching. Lastly, the physical properties of the metallopolymers were advantageous for thin film processing. The metallopolymers possessed not only high air, light, moisture, and thermal stability, but good solubility in organic solvents useful for spin coating deposition.

The role of the metal must be closely considered when producing metallopolymers, especially when considering that Φ_{RT} relies heavily on luminescence from the metal centered and ligand centered transitions. Pt and Pd acetylide conducting metallopolymers were produced from highly luminescent monomers.[49] The resulting Pt and Pd metal centers facilitated fluorescence quenching in the case of the polymers, and Φ_{RT} dropped from 62 to 8.8% for the Pt(II) acetylidine metallopolymer and 32 to 2.2% in the case of the Pd(II) metallopolymer. Furthermore, the lifetimes from monomer to polymer dropped by an order of magnitude, into the ps regime, denoting that vibrational decay processes were preferred.[53-56]

Numerous other metallopolymers have been produced using transition metal/polymer lumiphores. Chen *et al.* demonstrated that highly electroluminescent metallopolymers could be produced using fluorene-carbazole polymers appended with

($Ir(ppy)_3$) and ($btp_2Ir(acac)$) complexes. Effective red-emitting devices were created from the metallopolymers, with significant device improvement observed compared to a poly(fluorene) polymer system.[51-52] Devices produced from different poly(fluorene)/Ir phosphor blends only reached max efficiencies of 0.049 – 1.00 cd/A, max brightness near 57-1459 cd/m^2, and turn-on voltages ranging from 5.7 – 8.0 V. Incorporating a combination of metal phosphors and charge transporting poly(vinyl carbazole) leads to top performing LED devices with luminance efficiencies at 1.28 cd/A, max brightness of 5029 cd/m^2, and turn-on voltage of 3.3 V. The hole mobility for the metallopolymer was found to be 3.1×10^{-7} cm^2/V, two orders of magnitude lower than the hole mobility of poly(fluorene) at 7.7×10^{-5} cm^2/V. The decrease in hole mobility provided by the Ir(III) phosphors facilitate electron and hole trapping, greatly improving the performance in LEDs.

Lanthanide metallopolymers demonstrate great potential for use in light-emitting diodes. The shielding effect from the 5*s* and 5*p* orbitals on the core 4*f* orbitals leads to extremely sharp emission bands and therefore high color purity. The 4*f* to 4*f* transitions are forbidden electronic transitions, therefore, the Ln(III) ions must be indirectly excited *via* the antenna effect. Characterisitic Eu(III) emission was observed in conducting Eu(III) metallopolymers developed by Holliday *et al.* An ethylendioxythienyl-appended phenanthroline backbone effectively sensitized Eu(III) emission, denoted by the hypersensitive peak at 615 nm. Electropolymerization of the Eu(III) monomer stimulated a conformation change in the sensitizing backbone, resulting in a blue-shift of the triplet energy level. The Eu(III) metallopolymers displayed visible red emission under a UV lamp, and well-defined Eu(III) emission peaks were observed in the spectra. There are other Eu(III) metallopolymer systems present in the literature with more efficient

luminescence, but the conducting metallopolymer approach allows for easy control of film thickness and additional copolymers.[50]

Hybrid materials have been researched in hopes of fabricating a full color display using red, green, and blue light-emitting materials. Synthesis of white-light emitting materials can be done either by layering three different emitting materials, or by co-depositing the three materials as one layer.[57-58] PEDOT:PSS electrodes on plastic were spin-coated with PFO and ZnO nanorods were grown atop it at 90 °C creating hybrid white light emitting LEDs. The EL emission shows a broad intense peak from 348 to 700 nm. The ZnO nanorods emit typically in the red region, and an emission band at 666 nm and another near 380 nm assigned to a surface defect ZnO UV emission. A Förster energy transfer process between the PFO and ZnO nanorods created a green emission band at 513 nm. PFO emission band showed up in the violet and blue region at 435 and 464 nm. The hybrid material emits white due to the multiple and broad emission bands from several components of the thin films. The flexible substrate combined with the white light emission make these device films very promising for foldable white LEDs.[124] Other work with ZnO nanorod arrays/PFO hybrid materials have rendered similar results, with color coordinates of (0.2115, 0.3724) corresponding to almost pure white light emission.[57]

Hybrid LEDs compromised of ITO/ZnO/ F8BT/MoO_3/Au were fabricated. In these studies, ZnO growth temperatures were of interest. The growth temperatures used were 150, 250, 350, and 450 °C. Using XRD techniques it was found that (100), (002), and (101) orientations were found for 150 -350 °C. At 450 °C the (002) orientation was favored. Efficient devices were produced as low as 250 °C, with a V_{ON} of 4.1 V and 12260 cd/m^2 maximum luminance. Additionally, a maximum current density of 0.73 cd/A at 5014 cd/m^2 and a maximum luminous efficacy of 0.72 m/W were found. For the ZnO/F8BT devices produced at 450°C, the luminance is lower with a V_{ON} at 5.3 V. However, the maximum current density of 1.35 cd/A at 4300 cd/m^2 is much higher,

leading to an efficacy of 0.98 m/W. The relatively low temperature for ZnO growth makes this preparation for ZnO NPs-based devices attractive for industrial processing.[58]

Red-emitting $ZnCuInS_2$-ZnS (ZCIS) alloy nanocrystals were combined with yellow-green emitting poly[(9,9-dioctyl-2,7-divinylene fluorenyl ene)-*alt*-*co*-(2-methoxy-5-(2-ethylhexyloxy)-1,4-phenylene)] (PFPV) to create white-light emitting hybrid LEDs.[129] The ZCIS-ZnS nanoparticles were made using an inorganic precursor solution of DDCZ (Zinc diethylthiocarbamate) in tri-octylphosphine and 1-octadecene.[130] CuI and InI_3 and were dissolved in oleic acid. The ZnS and Cu-In solutions were mixed in a flask and heated at 210 °C for 10 minutes. The top ZnS shell by using the same ZnS solution in oleic acid and reacting for 5 min at 200 °C. The resulting nanoparticles were washed with methanol several times. The ZCIS/ZnS nanoparticles were mixed with PFPV and polystyrene in toluene and coated directly onto a LED chip. Additionally, a hybrid phosphor was filled into the mold. Initial PL spectra of the ZCIS nanoparticles showed that the emission profile was blue-shifted from 655 nm to 575 nm based on Zn content. Unfortunately, poor quantum yields of 5-7% were measured, limiting the performance of $ZnCuInS_3$ samples. ZnS was used to passivate the defects on the surface of ZCIS because of good chemical stability, large band gap, similar lattice, and non-toxicity. The ZnS greatly improved performance by providing less non-radiative pathways for electron and hole separation. Passivation also greatly increased performance by providing favorable anti-site defects that facilitated localization of electrons and holes predominantly in the CIS core. This passivation increased PL intensity and greatly increased the quantum yield to approximately 46%. PFPV emission bands overlapped with the absorption bands of the ZCIS/ZnS. A Förster energy transfer process developed between the inorganic and organic materials when polymer/NP blends were within the Förster radius. Broad emission occurred when PFPV:ZCIS/ZnS was 1:15. White light emitting LEDs produced from PFPV:ZCIS/ZnS had luminous efficacy of 4.15 lm/W and CIE chromaticity coordinates of (0.3891, 0.3357) at 20 mA. Work with ZCIS/ZnS

showed further promise as a red converter for white light. More so, based on the Zn content and polymer/NP blending conditions, the color of the LED can be readily tuned.[59]

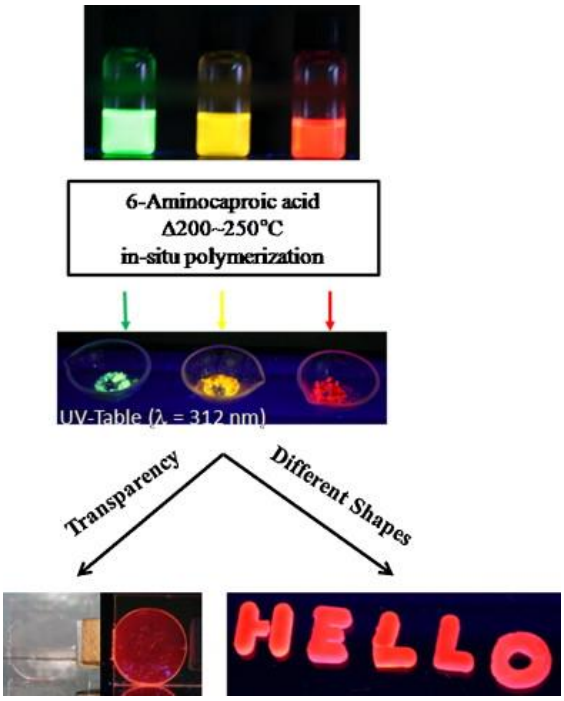

Figure 6. *In-situ* polymerization of the CdSe NPs yields highly luminescent hybrid polymers. The drop cast polymers are transparent in ambient light conditions. Edited and reprinted with permission from ref 60. Copyright 2007 Elsevier.

A wide array of polymers can be used as active layers in PLEDs, and work by Yuan *et al.* focused on using 5 wt% CdSe NPs, ranging from 3.2 nm to 6.6 nm in diameter, with a nylon monomer, 6-aminocaproic acid, solution in a one-pot *in situ* polymerization at 220-250 °C to form inorganic-organic hybrid blends. NP size was verified pre-polymerization using TEM imaging, with the size of CdSe NPs being controlled by changing the reaction time of a hot injection synthetic method featuring a hexyldecylamine capping agent. The emission profile became more red-shifted as the

NPs increased in size, and green (QY=42%), yellow (QY=45%), orange (QY=40%), and red (QY=60%) emitting samples were studied. No significant decrease in quantum efficiencies or shift in emission was evident after polymerization and simple UV-lamp experiments showed transparency of the films. The nylon component enabled easy modification of the shape of the devices yielding highly luminescent hybrid polymers that can be dispersed through simple drop-casting (Figure 6). Temperature degradation occurred for the films after 40 °C suggesting that the nylon has a detrimental effect on the chemical stability of the hybrid material.[60]

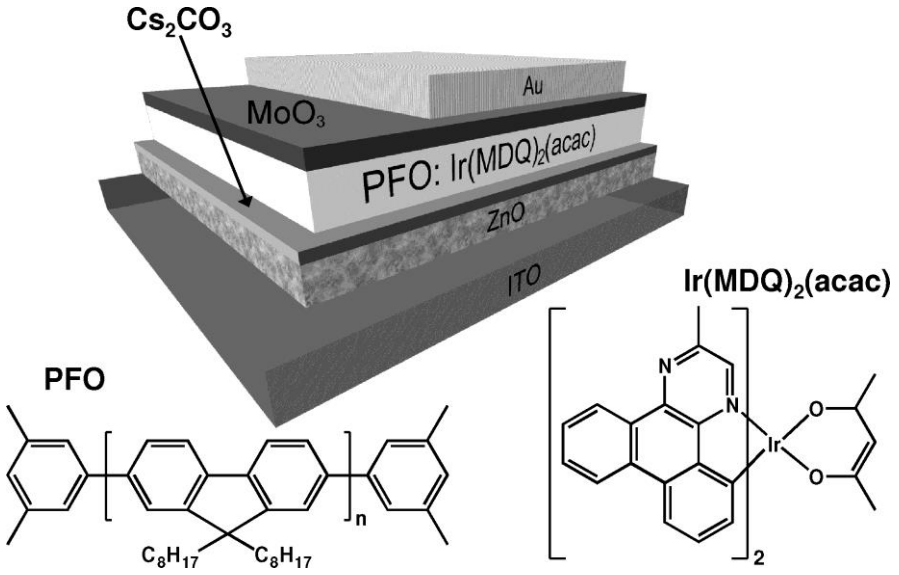

Scheme 1. The device layout scheme and electroluminescent organic components PFO and Ir(MDQ)$_2$(acac).[61-65]

Air-stable ZnO NPs were combined with blue emitting PFO, poly(9,9-dioctylfluorenyl-2,7-diyl), and iridium-(III)*bis*(2-methyldibenzo[f,h]quinoxaline) (acetylacetonate), Ir(MDQ)$_2$(acac), as an orange-emtting dye, to create a hybrid LED that would utilize both NPs for charge injection and a heavy metal phosphor as a method to create efficient films. ITO/ZnO/Cs_2CO_3/PFO:Ir(MDQ)$_2$(acac)/MoO_3/Au devices (Scheme 1) with different concentration of the triplet emitter by wt% were made in a

series to explore the different device properties based on Ir^{3+} dye. V_{ON} was low for the devices, with initial devices showing luminance as low as 1.5 V – 2.0 V. The *J-V* characteristics are not linear, with a large increase in the luminance starting shortly after 2 V, and maximum luminance above 2000 cd/m^2 at 8 V. This rapid increase in current density could be contributed to the emission zone at low voltage between the ZnO and Cs_2CO_3 centering near the surface of the cathode, enabling efficient quenching of the excitons formed. Regulation of the $Ir(MDQ)_2(acac)$ to extremely low wt% showed a proportional decrease in luminance, with the device performance with 0.5 wt% Ir^{3+} triplet emitter exhibiting the best results of +2000 cd/m^2 at 8 V, and 0.004 wt% Ir^{3+} dye devices having maximum luminance of only 300 cd/m^2 at 8 V. Luminance efficacy measurements gave a value of 2.7 cd/A, which while not the highest for these types of devices, shows that inclusion of phosphors in hybrid devices can be extremely beneficial to device performance.[61-63] The PFO blue emission increased as $Ir(MDQ)_2(acac)$ concentration decreased, and further analysis showed that the orange EL emission moved to white emission as the $Ir(MDQ)_2(acac)$ concentration moved from 0.5 wt% to 0.02 wt%. Further endeavors in these types of systems looks promising for the production of effective, color-tunable, hybrid light-emitting devices, and more work could render very effective PLEDs. An aqueous chemical growth process was used to grow *n*-ZnO nanorods onto a blend of *p*-type polymers, first PFO/NPD (4,4'-*bis*[*N*-(1-napthyl)-*N*-phenyl-amino]biphenyl) on PEDOT:PSS and then PVK/TFB (poly(9, 9-dioctyl-fluorene-*co*-*N*(4-butylphenyl)diphenylamine) on PEDOT:PSS. These hybrid films were studied, and photoluminescence spectra found that the ZnO PFO/NPD devices emitted yellow-green where ZnO dominated photoluminescence at 554 nm as compared to the 458 nm emission from only PFO/NPD. The other hybrid films consisting of ZnO on PVK/TFB also showed ZnO dominant emission slightly red-shifted at 568 nm, most likely due to defects, with PVK/TFB emitting weakly at 458 nm. Blended emission occurs for the hybrid materials with whitish bluish emission dominating the visible light from the films.

EL measurements found that maximum current was 0.12 mA at 16 V for the PFO/NPD, and 0.10 mA at 18 V for the PVK/TFB devices. Almost pure white emission was attained for these devices, but a different device structure and charge injection layers may aid in producing devices with higher current flow and luminance.[64,65]

Metallopolymer and Hybrid Sensors: Ultra-Sensitive Recognition

Direct electronic communication between the metal center and polymer backbone provide effective motifs for recognition of small molecules, VOCs, and ions. Metallopolymer sensors have offered not only high selectivity as sensors, but push the boundaries of detection limits. Simple sensor devices have been developed from these materials with sensitivities as low as 10^{-11} M. The benefits of metallopolymer-based sensors extend further, and are exemplified by the host of different recognition mechanisms observed in these systems. Potentiometric, amperiometric, calorimetric, fluorimetric, optical, and other methods are applied for analyte recognition. In some cases multiple sensing mechanisms are possible from the same material.

Changes in charge transfer, polymer conformation, and redox overlap between the metal and the polymer directly impact the conductivity of the conducting polymer systems. This change in redox conductivity operates as an ultra-sensitive mechanism of molecular recognition. An alternative method to utilizing the metal site for recognition is to incorporate ionophoric ligands directly into a conducting polymer backbone. Swager *et al.* first used this approach using cyclophane receptor units incorporated into a *para*-poly(phenyleneethynylene) material.[66,67] The conducting polymer system was a highly selective sensor for paraquat over other small molecules, with an observed 65-fold

fluorescence enhancement measured in the presence of the paraquat. Since then, amperiometric and fluormetric metallopolymer sensors, as shown in Figure 7, have been developed for small molecules like NO_x, VOCs, and a wide variety of ionic analytes.

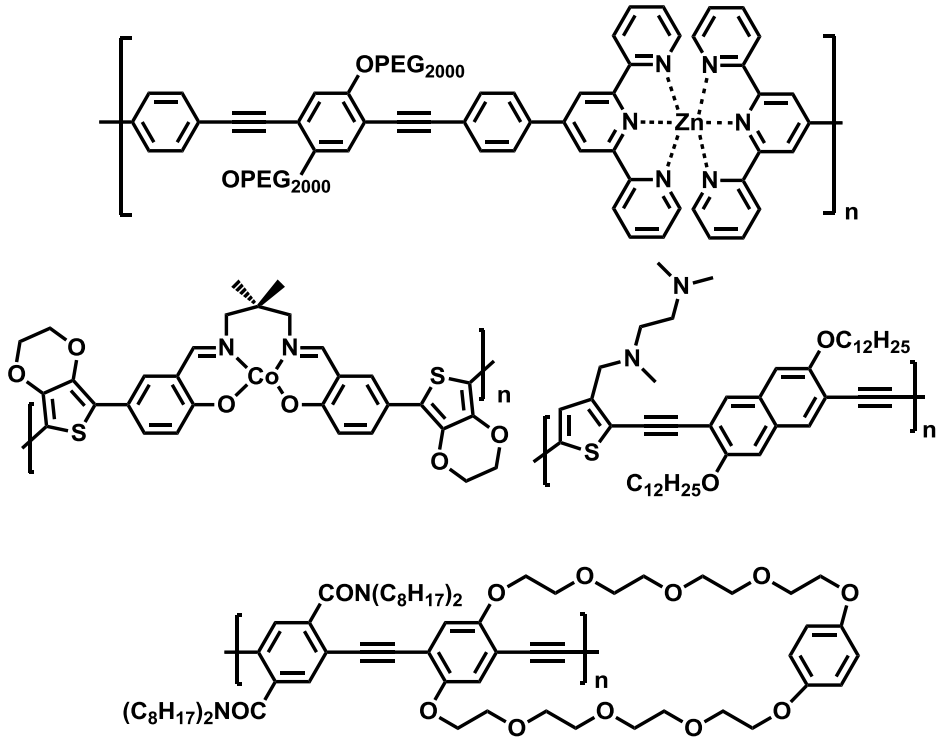

Figure 7. Examples of conducting polymers used as ultra-senstive fluorometric and amperiometric sensor materials.[68-71]

In 2006, Swager and Holliday used an electropolymerizable Co(II) salpen metallopolymer as a solid state sensor for NO and NO_2 gas.[69] The redox matching between the Co(II) center and the $EDOT_2$salpen polymer aided in producing a highly conductive metallopolymer with a low detection threshold. Simple amperiometric sensors were produced by electropolymerizing the Co(II) monomer onto an interdigitated microelectrode. The Co metallopolymer films showed detection limits below 1 ppm for NO_x gas. Additionally, polymer films produced from the $EDOT_2$salpen ligand monomer

showed no discernible recognition of the NO_x analyte. The rational design of this metallopolymer resulted in a highly effective material for sensor applications. Each component of the monomer served a purpose, the neopentyl backbone increased solubility, EDOT groups resulted in the best redox matching between the Co(II) center and the polymer backbone, and the Co(II) center was chosen due the relative stability and known Co-NO_x binding present in literature.

He *et al.* developed a very useful difluorovinylene aromatic ether polymer as a manifold for anionic and cationic recognition.[70] Initial studies with the polymer focused on the change in emission intensity in the presence of different transition metal ions, including Zn(II), Cd(II), and Cu(II) ions. A bathochromic shift and a emission intensity increase in the presence of Zn(II) ions was observed with the polymer. Other d^{10} divalent ions quenched the fluorescent emission intensity of the polymer, and the unbound polymer system demonstrated highly selective fluorometric ionic recognition. Further studies of the Zn(II) metallopolymer showed the material was a highly effective ratiometric fluorescent sensor for fluoride anions. Also, the Cu(II) metallopolymer utilized well known copper reactivity to serve as highly selective fluoride and cyanide fluorescent sensor. Similarly, thiophenyl-*N*,*N*,*N*′-trimethylethylene-diamino-poly(phenyleneethynylene) polymers were used for the recognition of Cu(II) ions in solution.[71] The polymer in the native state showed typical fluorescent response, while a "turn-off" response occurred in the presence of the Cu(II) ions. Post polymerization metallation with Cu(II) ions resulted in a "turn-off" in the fluorescent response. High sensitivity to cyanide ions was observed in the Cu(II) metallopolymer as a "turn-on" in the fluorescent response. An effective ATP sensor was developed using similar

principles from a poly(ethylene glycol) (PEG) decorated *bis*(terpyridine) zinc coordination polymer. Fluorescent response changed as the metallopolymer was exposed to cyanide and phosphates under aqueous conditions. The sensors registered analyte presence at concentrations between 10^{-6} to 10^{-7} M.

Hybrid NP/conducting polymer sensors utilize the conducting polymer component to either increase surface area or as transducer to improve sensitivity. In one example, Au NPs were electrochemically deposited onto an anodized glassy carbon (GC) electrode. The hybrid electrode was prepared by pre-treating the GC electrode with a pH 7.2 buffer solution at 2.0 V for 20 s. Following the buffer, potential scanning from 0.2 to −1.0 V with a 0.1 M KCl solution containing 0.5 mM $HAuCl_4$ for 10 cycles produced the Au NPs on the electrode surface. Poly-brilliant cresyl blue (poly(BCB)) was then electropolymerized onto the Au NPs/GC electrode resulting in a hybrid sensor for H_2O_2 content in commercial cleaners. Initial experiments were performed using 3 μL of a peroxide cleaning solution and amino trimethylene phosphonic acid or hydroxylethylidene diphosphonic acid as the non-interfering organic stabilizer.[72] The phosphonic acid derivatives hinder decomposition of the H_2O_2 under the experimental conditions. For five trials of a 3% H_2O_2 commercial solution, the average measured value of H_2O_2 was found to be 2.93% with a relative standard deviation as low as 2.5%. The sensor application was extended further by testing the peroxide content in H_2O_2-spiked urine. Experiments measuring the known concentration of H_2O_2 produced accurate results. Three different urine samples were prepared with 600, 700, and 800 μM concentrations and measurements performed under low reduction potentials were within a 3% error.[72-74]

A biocompatible chitosan-Au NP matrix for caffeic acid sensing was produced through a green synthetic route developed by Di Carlo *et al.* A combination of deacetylated chitosan was mixed with an organic acid (primarily acetic acid (AA), malonic acid (MA), or oxalic acid (OA)) and $HAuCl_4$ to bring the solution to a gold concentrion of 1 mM, as shown in Figure 8.[75-76] Upon addition of the gold precursor and refluxing at 70 ºC, the hybrid material was then isolated, diluted, and drop-cast onto the electrode surface. Lowering the pH stimulated reduction of the $AuCl_4^-$ and increased the rate of Au NP growth. Reduction times of ~5 min were observed for OA and MA, which is significantly faster than the 70 min AuAA-CHIT reduction time. UV-Vis spectroscopy was used to determine the size of the Au NPs. NP size in AuAA-CHIT and AuMA-Chit was approximated to 10 nm based on surface plasmon resonance (SPR) peak position and intensity. AuOA-Chit samples showed a significant red shift, indicative of larger NPs of heterogeneous size. FE-SEM measurement confirmed the diameter of AuAA- and AuMA-Chit samples to be approximately between 10 - 15 nm in diameter, with AuAA-Chit samples having a higher density than the AuMA-Chit samples. AuOA-Chit samples showed uniquely different morphology and much higher gold content indicating a highly reactive surface layer. XRD measurements were used to determine the diameter size of 37 nm for the AuOA-Chit samples. Further studies showed that the AuAA-Chit-modified Au electrode had the smallest charge-transfer resistance 11.8 ± 0.16 KΩ, and caffeic acid sensing studies were primarily performed using this system. Exceptional limits of detection, 2.50×10^{-8} M, were found for the samples by means of differential pulse voltammetry. LOD and LOQ values were slightly higher than common HPLC methods used for caffeic acid.[76] The sensors proved to be very sensitive with no

interference with catechin and high selectivity toward caffeic acid over ascorbic acid. The environmental and biocompatible polysaccharide, chitosan, when coupled to the highly sensitive and selective sensing capabilities of the Au NPs, demonstrate the great potential of functional hybrid NP sensors.

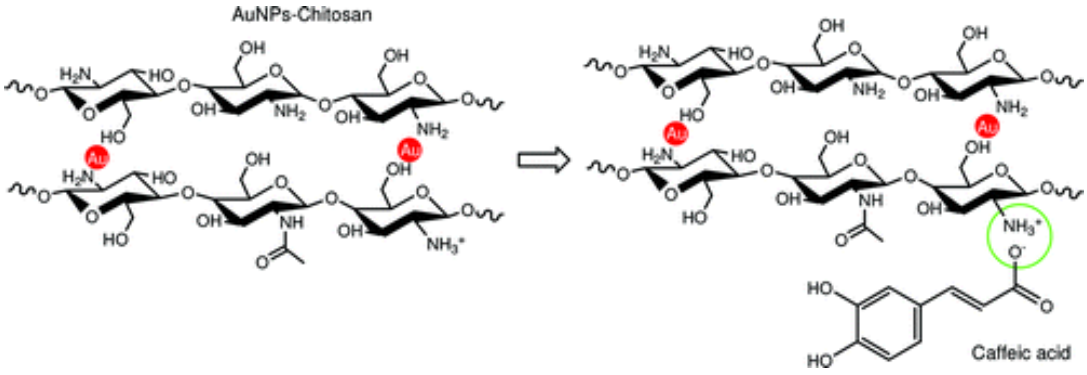

Figure 8. Modified deacetylated chitosan allowed for ordered coordination of the Au NPs, leading to a biocompatible caffeic acid sensor.

Hybrid Conducting Polymer Catalysts

The incorporation of catalytic metals in conducting polymer backbones presents a unique opportunity to produce new hybrid homogeneous/heterogeneous systems for use in catalytic transformations. Numerous examples of semiconducting NP/conducting polymer hybrid nanocomposites are present in the literature, but there are only a handful of examples of metallopolymer catalysts (Figure 9).[77-80] Producing catalytic monomers or inserting catalytic metals post-polymerization is synthetically complex and difficult.

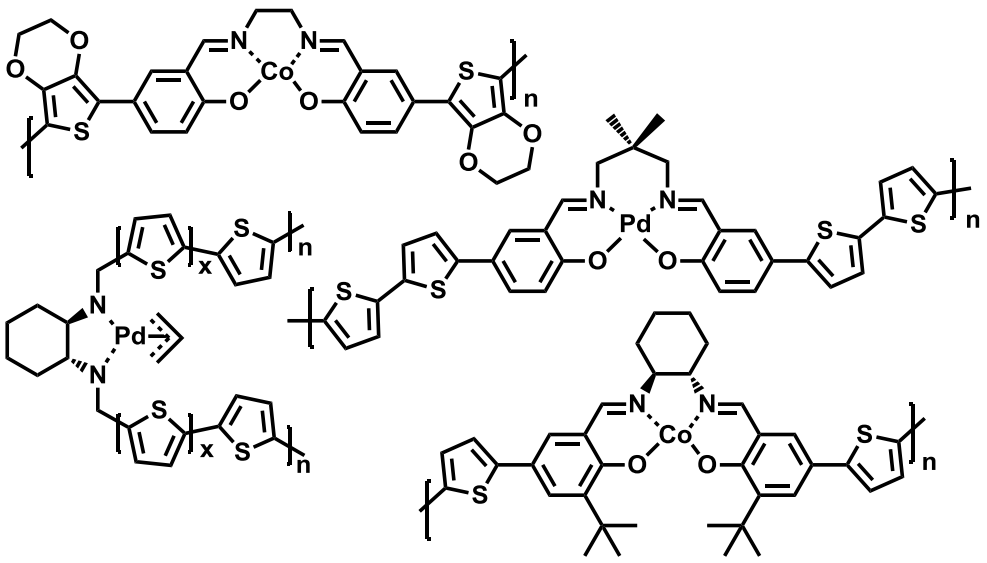

Figure 9. Examples of metallopolymer catalysts in the literature.[77-81]

The Swager group utilized Co(II) electropolymerizable salen complexes not only as the aformentioned amperiometric sensors, but also as effective electrocatalysts.[79] The metallopolymer films were used as electrocatalysts in the transformation of H_2O from O_2. H_2O_2 production is a common side product in electrocatalysis of O_2 in acidic media. A rotating disk-ring electrochemical experiment indicated that a preferential 4 e^- reduction process lead to H_2O as the only product in electrocatalysis. Not only was the metallopolymer catalyst selective, but almost complete conversion of O_2 to H_2O occurred. Another poly-Co(salen) electrocatalyst demonstrated only 39% conversion of O_2 to H_2O.[81] This system used an alternative polymer matrix to produce the metallopolymer. The direct communication and synergistic redox conductivity increase in the thiophene-based Co(II) metallopolymer sensor greatly improved performance.

Another example of metallopolymer-based catalysis utilized similar Co(II)-based monomers and polymers. $FeCl_3$ and $NOBF_4$ were used as chemical oxidants to

chemically polymerize thiophenyl- and pyrolyl-based Co(II) salen complexes. The insoluble polymer networks were produced effectively, and were tested to promote the production of a diol product from the kinetic resolution of epibromohydrin.[78] A variety of reactor types were studied and yields between 47-82% and enantioselectivities ranging from 80-99% were obtained. The cobalt metallopolymer could be recycled up to five times when used in silica media in a fixed-bed reactor, with conversion of 72-83% and ee around 75%. Further studies were conducted with cobalt(III) copolymers with similar enantioselectivities and yields when compared to the fixed-bed reactor testing. In this case there was no need to incorporate the chiral cobalt catalyst into a silica support, and the Co(III) copolymers served as highly effective homogeneous/heterogeneous metallopolymer films.

While cobalt salen-type metallopolymers have shown promise in catalysis, several Pd(II) metallopolymers have been produced as catalysts in oxidation and C-C cross coupling reactions.[77,80] The Wolf group utilized a simple electropolymerizable cyclohexyldiamine to incorporate Pd(II)-allyl into a metallopolymer network. XPS surface analysis and UV-Vis spectroscopy indicated that electropolymerization formed homogeneous Pd(II) containing metallopolymer films. The metallopolymer films were then tested as a catalyst for cross-coupling reaction of fluoroiodobenzene to an aryl boronic acid, aryl alkyne, and ethyl acrylate. In each case the metallopolymer catalyst yielded ~90% product and indicated that it would be useful in Suzuki, Sonagashira, and Heck reactions. A more desirable Heck reaction transformation of α,β-unsaturated 2-haloanilide to a racemic mixture of oxindole was also tested with an isolated yield of

57% after 48 h at 80 ºC. Pd(II) metallopolymers showed not only chemoselectivity, but XPS studies indicated no degradation or decline in Pd(II) in the films after 5 reuses.[77]

A Pd(II) metallopolymer/Pd NP hybrid nanocomposite was created as an electrochemical catalyst for oxygen reduction. The Pd(II) metallopolymer served as a matrix for NP growth with seeding points distributed evenly throughout the films. The NPs were produced through a room-temperature chemical process by cycling between a aqueous $Pd(Cl)_2$ solution and $Na_2CO_3/NaHCO_3$ buffer solution. TEM microscopy showed that the size of the NPs could be controlled by the number of cycles used in the NP growth process. The Pd(II) metallopolymer/Pd NP hybrids indicated an effective oxygen reduction response. Low overpotential primarily produced hydrogen peroxide, while higher overpotentials primarily produced H_2O. While the electrocatalytic materials were not efficiently selective, the measured oxygen reduction was rougly five times higher when compared to Pd(II)-modified carbon nanotubes.[80]

A series of different Pd NP/polymer hybrids, developed by Mallick *et al.*, were used for both hydrogenations and Heck coupling C-C formation reactions. Pd NPs/poly-aminophenol systems were formed by an *in situ* polymerization of aminophenol with $Pd(OAc)_2$.[81] Raman, IR, and UV-Vis spectroscopies showed that benzoid and quinoid components were in the composite. Polaron-bipolaron peaks at 420 nm and excitonic transition peaks at 610 nm were present in the UV-Vis and Raman spectra, respectively. XPS, SEM, TEM/EDX showed the formation of Pd NPs that were both uniform in size and distribution throughout the nanocomposite. TEM images showed that the polymer chains were roughly 100-150 nm in diameter and ~1μm in length. Pd NPs, 2-3 nm in size, were encapsulated in cage-like-fashion in the organic component. The hybrid

material was then utilized as a catalyst in Heck reactions of aryl iodides with various olefins and aryl bromides with acrylic acid. Relatively mild conditions were used for the reaction; triethylamine was used as a base and the reaction was run at 80 ºC for 8 hours. The yield and conversion for both types of reactions with the Pd NP nanocomposite was high with yields ranging from 81-96%. Even for more deactivated aryl bromides, the Heck reaction still had relatively high yields of 75%. Kinetic studies revealed that substituted aryl iodide had conversion rates that were 20% greater than rates of unsubstituted aryl iodide. When compared to other Pd catalysts the Pd NP/poly-aminophenol performed well, with relatively high turnover numbers (TON) with minimal catalyst loading.[82]

Some research approaches have focused on producing cyclohexene from the partial hydrogenation of benzene. Selectively producing cyclohexene over the fully hydrogenated cyclohexane has proven to be a complex challenge. Some systems show preferential production of the active double-bond cyclohexene. Effective catalysts, such as the Ru-black/ZnO materials produced by Nagahara *et al.*, are few with examples of effective hybrid catalyst even more scarce.[83] Two Pt NP materials have shown promise: one implanted into a modified chitosan membrane and the other into a polyimide system.[84,85] Pt NP/polyimide system showed good selectivities toward cyclohexene with 72.4% selectivity. However, the less than 1% conversion for the costly polyimide system turned the focus toward the cheap and easily modified chitosan as the organic platform in an industrially viable hybrid NP nanocomposite. Modifications of the chitosan network, *via* addition of varying degrees of N-*n*-propyl groups produced a marked effect on catalytic performance. While conversion was low, it was observed that both selectivities

and conversion could be improved by increased modification to as high as 85.6% and 1.36%, respectively. Furthermore, relatively small amounts of Pt NPs were necessary to produce significant changes in selectivity and conversion. Mono-dispersed NPs (approximately 5 nm in diameter) stimulated effective catalytic performance.

Combining both the large magnetic susceptibility and high conductivity of magnetite (Fe_3O_4) NPs with the flexibility and conductivity of polypyrrole created an effective hybrid material for electrocatalysis.[86] Reduction of oxygen by conducting polymers has recently been explored. The coupling of magnetite to conducting polymers (26 m/m%) showed great promise as electrocatalysts with rotating disk electrode (RDE) studies of the $4e^-$ reduction of O_2.[87-88] Dark and illuminated measurements showed that the photocurrent in the illuminated hybrid materials was twice that of the dark current. Additionally, the hybrid materials performed better than the materials separately. The electrocatalytic cycle of O_2 reduction by the NP/polymer was further probed by studying the intermediate electrocatalytic reduction of H_2O_2, an intermediate step in O_2 reduction. The NP/PPy hybrid showed 7.5 times higher catalytic activity toward H_2O_2 reduction than the materials separately. This particular electrocatalyst shows promise in solar fuel cells.

A Pd NP/IL polymer catalyst was synthesized using 1-Aminoethyl-3-vinylimidazolium bromide ([VAIM]Br) grafted on a cross-linked polymer polydivinylbenzene (PDVB) hybridized with immobilized Pd nanoparticles. The copolymer was formed using azobisisobutyronitrile (AIBN) as an initiator and NaOH as a cross-linking agent. The polymer solution was mixed with H_2PdCl_4 solution and reduced with $NaBH_4$ to create the Pd NP/PDVB-IL hybrid material. SEM and TEM micrographs

were taken of the catalyst before and after each use up to the third use. These micrographs revelead that the Pd NPs were left both intact and ordered in the material after being subjected to the reaction conditions. XPS measurements revealed a Pd spin-orbit pair for both the fully reduced Pd(0) and Pd(II). The majority of the NPs present are Pd(0) based on peak values in the XPS spectra. The Heck reaction of iodobenzene and methyl acrylate was carried out with a wide variety of bases and temperatures. It was found that at 120 °C with NEt_3, a 97% yield could be achieved in 4 hours. These optimized reaction conditions were then applied in Heck reaction of a variety of iodoarenes with different olefins.[89]

A similar catalyst was made using Pd NPs in a copolymer 3-(2,3-dihydroxypropyl)-1-vinylimidazolium chloride and styrene (Pd@poly-Sty-*co*-DiOH-Cl). Additionally, similarly high yields were found in Suzuki reactions with this Pd NP copolymer. A broad spectrum of reactions were conducted with electron rich and electron deficient arene precursors and further uses of the catalyst showed great recyclability with no significant decrease in yield after six uses. $Pd(OAc)_2$ was reduced with $NaBH_4$ into Pd NPs in a copolymer of 3-butyl-1-vinylimidazolium iodide and divinylbenzene. These findings are similar to work by Han, Wang, and Liu, using Pd NP copolymers as a catalyst for Sonagashira C-C coupling reactions.[90,91] High yields were attained with H_2O as a solvent under 3.0 MPa CO at 130 °C for 6 hours. The Pd(0)/Pd(II) NP/polymer hybrid materials showed great catalytic performance for an array of C-C coupling reactions in the presence of the ionic liquid copolymers. This NP/polymer hybrid materials retained recyclability and catalytic activity. Partial solvation of the hybrid catalyst by the ionic liquid component from the organic polymer

increased the catalytic surface area. The highly active Pd NPs permitted for minimal amounts of catalyst to be used in each case.[91]

SCOPE OF THESIS

We seek to improve the performance and function in several thiophene-based conducting metallopolymer and conducting polymer/NP hybrids by understanding the electronic interactions between the inorganic and organic components. Grasping the electronic relationship of each component to the function of a conducting polymer system is paramount to improving the function of this class of materials. Changing a single component in the conducting polymer-based material, even slightly, can have a dramatic effect on the effectiveness of the polymer in a functional device. The electronic interface between organic and inorganic components can be studied by tuning and controlling either the organic HOMO-LUMO or the inorganic conduction and valence bands in the hybrids. Herein, we will study the interface in conducting polymer/NP materials by incorporating a highly tunable inorganic component, such as Cu_2ZnSnS_4 semiconducting NPs, into a metallopolymer film. The nanoparoticles will provide a synthetic and spectroscopic handle to probe the electronic behavior at the interface in the hybrid materials. Aligning the energy levels in these systems could lead to a better *p*-*n* junction and change the photoelectronic behavior.

Further studies beyond hybrid material photoelectronic devices, will focus on the synthesis, characterization, and the change in conductivity of an electropolymerized ionophoric polymer sensor in the presence of metal cations. Tuning the sterics and the electronic character of the receptor environments should result in varying selectivity and sensitivity. A series of aroyl(thiourea) appended bithiophenyl and ethylenedioxy-

thiophenyl polymers will be produced to study the effect of intramolecular and intermolecular electronics on ionic recognition. Post polymerization complexation in the systems will be investigated to understand the role of redox conductivity in conducting polymer functionality. The intercalation of metal ions into the conducting polymer and eventual adsorption should lead to completely different electronic band structure and resulting electronic characteristics.

The highly conjugated thiophene based systems are naturally highly luminescent materials and highly effective chromophores can be produced through understanding the photophysics of the materials. Incorporating BT and EDOT groups into highly conjugated ligand chromophores allows for not only electropolymers, but can lead to unique photophysical behavior in the monomer and conducting polymers. Novel highly conjugated EDOT-appended phenazine and quinoxaline chromophores were produced to study the effect of incorporating electropolymerizable groups onto already known ligand chromophores. Studying these systems as sensitizers for Ln(III) emission could lead to a better understanding of how the extended conjugation introduced by adding the electropolymerizable groups effects luminescence efficiencies of the complexes. A library of Ln(III) monomers and metallopolymers has been synthesized and characterized to probe the electronic behavior in the highly conjugated electropolymerizable phenazine and quinoxaline systems.

Incorporating catalytic metals into a redox active conducting polymer presents a unique opportunity to attenuate the electron density on the metal center by electrochemically doping the polymer backbone. The modulation of the electron density in turn will attenuate the bond distance between the metal and any ancillary ligands.

Controlling the redox activity of the polymer, and indirectly the active metal, should facilitate the activation and conversion rate of catalysis. Redox-active electropolymerizable $P^{O}C^{O}P$ ligands have been synthesized to serve as a platform to study this change in catalysis. Furthermore, several model complexes and a Rh(I)(CO)$P^{O}C^{O}P$ metallapolymer will be produced to observe the electrochemically-induced ancillary ligand attenuation. A Rh(III) $P^{O}C^{O}P$ metallopolymer have been produced to investigate the effect oxidation of the polymer backbone has on the hydrogen-transfer hydrogenation of cyclohexanone to cyclohexanol.

Chapter 2: Composition Effects on the Photodiode Behavior of $(Cu_2Sn)_{x/3}Zn_{1-x}S$ ($0 \leq x \leq 0.75$) NPs in a Cu(II) Conducting Metallopolymer

INTRODUCTION

The search for new photovoltaic materials has led to focused research on hybrid organic-inorganic nanocomposites.[31-52] Combination of the two components yields a new class of materials with unique electronic properties useful for applications in various opto-electronic devices. By integrating an organic material with an inorganic material, the properties of the two materials can be utilized in the final product.[92,93] The organic material will typically act as the hole transport material while the inorganic material will act as the electron transport material, as shown in Scheme 2.[93,31] Charge recombination is mitigated by forming a bulk heterojunction between the two components, leading to a material with domains small enough for effective separation and flow between the electron-hole pairs.

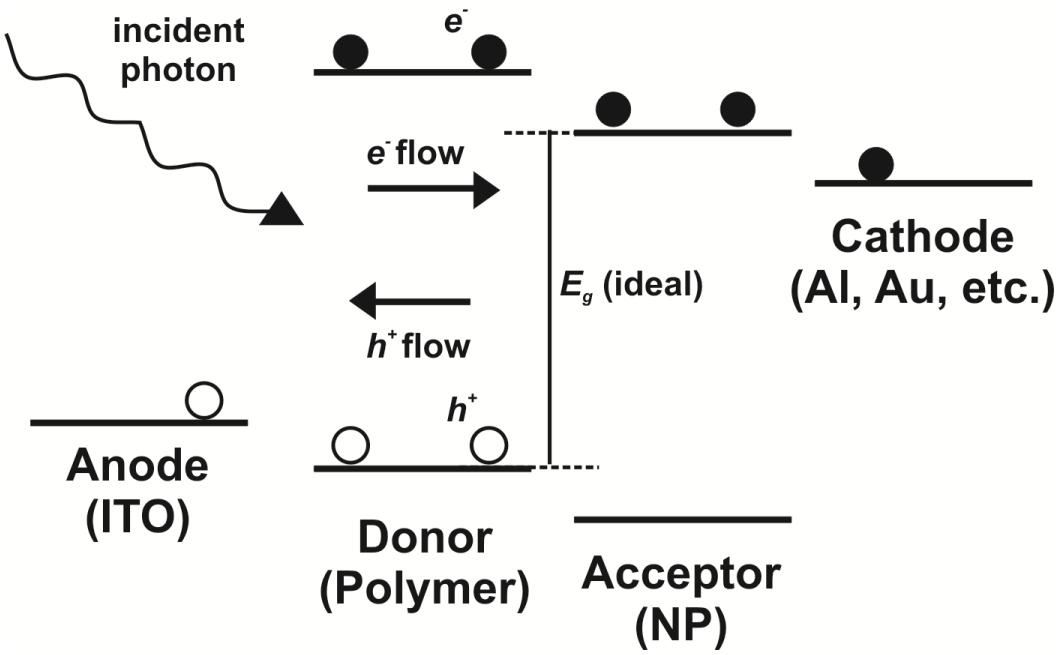

Scheme 2. The flow of electron-hole pairs in a hybrid inorganic-organic PV device.

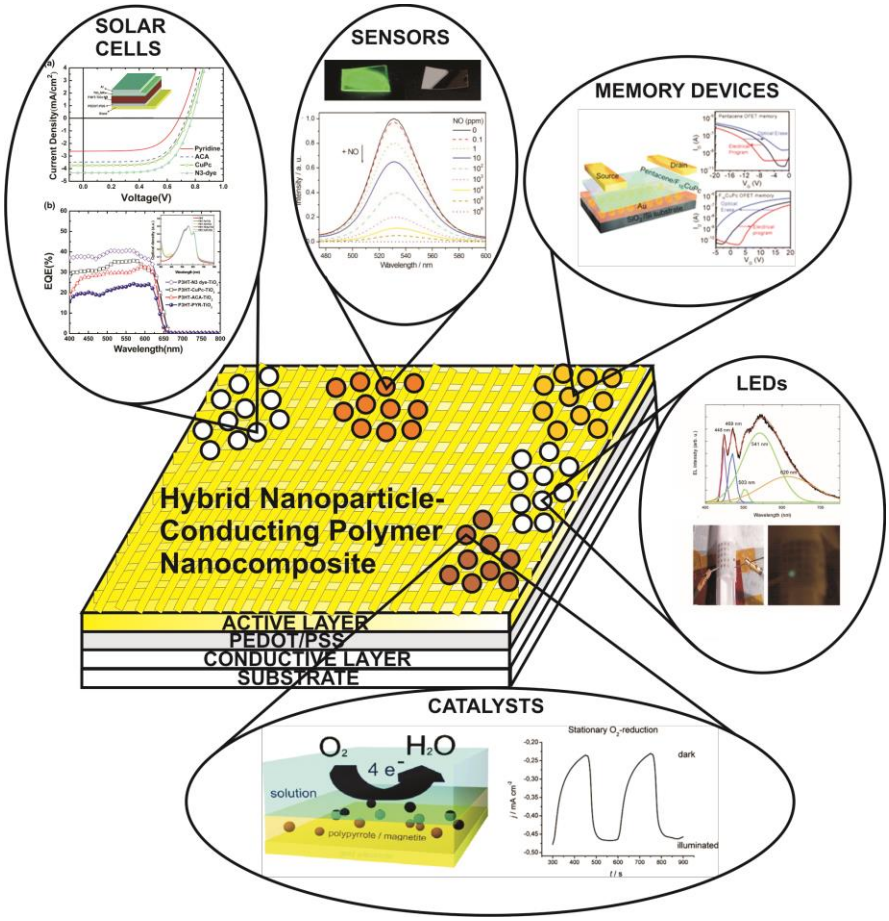

Figure 10. Hybrid materials have been utilized for many useful applications. State of the art devices have been produced using a broad variety of polymers with well known NPs, like CdSe, PbS, ZnO, FeO, Fe_2O_3, and many others.

In order to achieve efficient charge transfer, a good interface between the donor polymer and NP acceptors is very important. Increasing interfacial areas improves the overall function of the material. Incorporation of metal and semiconductor NPs (NPs) into an organic material yields a material with high interfacial area. Along with high interfacial area, the use of NPs allows for easy tuning of the band gap, due in part by the quantum confinement effect. Modulation of the band gap can be achieved by varying the size and composition of the NP.[32] Incorporating NPs into a polymer matrix has been

approached from various synthetic pathways including the use of functional group appended polymers, surfactants, layer by layer deposition, coevaporation, and post-synthesis mixing of the two materials.[92-95] Each method is advantageous due to ease of synthesis and NP loading. By changing the NP composition or size, the band gap of the NP is altered and can therefore be aligned with the bandgap of the polymer ensuring efficient exciton dissociation, as shown in Scheme 2. Altering the bandgap leads to changes in the absorption of the material, for example by changing the composition of the NPs from CdS to PbS, there is an increase in absorbance from <700 to ~1500 nm. Conducting hybrid nanocomposites have been utilized for a wide variety of applications, such as photovoltaic devices, LEDs, sensors, memory devices, and catalysts (Figure 10). The bulk of research in these materials focuses on applications in photovoltaic materials.

Using polymers as the organic component in hybrid materials, especially conjugated polymers has been researched due to the high conductivities, electroluminescence, chemosensitivity, and electrochromism.[94] While some polymers may be insoluble, synthetic variations have been made in an effort to increase solubility and processability.[94] Conjugated polymers can also be synthetically modified with end groups that will act as capping ligands for NPs introduced into the polymer matrix. Further synthetic modification to conjugated polymers has lead to NPs attached to side-groups giving a conducting polymer with pendant NPs. It is important to note that segregation of the organic and inorganic components is commonly detrimental to performance as functional materials, and phase integration must be promoted during synthesis of the hybrid nanocomposites. Phase segration occurs over time and long range order and stability must be considered during the synthesis of the hybrid materials.

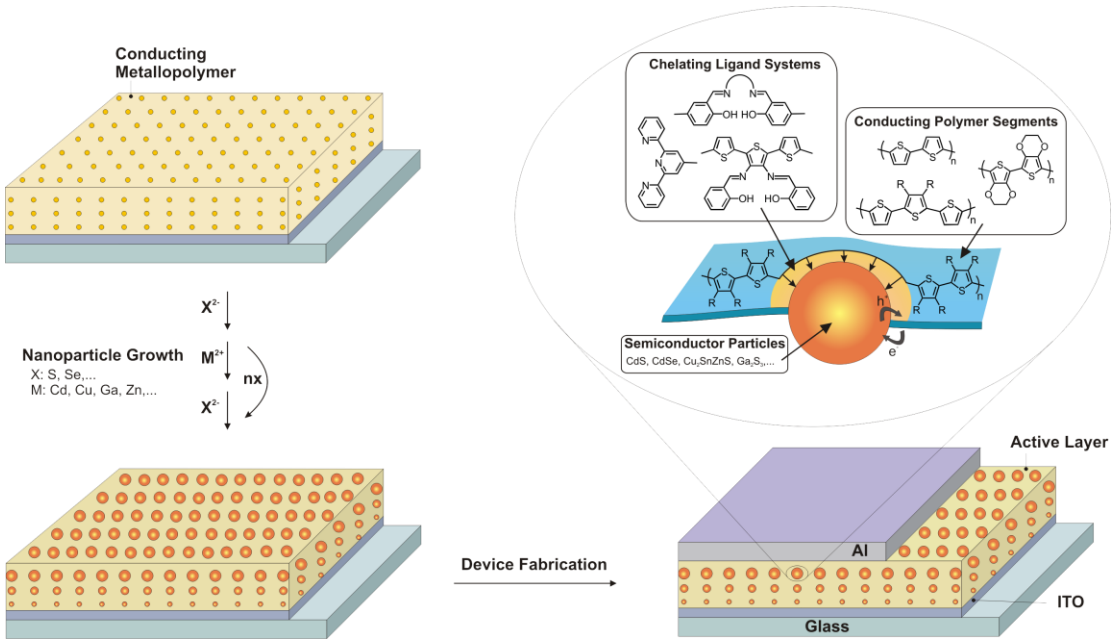

Scheme 3. The scheme outlines the approach taken to produce an array of different NPs in a conducting metallopolymer matrix. Wolf type II and type III metallopolymers were used as a seeded growth platform.

This problem inspired our group toward a novel synthetic approach to conducting metallopolymer/NP composites.[97,98] Typical routes to hybrid nanocomposites suffer from either a lack of versatility or face difficulties maintaining and controlling long-range order between the two phases. The method developed in our group uses conducting metallopolymer scaffolds as seeding points for NP growth. Scheme 3 outlines the room temperature solution-based process and the diverse number of metallopolymers and NPs combined.

The metallopolymer seed point process holds several advantages over other known hybrid material processes, such as the infiltration method, solvothermal mixing method, and successive ionic layer adsorption and reaction (SILAR) method. The first

method utilizes a block copolymer template that is organized through a UV-activated cross linking reaction. Atomic layer deposition (ALD) is then used to produce a nanostructured metal oxide NP surface.[99-101] The method produces very highly ordered films of uniform NP size at room temperature, however, the process is restricted to oxide-type and pure metal NPs and the block copolymer must be changed to modify the size of the NPs. Furthermore, this process while useful to produce NP films is actually not capable of producing hybrid films.

Solvothermal mixing methods are the most common and feature mixing of the pre-fabricated NPs and polymers *via* solvent deposition. This approach to hybrid photovoltaic materials is very versatile, allowing for any soluble polymer and NP to be used in the process. Many difficulties occur within the produced hybrids, and phase segregation is a major problem.[31-36] Breakthroughs in producing more ordered block copolymers and low temperature NP synthesis have made this method more effective, but the lack of room temperature growth and long range order hinder the industrial viability of this method. Alternatively, the SILAR method utilizes ionic solutions adsorbed onto substrates to gradually grow NPs through subsequent reactions and ion exchange/reduction cycles.[102-104] Similar to the ALD method, this method has not been adapted fully to hybrid materials. Furthermore, the films require a large amount of cycles to produce films, typically 40-100 cycles, and the synthesized NPs are of varying size and roughness.

Initial work with the seeded growth process rendered samples with highly ordered NPs of homogeneous size in the metallopolymer. TEM images below portray the distribution of NPs in the seeded growth process. Figure 11 helps illustrate the differences between NP distribution, size continuity, and roughness between the previously described methods. NP aggregation is present in the CdSe NP/P3HT hybrids from Alivasatos's work using solvothermal methods. TEM images of Cu_2ZnSnS_4 (CZTS) NPs produced from SILAR methods suffered from similar problems, with a large size distribution found for the NPs. We have seen with CZTS NP/metallopolymer hybrid materials grown *via* the seeded growth process uniform growth and high order in the TEM images.

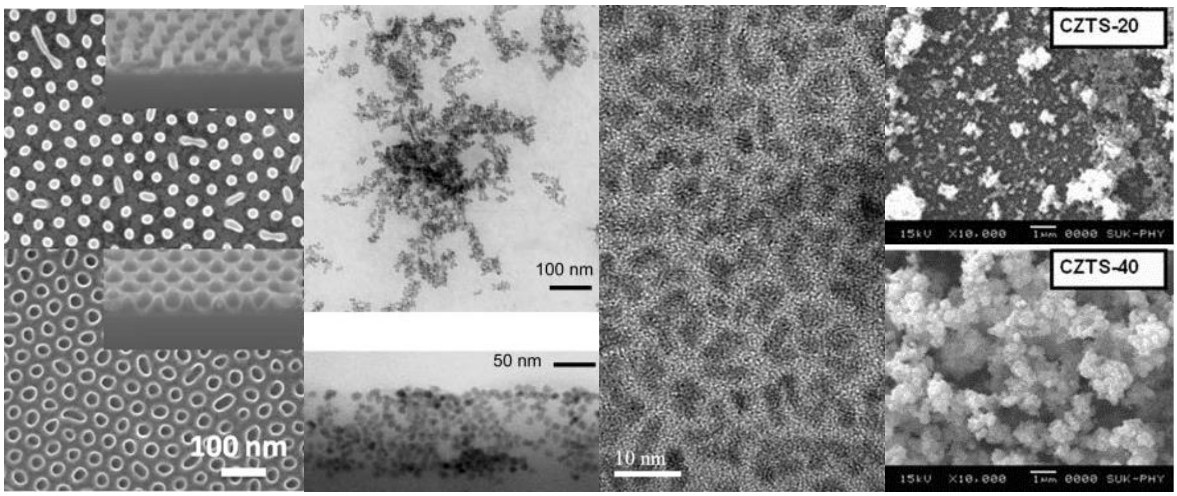

Figure 11. TEM images of NP growth processes discussed herein. NP aggregation and size inconsistencies are dominant in SILAR and solvothermal methods.

Cu-based Hybrid Materials

The seeded growth process allows for a wide variety of hybrids to be produced, and initial photovoltaic device studies with Cd-based metallopolymer/CdS NP films

achieved power conversion efficiencies (PCE) near 0.08%. Further investigation of the energy level relationship between the organic and inorganic components indicated that the two materials possessed poor energy alignment. This is reflected by poor short circuit current (J_{SC}) and lower fill factors (FF) measured in the prototype devices. To overcome this problem, CdSe NPs were instead grown into the Cd metallopolymer. However, while the CdSe NPs conduction and valence bands had a better alignment to the HOMO-LUMO of the Cd(II) metallopolymer, no increased device performance was observed. An alternative approach to including CdSe NP in the Cd(II) metallopolymer was utilizing CZTS NPs in a Cu(II) metallopolymer instead. There are only a few cases of Cu-based semiconducting NPs as components in hybrid solar cells.[105-109] Of these, hybrid materials made from $CuInS_2$(CIS), $CuInSe_2$(CISe), and CuInSSe(CISSe) are the only inorganic-organic Cu-based hybrid materials that show any photovoltaic response. CIS and CISe are viable replacement to the less stable and more toxic Cd-based inorganic semiconductors, due to easy band-gap tuning, strong aversion to light-induced degradation, and lower toxicity.[108,109]

Initial studies in CIS nanocomposites by Arici *et al.* were with colloidal TPP (triphenyl phosphate) capped $CuInS_2$ in the chalcopyrite phase with PEDOT:PSS.[108] At AM 1.5 conditions (80 mW cm^{-2}) the V_{OC} was 0.15 V, the J_{SC} was 4 μA cm^{-2} with a low efficiency of 0.003%. Piber and coworkers extended on this approach using the same type of material, and made devices exhibiting a V_{OC} ranging from 0.36 V- 0.48 V, a J_{SC} from 2.7 to 46.6 μA cm^{-2} and efficiencies up 0.011%. Another effort in creating simple CInSe hybrid solar cells started with a simple spin-coated blend of TOPO-capped

CInSe/P3HT. The devices showed modest photovoltaic behavior with low short circuit current of 0.3 mA cm^{-2} and high open circuit voltage of approximately 1 V.[105]

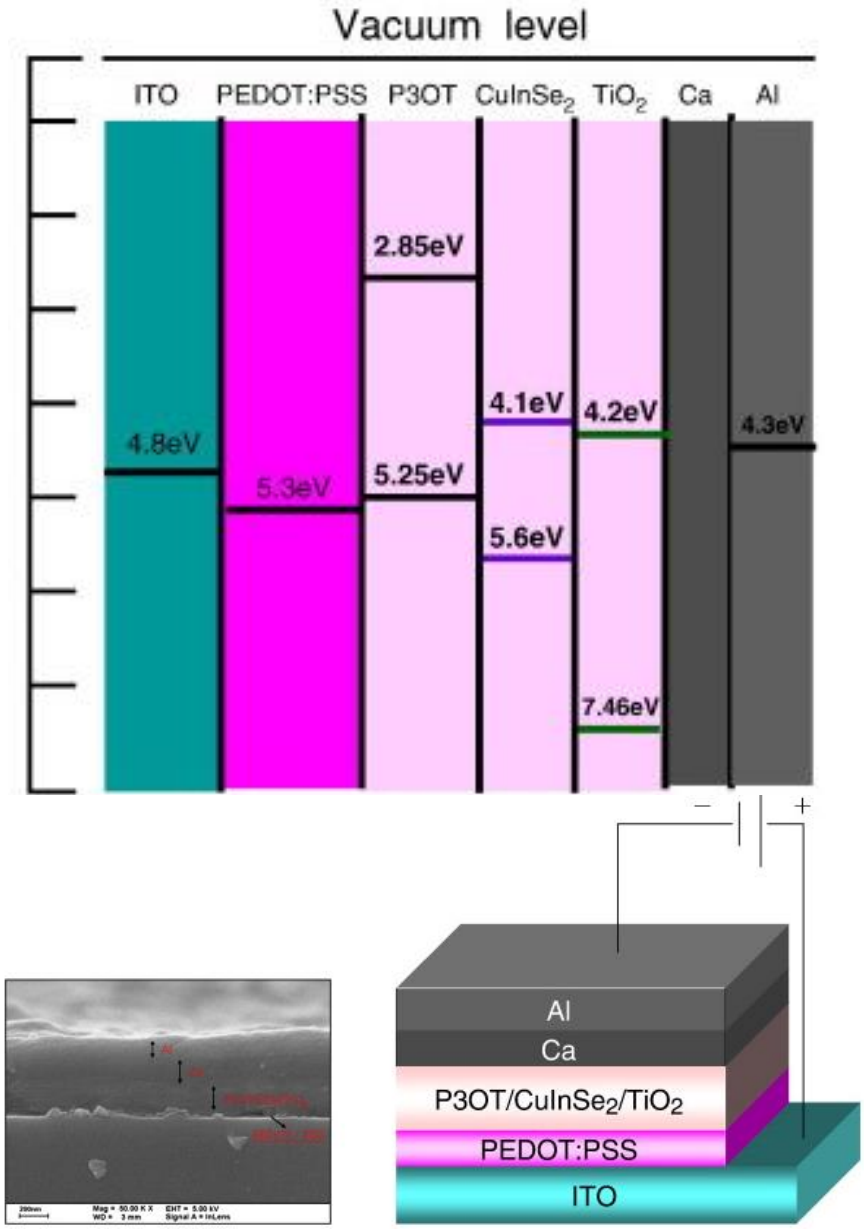

Scheme 4. The energy level diagram and device schematic of the P3OT-capped $CuInSe_2/TiO_2$ device. Edited and reprinted with permission from ref 107. Copyright 2011 Elsevier.

Over the past few years more promising CIS and CISe hybrid material devices have appeared in the literature. Wang *et al.* used MEH-PPV (poly(2-methoxy-5-(2-ethylhexyloxy)-1,4-phenylene vinylene) as electron donor into CIS NPs, due to both favorable energy levels and electron affinities, to create a hybrid material that has a spectral response from 300 to 900 nm. The charge transfer process of the MEH-PPV to CIS NPs with 4-*tert*-butylpyridine capped ligands, studied through photoluminescence and IPCE experiments, occurred much more efficiently with the presence of the capping agent. A relatively high V_{OC} of 0.62 V, J_{SC} of 7.76 μA cm^{-2}, FF of 0.23, and IPCE of 0.128% were achieved for the capped CIS NP devices, and lower IPCE of 0.047% was achieved for uncapped CIS (V_{OC} of 0.35 V, J_{SC} of 2.85 μA cm^{-2}, FF of 0.23). [106]

In 2011, Wu *et al.* utilized TOPO-capped CISe NPs doped with 15 wt % TiO_2 and with regioregular poly(3-octylthiophene-2,5-diyl) P3OT, to form a hybrid solar cell on PEDOT:PSS/ITO substrate, as shown in Scheme 4.[107] The devices were made through spin-coated deposition, followed by annealment at 140 °C and 90 °C. A series of devices were studied in which the ratio of CISe NPs and PO3T were changed from 1:0 to 1:25 showing that the ratio of 1:15, thus named POC115, had the highest photovoltaic activity with a V_{OC} of 0.33 V, J_{SC} of 1.42 mA/cm^2, FF of 0.40, and PCE of 0.189%.[110] Further studies of this ratio POC115 were done by changing annealment temperature of the final device and annealing time. The best results were found at an annealment temperature of 125 °C in 30 minutes, with a marked increase in photovoltaic activity, with the best device having a V_{OC} of 0.49 V, J_{SC} of 3.20 mA cm^{-2}, FF of 0.43 and a PCE of 0.674%.[111] The methodical approach of optimization yielded devices with relatively good PCE and device characteristics. In other work, zinc containing CIS NP hybrid materials were

synthesized using copper, zinc, and indium salts, thiourea, and poly(3-(ethyl-4-butanoate) thiophene (P3EBT) dissolved in pyridine coated on ITO/glass and heated to 180 °C.

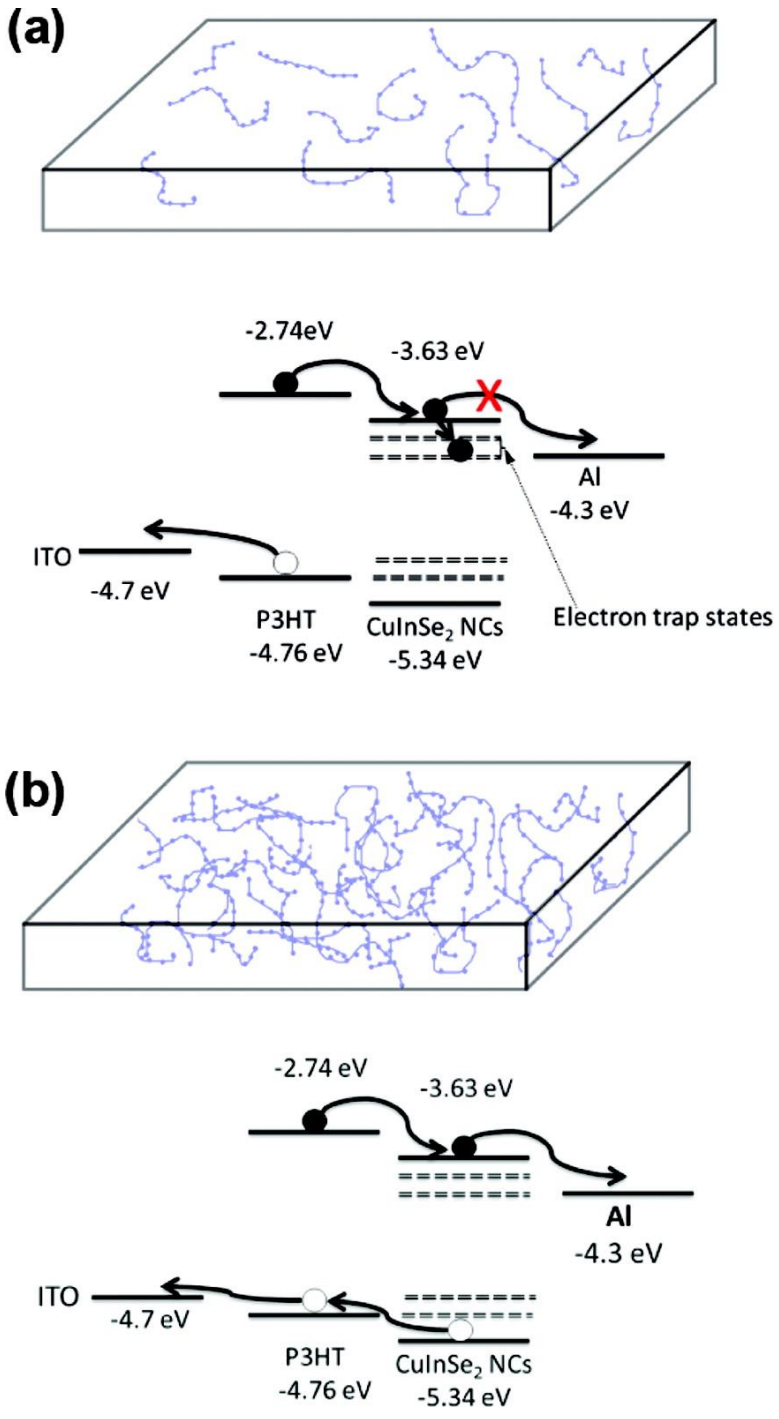

Scheme 5. The energy levels and charge carrier transport in the $CuInSe_2$/P3HT. (a) CISe NP weight ratio of 1:19, and (b) a CISe NP weight ratio of 6:1.[112]

The two types of devices were studied and the introduction of Zn salts in ratio of Zn/Cu of 0.1, leading to an increase in the open circuit voltage. The CIS NP/P3EBT devices had a V_{OC} of 0.540 V, J_{SC} of 1.20 mA cm^{-2}, FF of 0.27 and a PCE of 0.29%, and the Zn-CIS NP/P3EBT devices V_{OC} of 0.660 V, J_{SC} of 1.40 mA cm^{-2}, FF of 0.27 and a PCE of 0.42%. Zn-CIS increased open circuit voltage, but opened the inorganic component to oxidation, and degradation of the films caused a marked decrease in device performance after 48 hours.[108]

A combination of $CuInSe_2$ NPs, made in a large gram scale through a colloidal route, was combined with P3HT to make hybrid devices.[112] The HOMO-LUMO levels, the trap energies, and the affect of annealing temperature on device performance were studied. Electrochemical methods were utilized to find the valence and conductance bands of the $CuInSe_2$ NPs as well as the presence of electron trap states, and Scheme 5 depicts how the CISe NP/P3HT nanocomposites with small amount of $CuInSe_2$ NPs (1:19) and with more $CuInSe_2$ NPs (6:1) (Scheme 5a) suffer from multiple electron trap state pathways, while bulk $CuInSe_2$ (Scheme 5b) showed no trap states in the CV. Devices were made from the 6:1 ratio and annealed for 20 minutes from 110 °C to 250 °C. Annealment at 220 °C produced the best devices with V_{OC} of 0.56 V, J_{SC} of 0.56 mA cm^{-2}, *FF* of 29.7%, and PCE of 0.7%. The band alignment for the $CuInSe_2$ NPs/P3HT leads to multiple electron trap states hindering efficient charge transport, and further reverse bias studies confirmed that the hybrid devices' charge current was hole-dominated. Exchanging ligands onto the $CuInSe_2$ NPs may markedly improve the function of NPs in the solar cell by negating the electron trap states *via* a more suitably formed interface.[109]

Tunable CZTS NPs

CZTS NPs possess similar electronic and structural properties to CIGS and CIS semiconducting nanomaterials, while utilizing less expensive, earth-abundant, and environmentally benign metals. The band gap of CZTS NPs(~1.4-1.5 eV) lies in the region for optimal absorption of the solar spectrum and displays a high absorption coefficient of ~10^4, which should allow for a high degree of solar absorption.[113-127] These characterisitics make CZTS materials attractive for large scale use in photovoltaic devices, and industrial template directed processes for CZTS are present in the literature.[114,116] Quaternary semiconductors, like CZTS, have already shown the capability for modification of the crystal lattice to sub-stochiometric compositions while keeping the same crystal structure and packing. This occurs by replacement of Zn sites by Cu or Sn in the crystal lattice, hindering the formation of ZnS NPs.[117]

Few cases of modification of the composition of CZTS have been reported, and much of the work has occurred by Cabot *et al.* and Zhan *et al.*[118,119] While other semiconducting NPs, such as CdSe or even CIS, have been introduced into an organic material to form hybrid PV devices, research on CZTS NPs in a organic matrix is nonexistent. At ~4 nm diameter, the conductance band and valence band for CZTS are at -3.30 eV and -4.53 eV, acting as a p-type semiconductor in relation to poly-**1**.[120-122] Scheme 6 depicts the energy band alignment between CZTS *p*-type semiconductor NPs and the polymer *p*-type material. Tuning the bands through modification of the zinc composition, $(Cu_2Sn)_{x/3}Zn_{1-x}S$, would allow for *n*-type character of the NP in relation to the metallopolymer. Creating a proper *p-n* heterojunction should greatly affect the photodiode behavior of the hybrid material, even leading to photovoltaic activity. The

usefulness of the seeded growth process will be probed by modifying the ratio of Cu:Zn:Sn in the metal solution wash. Controlling the stochiometry of CZTS NPs by sub-stochiometric composition, $(Cu_2Sn)_{x/3}Zn_{1-x}S$ $(0 \leq x \leq 0.75)$, within a metallopolymer matrix. Several different compositions of CZTS NPs were grown into the matrix with $(Cu_2Sn)_{x/3}Zn_{1-x}S$ (x = 0.15-0.75).

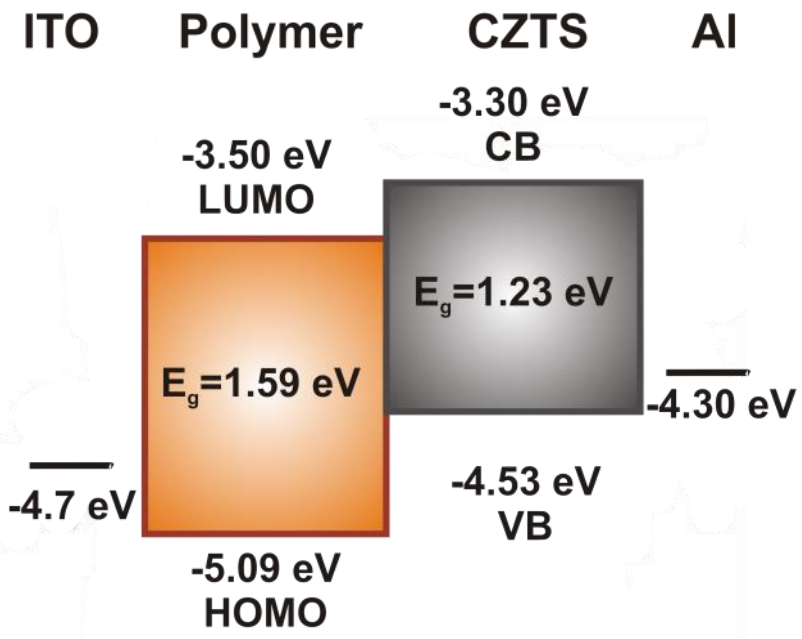

Scheme 6. The relationship between CZTS NPs to the Cu(II) metallopolymer can be changed based on NP composition. The energy alignment shown characterizes both the polymer and CZTS acting as *p*-type materials.

EXPERIMENTAL

General Methods

Air- and moisture-sensitive reactions were carried out in heat gun dried glassware using standard Schlenk techniques under an inert nitrogen atmosphere. All solvents were dried using an Innovative Technology, Pure Solv solvent purifier with double purifying column. All other chemicals were used as received from commercial suppliers. NMR spectra were recorded with a Varian Unity +300 (^{1}H, 300 MHz, ^{13}C{^{1}H} 75 MHz) and were referenced to residual solvent peaks. Chemical ionization (CI) mass spectra were collected on a Micromass Autospec Ultima mass spectrometer. X-ray photoelectron spectroscopy (XPS) was carried out on a PHI 5700 XPS system equipped with a dual Mg X-ray source and monochromatic Al X-ray source complete with depth profile and angle-resolved capabilities.

Synthesis

Synthesis of the ligand

Synthesis of ligand precursor, 2-(tributylstannyl)bithiophene and 5-(2,2'-bithiophene-5-yl)-2-hydroxybenzaldehyde, and **L** were performed following literature procedures.[128,129]

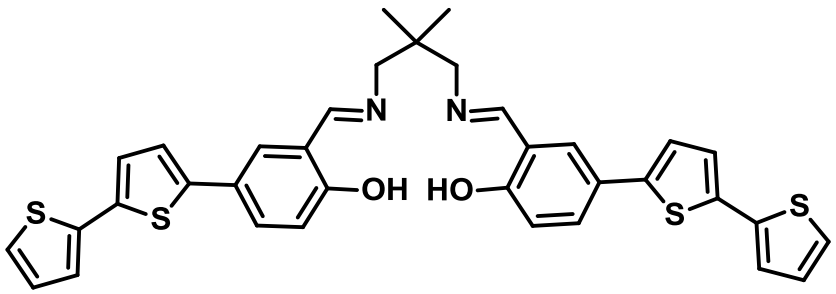

***N,N'*-((2,2'-dimethyl)propyl)*bis*(5-(2,2'-bithiophene-5-yl)salcylidenimine (L).**

To a solution of 5-(2,2'-bithiophene-5-yl)-2-hydroxybenzaldehyde (1.00 g, 3.49 mmol) in CH_2Cl_2 (200 mL) was added EtOH (200 mL), and 1,3-diamino-2,2'-dimethylpropane (0.1784 g, 1.75 mmol). The reaction mixture was stirred at room temperature for 8 hours, and then the CH_2Cl_2 was removed *in vacuo* resulting in an orange suspension in EtOH. The reaction mixture was filtered to give an orange solid that was then dried to give the desired product (0.904 g, 80%). m.p. 138 °C. ^{1}H NMR (CD_2Cl_2): δ 13.64 (s, 2H), 8.40 (s, 2H), 7.58 (dd, *J* = 2.4, *J* = 9.0, 2H), 7.51 (d, *J* = 2.1, 2H), 7.24 (dd, *J* = 1.2, *J* = 3.0, 2H), 7.19 (dd, *J* = 1.2, *J* = 3.0, 2H), 7.12 (s, 4H), 7.03 (dd, *J* = 3.9, *J* = 6.0, 2H), 6.98 (d, *J* = 8.7, 2H), 3.54 (s, 4H), 1.11 (s, 6H). ^{13}C{^{1}H} NMR: compound was not sufficiently soluble in any common solvent to obtain a spectrum. UV-Vis (λ_{max} (ε), CH_2Cl_2): 349 nm (24,000 $cm^{-1}M^{-1}$). HRMS (CI) m/z calculated for $C_{35}H_{30}N_2O_2S_4$ 638.1190 [M+], found 638.1188. Elemental anal calcd. (found) for **L**: C, 65.79 (65.48); H, 4.73 (4.50); N 4.38 (4.30); S, 20.07 (20.03).

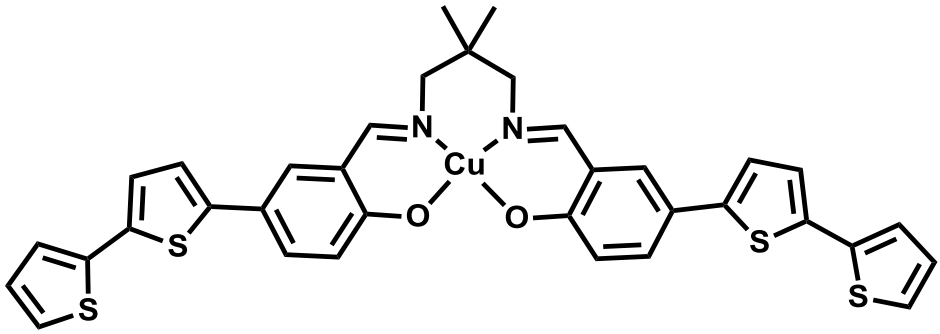

***N,N'*-((2,2'-dimethyl)propyl)bis(5-(2,2'bithiophene-5-yl)salcylideniminato copper(II) (1).**

To a solution of ligand (L) (0.128 g, 0.2 mmol) in CH_2Cl_2 was added to $Cu(O_2CCH_3)_2$ (0.036 g, 0.2 mmol) in 1 mL of methanol. The mixture was stirred under reflux for 48 hours and the green precipitate formed was then filtered. The filtrate was concentrated to

~1 mL and recrystallized from ether. A dark green crystalline solid was obtained (0.110 g, 78.5%). Dark green crystals suitable for X-ray diffraction were obtained by subjecting the filtrate to slow vapor diffusion in diethyl ether. ^{1}H NMR ($CDCl_3$): δ 8.18 (s, 2H), 7.30-6.78 (m, 16H), 5.24 (s, 2H), 3.61 (s, 4H), 1.35 (s, 6H). UV-Vis (λ_{max} (ε), (CH_2Cl_2): 368 nm (38394 $cm^{-1}M^{-1}$). FTIR (Nujol): 3020 (C-H), 2974 (C-H), 2924 (C-H), 1625 (C=N), 1523 (N-H), 1474 (m), 1416 (m), 1261 (s), 1044 (s), 926 (m), 873 (=C-H), 775 (=C-H), 669 (=C-H) cm^{-1}. HRMS (CI) m/z calculated for $C_{35}H_{29}CuN_2O_4S_4$ 700.0408 [M+], found 700.0408. m.p. 184-188 °C. Elemental anal calcd. (found) for **1**: $C_{37}H_{31}Cl_2CuN_2O_4S_4$: C, 55.06(55.16); H, 3.85(3.89); N, 3.57(3.52).

NP Growth

Electropolymerized thin films were treated with H_2S gas for two minutes then rinsed thoroughly with dry CH_2Cl_2. The film was then treated with a metal solution of equimolar amounts of $Cu(NO_3)_2$, $Zn(NO_3)_2 \cdot 6H_2O$, and $Sn(Cl)_2$ in CH_2Cl_2/MeOH (2.00×10^{-3} M) for two minutes followed by CH_2Cl_2 rinse. The film was then treated with the chalcogenide source for two minutes, and rinsed once again. This process was repeated up to six times for each film.

Transmission Electron Microscopy

TEM experiments and EDS studies were carried out on a JEOL 2010F microscope. Films were grown electrochemically onto carbon coated gold grids purchased from Electron Microscopy Sciences. Electropolymerization occurred under the same parameters as the film with cycling from -0.5V to 1.5V three times. Films were kept in

an air-free environment and NPs were grown directly onto the grid. After rinsing the film with DCM and drying for 48 hours under vacuum the films were looked at under the microscope. NP growth was performed the same as above. Analysis of the NPs was done using Gatan Digital Micrograph software. Size distribution data is reported for 100-115 NPs.

Film thickness and Conductivity Measurements

Film thickness was determined using a Veeco Dektak Profilometer. Films were prepared on ITO coated glass that was first treated by successive sonnication in deionized water, ethanol, acetone, and methylene chloride. Electropolymerization was done as previously described for 20 cycles at a scan rate of 100 mV/s. Thickness measurements are reported as an average of twelve measurements taken on two films.

Crystal Structure Determination

Data were collected on a Nonius Kappa CCD diffractometer with graphite monochromated Mo-Kα radiation (λ = 0.71073 Å) at 153 K. Absorption corrections were applied using GAUSSIAN. The structures were solved by direct methods and refined anisotropically using full-matrix least-squares methods with the SHELX 97 program 165 package.[130,131] The coordinates of the non-hydrogen atoms were refined anisotropically, while hydrogen atoms were included in the calculation isotropically but not refined. Neutral atom scattering factors were taken from Cromer and Waber.[133,134] The crystallographic data and structure refinement for complex **1** are listed in Table 1. Selected bond lengths and angles for **1** are given in Table 2, respectively.

Electrochemistry

Electrochemical syntheses and studies were done under a nitrogen atmosphere in a dry-box using a GPES system from Eco. Chemie. B. V. All of the electrochemical experiments were carried out in a three electrode cell with a $Ag/AgNO_3$ reference electrode (silver wire dipped in a 0.01 M silver nitrate solution with 0.1 M Bu_4NPF_6 in CH_3CN), a Pt button working electrode (1.6 mm diameter), and a Pt wire coil counter electrode. To calibrate the reference electrode, ferrocene was used as an external reference to which potentials were corrected. All electrochemical experiments were performed CH_2Cl_2 solutions in a supporting electrolyte composed of 0.1 M tetrabutylammonium hexafluorophosphate. The $[(n\text{-}Bu)_4N][PF_6](TBAPF_6)$ was recrystallized three times from hot ethanol, then dried for 4 days at 100 °C under vacuum. Films for Cu_2ZnSnS_4 NP growth were electropolymerized using a 4×10^{-4} M monomer solution. The films were grown by cycling between -0.5 V to 1.5 V at $v = 100$ mVs^{-1}.

Table 1. Crystal data and structure refinement for **1**.

	Cu complex
Formula	$C_{36}H_{30}N_2O_2Cl_2S_4Cu$
Fw	785.30
Cryst syst.	triclinic
Space group	P-1
a, Å	10.282(2)
b, Å	13.176(3)
c, Å	13.204(3)
α, deg	107.65(3)
β, deg	97.12(3)
γ, deg	90.65(4)
V, Å^3	1689.1(6)
Z	2
D_{calc}, g cm^{-3}	1.544
temp, K	153(1)
F(000)	806

Table 1. continued.

μ, mm^{-1}	1.089
θ rang, deg	3.12-27.52
reflns meads	11372
reflns used	7686
params	424
R^a ($I > 2\sigma(I)$)	R1 = 0.0454
	wR2 = 0.1086
R^a (all data)	R1 = 0.0733
	wR2 = 0.1250
S	1.050

^{a} R1 = $\Sigma||F_o| - |F_c||/\Sigma|F_o|$. wR2 = $[\Sigma w[(F_o^2 - F_c^2)^2]/\Sigma[w(F_o^2)^2]]^{1/2}$. w=1/$[\sigma^2(F_o^2)+(0.075P)^2]$, where P = $[\max(F_o^2,0)+2F_c^2]/3$.

Table 2. Selected Bond Lengths (Å) and Angles (°) for the **1**.

Cu(1)-O(1)	1.892(2)	O(1)-Cu(1)-N(2)	152.08(9)
Cu(1)-O(2)	1.9044(19)	O(2)-Cu(1)-N(2)	94.69(9)
Cu(1)-N(2)	1.942(2)	O(1)-Cu(1)-N(1)	94.79(9)
Cu(1)-N(1)	1.944(2)	O(2)-Cu(1)-N(1)	153.47(9)
O(1)-Cu(1)-O(2)	91.47(9)	N(2)-Cu(1)-N(1)	91.75(10)

Figure 12. ORTEP single crystal representation for the Cu(II) salpen monomer, **1**.

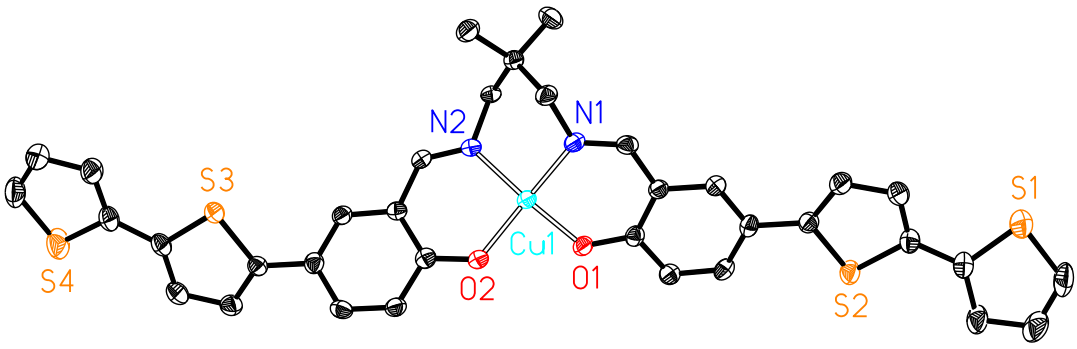

RESULTS AND DISCUSSION

Characterization of Cu(II) Metallopolymer

The orginial Cd(II) metallopolymer system utilized an electropolymerizable ligand that could be complexed with a wide variety of metals. Ga_2S_3 NPs were grown into a Ga(III) metallopolymer, and many different other systems have been produced as well.[97,98] A Cu(II) metallopolymer was produced using the same ligand, as a scaffold for CZTS NP growth. Scheme 7 shows the synthetic route for the electropolmerizable ligand.

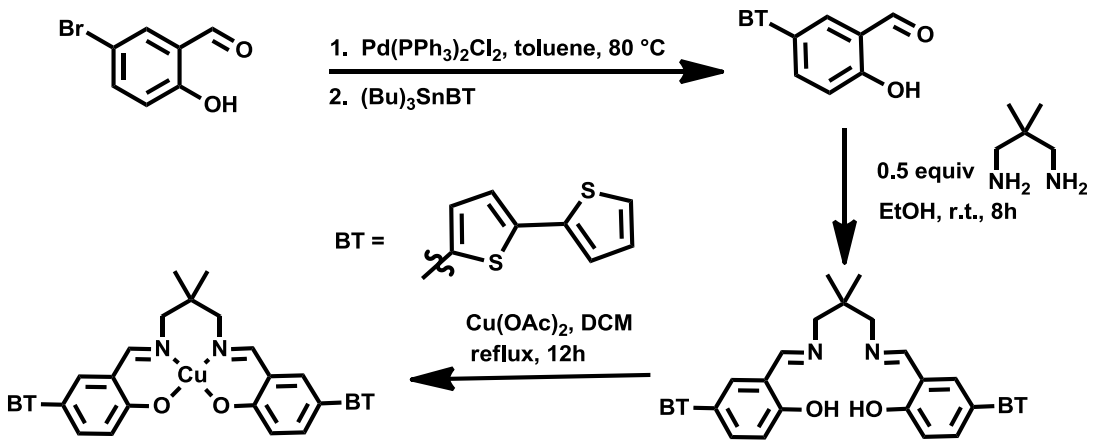

Scheme 7. The synthetic scheme for the electropolymerizable ligand and electropolymerizable Cu(II) complex.

To produce the desired template for CZTS NP growth the electropolymerizable salpen-type ligand (L) was complexed with Cu(II) acetate in DCM (Scheme 8). Formation of the desired Cu(II) complex was confirmed by disappearance of the O-H hydrogen resonance of the ligand at δ 13.64 ppm. The resulting dark green precipitate

was then crystallized by slow vapor diffusion of hexanes into a solution of the monomer in dichloromethane, and the structure confirmed by single X-ray crystallography. The coordination environment of Cu(II) is a distorted square planar geometry and the bond lengths are in agreement with the Cu(II) salpen complex reported previously.[135,136] The bond angles are larger, which is most likely due to the flexible backbone which causes a twist out of plane. Electropolymerization of the Cu(II) monomer (**1**) created conducting metallopolymer thin films (poly-**1**) on a variety of working electrodes including platinum wire and buttons, ITO coated glass, stainless steel plates, and gold coated TEM grids.

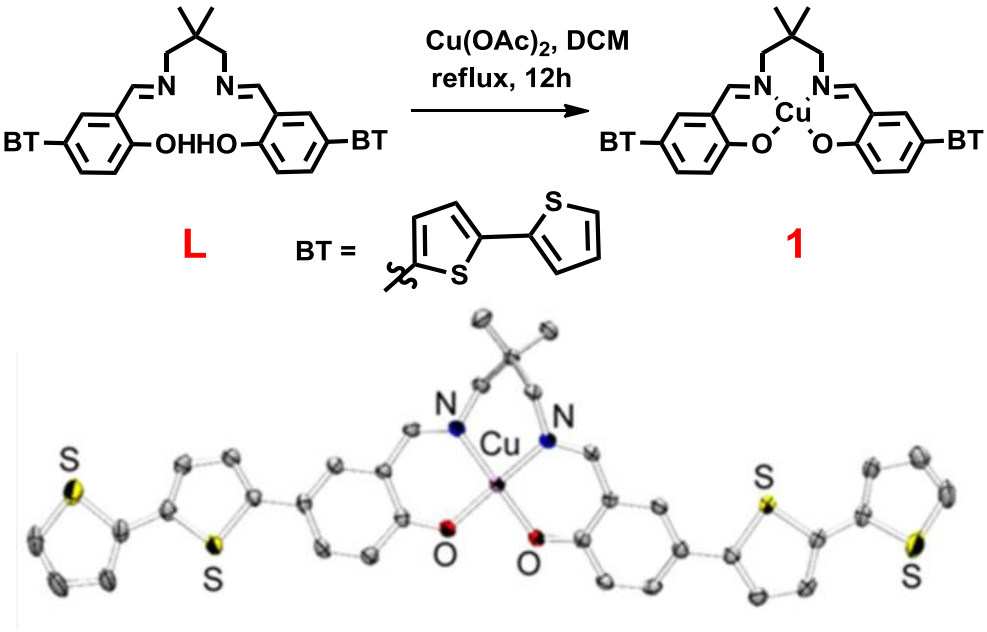

Scheme 8. The synthetic route to form the Cu(II) salpen metal complex (**1**) from the salpen ligand (**L**). A single crystal was isolated from DCM/hexanes and the structure solved, an ORTEP diagram with a labeling scheme showing a 50% probability level. Hydrogen atoms have been omitted for clarity.

Cu(II) Metallopolymer Studies

X-ray photoelectron spectroscopy (XPS) of the thin films showed that the ratio of Cu:S was 1:4.9 (theoretical ratio of 1:4) which supports the formation of the desired polymer films. Profilometry and four point probe conductivity measurements ($\tau = 105 \pm 6$ nm and $\sigma = 6.9 \times 10^{-3}$ S/cm for 20 scans) of the thin films demonstrated the polymers were conductive and homogenously deposited. Electrochemistry (Figure 13) of the conducting polymer on a platinum button demonstrated linear scan rate dependence in the range of 10-500 mV/s, which is consistent with an electroactive conducting polymer that is not limited by counterion diffusion. To produce homogenous hybrid films, the metal salt solutions used in the NP growth process must penetrate through the entirety of the polymer films. The linear scan rate dependence reflects that the polymer material has ionic porosity allowing for effective intercalation of the growth solutions to the electrode surface. The inherent ionic porosity of thiophene-based polymer films supports that NPs grow throughout the film.

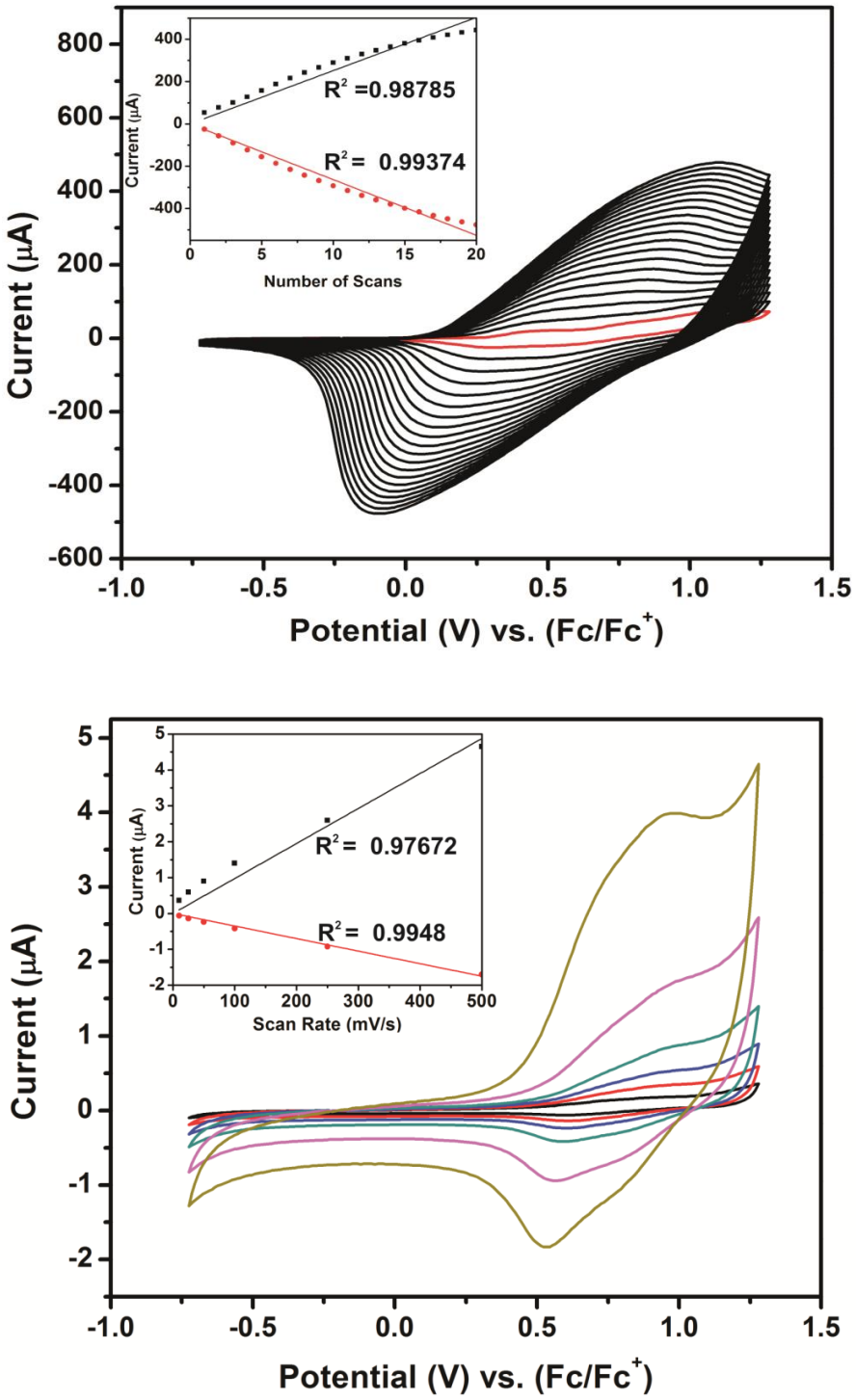

Figure 13. (a) Electrochemical deposition of poly-**1** onto ITO-coated glass electrode. (inset) the linear dependence of current vs. number of scans. (b) Current vs. Scan rate for poly-**1**. (inset) the linear dependence of the current vs. scan rate.

CZTS and $(Cu_2Sn)_{x/3}Zn_{1-x}S$ NP Growth and Characterization

Nanoparticle Growth Process

CZTS NP growth was achieved using a similar process to CdS NP growth in the Cd(II) metallopolymer, as shown in Scheme 9. The metal ion solution initially needed tuning, with initial trials beginning with $Cu(NO_3)_2$, $Zn(NO_3)_2$, and $SnCl_2 \cdot 3H_2O$ (2:1:1) salts dissolved in DCM/MeOH (1:1 v/v). As the films were exposed to metal ion solution, it was observed that a white precipitate of $SnCl_2$ formed during NP growth. The precipitation was detrimental to proper NP growth and mild changes yielded cleaner NP growth. Using recrystallized anhydrous metal salts yielded uniformly distributed NPs within the Cu(II) metallopolymer film, as supported in Figure 14.

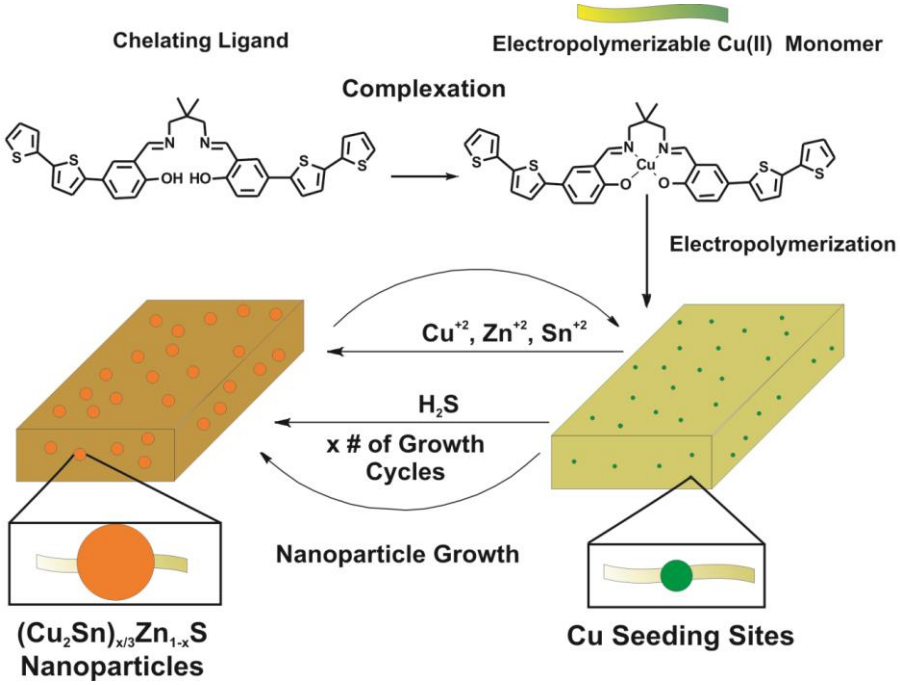

Scheme 9. The scheme for electropolymerization, seeding, and NP growth process used to grow CZTS NPs in Cu(II) metallopolymer.

TEM/EDX Characterization

The utility of the NP process in growing sub-stochiometric $(Cu_2Sn)_{x/3}Zn_{1-x}S$ NPs in the Cu(II) metallopolymer was probed by producing different ratios. The different ratios of $(Cu_2Sn)_{x/3}Zn_{1-x}S$ ($0 \leq x \leq 0.75$) NPs were grown by changing the stochiometry of the metal salts to the desired ratio. This simple modulation of the metal ion solution proved to be highly effective in producing sub-stochiometric CZTS NPs. The metallopolymer and CZTS NPs were deposited and grown onto Au/C TEM grids and studied using TEM and EDX spectroscopy, as shown in Figure 14 and 15. Composition analysis of the NP films, as summarized in Table 3, reflected the desired $(Cu_2Sn)_{x/3}Zn_{1-x}S$ stochiometry.

Table 3. Atomic ratios of the elements found from TEM/EDX experiments. Paranthetical values are theoretical values using the NP formual and metallopolymer composition

Empirical Formula	Formula	%Cu	%Zn	%Sn	%S
$(Cu_2Sn)_{(.75/3)}Zn_{(1-.75)}S$	Cu_2SnZnS_4	22.2 (25)	12 (12.5)	11.5 (12.5)	54.25 (50)
$(Cu_2Sn)_{(.60/3)}Zn_{(1-.60)}S$	$Cu_{1.6}Sn_{0.8}Zn_{1.6}S_4$	19.2 (20)	18 (20)	9.1 (10)	53.7 (50)
$(Cu_2Sn)_{(.45/3)}Zn_{(1-.45)}S$	$Cu_{1.2}Sn_{0.6}Zn_{2.2}S_4$	13.1 (15)	26.7 (27.5)	6.9 (7.5)	53.3 (50)
$(Cu_2Sn)_{(.30/3)}Zn_{(1-.30)}S$	$Cu_{0.8}Sn_{0.4}Zn_{2.6}S_4$	11.7 (10)	30.9 (35)	5.3 (5)	52.1 (50)
$(Cu_2Sn)_{(.15/3)}Zn_{(1-.15)}S$	$Cu_{0.4}Sn_{0.2}Zn_{3.4}S_4$	4.7 (5)	40.2 (42.5)	2 (2.5)	53.1 (50)

The size distribution for the range of $(Cu_2Sn)_{x/3}Zn_{1-x}S$ NPs showed little change in diameter when compared to the 4.5 ± 0.54 nm stochiometric Cu_2ZnSnS_4 NP-enriched polymer films. The stochiometry of the NPs was manipulated solely by changing the

ratios of the salts in the metal solution bath. XPS surface analysis of hybrid materials on stainless steel was performed to gather compositional data on the entire $(Cu_2Sn)_{x/3}Zn_{1-x}S$ NPs/poly-**1** films. XPS data (Figure 16) for the hybrid films showed some incongruencies, specifically the Zn^{2+} species in the films did not appear in the XPS despite being present in EDX compositional data.

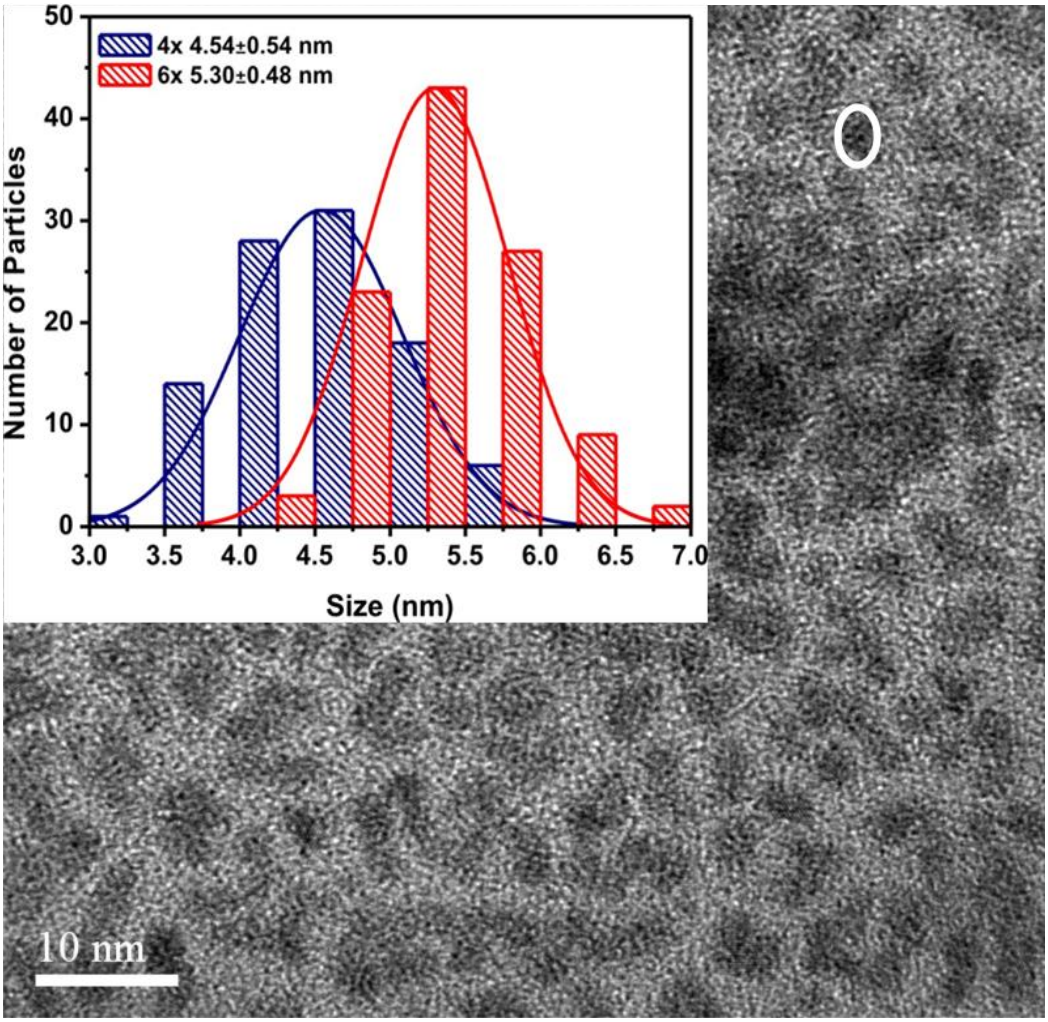

Figure 14. TEM image showing CZTS NPs grown in the Cu(II) metallopolymer film. Increasing growth cycles resulted in larger NP diameter. Size distribution studies were performed after four and six growth cycles.

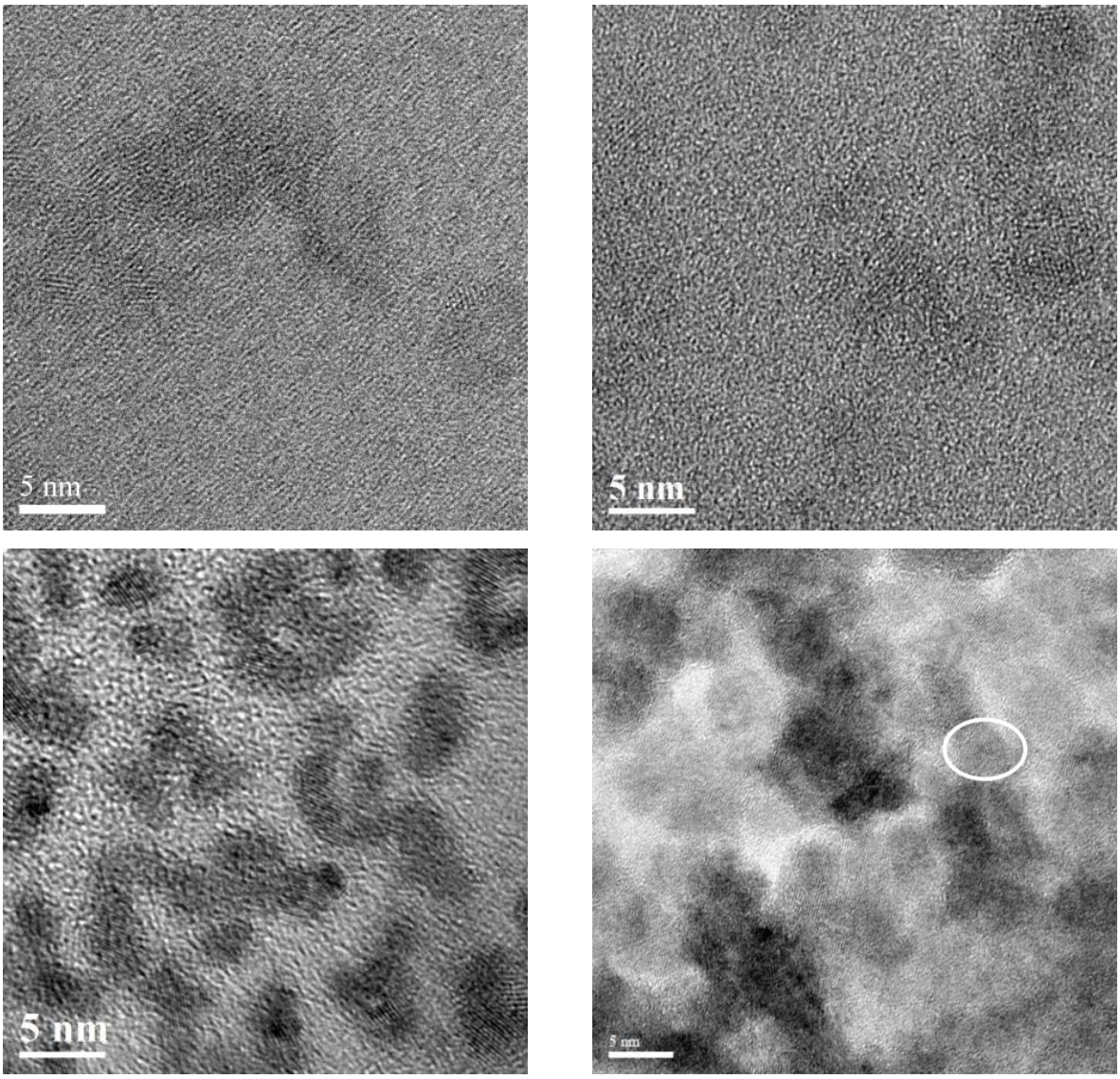

Figure 15. Selected TEM micrographs for the $(Cu_2Sn)_{x/3}Zn_{1-x}S$ ratios x = 0.15, 0.30, 0.45, 0.6, 0.75.

XPS Surface Analysis of the Hybrid Materials

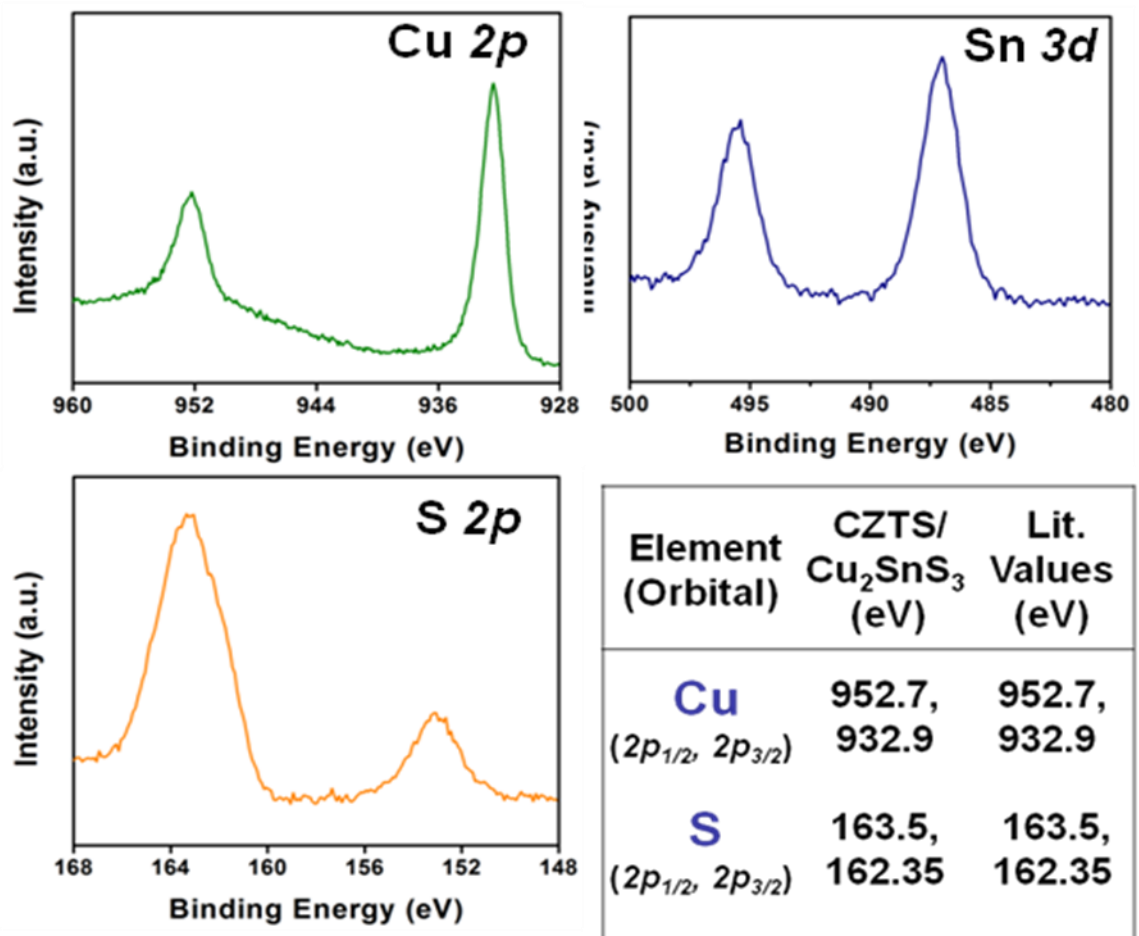

Element (Orbital)	CZTS/ Cu_2SnS_3 (eV)	Lit. Values (eV)
Cu ($2p_{1/2}$, $2p_{3/2}$)	952.7, 932.9	952.7, 932.9
S ($2p_{1/2}$, $2p_{3/2}$)	163.5, 162.35	163.5, 162.35
Sn ($3d_{3/2}$, $3d_{5/2}$)	495.45, 487.05	494.7, 486.3

Figure 16. XPS surface analysis spectra and the binding energies found for Cu, Sn, and S. The table compares experimental values to literature values.[117-127]

The presence of weak Zn^{2+} peaks in the XPS spectra pointed to the formation of Cu_2SnS_3 on the surface of the NP. Powder X-ray diffraction experiments were used to probe all regions of the NP, specifically to explore the possibility of a core-shell type structure. XRD data supported compositions found from both the EDX and XPS spectra presenting 2θ peaks for both CZTS and Cu_2SnS_3 in the diffraction pattern (Figures 17).

Quantitative analysis of the XRD pattern of the CZTS NP hybrid films in the polymer matrix suggested a core shell structure with a thin surface shell of Cu_2SnS_3 (5.2 Wt%) present. The formation of Cu_2SnS_3 is due to Zn segregation into the core to minimize the free energy of NP formation. The surface energy of Zn^{2+} (0.0627 eV/Å^2) is higher than Sn^{2+} (0.0569 eV/Å^2) and as a consequence the Cu_2SnS_3/Cu_2ZnSnS_4 core-shell NPs formed are more stable than a pure CZTS NP phase.[136.137]

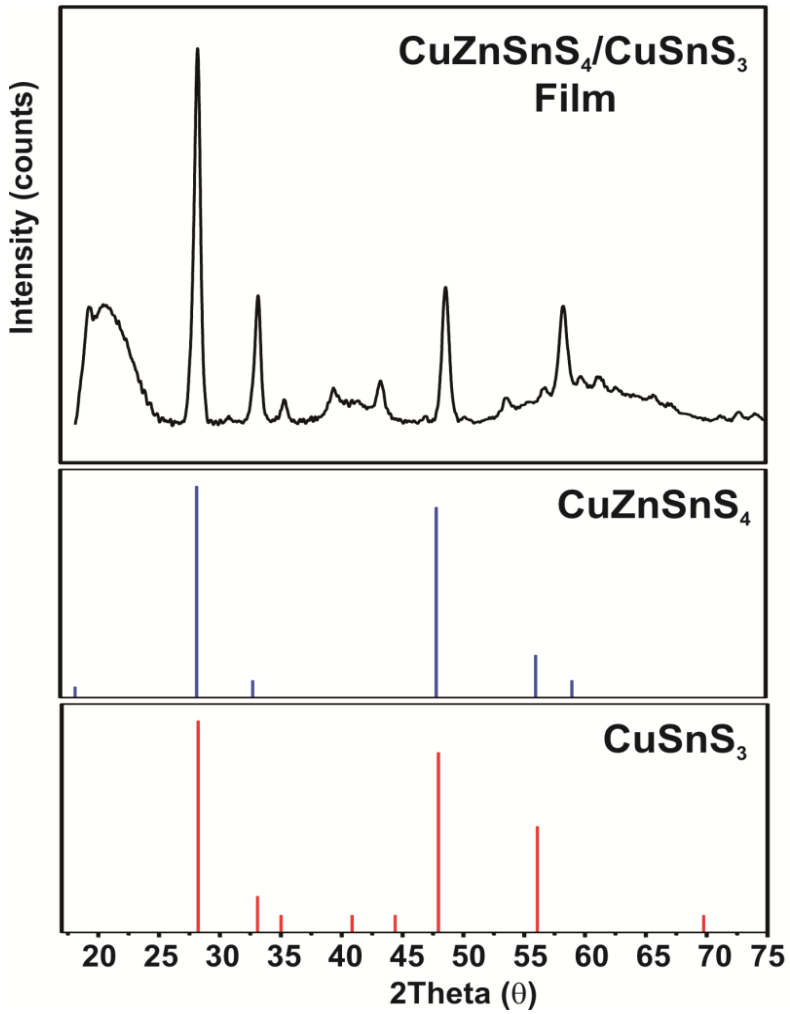

Figure 17. PXRD of the $(Cu_2Sn)_{x/3}Zn_{1-x}S$ NP/ metallopolymer film.

Spectroelectrochemistry of the Hybrid Films

Spectroelectrochemistry of the hybrid films was performed to determine the optical band gap and LUMO levels of the metallopolymer and the $(Cu_2Sn)_{x/3}Zn_{1-x}S$ NPs in the polymer matrix, as shown in Figure 18. Absorption spectra of the Cu (II) monomer (**1**) showed a π-π* transition at 435 nm which corresponds to previous literature complexes that utilize bithiophene electropolymerizable endgroups.[97] Upon oxidation of the metallopolymer, absorption from several transitions occurring in the system were observed. Spectroelectrochemical data shown in Figure 19 for $(Cu_2Sn)_{x/3}Zn_{1-x}S$ (x=0.75) showed a π-π*transition at 452-459 nm, and as the potential increased polaron and bipolaron formation began at 630-870 and 1000-1200 nm, respectively. The polaron and bipolaron formation transition peaks correlate strongly to those found in literature.[97] At lower potentials, before polaron and bipolaron transitions occurred, the onset of the peak CZTS could be elucidated from the UV-Vis spectra. The onset of peaks corresponding to transitions of the CZTS NPs was measured for every ratio (x = 0.15-0.75). The optical band gaps were then calculated using previous literature methods, and found to be 1.41-2.85 eV.[120,124,133]

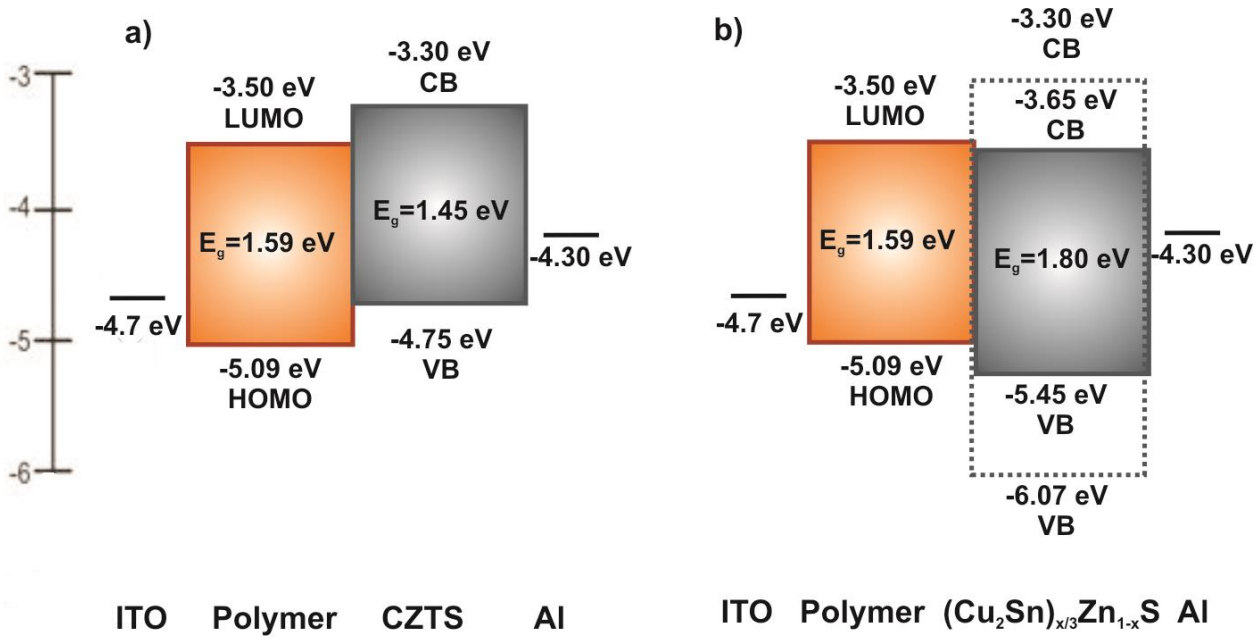

Figure 18. The relationship between the electronic energy levels CZTS NPs to the Cu(II) metallopolymer can be changed based on NP composition. a) The energy alignment shown characterizes both the polymer and CZTS NPs acting as p-type materials b) Composition modification changes the VB and CB of the $(Cu_2Sn)_{x/3}Zn_{1-x}S$ creating a p-n heterojunction and E_g = ~1.2-1.3 eV. The dotted line represents the literature range of values for $(Cu_2Sn)_{x/3}Zn_{1-x}S$ for the energy levels, from -3.30 eV to -6.07 eV.

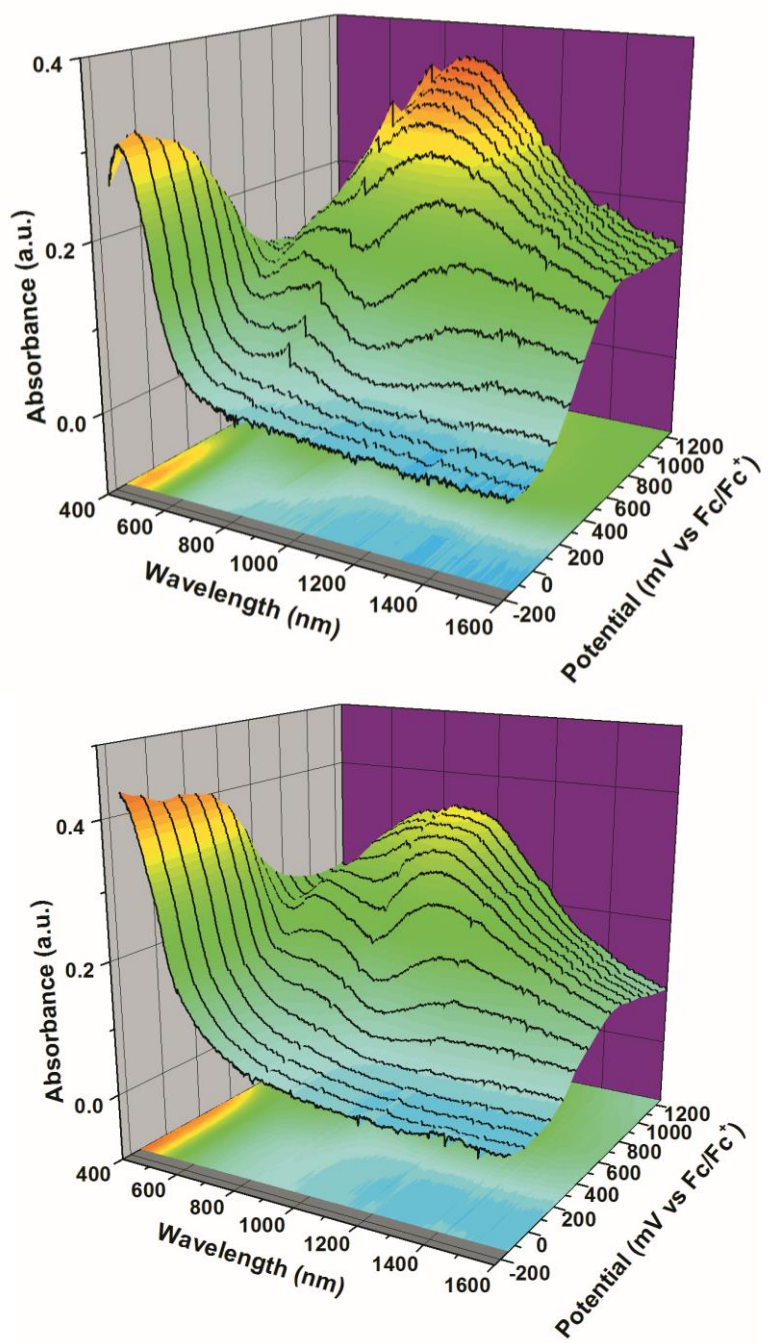

Figure 19. a) The spectroelectrochemistry of CZTS NP/poly-**1** hybrid where x = 0.75, b) The spectroelectrochemistry of CZTS NP/poly-**1** hybrid where x = 0.60. Literature methods were used to find optical band gap of the $(Cu_2Sn)_{x/3}Zn_{1-x}S$ (x = 0.60, 0.75) NPs.[132] The optical band gap of the increases as the materials become more Zn-rich in NP composition.

Table 4. A representative absorbance vs. band gap for the $(Cu_2Sn)_{x/3}Zn_{1-x}S(0\leq x\leq 0.75)$ (a) 0.15, (b) table of optical band gaps. Method adapted from literature.[132,133]

a

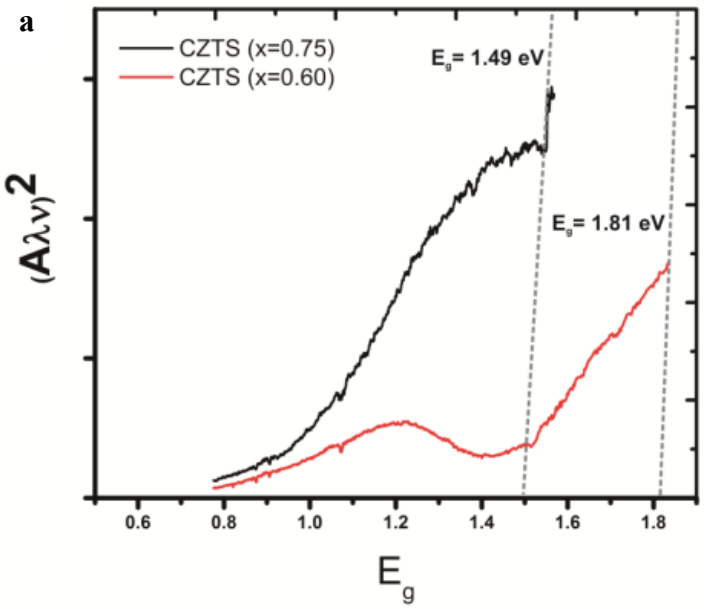

b.

Materials	Optical Band Gap (eV)
X = 0.15	2.85
X = 0.30	2.32
X = 0.45	2.01

The optical band gaps, summarized in Table 4, of CZTS NPs (x = 0.60) indicated the energy level alignment between the CZTS NPs (x = 0.60) and the *p*-type Cu(II) metallopolymer would allow better electron and hole flow. Furthermore, charge recombination should be lessened when compared to the stochiometric CZTS NP hybrid films. The other ratios produced showed much larger optical band gaps. The conductance and valence bands in these hybrid materials should be misaligned for proper photovoltaic behavior as indicated by the lack of a proper *p*-*n* heterojunction. Similar to other research with sub-stochiometric CZTS, decreasing the Cu(II) and Sn(II) content in the NP led to a dramatic increase in the band gap. The movement toward ZnS NPs in the composite films was further tested by fabricating photovoltaic device prototypes. A series of at least 100 – 150 devices was fabricated for each ratio in the $(Cu_2Sn)_{x/3}Zn_{1-x}S$ (x = 0.15, 0.3, 0.45, 0.6, and stochiometric 0.75) NP/Cu(II) metallopolymer films. Photovoltaic devices were produced not only to study the effectiveness of the organic-

inorganic nanocomposites as functional materials, but also to study the importanct of NP stochiometry on performance.

PVDevice Fabrication and Composition Effects on Performance

Device Prototype Scheme

The devices were fabricated in the configuration Ag paste/Al contact/CZTS NP: Cu(II) metallopolymer nanocomposite/PEDOT:PSS/ITO/glass. Scheme 10 shows the method and construction of the hybrid devices. First, the ITO substrate was etched using ozone plasma to create a pattern that would allow proper Al cathode function and minimize shorts. The patterned ITO was then used as the platform to electropolymerize the Cu(II) monomer to the Cu(II) metallopolymer seeding film. Then $(Cu_2Sn)_{x/3}Zn_{1-x}S$ (x = 0.15, 0.3, 0.45, 0.6, and stochiometric 0.75) NPs were grown using the same method, a total of four cycles for each type of NP. Al contacts were thermally deposited onto the surface of the films in a vacuum deposition chamber. Ag paste was applied to the top contacts to allow a better interface between the devices and the *J-V* curve measurement instrumentation.

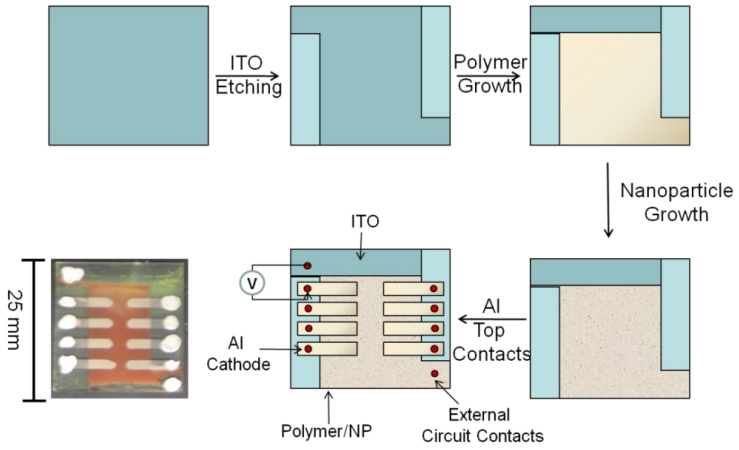

Scheme 10. The method utilized to construct the $(Cu_2Sn)_{x/3}Zn_{1-x}S$ NP/Cu(II) metallopolymer hybrid devices.

J-V Curve Analysis

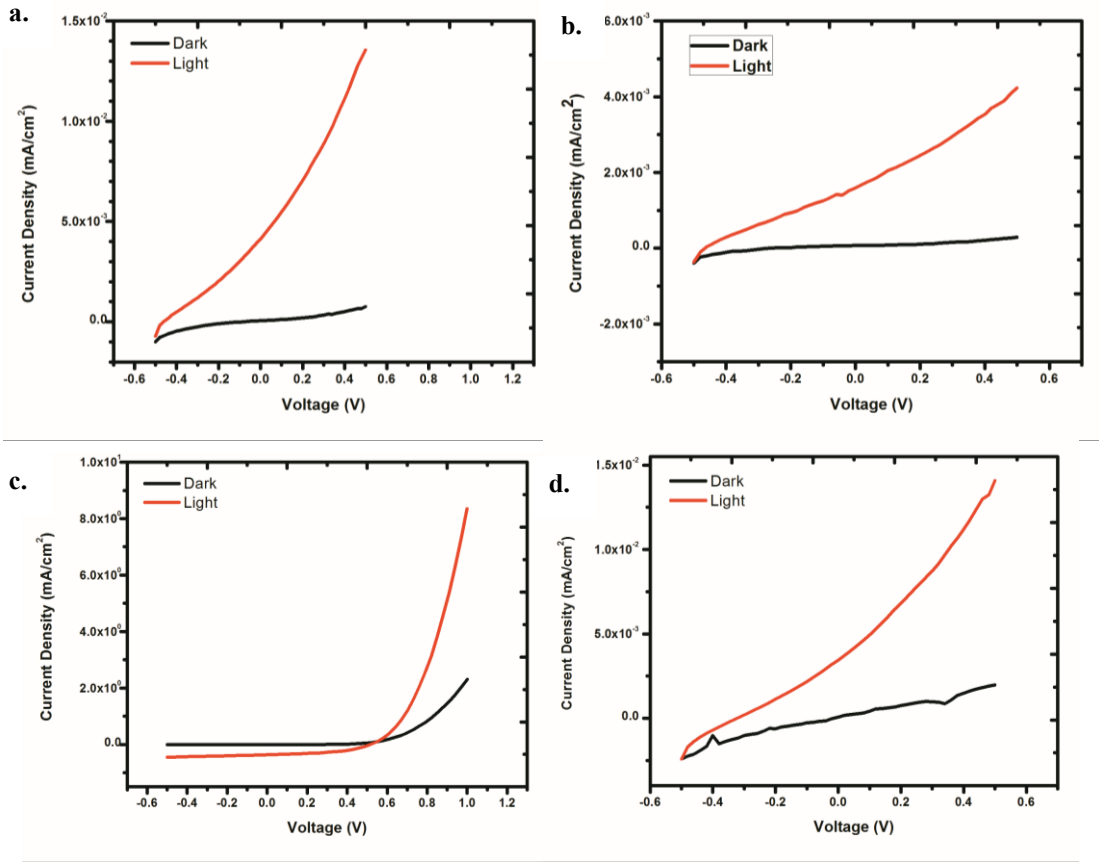

Figure 20. The *J-V* curves for (a) x = 0.30, (b) x = 0.45, (c) x = 0.60, (d) x = 0.75.

J-V curve analysis of the devices indicated that NP composition directly influenced the behavior of the hybrid devices. The majority of the initial devices suffered from shorts, and special care must be taken in the application of the Ag paste. Many of the other ratios showed similar behavior, with CZTS NPs where x = 0.15, 0.3, and 0.45 showing only photoconductivity behavior, as seen in Figure 20. The Zn-rich CZTS NPs, where x = 0.60, possessed much more attractive behavior. The devices performed consistently with approximately 80% of all devices displaying photovoltaic behavior.

Typical semiconductor behavior for CZTS NPs (x = 0.75) is *p*-type, and would produce a poor electronic interface for charge carriers with the *p*-type metallopolymer

organic semiconductor.[119-124] An increase in charge recombination would occur and negatively affect photovoltaic device performance. Devices fabricated for CZTS NP (x = 0.75) hybrid films displayed only ohmic photocurrent behavior, as showin in Figure 20. Similar photoelectrical characteristics occurred for the $(Cu_2Sn)_{x/3}Zn_{1-x}S$ NPs for x = 0.15, 0.30, 0.45 (Figure 20), with the bulk of devices possessing photocurrent behavior. For the Zn-rich $(Cu_2Sn)_{x/3}Zn_{1-x}S$ NP PV devices (x = 0.60), the photoelectrical behavior was uniquely different. In Figure 21 the *J-V* curve for $(Cu_2Sn)_{x/3}Zn_{1-x}S$ (x = 0.60) NP device exhibits photodiode behavior and the J_{sc} is several orders of magnitude higher than stochiometric CZTS/Cu(II) metallopolymer films. The photovoltaic characteristics were much higher with a J_{sc} = 0.375 mA/cm^2, *FF* = 0.471, V_{oc} = 0.543 V, and a η = 0.096%, reflecting much better energy transfer occurs in the device.

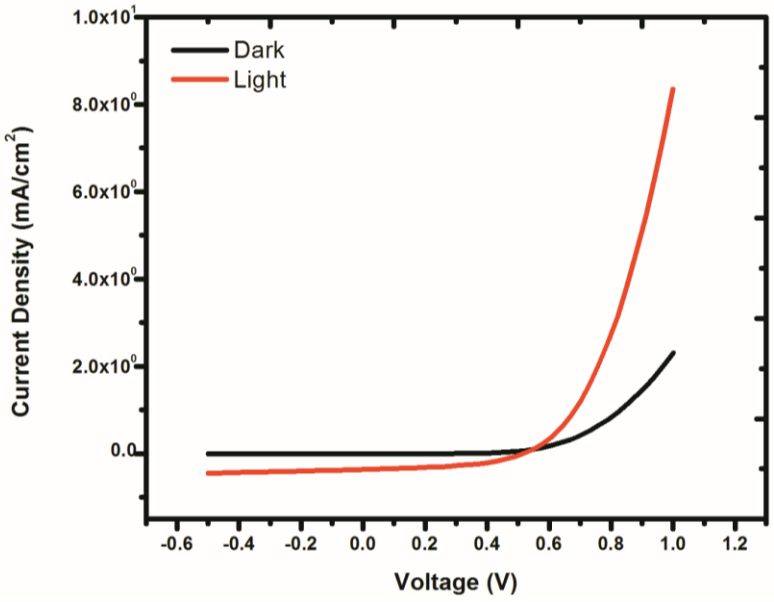

Figure 21. The *J-V* curve for the hybrid films where x = 0.60. Photodiode behavior was present exclusively for this ratio.

CONCLUSIONS

The effect of CZTS NP compostion on device performance was studied using spectroelectrochemistry, XPS, XRD, and transmission electron miscroscopy/energy dispersive X-ray analysis (TEM/EDX). The composition of the NPs could be controlled using a room temperature seeded growth process. *J-V* curve analysis showed that the composition of the CZTS NPs directly impacted the device performance. The device performance for x = 0.60 supports that energy level considerations in these types of hybrid materials must be taken into account to produce more efficient PV devices. Changing the composition produced significant effects on device performance due to better carrier mobility in the interface formed by the more Zn-rich material. Further modification of the structure of the devices, including the addition of an electron or hole transporting layer, could render a more highly efficient device. In future work we will look at the role of crystallinity on device performance by annealment of the polymer films.

Chapter 3: Electropolymerizable Mono- and Bisaroylthiourea Monomers as Highly Sensitive and Selective Amperiometric Heavy Metal Cation Sensors

INTRODUCTION

An unfortunate result of unchecked industrial scale production of chemicals and materials is toxic metal waste proliferation into water supplies. The problem is complicated, and is highly damaging for countries in Asia and Africa that lack the infrastructure to properly remediate and identify toxic levels of metal cations in groundwater. Identifying areas suffering from toxicity problems is integral to decreasing occurrences of environmentally caused diseases, such as acute lead toxicity. Pb(II) toxicity is especially detrimental to children and the elderly, with symptoms as harsh as mental retardation and stomach cancer occurring from prolonged exposure. Creating inexpensive and effective sensors for ground water would directly diminish those added to the already millions of sufferers. It is necessary for the sensors to be highly sensitive, as Pb(II) ions are toxic at levels as low as 0.2 ppm.[138]

Ion Selective Electrodes

A broad variety of materials have been used to prepare effective ionic sensors. Many types of sensors have been produced; amperiometric, potentometric, and optical sensors.[66,69,139] Each type of sensor has distinct advantages and disadvantages. The optical sensors utilize changes in electronic transitions to induce visible detection of ions. These approaches are extremely sensitive for determining the presence of metal ions in an analyte but require a spectrophotometer for implentation. In specific examples, metal detection occurs as a function of discrete color changes in the sensor material.[140-142]

However, quantification of ion concentration can prove to be difficult through optical methods and rely on difficult to transport detection systems.

Many of the testing kits currently employ potentiometric/amperiometric sensors as the method for cation detection in groundwater. These systems have good detection limits, typically from 10^{-5} to 10^{-8} M. Introducing the right sensor ligand, or ionophore, can lead these sensors to be highly selective. Typical potentiometric sensors are composed of ionophore/polymer membrane blends, usually with a conducting polymer incorporated as a transducer.[139,143-152] Figure 22 depicts an example of a conventional potentiometric ion selective electrode.

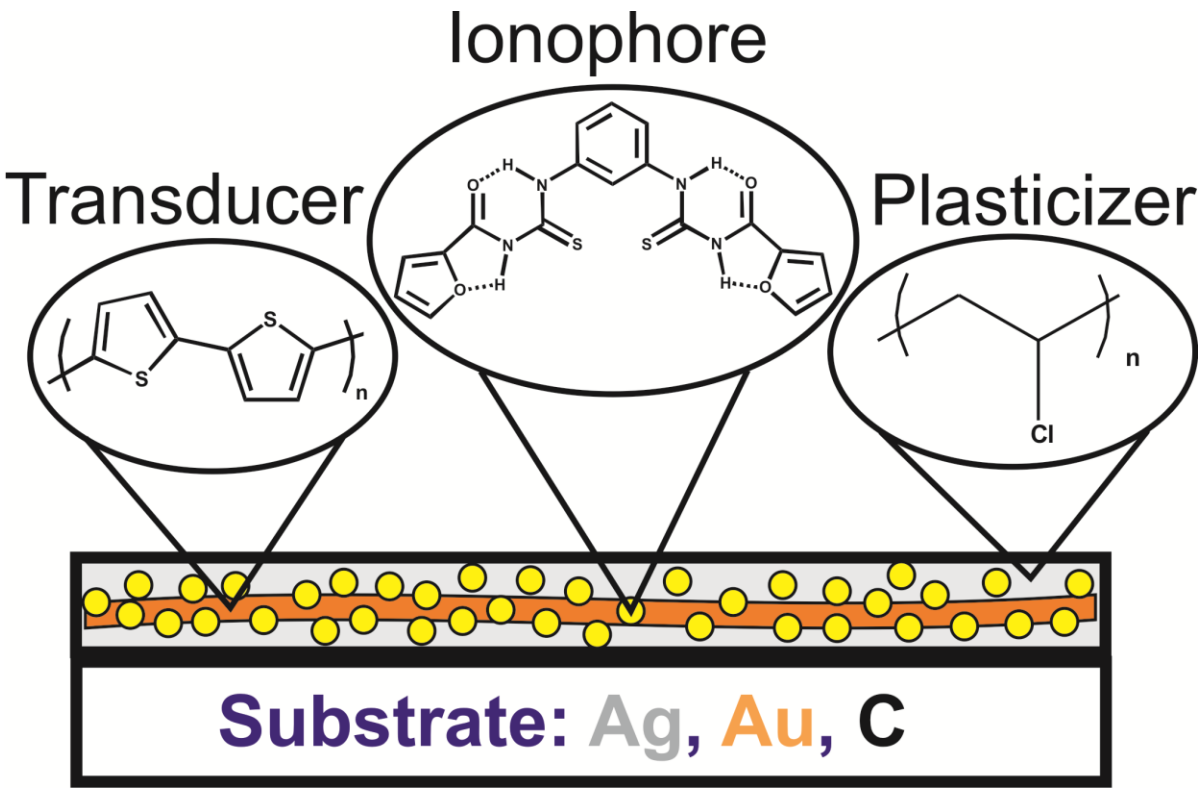

Figure 22. Graphical representation of a multi-component ion selective electrode used in a potentiometric sensors.

Polymer blends, typically composed of organic ionophores embedded into polymeric materials like polyvinylchloride (PVC), have shown effective sensing of numerous toxic metal ions.[139] However, problems are associated with these types of sensors including poor lower limits of detection (LLOD), decomposition of the polymer component, and poor selectivity toward important cations like Pb(II), Hg(II), and Cd(II). Leaching of the plasticizer into analyte samples inhibits detection and decreases lifetime of the sensor.[147-149] Ionophores are tailored to the analyte, with the different binding groups on the ionophore directing the selectivity of the sensor. Modification of the number of binding moieties, the hardness/softness of the moieties, the functional group types, and the steric strain in the ionophore are all variables that affect the selectivity and interaction strength of the ionophore. A host of ligands selective toward Pb(II) ions have been developed, each utilizing multidentate binding modes.[139,153-155] Figure 23 outlines several structures of exceptional ionophores utilized in Pb(II) sensors. It is important to note that when choosing an ionophore, the redox chemistry and reactivity of the ligand binding moieties should be considered. Also, the ionophore should have a strong affinity for the analyte, but not strong enough to lead to irreversible complexation and eventual poisoning of the sensor membrane.[139] Furthermore, the receptor portion of the ionophore must be readily accessible to the ion throughout the entire sensor.

Choosing an Ionophore

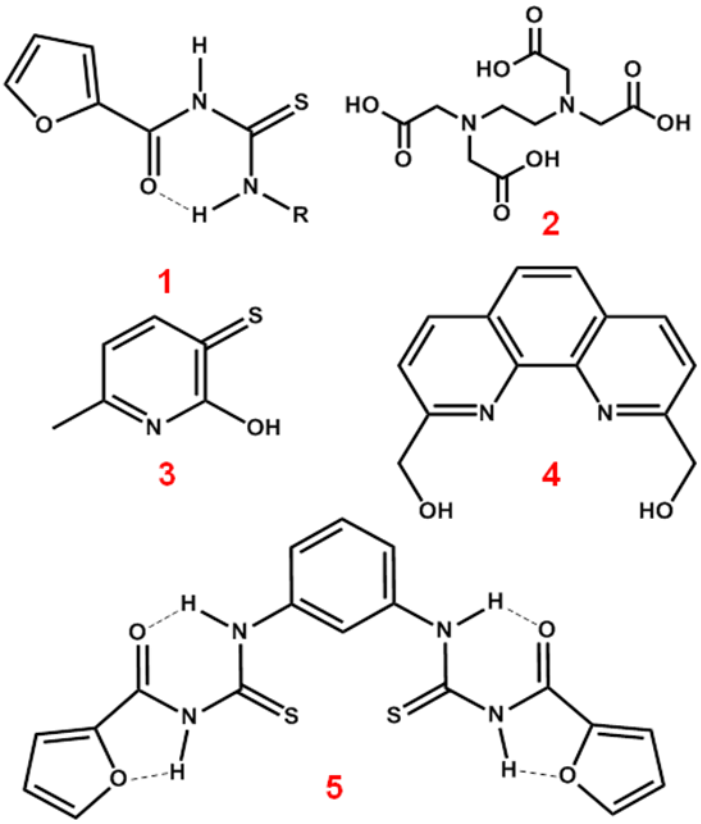

Figure 23. Several structures of Pb(II) ionophores present in the literature. Structure 2, EDTA, is included for comparison of the current medical standard for heavy metal chelation therapy.

Ethylenediaminotetraacetic acid (EDTA), structure **2**, is included as a reference to benchmark compounds used for toxic metal chelation therapy. EDTA binds in several different modes from bidentate to hexadentate. However, while the molecule is highly effective at removing metal cations, chelation is non-selective and all metals are stripped out of the media. Sensors using ionophores with little selectivity suffer from "false" positives, amongst other problems, due to the large assortment of cations present in groundwater. The other structures featured have shown high selectivity toward Pb(II) ions. Compound **3** has been used in conjunction with PVC (polyvinyl chloride) and DOP

(di-*n*-octyl phthalate) to create ion selective electrodes (ISE)s. However, the sensors were not highly selective toward Pb(II) ions, and interference from Cu(II) and Ag(I) ions occurred.[156] Furthermore, the limits of detection (LOD) measured demonstrated that the sensors were not sensitive enough for detection of less than 10^{-6} M metal cations.[156-160] Structures **1**, **4**, and **5** have shown high selectivity toward Pb(II), even in the presence of competitive ions like Hg(II), Cu(II) and Zn(II) cations.[161]

Effective fluorometric and amperiometric sensors have been developed from polymeric and metallopolymer systems. Chemoresistive gas sensors produced from conducting metallopolymers have demonstrated the benefits of exploiting highly conductive hybrid systems.[66,69] Redox matching of the metallopolymer with the analyte led to very high differentiation in the chemoresistive sensors. Examination of redox matching between *poly*-Co(II)EDOT$_2$salen (salicylaldehyde ethylenediamine) metallopolymer and NO demonstrated that conducting metallopolymers could be used to sense NO over NO_2. Other conducting polymer systems have demonstrated chemoresistivity in the presence of halogenated solvents, leading to highly effective VOC sensors.[67,68] Conducting polymers have proven to be useful materials for sensing gases and small molecules, and cation recognition by conducting polymer systems could lead to effective heavy metal sensors.

Mono- and Bis- (Thiourea)benzene Pb(II) Ionophores

As mentioned earlier, the size of the interacting area and the affinity of the binding moieties for Pb(II) ions are very important to develop an effective ionophore. There are several examples in the literature that accentuate the role of the ionophore

geometries on Pb(II) selectivity.[161] Preorganized multidentate systems with rigid structure typically serve as selective ionophores due to the discrete space within the structure for metal interaction. Gephart *et al.* utilized 2,9-*bis*(hydroxymethyl)-1,10-phenanthroline (PDALC) (structure **4** in Figure 24) as a selective ligand for Pb(II) ions.[161] Due to the rigidity and size of the coordinating area in the PDALC, larger ions such as Pb(II) ions, were preferred over smaller ions like Zn(II) and Ni(II).

Other work has capitalized on not only using rigid and discrete coordinating areas, but binding groups tailored to the softness of large Pb(II) ions. Aroylthioureas have demonstrated high selectivity for larger metal cations, such as Pb(II), Sn(II), and Hg(II) ions.[158] The high level of hydrogen bonding present in these types of ionophores, especially furanylthioureas, aids in creating formal areas for sensing. Furthermore, the proximity of the thione near several amides encourages selectivity toward Hg(II) and Pb(II) over other competitive ions like Cu(II) and Zn(II).[157] Due to the ease of synthesis, many compounds have been studied to demonstrate the effect of sterics and electronics on selectivity and performance.[139]

Wilson *et al.* utilized 1,3-*bis*(*N*-benzoylthioureido)benzene and 1,3-*bis*(*N*-furoylthioureido)benzene as effective materials for Pb(II) ion sensing. The sensors consisted of the ionophore (2.0 - 8.0% by weight) cast from a dilute THF into a PVC/dioctyl sebacate/*o*-nitrophenyloctyl ether (DOS/*o*-NPOE) polymeric membrane followed by an epoxy-graphite contact. Several of the compositions resulted in stable sensors, but the sensors had low sensitivity with LODs from 10^{-2} – 10^{-6} M. The ionophores were highly selective for Pb(II), and only Ag(I) ions offered competitive selectivity coefficients. Other aroylthiourea sensors were produced from a library of

ionophores readily synthesized from aroyl chlorides and ammonium isothiocyanate.[159] A broad spectrum of furanyl-based thioureas were synthesized with different steric and electronics *via* changing the group attached to the amide functionality. The case of hexyl appended amide functional groups, the best performing sensors had LODs approaching 10^{-7} M and main competition only from Hg(II) and Ag(I) ions. The hexylphenyl appended furanylthioureas also showed high selectivity for Pb(II) ions.

Our work will focus on utilizing a 3,4-ethylene(dioxy)thienyl (EDOT) or 2,2'-bi(thienyl) (BT) appended furanylbis (thiourea) to create a polymer material, as a solid state sensor (Figure 24). Various examples in the literature have demonstrated that thiophene-based electropolymerized metallopolymers have well-controlled growth behavior with respect to thickness and good ionic porosity in the material. Utilizing these porous EDOT and BT-based materials should provide natural pathways for the metal ions to intercalate through and interact with the ionophore sites throughout the polymer film.

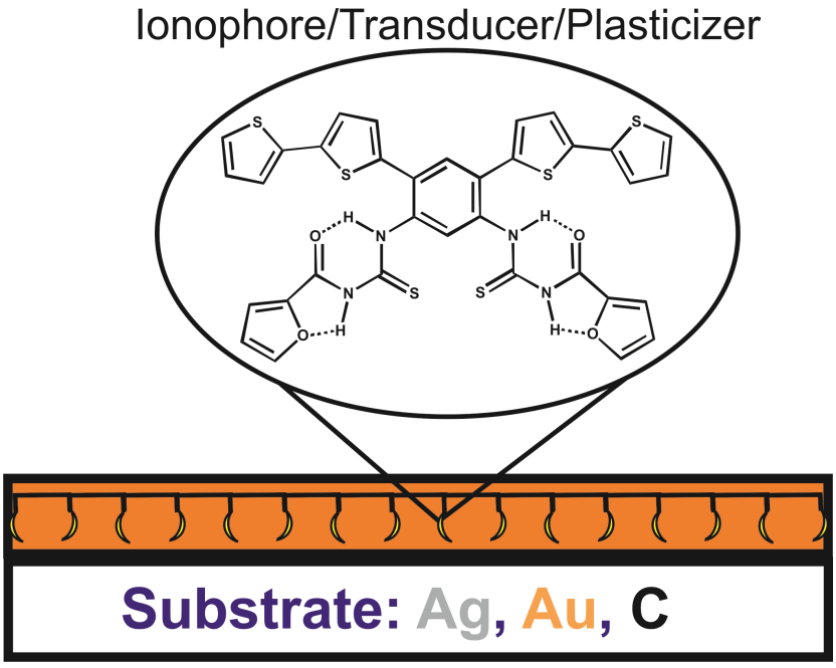

Figure 24. The proposed structure and setup of a conducting polymeric Pb(II) sensor.

EXPERIMENTAL

General Methods.

Air- and moisture-sensitive reactions were out in heat gun-dried glassware using standard Schlenk techniques under an inert nitrogen atmosphere. All solvents were dried using an Innovative Technology, Pure Solv solvent purifier with double purifying column. All other chemical were used as received from commercial suppliers. NMR spectra were recorded with a Varian Unity +300 (^{1}H, 300 MHz, ^{13}C{^{1}H} 75 MHz) and were referenced to residual solvent peaks. Chemical ionization (CI) mass spectra were collected on a Micromass Autospec Ultima mass spectrometer. X-ray photoelectron spectroscopy (XPS) was carried out on a PHI 5700 XPS system equipped with a dual Mg X-ray source and monochromatic Al X-ray source complete with depth profile and angle-resolved capabilities.

Film Thickness and Conductivity Measurements.

Film thickness was determined using a Veeco Dektak Profilometer. Films were prepared on ITO coated glass that was first treated by successive sonication in deionized water, ethanol, acetone, and methylene chloride. Electropolymerization was done as previously described for 20 cycles at a scan rate of 100 mV/s. The thickness measurements are reported as an average of twelve measurements taken on two films. *In situ* conductivity measurements were performed by electrodeposition of the conducting polymers poly-**5-8b** onto an Pt interdigitated electrode purchased from CH Instruments Inc. Films were deposited at scan rate of 100 mV/s for eight cycles and following electropolymerization were then studied at a drain offset of 40 mV at a scan rate of 10 mV/s.

Electrochemistry.

Electrochemical syntheses and studies were done under a nitrogen atmosphere in a dry-box using a GPES system from Eco. Chemie. B. V. All of the electrochemical experiments were carried out in a three electrode cell with a $Ag/AgNO_3$ reference electrode (silver wire dipped in a 0.01 M silver nitrate solution with 0.1 M Bu_4NPF_6 in CH_3CN), a Pt button working electrode (1.6 mm diameter), and a Pt wire coil counter electrode. To calibrate the reference electrode, ferrocene was used as an external reference to which potentials were corrected. All electrochemical experiments were performed CH_2Cl_2 solutions in a supporting electrolyte composed of 0.1 M tetrabutylammonium hexafluorophosphate. The $[(n\text{-}Bu)_4N][PF_6](TBAPF_6)$ was recrystallized three times from hot ethanol, then dried for 4 days at 100 °C under vacuum.

Crystal Structure Determination.

Crystals of monomer **5**, **8a**, and **8b** were grown from the slow evaporation of a chloroform solution. The single–crystal x-ray diffraction data were collected at 153 K on a on a Rigaku SCX-Mini diffractometer with a Mercury CCD using a Rigaku Tec 50 low-temperature device. The complex was collected using a graphite monochromator with MoKα radiation (λ = 0.71075Å). Absorption corrections were applied using Multi-scan. Details of crystal data, data collection and structure refinement are listed in the crystal tables section. Data reduction was performed using the Rigaku Americas Corporation's Crystal Clear version 1.40.[162] The structures were solved by direct methods using SIR97[163] and refined anisotropically using full-matrix least-squares methods with the SHELX 97 program package.[164] Structure analysis was aided by use of the programs

PLATON98[165] and WinGX.[166] The coordinates of the non-hydrogen atoms were refined anisotropically. The amine H atoms were located in a difference-Fourier map and both positional and isotropic displacement parameters were refined. All other H atoms were positioned geometrically and refined using a riding model, with C-H = 0.95-0.99 Å and with U_{iso}(H) = 1.2 times U_{eq}(C). Neutral atom scattering factors and values used to calculate the linear absorption coefficient are from the International Tables for X-ray Crystallography (1992).[167]

Synthesis

Synthesis of the Ionophores

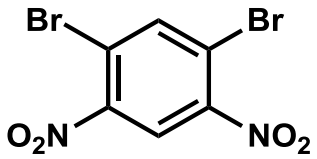

1, 5-Dibromo-2, 4-dinitrobenzene. 1, 3-Dibromobenzene (5.7 g, 24.2 mmol) was added slowly to a stirred mixture of concentrated sulfuric acid (5.3 mL) and fuming nitric acid (5.3 mL) in a 25 mL round bottom flask and cooled in an ice bath. The temperature of the reaction was kept at c.a. 0 °C during addition, and then at room temperature for 40 min. after the addition was complete. The reaction mixture was then stirred with an excess of crushed ice. A solid yellow precipitate formed and was collected by filtration and washed with water until the filtrate was neutral. The crude solid was recrystallized in a mixture of boiling ethanol (100 mL) and acetone (10 mL) and cooled in the fridge overnight. Two groups of crystals were collected and washed with cold ethanol to give 5-dibromo-2, 4-dinitrobenzene as a bright yellow crystalline solid (5.2 g, 66%) m.p. 117-118 °C. ^{1}H NMR ($CDCl_3$) 8.44 (s, 1H), 8.21 (s, 1H).

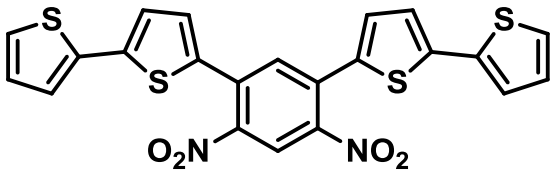

(1). To a 200 mL Schlenk flask under inert atmosphere, 1,5-dibromo-2,4-dinitrobenzene (3.25 g, 10 mmol) and *trans*-dichlorobis(triphenyl)phosphine palladium (II) (0.35 g, 0.5 mmol) were added. THF (100 mL) was added and the yellow solution was brought to 60 °C and stirred for 15 minutes. 2-(Tributylstannyl)bithiophene [128](10.0 g, 0.022 mmol) was added slowly to the reaction vessel and the resulting orange solution slowly turned to a dark red, and was stirred under reflux overnight. The solvent was then removed leaving a crude dark solid, which was redissolved in dichloromethane (DCM) and adsorbed onto silica. The crude product on silica was then purified using column chromatography (DCM and hexanes 1:2, 300 mL slurry, R_f = 0.25). The column separated into three distinct bands with the first being a small amount of quarterthiophene, the second being mono-substituted byproduct, and the third being the desired product, which came off as red solution from which a crystalline red solid readily precipitated (3.65 g, 73.7%) m.p. 176.8 °C, FTIR (solid): 1531 (s, N-O), 1340 (s, N-O) cm^{-1}. ^1H NMR ($CDCl_3$): 8.23 (s, 1H), 7.76 (s, 1H), 7.30-7.27 (dd, *J* = 0.8, *J* = 3.0, 2H), 7.22-7.20 (dd, *J* = 1.0, *J* = 2.0, 2H), 7.17-7.11 (dd, *J* = 1.1, *J* = 6.0, 4H), 7.05-7.02 (dd, *J* = 1.0, *J* = 3.0, 2H). $^{13}C\{^1H\}$ NMR: product was too insoluble in deuterated solvents to acquire a spectra. HRMS (CI) m/z calculated for $C_{22}H_{12}N_2O_4S_2$ 496.9700 $[M + H]^+$, found 497.100. Elemental analysis calculated (found): C, 53.21 (52.51); H, 2.44 (2.43).

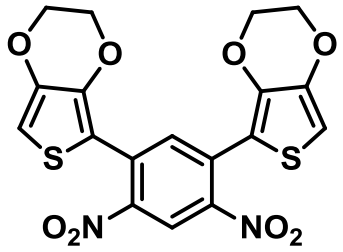

(2). To a 200 mL Schlenck flask under inert atmosphere, 1,5-dibromo-2,4-dinitrobenzene (3.25 g, 10 mmol) and *trans*-dichlorobis(triphenyl)phosphine palladium (II) (0.35 g, 0.5 mmol) were added. THF (100 mL) was added and the yellow solution was brought to 60 °C and stirred for 15 minutes. 2-(Tributylstannyl)-3,4-ethylenedioxythiophene[128] (9.30 g, 0.022 mmol) was added slowly to the reaction vessel and the resulting light orange solution slowly turned to a dark orange, and was stirred under reflux overnight. The solvent was then removed leaving a crude dark solid, which was redissolved in DCM and dried onto silica. The crude product on silica was then purified using column chromatography (DCM and hexanes 2:1, 6 inch column, R_f = 0.36). The column separated into three distinct bands with third being the desired product, which came off as a rose colored solution that produced a semi-crystalline lustrous yellow precipitate (3.25 g, 72.6%). m.p. 176 °C (dec.), FTIR (solid): 1524 (s, N-O), 1342 (s, N-O) cm^{-1}. ^1H NMR ($CDCl_3$): 8.48 (s, 1H), 7.61 (s, 1H), 6.59 (s, 2H), 4.23 (s, 4H) $^{13}C\{^1H\}$ NMR ($CDCl_3$): product was too insoluble in deuterated solvents to acquire a spectra. HRMS (CI) m/z calculated for $C_{18}H_{12}N_2O_8S_2$ 449.2300 $[M + H]^+$, found 449.2500. Elemental analysis calculated (found): C, 48.21 (48.23); H, 2.70 (2.50).

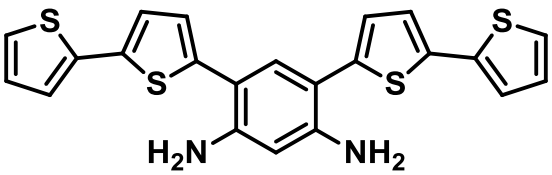

(3). To a 50 mL three-neck flask under inert atmosphere, **1** (1.00 g, 2.02 mmol) and Fe powder (1.74 g, 24.6 mmol) was added and stirred vigorously for 15 minutes. Then THF (25 mL) was transferred into the flask and the solution was stirred at 50 °C until the red solid dissolved. Acetic acid (8 mL) and dry ethanol (8 mL) were added and the reaction was stirred under reflux for 90 minutes. The solvent was removed from the dark purple solution, leaving a rusty brown precipitate. The crude product was adsorbed onto silica and purified using column chromatography (DCM, 250 mL silica gel, $R_f = 0.15$) yielding a green semi-crystalline solid (0.26 g, 29.5%). m.p. 178.3 °C (dec.), FTIR (solid): 3347 (m, N-H), 1590 (m, N-H)cm^{-1}. ^1H NMR ($CDCl_3$): 7.25 (s, 1H), 7.24 (s, 1H), 7.20 (d, J = 1.5, 1H), 7.18 (d, J = 1.5, 1H), 7.16 (d, J = 2.0, 1H), 7.15-7.13 (dd, J = 12.0, J = 14.0, 2H), 7.12 (s, 1H),7.02 (s, 2H), 7.01 (dd, J = 1.0, J = 4.0, 2H), 6.15 (s, 1H), 4.10-4.05(s, 4H). $^{13}C\{^1H\}$ NMR ($CDCl_3$): 145.2, 140.0, 137.6, 136.1, 133.6, 127.9, 126.1, 124.2, 123.7, 111.2, 101.9. HRMS (CI) m/z calculated for $C_{22}H_{16}N_2S_4$ 437.6547 $[M + H]^+$, found 437.6555. Elemental analysis calculated (found): C, 60.52 (60.46); H, 3.69 (3.30).

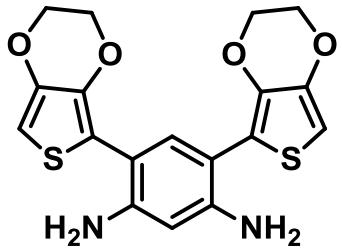

(4a). To a 100 mL three-neck flask in inert atmosphere, **2** (1.00 g, 2.23 mmol) and THF (35 mL) were added. Then $LiAlH_4$ (840 mg, 22.3 mmol) was added in small portions resulting in a dark red solution. The solution was stirred for two hours resulting in a green solution, and was then stirred overnight at 60 °C. The green solution was cooled to room temperature and ethanol was slowly added over 20 minutes, followed by water, to quench any left over $LiAlH_4$. The resulting orange solution with a grey precipitate was

extracted with DCM (3 × 75 mL) and the organic layer was collected and dried over $MgSO_4$. The DCM solution was filtered and the solvent was removed *in vacuo* to yield a dark red precipitate (0.33 g, 38.1%). m.p. 156.4 °C (dec.), FTIR (solid): 3345 (m, N-H), 1588 (m, N-H) cm^{-1}. ^1H NMR ($CDCl_3$): 7.43 (s, 1H), 6.82 (s, 1H), 6.40 (s, 2H), 4.25 (s, 8H), 3.55 (b, 4H). $^{13}C\{^1H\}$ NMR ($CDCl_3$): 141.7, 137.7, 134.1, 122.2, 119.3, 115.1, 99.5. HRMS (CI) m/z calculated for $C_{18}H_{16}N_2O_4S_2$ 389.4600 $[M + H]^+$, found 389.4897. Elemental analysis calculated (found): C, 55.65 (54.98); H, 4.15 (4.31).

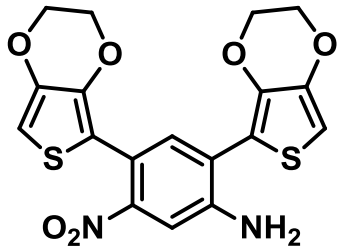

(4b). To a 50 mL three-neck flask in N_2 atmosphere, **2b** (1.00 g, 2.36 mmol) and Fe powder (1.37 g, 24.6 mmol) was added and stirred vigorously for 15 minutes. Then THF (25 mL) was cannula transferred into the flask and the solution was stirred at 50 °C until the yellow solid dissolved. Acetic acid (8 mL) and dry ethanol (8 mL) was added and the reaction was stirred under reflux for 90 minutes. The solvent was removed from the dark red solution, leaving a dark orange precipitate. The crude product was dried onto silica and purified using column chromatography (DCM, 250 mL silica gel, $R_f = 0.40$) yielding an orange semi-crystalline solid. dec. 197 ºC ^1H NMR ($CDCl_3$): 7.34 (s, 1H), 7.25 (s, 1H), 6.47 (s, 1H), 6.33 (s, 1H), 4.45 (s, 4H), 4.35 (s, 4H). $^{13}C\{^1H\}$ NMR: product was too insoluble in deuterated solvents to acquire a spectra.

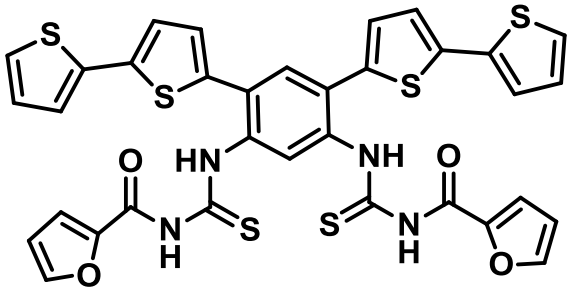

(5). To a 50 mL three-neck flask in inert atmosphere, ammonium thiocyanate (0.305 g, 4 mmol) and 10 mL of acetone were added. A solution of furoyl peroxide (0.522 g, 4 mmol) in 5 mL acetone was added dropwise and stirred vigorously for 1 hour under reflux. The foggy white suspension was cooled to room temperature and then **3** (0.436 g, 1 mmol) in 5 mL acetone was added at once. The yellow solution was stirred overnight under reflux, and then cooled to room temperature. After cooling, the solution was added into 50 mL ice water, resulting in a white solution with a yellow precipitate. The aqueous solution was extracted using chloroform (3 × 50 mL) and the yellow solution was concentrated to 20 mL and placed in a refrigerator. Yellow crystals formed in the flask suitable for single crystal X-ray diffraction after 72 hours (0.60 g, 80.75%). m.p. 236.4 °C, ^{1}H NMR ($CDCl_3$): 12.15 (s, 2H), 9.32 (s, 2H), 8.47 (s, 1H), 7.81 (s, 1H), 7.64 (d, 2H), 7.30 (d, J = 2.0, 2H), 7.25 (t, J = 1.0 2H), 7.2 (t, J = 3.4, 2H), 7.03 (t, J = 2.0, 2H), 6.66 (d, J = 4.5, 2H). ^{13}C{^{1}H} NMR: product was too insoluble in deuterated solvents to acquire a spectra. HRMS (CI) m/z calculated for $C_{34}H_{22}N_4O_4S_6$ 743.9500 $[M + H]^+$, found 743.9588. Elemental analysis calculated (found): C, 54.96 (54.17); H, 2.98 (2.49).

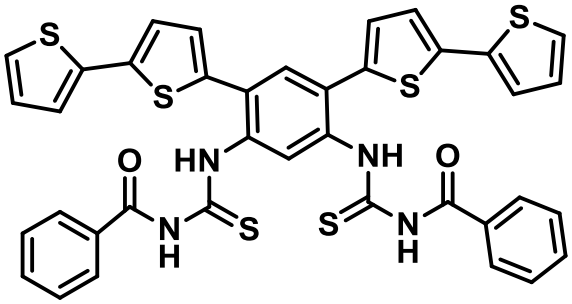

(6). Similar procedure to **5**, except benzoyl chloride (0.562 g, 4 mmol) was used. Reaction yielded an off-white precipitate (0.70 g, 91.7%). m.p. 237.3 °C ^{1}H NMR ($CDCl_3$): 12.41 (s, 2H), 9.20 (s, 2H), 8.50 (s, 1H), 7.90(d, 6H), 7.81 (s, 1H), 7.68 (d, J = 2.6, 2H), 7.56 (d, J = 2.0, 4H), 7.30 (d, J = 3.0, 2H), 7.25 (t, 2H), 7.21 (t, 2H), 7.03 (s, 2H). HRMS (CI) m/z calculated for $C_{38}H_{26}N_4O_2S_6$ 764.0300 $[M + H]^+$, found 764.0300. Elemental analysis calculated (found): C, 59.82 (60.11); H, 3.43 (3.47).

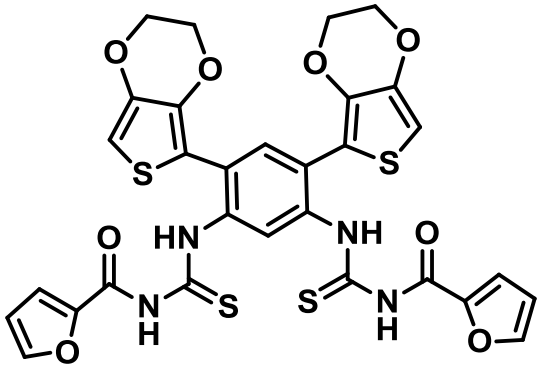

(7a). Similar procedure to **5**, except the diamine **4a** (0.388 g, 1 mmol) was used. Reaction yielded a dark red precipitate (0.554 g, 79.8%). m. p. 210.8 °C ^{1}H NMR ($CDCl_3$): 12.25 (s, 2H), 9.20 (s, 2H), 8.18 (s, 1H), 7.91(d, J = 4.2 4H), 7.48 (d, J = 5.6 6H), 6.44 (s, 2H), 4.21 (s, 8H). ^{13} C{^{1}H} NMR ($CDCl_3$): product was too insoluble in deuterated solvents to acquire a spectra. HRMS (CI) m/z calculated for $C_{30}H_{22}N_4O_8S_4$ 695.7800 $[M + H]^+$, found 695.7900. Elemental analysis calculated (found): C, 51.86 (52.23); H, 3.19 (3.01).

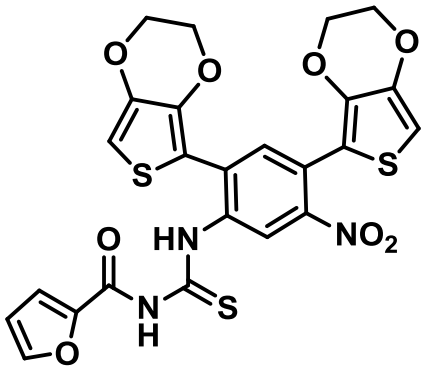

(7b). Similar procedure to **5**, except the amine **4b** (0.418 g, 1 mmol) was used. Reaction yielded an orange precipitate (0.493 g, 85.6%). m.p. 186.9 °C (dec.) ^{1}H NMR ($CDCl_3$): 12.25 (s, 2H), 9.20 (s, 1H), 8.77 (s, 1H), 7.62 (s, 1H), 7.59 (s, 1H), 7.34 (d, J = 1.0, 1H), 6.62 (d, J = 1.0, 1H), 6.50 (s, 1H), 6.43 (s, 1H). HRMS (CI) m/z calculated for $C_{34}H_{26}N_4O_6S_4$ 715.8500 $[M + H]^+$, found 715.8600. Elemental analysis calculated (found): C, 57.13 (57.29); H, 3.67 (3.81).

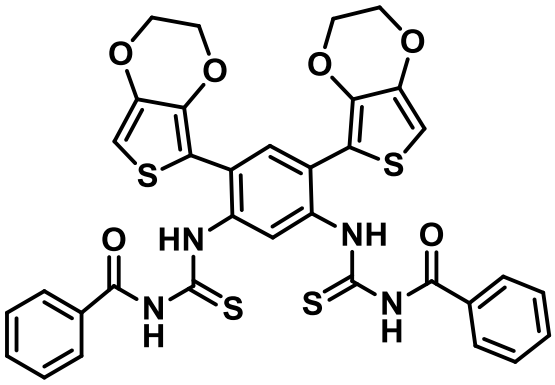

(8a). Similar procedure to **5**, except benzoyl chloride (0.562 g, 4 mmol) was used to generate the salt intermediate, and diamine **4a** (0.388 g, 1 mmol) was used as the amino reagent. Reaction yielded a dark red precipitate (0.602 g, 84.3%). m.p. 210.9 °C ^{1}H NMR ($CDCl_3$): 12.35 (s, 2H), 9.20 (s, 2H), 8.18 (s, 1H), 7.91(d, J = 3.3, 4H), 7.48 (d, J = 6.0, 6H), 7.34(s, 1H), 6.44 (s, 2H), 4.21 (s, 8H). HRMS (CI) m/z calculated for

$C_{24}H_{17}N_3O_8S_3$ 572.600 $[M + H]^+$, found 572.600. Elemental analysis calculated (found): C, 50.43 (50.97); H, 3.00 (3.24).

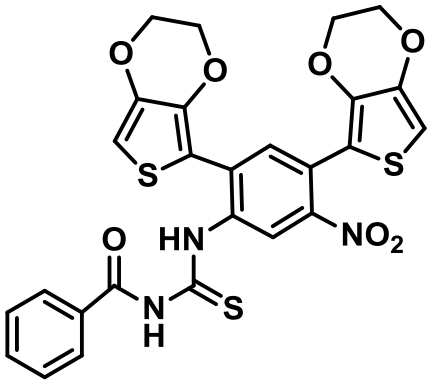

(8b). Similar procedure to **5**, except benzoyl chloride (0.562 g, 4 mmol) was used to generate the salt intermediate, and amine **4b** (0.418 g, 1 mmol) was used as the amino reagent. Reaction yielded an orange precipitate (0.551 g, 94.7%). m.p. 187.2 °C (dec.) ^{1}H NMR ($CDCl_3$): 12.62 (s, 1H), 9.31 (s, 1H), 8.67 (s, 1H), 7.60(d, *J* = 9.0, 1H), 7.34 (d, *J* = 2.3, *2H*), 7.22 (d, *J* = 11.0, 2H), 7.17 (m, 1H) 6.50 (s, 1H), 6.43 (s, 1H), 4.27(s, 8H). HRMS (CI) m/z calculated for $C_{26}H_{19}N_3O_7S_3$ 582.6400 $[M + H]^+$, found 582.6400. Elemental analysis calculated (found): C, 53.49 (53.57); H, 3.29 (3.41).

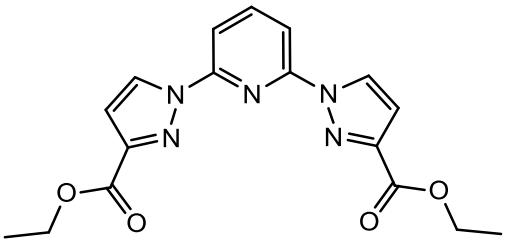

2,6-*bis*(3-ethylesterpyrazol-1-yl)pyridine.[181] To a solution of 3-ethylesterpyrazole (2.82g, 20 mmol) and 25 mL of dry DMF in a 100 mL Schlenk flask, Potassium (0.86 g, 22 mmol) was added in small chunks and left to stir at 60 °C until fully dissolved. 2,6-dibromopyridine (1.56 g, 6.6 mmol) was then added to the solution and heated to 120 °C for 4 days. The dry DMF from the muddy brown solution was removed *in vacuo*, and the

resulting dark brown residue was dissolved in CH_2Cl_2 and washed with water (2x100 mL) and brine (100 mL). The resulting orange brown solid was then further purified by column chromatography using silica gel and a mixture of hexanes/ethyl acetate/$CHCl_3$ (6:2:1) (1.42 g, 62.9%) (R_f = 0.90). ^{1}H NMR ($CDCl_3$) 8.60 (s, 2H), 8.11(d, *J* = 1.0, 2H), 7.72(t, *J* = 1.5, 1H), 7.46(d, *J* = 0.*8, 2H*), 7.24(s, $CDCl_3$), 6.99(s, 2H), 4.44(q, 4H), 1.38(t, *J* = 2.5, 6H). MS(CI) m/z calculated: 356.35[M^+], found 356.43.

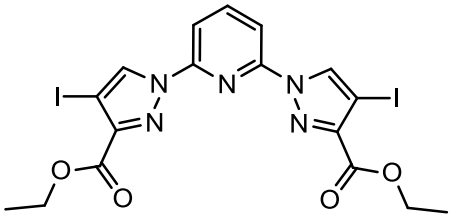

2,6-*bis*(3-ethylester-4-iodopyrazol-1-yl)pyridine (9).[182] To a solution of 2,6-*bis*(3-ethylesterpyrazol-1-yl)pyridine (0.5 g, 1.42 mmol) in acetic acid (4 mL) and H_2SO_4 (0.5 mL, 30% in water) in a round bottom flask under nitrogen, A solution of HIO_3 (0.1 g, 0.57 mmol), I_2 (0.29 g, 1.14 mmol), and two drops of concentrate sulfuric acid was added slowly over 30 minutes. The following pink solution was left to stir 3 hours at 60 °C. The excess I_2 was quenched with aqueous sodium thiosulfite and the resulting yellow solution was then neutralized using $NaHCO_3$/Na_2CO_3 solution in a 1:1 ratio. The solution was extracted with chloroform (3×50 mL) resulting in a pink solution. The solvent was removed leaving a reddish tan solid (0.702g, 81%). ^{1}H NMR ($CDCl_3$) 8.72 (s, 2H), 8.11(d, *J* = 1.5, 2H), 7.72(t, *J* = 1.0, 1H), 4.44(q, 4H), 1.38(t, *J* = 2.5, 6H). MS(CI) m/z calculated: 608.14[M^+], found 608.7.

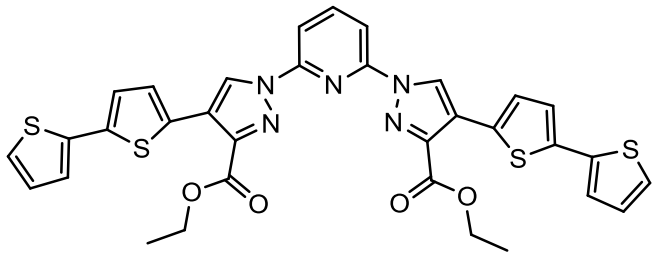

2,6-*bis*(4-(2,2'bithiophene-5-yl)-3-ethylesterpyrazol-1-yl)pyridine (10a). A mixture of 2,6-*bis*(3-ethylester-4-iodopyrazol-1-yl)pyridine (0.50 g, 1.04 mmol) and $Pd(PPh_3)_2Cl_2$ (0.045g, 0.05 mmol) were loaded into a 50 mL Schlenk flask under a nitrogen atmosphere. The mixture was dissolved in 10 mL of THF, and stirred until completely dissolved. The solution was heated to 75 °C and 2-(tributylstannyl)bithiophene[128] (0.745 g, 2.3 mmol) in 5 mL dry THF was cannula transferred to the flask. The solution was heated at 80 °C for 36 hours. After cooling to room temperature, the solvent was removed *in vacuo* and the resulting black precipitate was dissolved in CH_2Cl_2 and filtered through a silica plug using CH_2Cl_2. The resulting orange filtrate solution was removed of solvent *in vacuo* yielding a light orange solid (0.249 g, 39.6%) ^{1}H NMR ($CDCl_3$) 8.63 (s, 2H), 8.11(d, *J* = 1.5, 2H), 7.82(m, 4H), 7.75(m, 4H), 7.72(t, *J* = 1.0, 1H), 7.30(t, *J* = 2.0, 2H), 4.45(q, 4H), 1.43(t, *J* = 2.5, 6H). MS(CI) m/z calculated: 684.84[M^+], found 684.7.

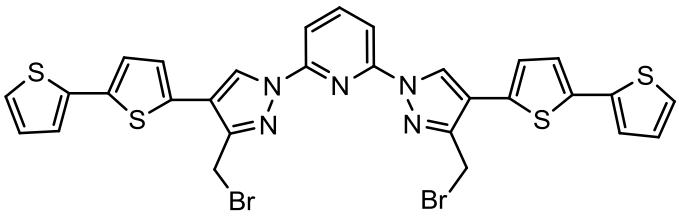

2,6-*bis*(4-(2,2'bithiophene-5-yl)-3-bromomethylpyrazol-1-yl)pyridine (11a). 2,6-*bis*(4-(2,2'bithiophene-5-yl)-3-ethylesterpyrazol-1-yl)pyridine (0.250 g, 0.37 mmol) in Schlenk flask under nitrogen atmosphere was dissolved in THF (10 mL) and the solution was cooled to -5 °C. $NaBH_4$ (0.029 g, 0.74 mmol) in one portion, and the solution was

stirred at -5 °C for 1 hour, and aliquots of a saturated NH_4Cl solution were added until a precipitate appeared. The solution was filtered and the solvent was removed to obtain an orange solid, which was dissolved in distilled DMF (100 mL) in a round bottom Schlenk flask under argon atmosphere. PBr_3 (0.216 g, 0.8 mmol) was added at room temperature and the solution was stirred at room temperature for 12 hours. The solvent was distilled under reduced pressure and the residue was dissolved in a H_2O/CH_2Cl_2 mixture (5 mL each), and the aqueous layer was neutralized to pH 7-8 with $NaHCO_3$ solution. The aqueous phase was extracted with CH_2Cl_2 (4 × 200 mL) and the combined organic phases were washed with brine, dried over Na_2SO_4, filtered and the solvent was removed in vacuo. The residue was purified by flash chromatography on silica gel (CH_2Cl_2, 100%) yielding a light yellow orange solid (0.127 g, 49.6%). ^1H NMR ($CDCl_3$) 8.64 (s, 2H), 8.12(d, 2H), 7.80(d, 4H), 7.77(d, 4H), 7.72(t, 1H), 7.30(t, 2H), 4.67(s, 4H).

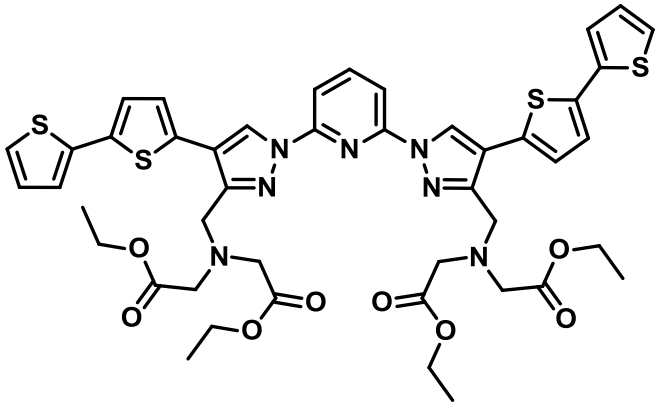

2,6-*bis*(4-(2,2'bithiophene-5-yl)-3-diethyliminodiacetatopyrazol-1-yl)pyridine (12a). 2,6-*bis*(4-(2,2'bithiophene-5-yl)-3-bromomethylpyrazol-1-yl)pyridine (0.243 g, 0.336 mmol) and diethyl iminodiactate (0.66 mL, 0.74 mmol). K_2CO_3 (0.93 g, 6.72 mmol), and TFA (1 mL) was dissolved in a solution containing THF (10 mL) and CH_3CN (18 mL), and the heterogeneous solution was stirred at 50 °C overnight. The solution was filtered

and the filtrate was concentrated under reduced pressure. The residual oil was dissolved in CH_2Cl_2 (20 mL) and washed with water (3×20 mL) and brine (100 mL). The organic phase was dried over Na_2SO_4, filtered and the solvent was removed *in vacuo*. Flash chromatography over silica gel (CH_2Cl_2/MeOH, 98:2) afforded a orange solid (0.100 g) ^{1}H NMR ($CDCl_3$) 8.66 (s, 2H), 8.12(d, 2H), 7.79(d, 4H), 7.75(d, 4H), 7.72(t, 1H), 7.30(t, 2H), 6.55 (d, 2H), 4.16 (q, 2H), 4.00 (s, 2H), 3.56 (s, 4 H), 2.23 (s, 3H), 1.28 (t, J = 2.5, 6H).

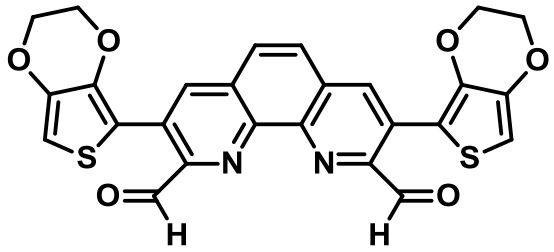

3,8-*bis*(ethylenedioxythien-5-yl)-1,10-phenanthroline-2,9-dicarbaldehyde (14).[177] 3,8-*bis*(ethylenedioxythien-5-yl)-2,9-dimethyl-1,10-phenanthroline (488 mg, 1 mmol) and SeO_2 (333 mg, 3 mmol) were added to a 100 mL Schlenk flask. To the flask was added 25 mL of dry dioxane, and the resulting orange solution was stirred for 12 hrs at reflux. The dark red solution was allowed to cool to room temperature and filtered through a celite pad. The solvent from the filtrate was removed under vacuum, and the crude red precipitate was recrystallized using hot ethanol and placed in a refrigerator at 0 ºC. The pale red-orange crystals were gathered by vacuum filtration in a 72.1 % yield (345 mg). m.p. 180.5 ºC ^{1}H NMR ($CDCl_3$): 13.33 (s, 2H), 8.88 (d, J = 15.6, 2H), 7.70 (s, 2H), 6.50 (s, 2H), 4.45 (s, 8H). LRMS (CI) m/z calculated for $C_{25}H_{15}N_2O_6S_2$ 517.558 $[M + H]^+$, found 517.54.

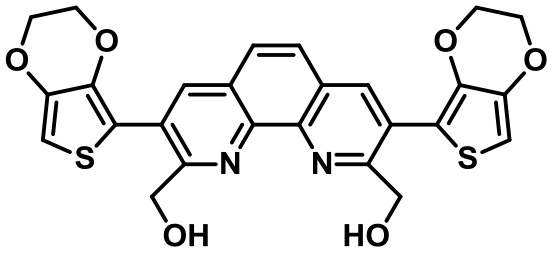

3,8-bis(ethylenedioxythien-5-yl) neocuproine (15).[178] **14** (150 mg, 0.29 mmol) was added to a 100 mL Schlenk flask under N_2 atmosphere and dissolved in THF (12 mL). $LiAlH_4$ (55 mg, 1.45 mmol) was added in one portion and the reaction mixture slowly turned to a very dark red color. The reaction was stirred at room temperature for one hour, and then under reflux overnight. The resulting light green solution was cooled to room temperature and the solvent removed under vacuum. Ethanol (40 mL) was added to the grey precipitate, and then removed under vacuum. The light grey precipitate was filtered and washed with 200 mL of CH_2Cl_2. The filtrate was washed first with a brine solution (2 × 75 mL) and then water (1 × 75 mL). The organic phase was dried with $MgSO_4$ and filtered through a celite pad. The CH_2Cl_2 was removed under vacuum, and the resulting orange powder needed no further purification. Yield: 130 mg (88%) m.p. 155.8 ºC ^{1}H NMR ($CDCl_3$): 8.79 (d, J = 13.7, 2H), 7.80 (s, 2H), 6.50 (s, 2H), 4.45 (s, 8H), 3.89(s, 2H), 3.1 (s, 4H) . LRMS (CI) m/z calculated for $C_{25}H_{15}N_2O_6S_2$ 521.588 $[M + H]^+$, found 521.590.

RESULTS AND DISCUSSION

Electropolymerizable Mono- and Bis(aroylthiourea)benzene

The ease of modification, robustness, and selectivity of the mono- and *bis*(aroylthiourea)benzenes makes them attractive cores for conducting polymers. We aimed to utilize the sensitivity of thiophene-based conducting polymers by synthesizing novel thienyl appended mono- and *bis*(aroylthiourea)s. These new compounds can be electropolymerized under oxidative potentials to create polymer thin films. The conducting polymer membranes should act as single piece ion selective electrodes, due to the ionophore being in direct electronic communication with the polymer. Figure 25 depicts one electrode material that will be synthesized to sense Pb(II) ions.

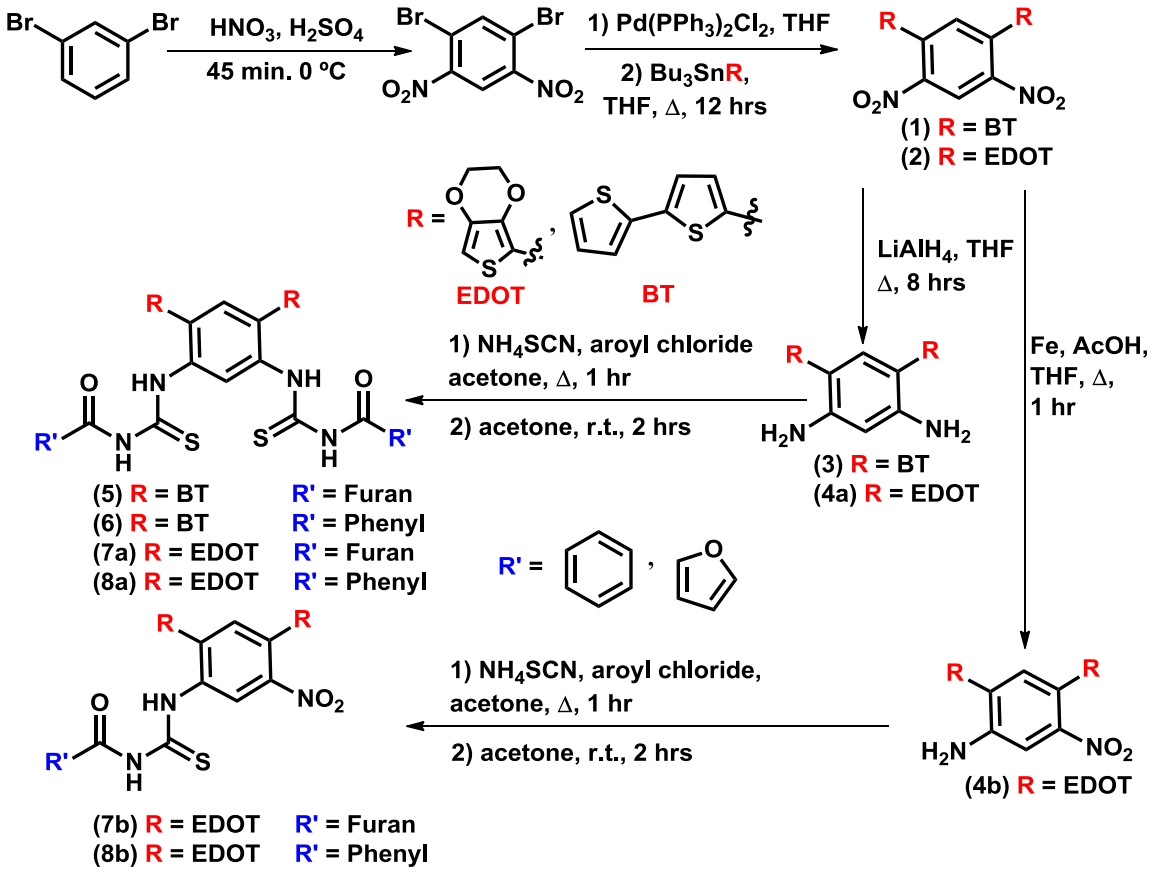

Scheme 11. Synthetic scheme for the electropolymerizable ionophoric monomers.

Bis(aroylthiourea)benzene ionophores can be easily included into an electropolymer backbone creating a single component ISE membrane. Conducting polymers are highly senstive to the surrounding environment and selective ionophore polymers would benefit not only from this heightened sensitivity, but many of the degradation problems could potentially be negated. LODs for potentiometric Pb(II) ISE membrane sensors are near 10^{-6} to 10^{-7} M. Addition of ionophores into conducting polymers, such as polyaniline and polythiophene, have shown enhancement of the sensitivity of ISEs. Utilizing polymer backbones has led to polymer/plasticizer blends with LODs from 10^{-7} to 10^{-9} M. The increase in sensitivity is directly linked to the conductivity and electronic properties of the polymers. A polyaniline/ionophore blend showed remarkable LODs with no decrease in function of the membranes after fifteen months.[157] The sensor utilized not only the added stability, but the ionic permeability of the sensor greatly amplified the capabilities of the ionophore.

The synthetic route, in Scheme 11, followed a procedure emphasizing the production of mono- and diamine precursors as useful handles leading to several aroylthioureabenzene derivatives. The synthetic pathways to aroyl and furoyl *bis(*thiourea)s **5-8b** started from 4,6-dibromo-1,3-dinitrobenzene which was made in high yield from a simple nitration using fuming nitric acid and sulfuric acid. The precursor material was then used as the halogen partner in a Stille coupling with tri(butyl)stannylbithiophene or tri(butyl)stannyl ethylenedioxythiophene, to form **1**, a dark red lustrous semi-crystalline material, or **2**, a bright yellow lustrous powder. Both **1** and **2** derivatives were fully characterized by ^{1}H and ^{13}C $\{^{1}H\}$ NMR, mass spectrometry, IR spectroscopy and elemental analysis by combustion. The nitro derivatives, **1** and **2**,

were then hydrogenated using activated Fe powder and AcOH/EtOH, producing a green crystalline material, **3**, and a pink crystalline material, **4a**. ^{1}H NMR was used to track the formation of the NH_2 groups, and IR spectra clearly showed the disappearance of the nitro groups as a sharp peak at ~1525 cm^{-1} to a broad smaller peak at ~1620 cm^{-1} and the appearance of a small broad peak at 3535 cm^{-1}.

Crystal Structures of the Ionophores

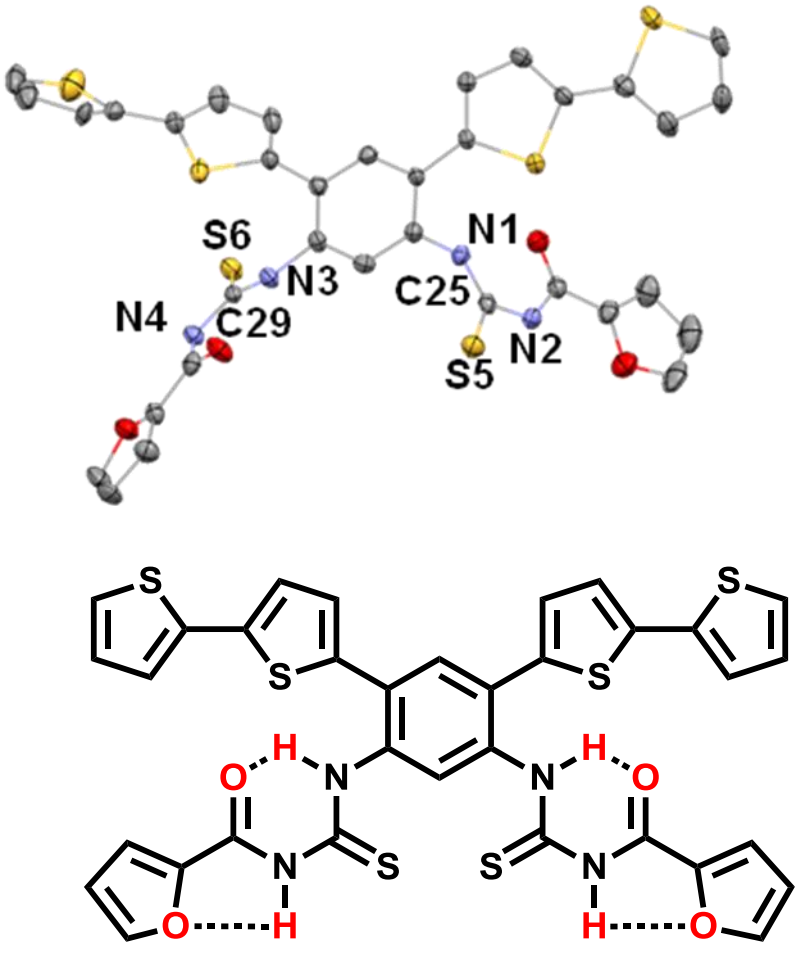

Figure 25. The crystal structure for structure **5**. ORTEP ellipsoids shown with a 50% probability level. Hydrogens were omitted from the structure for clarity.

A selection of *bis*(thiourea)s could then be synthesized from **3** and **4a**, through a high yielding reaction with the desired aroyl thiourea intermediate. The four different bis(thiourea)s were purified through recrystallization from DCM and hexanes. An X-ray quality single-crystal of **5** was isolated and the crystal structure was determined (Figure 25). Due to the large steric bulk around the central benzene, the furoylthiourea and bithienyl groups twist significantly out of plane. The amide hydrogen-furoyl oxygen and amide hydrogen-keto oxygen bonding interactions cause the entire furoyl thiourea moieties to lie in one plane.

Table 5. Selected bond (º) and the hydrogen bonding parameters for **5** derived from the single-crystal X-ray structure.

D-H…A	*D*-H	H…A	*D*…A	*D*-H…A
N1-H35…O1	0.88	2.302	2.721	109.2
N2-H36…O2	0.88	1.883	2.625	146.8
N3-H37…O3	0.905	1.926	2.663	137.2
N4-H38…O4	0.915	2.266	2.677	111.7
	N1-C25-S5	N2-C25-S5	N3-C29-S6	N4-C29-S6
Bond Angle (°)	119.5	125.4	127.2	117.9

Looking at the bond distances for H35---O1 and H37---O3, which are 1.883 Å and 1.926 Å respectively, suggest the furoyl oxygens may form an intramolecular hydrogen bond from the N1 and N3 amide groups. The geometry surrounding the hydrogens is significantly distorted, with 146.8° and 137.2° angles for the N1-H35---O1 and N1-H37---O3 atoms, which further supports intermolecular hydrogen bonding. Similar thiourea structures display this hydrogen bonding forming readily within the thiourea, the extent of this interaction increases with furoyl-type structures.[168] The

hydrogen bonding increases the stability of the *bis*(thiourea)s, with compounds **5**, **7a**, and **8a** possessing heightened chemical and thermal stability. The melting points of the ionophores are near 240 °C, and the monomers showed no decomposition in acidic or basic conditions. The crystal structure for **6**, showed similar hydrogen bonding between the keto-oxygen and the amide hydrogen. Unlike **5** however, the benzyl is not stabilized and significant twisting occurs in the thiourea portion of the structure.

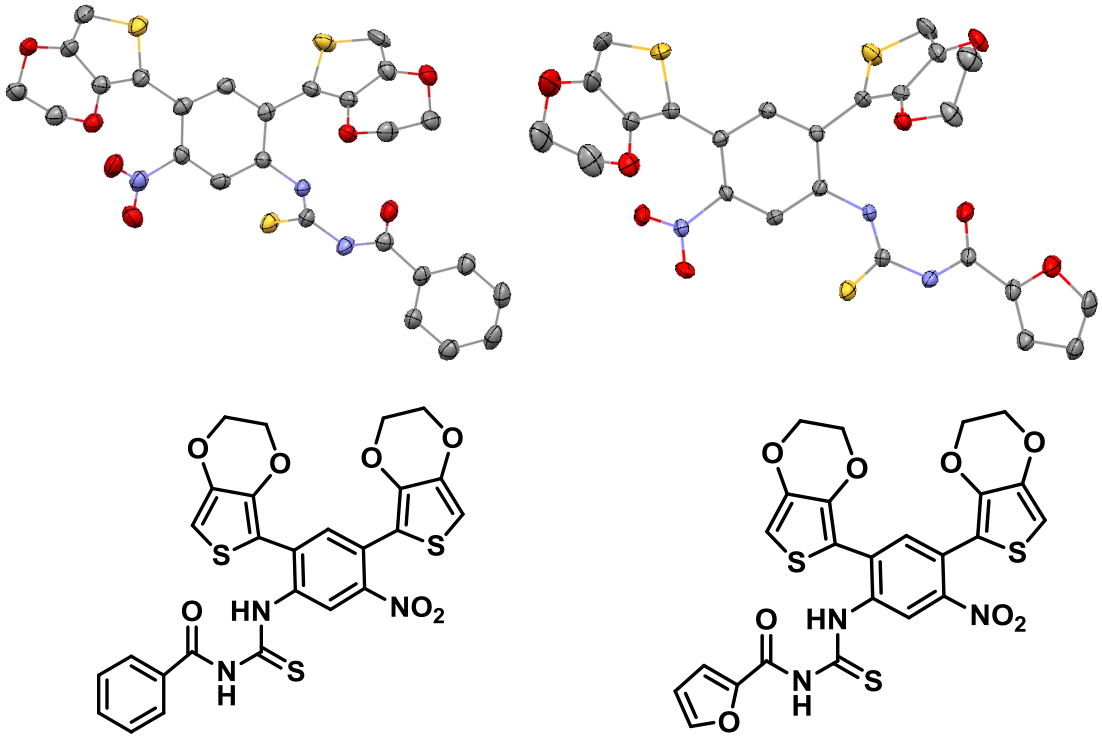

D-H…A	*D*-H	H…A	*D*…A	*D*-H…A
N2-H10…O5	0.78	2.28	2.886	136
N2-H10…O7	0.78	2.06	2.679	138
N3-H19…O3	0.90	-	-	-

D-H…A	*D*-H	H…A	*D*…A	*D*-H…A
N2-H10…O5	0.85	2.48	3.139	134
N2-H10…O7	0.85	1.94	2.657	141
N3-H19…O3	0.77	2.39	3.035	143

Figure 26. The crystal structure and hydrogen bonding parameters for structures **7b** and **8b**.

The hydrogenation of the dinitro compound **2** using $LiAlH_4$ yielded the aforementioned fully hydrogenated **4a**. Changing the reducing agent to Fe powder yielded the partially hydrogenated amine-nitro-compound **4b**. Adapting this process to control the partial hydrogenation of **1** proved to be unsuccessful. The formation of **3** was preferred, and the desired precursor to produce BT appended aminonitro precursor could not be produced. The amine precursor **4b** was used to produce **7b** and **8b** using reaction conditions analogous to the bis(thiourea) synthesis. Crystals were isolated for the mono(thiourea) monomers, **7b** and **8b,** by slow diffusion of hexanes into chloroform or dichloromethane. The crystal structures for both of the mono(thiourea)s showed similar hydrogen bonding found in **5** (Figure 26). Torsion in the backbone and the thiourea portion were found in **8b**, with much less order in the unit cell and structure.

Selectivity Measurements of the Aroylthioureabenzenes

Selectivity of the Bis(thiourea)s

Binding constant determination from various titration methods allows for more information to be gathered on the actual strength and affinity of a metal ion to ionophore system. Numerous studies have used titration experiments monitored by UV-Vis and NMR spectroscopy to determine not only the binding constants but the free energies involved in metal ion-system interaction. The appended thiophene-based groups are well known for having strong π-π^* transitions in the near ultraviolet-visible range, and **5-8** showed well defined transition bands with high molar absorptivities of 24,000 to 42,000 L mol^{-1} cm^{-1}. Initial binding experiments with the monomers were conducted to probe the use of UV-Vis spectral methods to study the binding strength of each monomer with

any particular metal ion analyte. Introduction of Pb^{2+} ions into a solution of thiourea monomer showed a gradual increase in absorbance as a function of metal ion concentration. Benesi-Hildebrand methods and a Job's plot analysis (Figure 28) of the data demonstrated a host-guest interaction of a 1:1 stochiometry of metal analyte ion to ionophore.[169,170]

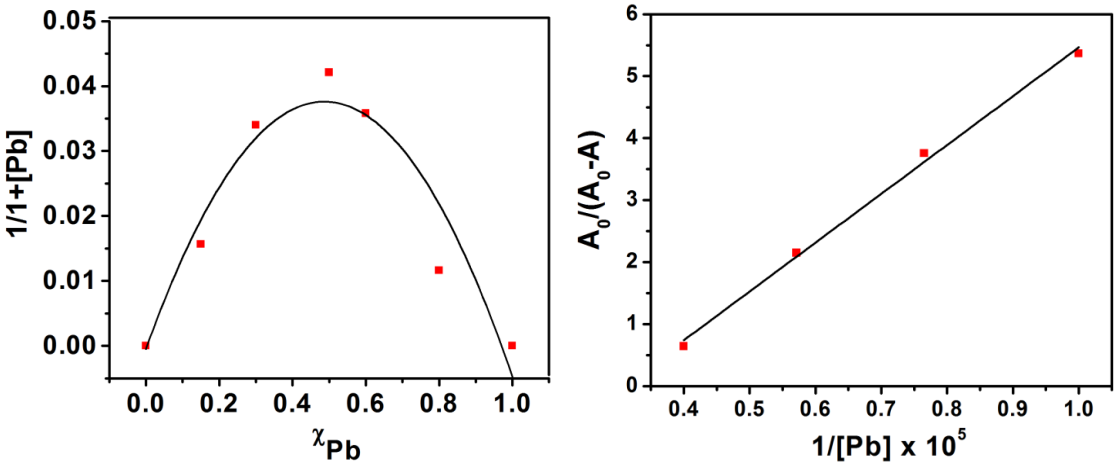

Figure 27. Representative Job's plot analysis (right) of the furanyl *bis*(thiourea) benzenes **5** and **7a** with metal ions showing a 1:1 host to guest speciation. A sample Benesi-Hildebrand plot (left) for ionophore **5** with Pb(II) ions.

The large steric bulk of the *bis*(thiourea)s facilitated the 1:1 interaction with the metal ions. Mono(thiourea)-based monomers **7b** and **8b** mostly interacted in a 1:1 fashion. Based on speciation studies of similar 1-furoylthioureas, this speciation is common for mono(thiourea)s with heavy metal cations.[156] Figure 27 shows the Benesi-Hildebrand analysis with Pb(II) ions used to find the association constant as a representative example. Binding energies fell into ranges similar to other ligands and ionophores. The mono(thiourea) ionophores were not selective toward Pb(II) exclusively like most of the more constrained *bis*(thiourea) monomers. Monomer **7b** was highly

selective toward Hg(II) and Cu(II), and in these cases the interaction occurred in a 1:2 metal to ionophore ratio. **8b** was selective toward Pb(II) and Hg(II), and the Hg(II) titrations occurred in a 1:2 ratio.

Table 6. The binding constants and association energies for **5** and **7a** with various metal ions.

	5		**7a**	
Metal Ion	**Binding Constant K_m (M^{-1})**	**ΔG° at 294 K (kJ•mol^{-1})**	**Binding Constant K_m (M^{-1})**	**ΔG° at 294 K (kJ•mol^{-1})**
Ag^{+}	-	-	-	-
Co^{+2}	-	-	-	-
Cu^{+2}	147	12.2±0.6	820	16.4±1.2
Fe^{+2}	1.7	1.3±0.4	2.8	2.5±0.3
Cd^{+2}	261	13.6±0.7	90.0	11.0±1.0
Hg^{+2}	783	16.3±0.8	307	14.0±0.4
Pb^{+2}	2560	19.2±0.2	1235	17.4±0.4
Sn^{+2}	1259	17.5±0.6	1111	17.1±0.4
Zn^{+2}	2.6	2.4±0.5	-	-

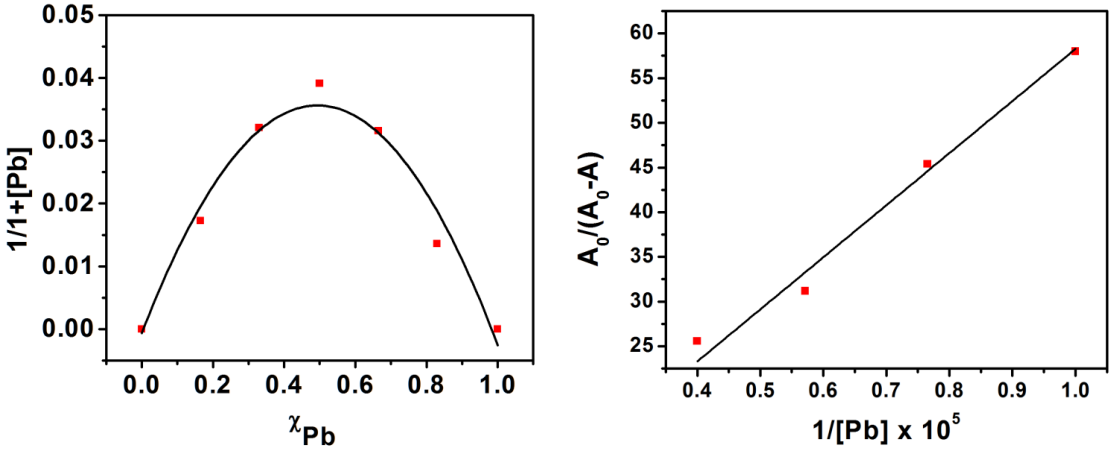

Figure 28. Representative Job's plot analysis (right) of the furanyl *bis*(thiourea) benzenes **6** and **8a** with metal ions showing a 1:1 host to guest speciation. A sample Benesi-Hildebrand plot (left) for ionophore **6** with Pb(II) ions.

Table 7. The binding constants and association energies for **6** and **8a** with various metal ions.

	6		**8a**	
Metal Ion	**Binding Constant K_m (M^{-1})**	**ΔG° at 294 K (kJ•mol^{-1})**	**Binding Constant K_m (M^{-1})**	**ΔG° at 294 K (kJ•mol^{-1})**
Ag^{+}	-	-	1.6	1.2±0.4
Co^{+2}	-	-	1.7	1.3±0.2
Cu^{+2}	2.3	2.0±0.8	44	14.9±0.2
Fe^{+2}	124.9	11.8±0.3	6.6	4.6±0.5
Cd^{+2}	4.7	3.8±0.2	376.9	14.5±0.4
Hg^{+2}	115.1	11.6±0.7	212.6	13.1±0.5
Pb^{+2}	159.7	12.4±0.9	1454.2	17.8±0.2
Sn^{+2}	1784.3	18.3±0.5	1345	17.6±0.4
Zn^{+2}	55.2	9.8±0.9	-	-

^{1}H NMR spectral titrations, monitoring the amide peaks at 9.2 - 9.5 δ and 12.3 - 12.5 δ, were also used to study the interactions between the monomers and heavy metal cations. The shifts in spectra were analyzed using the Benesi-Hildebrand method and Job's plot analysis, as shown in Figure 29. The interactions found for the *bis*(thiourea)s to the cations in a 1:1 ratio and 1:2 ratio for the mono(thiourea) ionophores.[171] Association constants and energies were in good agreement with those found from the UV-Vis titration data, as seen in Table 6-8. For instance, ^{1}H NMR titration showed Pb(II) $\Delta G°_a$ = 19.7 kJ•mol^{-1} for **5** and 18.6 kJ•mol^{-1} for **7a**. For the benzylthiourea monomers, ^{1}H NMR titration showed for Sn(II) binding $\Delta G°_a$ = 20.1 kJ•mol^{-1} for **6** and 16.8 kJ•mol^{-1} for **8a**.

Selectivity of the Mono(thiourea)s

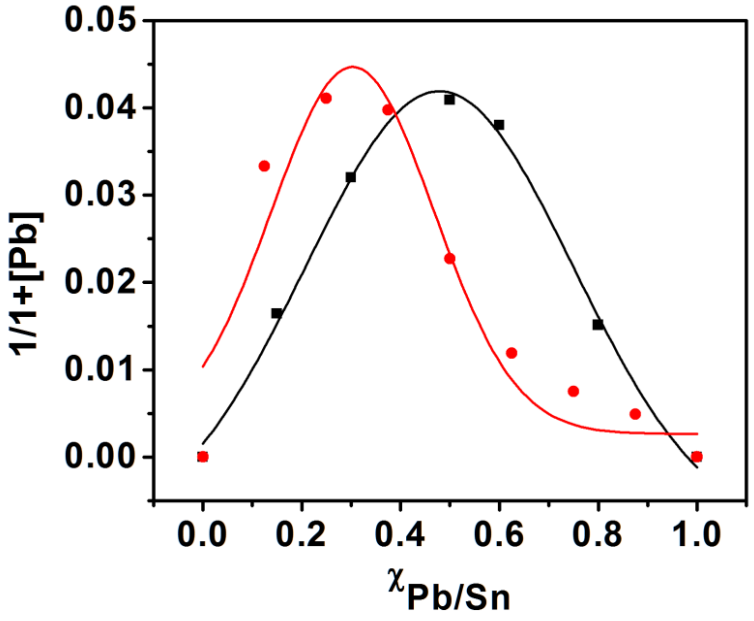

Figure 29. Representative Job's plot analysis of the furanyl mono(thiourea) benzenes **7b**and **8b** with metal ions showing a 1:1 host to guest speciation. The red trace represent the speciation of 1:2 found with Hg(II) and Sn(II) ions.

Table 8. The binding constants and association energies for **7b** and **8b** with various metal ions.

	7b		**8b**	
Metal Ion	**Binding Constant K_m (M^{-1})**	**ΔG° at 294 K (kJ•mol^{-1})**	**Binding Constant K_m (M^{-1})**	**ΔG° at 294 K (kJ•mol^{-1})**
Ag^{+}	133	11.9±0.1	119	11.7±0.2
Co^{+2}	-	-	-	-
Cu^{+2}	2224	18.8±0.4	1212	17.4±0.5
Fe^{+2}	673	15.9±0.7	100	11.3±1.3
Cd^{+2}	988	16.9±0.4	785	16.3±0.3
Hg^{+2}	1899	18.5±0.2	2376	19.0±0.7
Pb^{+2}	1231	17.4±0.8	2449	19.1±1.0
Sn^{+2}	546	15.4±0.2	333	14.2±0.9
Zn^{+2}	234	13.3±0.4	137	12.0±0.8

The mono(thiourea)s showed selectivity toward Cu(II), Hg(II), and Pb(II) ions, with no dominant selectivity as seen in the *bis*(thiourea)s. Based on the experimental values for binding constants and association energies, ionophores **5** and **8b** should produce the most selective polymers. While not directly comparative, these values should aid in understanding the polymer selectivity studies using XPS and electrochemical methods.

Electropolymerization of the Thiourea Ionophores

All six monomers were readily electropolymerized under multiple scans in oxidative conditions from -0.5 V to 1.5 V (vs. Fc/Fc^{+}) in 0.1 M $TBAPF_6$ in DCM. Figure 30-32 show electropolymerization data for monomer **5**, **7a**, and **7b**, representative of all six monomers. The furoyl type compounds polymerized readily, but an eventual regression in linearity of growth was present in all three cases. All six polymers poly-**5** through poly-**8b**, were electropolymerized onto a variety of substrates including Pt buttons, stainless steel, and indium tin oxide (ITO) glass electrodes. The phenyl class of thiourea polymers was more soluble when compared to the furoyl derivatives which may explain more linear polymer growth up to 20 cycles. The scan rate dependence studies showed a linear relationship for all polymers. The linear growth and scan rate dependence reveals that the thiourea polymer films are very electroactive. Also, polymers formed are ionically porous, allowing electrolyte to intercalate through the films promoting further growth. Ionic porosity encourages more homogenous film growth, but also supports the notion that the metal ions are capable of interacting with the

entirety of the film instead of simply the polymer surface. The linear scan rate dependence also indicates that the diffusion of charge throughout the polymer film.

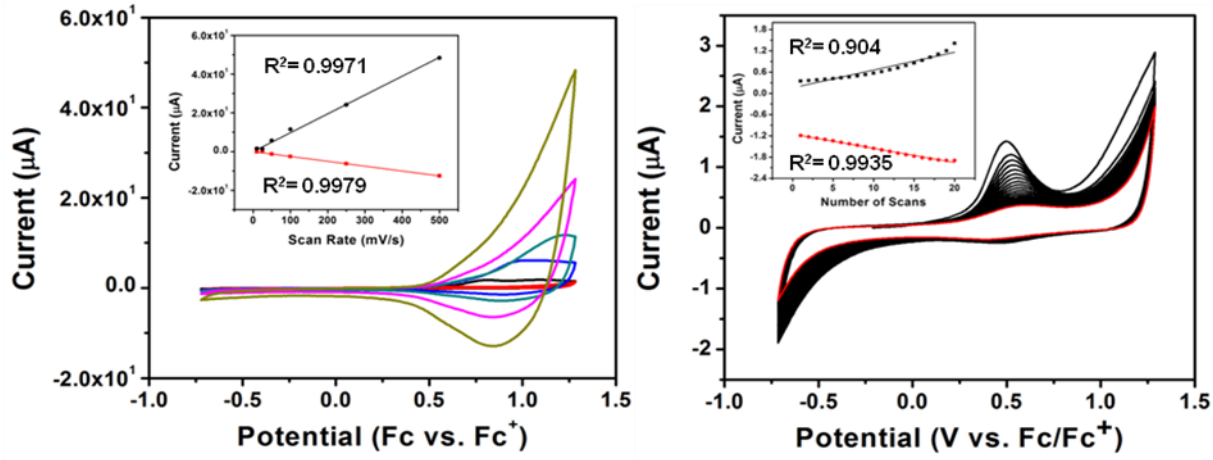

Figure 30. (A) Electropolymerization of **poly-5** using 20 cycles of film growth under oxidative current. (inset) The film growth dependence showing linear growth of the polymer over the growth cycles. (B) Cyclic voltammagrams at scan rates of 10-500 mV/s in monomer-free solution. (inset) linearity of scan rate for oxidative (black trace) and reductive (red trace) scans.

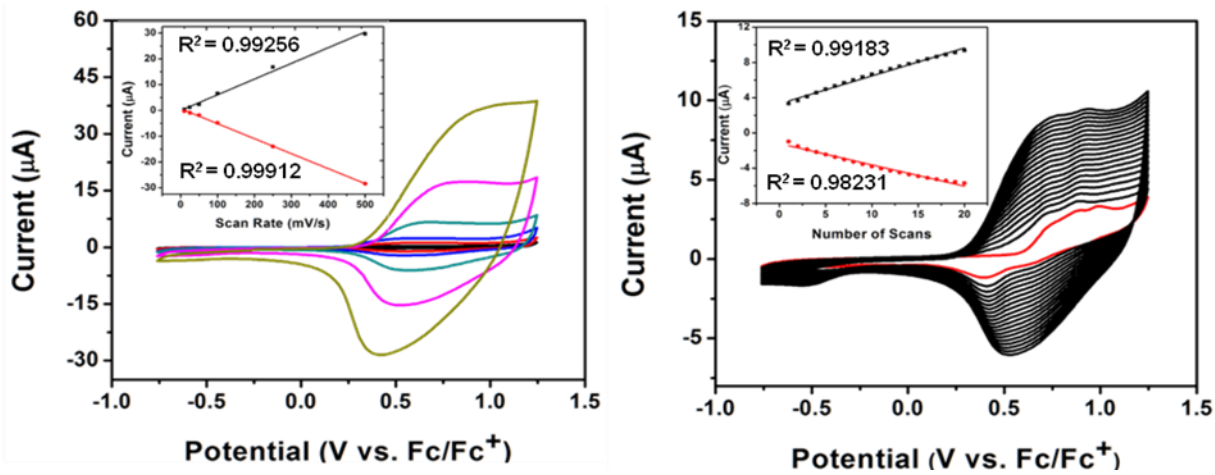

Figure 31. (A) Electropolymerization of **poly-7a** using 20 cycles of film growth under oxidative current. (inset) The film growth dependence showing linear growth of the polymer over the growth cycles. (B) Cyclic voltammagrams at scan rates of 10-500 mV/s in monomer-free solution. (inset) linearity of scan rate for oxidative (black trace) and reductive (red trace) scans.

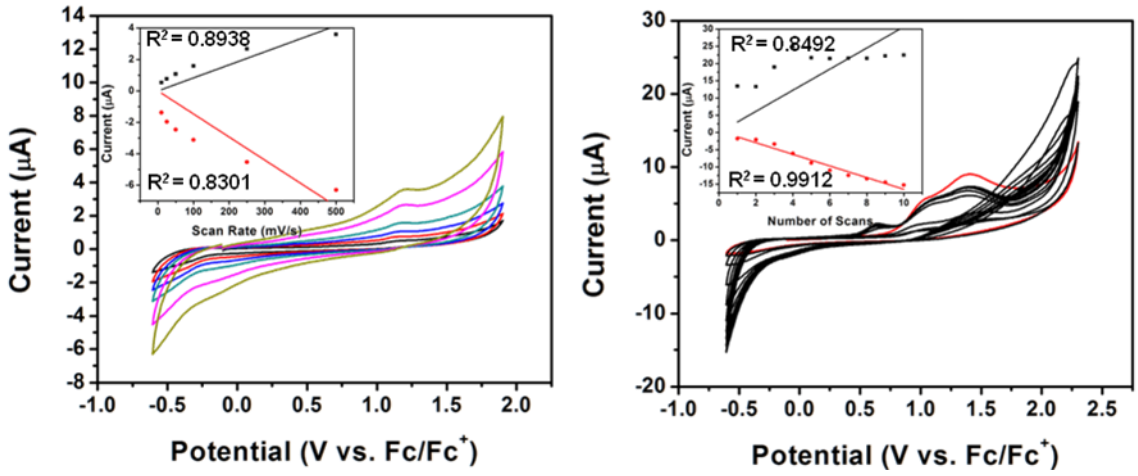

Figure 32. (A) Electropolymerization of poly-**7b** using 20 cycles of film growth under oxidative current. (inset) The film growth dependence showing linear growth of the polymer over the growth cycles. (B) Cyclic voltammagrams at scan rates of 10-500 mV/s in monomer-free solution. (inset) linearity of scan rate for oxidative (black trace) and reductive (red trace) scans.

Chemical Stability and Detection of Heavy Metals by the Polymers

Creating a selective ionophore is integral to producing an effective ISE. However, the chemical stability of the sensor is equally important, and many ISEs suffer from low lifetimes. Several experiments were conducted to probe the stability of polymers, poly-**5 -8b**. Initial experiments focused on the performance of the polymers under oxidative aqueous conditions. The polymers on ITO glass substrates were scanned between 0 V to 1 V in the presence of Pb(II) ions. XPS analysis of polymer films before and after interaction with Pb(II) ions was used to integrate amount of metal loading and approximate binding interactions.

Selective Adsoprtion Process of the Ionophoric Films

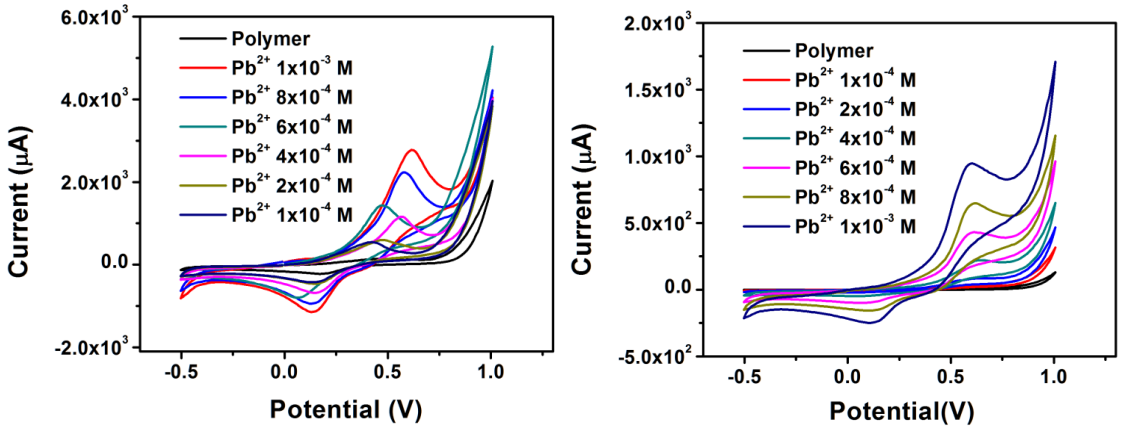

Figure 33. Cyclic voltammagrams of poly-**5** in the presence of Pb(II) ions (left) in 1 M KNO_3 solution. Cyclic voltammagrams of poly-**7a** in the presence of Pb(II) ions (right) in 1 M KNO_3 solution.

XPS spectra indicated ions adsorbed in an estimated one ion to every polymer unit (Figure 34). This relationship is reflected in the ratio of Pb^{4f5} to S^{2p} peaks for each polymer. The ratio was 6.05:1 for S to Pb in the case of poly-**5**, indicating that each polymer unit was impregnated with a Pb(II) ion. Similar experiments were performed with Fe(II), K(I), Ca(II), and Cu(II) ions, with no detectable Auger or XPS bands present. The films were then washed with an EDTA solution to remove the adsorbed Pb^{2+} ions, completing one cycle (Scheme 12). Furthermore, based on XPS surface analysis shown in Figure 34, exposure to EDTA solutions removed all Pb(II) ions. The Pb^{4f} peaks were not observed in the spectra. XPS binding energies for silica at ~153 eV were also observed as a silicon-based artifact, most likely grease, in the comparative spectra.

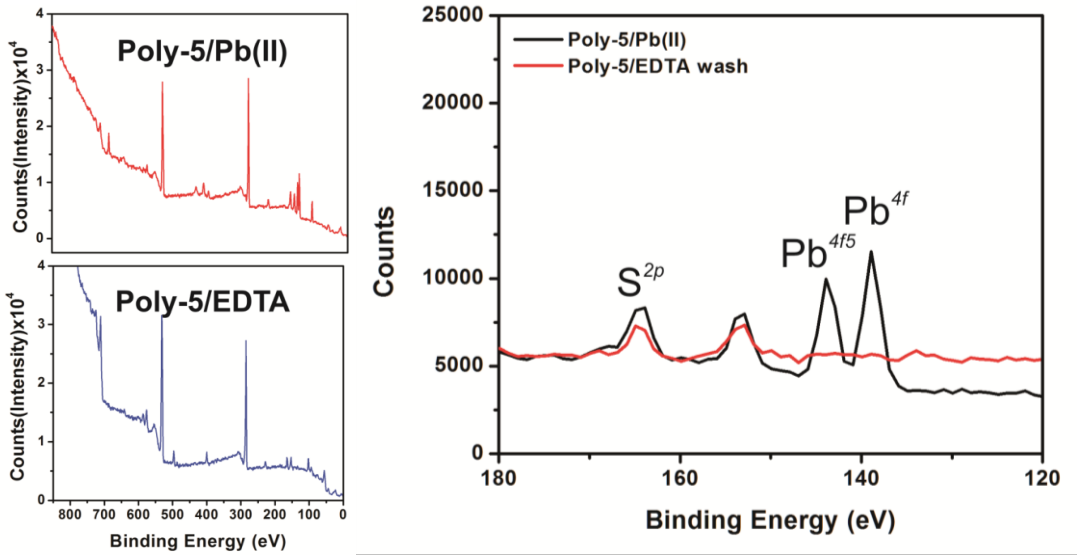

Figure 34. XPS spectra for poly- **5** after Pb(II) exposure and after EDTA exposure (left, bottom). Comparative spectra of the S^{2p} and Pb^{4f} peaks in the samples (right).

Further XPS studies were performed after exposing the films to ionic mixtures of Cu(II), Pb(II), and Sn(II) ions. Control experiments for each of the ions individually were also studied for comparison. The polymer films selectively adsorbed Pb(II) ions and showed XPS signatures similar to that shown in Figure 34. Furthermore, no detectable presence of either of the other ions was observed in XPS spectra.

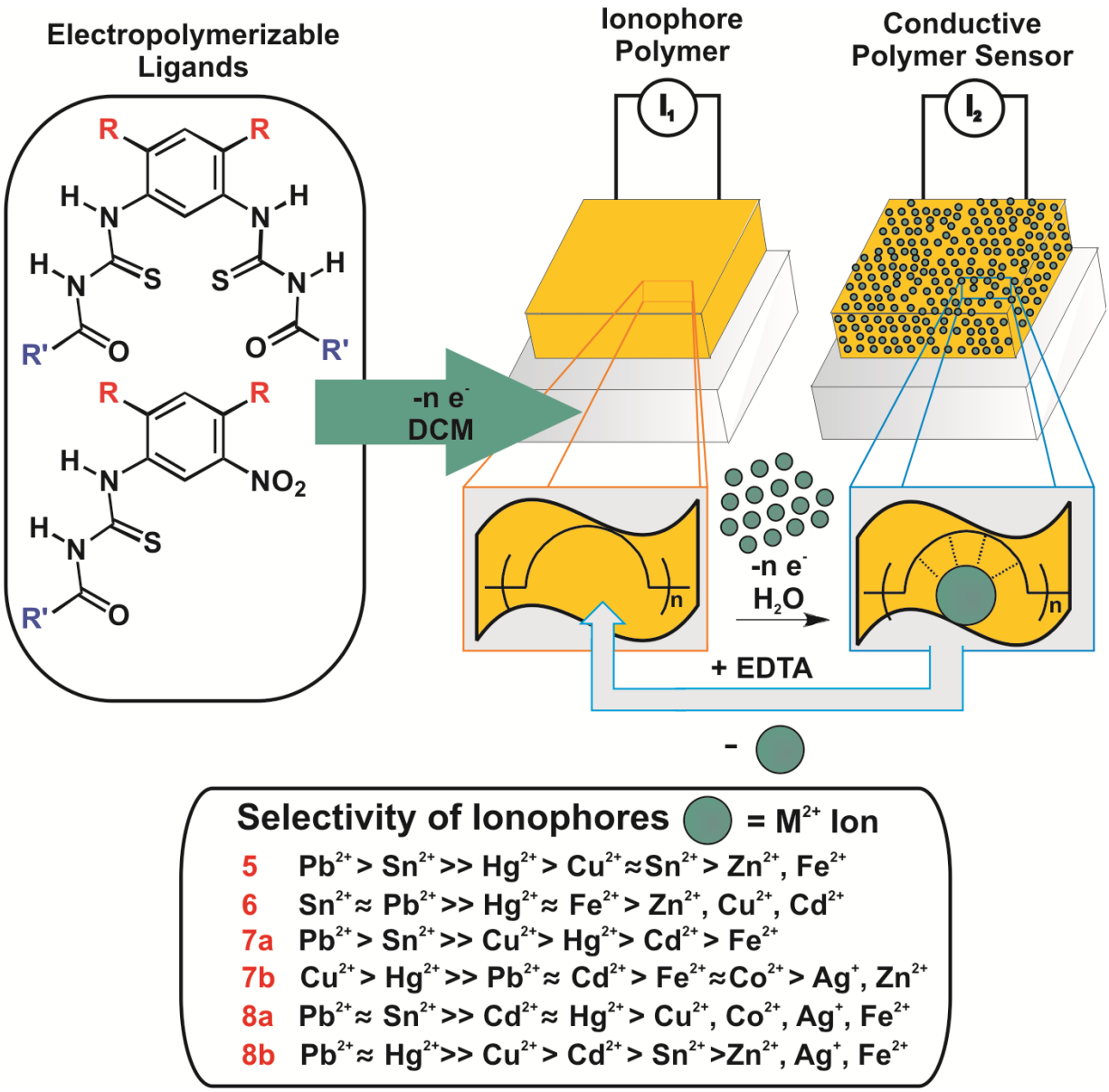

Scheme 12. Schematic of the M^{2+} electrochemical adsorption/removal process used to test the polymers capacity to reversibly interact with the cations and be recycled.

All polymers acted similarly to the previously reported *bis*(thiourea)benzene polymers.[156] This process was repeated every two weeks, over a year period, for all polymers, with no significant decrease in the current observed. Furthermore, incubation

of the polymer films in aqueous solutions showed no detectable degradation in the polymer. Polymer films on stainless steel showed good lifetimes, and the films were then studied in acidic and basic conditions. At pH levels below 2, the films slowly degraded over the period of a few days. Between the pH range of 2 to 10, the polymers showed no detectable degradation over a month incubation period. At highly basic conditions above pH 10, the polymers degraded swiftly in the matter of a few minutes. This was observed as the films changed from a lustrous orange color to a black brown colored film.

Selectivity and LODs of the Conducting Polymers

Selectivity of the Ionophoric Polymers

Monomer selectivity proved to be a good indicator of the selectivity of the ionophoric conducting polymer films. The calibration curves for the polymers were taken by measuring the I_{peak} of the CV current under different concentrations of Pb(II) ions. Figure 33 shows examples of cyclic voltammagrams gathered under these conditions. Selectivity coefficients were studied using techniques utilized for ionophore based amperiometric sensors. Coefficients were calculated against currents measured for Pb(II) ions with the polymer electrodes. The following equation adapted from methods of Wang *et al.* was used to calculate the coefficients for competitive ions:

$$I_t = K(C_i + \sum k_{ij}^{amp} C_j)$$

where i is the target analyte, I_t corresponds to the analyte peak current in the presence of the interferents, K is the slope of the calibration curve and C_i and C_j are respectively the concentrations of the analyte and interfering species.[172] Table 9 provides a summary of the coefficients relative to most selective cation found for each ionophore in the

monomer studies. Also, Figure 35 outlines the competitive cations for each polymer, and the level of interference observed for each different ion.

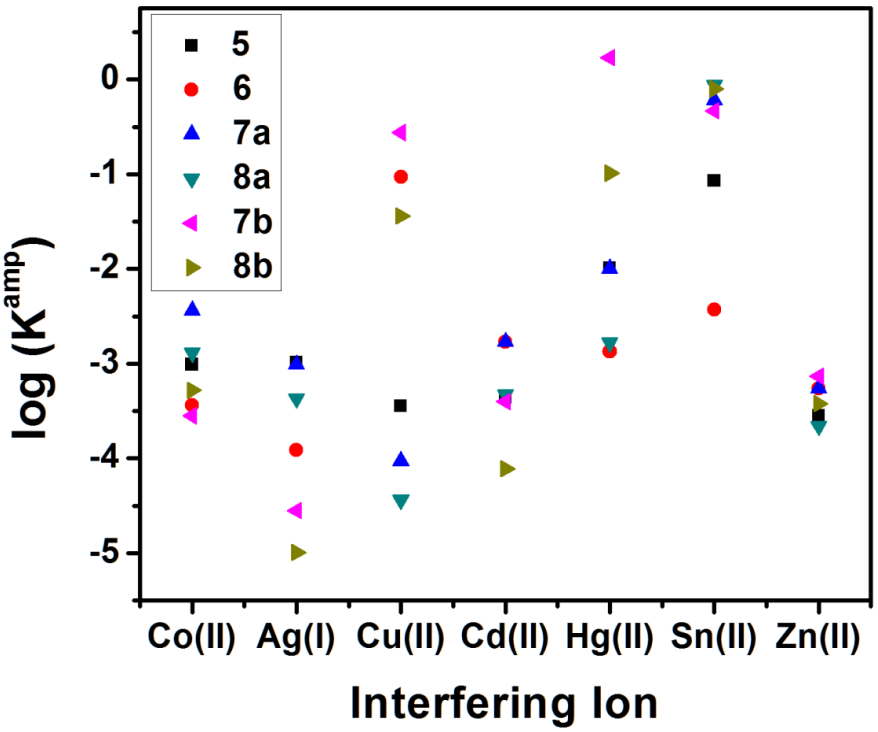

Figure 35. Distribution of selectivity coefficients for different ions versus log (K_{Pb}^{amp}).

Table 9. Selectivity coefficients of the different polymer ionophores versus log (K_{Pb}^{amp}).

	Conducting Polymer Ionophore					
Ion	**5**	**6**	**7a**	**7b**	**8a**	**8b**
Co^{+2}	-3.01	-3.44	-2.44	-2.89	-3.55	-3.28
Ag^{+}	-2.99	-3.91	-3.01	-3.37	-4.55	-4.99
Cu^{+2}	-3.45	-1.03	-4.03	-4.44	-0.56	-1.44
Cd^{+2}	-3.36	-2.77	-2.77	-3.33	-3.4	-4.11
Hg^{+2}	-1.99	-2.87	-2	-2.78	0.23	-0.99
Sn^{+2}	-1.07	-2.43	-0.22	-0.06	-0.33	-0.1
Zn^{+2}	-3.01	-3.44	-2.44	-2.89	-3.55	-3.28

Potentiometric selectivity coefficient $K_{pot\ A,B} = a\mathbf{A}/(a\mathbf{B})Z_A/Z_B$. log $K_{pot\ A,B} \cong 0$, strong interference: the sensor responds mainly to the interfering ion; log $K_{pot\ A,B}$ between -2 and -1, moderate interference; log $K_{pot\ A,B} < -3$, no interference.[156,172]

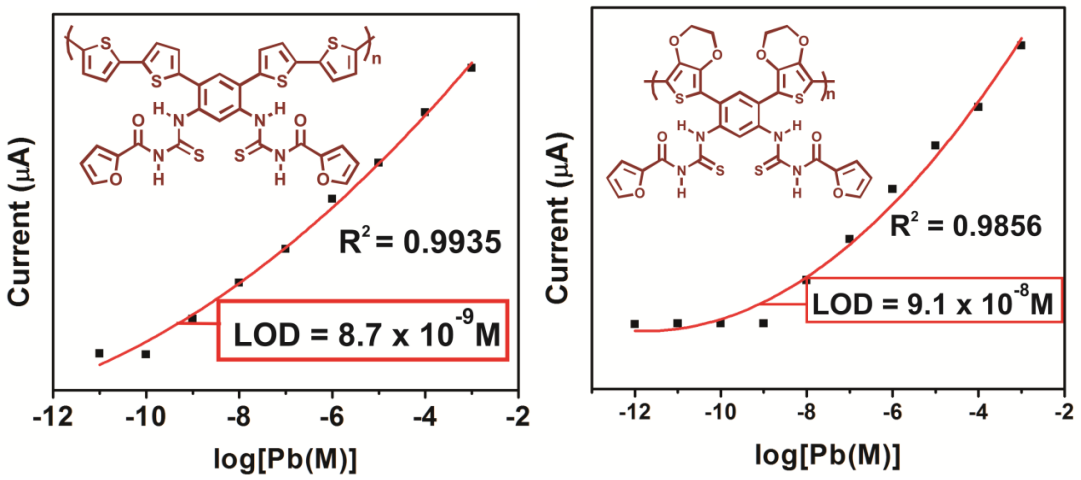

Figure 36. (A) The maximum current versus the log of each Pb^{2+} concentration (10^{-11} to 10^{-3} M) for poly-**5**. The onset of Nernstian response was used to find the limit of detection. (B) The maximum current versus the log of each Pb^{2+} concentration (10^{-11} to 10^{-3} M) for poly-**5**. The onset of nernstian response was used to find the limit of detection.

LODs for the Ionophoric Polymers

Stabilization provided by the furanyl group promotes rigidity in the thiourea components of the polymers *via* hydrogen bonding interaction (*vida supra*). The well defined sterics in the ionophores created an optimal site for only Pb(II) or Hg(II) ion interaction. Benzoyl-type polymers, poly-**6**,**8a**, and **8b**, had different selectivities than the furanyl varieties. Based on the selectivity coefficients measured for each polymer, the monomer association energies were a good indicator for polymer selectivity. Strong interference occurred from Cu(II), Sn(II), and Hg(II) ions. Figure 35 shows relative distribution of selectivity in the polymers, with poly-**5** and poly-**6** showing good selectivity except versus Sn(II) and Cu(II), respectively. The EDOT-based bis(thiourea) polymers, **7a** and **7b** showed high selectivity toward Pb(II) ions, with interference occurring mainly from Sn(II) ions. The mono(thiourea) polymers **7b** and **8b**, however,

showed little selectivity toward Pb(II) ions. The heavy interference from Hg(II), Sn(II), and Cu(II) ions demonstrate that the polymers had a higher affinity toward smaller ionic species. Further selectivity measurements versus K^{amp}_{Hg} showed that the polymers possessed good selectivity toward Hg(II) ions.

The polymer ISE sensors were produced by electrodeposition of the polymers as electrode confined films on Pt button, indium tin oxide (ITO), and stainless steel electrodes. Amperiometric sensing studies were then conducted in conjunction with an Ag/AgCl reference electrode and Pt wire counter electrode. The furanyl-type polymers, poly-**5**,**7a**,**7b**, were tested initially in the presence of a KNO_3 electrolyte. The conducting polymers retained composition under oxidative conditions, and no amperiometric response was observed based on the change in K^+ concentration. Electrochemical response of the polymer ISEs to $Pb(NO_3)_2$ was then studied using concentrations from 10^{-2} - 10^{-12} M in 1 M KNO_3 solution. Based on the amperiometric response to each analyte concentration, LODs for the polymer were extrapolated, as shown in Figure 36. Table 10 summarizes the Pb(II) LOD measured for each polymer sensor.

Table 10. Detection limits for each polymer ionophore toward Pb(II) ions.

Polymer ISEs	poly – **5**	poly – **6**	poly – **7a**	poly – **7b**	poly – **8a**	poly – **8b**
LOD (M)	8.7×10^{-9}	4.6×10^{-9}	9.1×10^{-8}	3.3×10^{-8}	4.4×10^{-9}	9.2×10^{-9}

Probing the Effect of Pb(II)-Doping on Redox Conductivity

Initial aqueous electrochemical experiments indicated that the conducting polymer films were sensing Pb(II) ions by a resulting increase in the peak current, I_{peak}. Amperiometric behavior in conducting polymers can be linked to several beneficial electronic interactions between the metal and polymer. In the case of the cobalt(I) EDOT-salen type systems, redox matching of the Co I/II redox couple to the oxidative potential of the EDOT polymer backbone led to a dramatic increase in redox conductivity.[69] This led to not only a highly conductive material, but due to the electronic behavior of the Co(I) center with NO and NO_2, an effective amperiometric sensor was estabilished. Similar to this case, Pb(II) doping leads to a dramatic increase in the conductivity of the material. Although this increase is not by virtue of a beneficial redox matching relationship, another mechanism assists in an increase in the redox conductivity.

Figure 37 shows sample *in situ* conductivity studies performed on the polymer before and after Pb(II) exposure.[173] Polymers were electrodeposited onto an interdigitated Pt electrode array by scanning from -0.25 – 1.5 (V vs. Fc/Fc^+). The drain current measured was then used to calculate the conductivities using the following equation outlined in literature:[174-176]

$$\sigma = \frac{i_D}{v_D} \times \frac{D}{n * T * L}$$

where i_D is the drain current, v_D is the offset potential, and T is the polymer thickness, D is the electrode gap (5μm), n is the number of gaps (149), and L is the electrode length (0.5 cm).[174-176] Poly-(3-methylthiophene) was used as a calibrating material, and drain

currents gathered were readjusted based on the known conductivity of 3-MeTh (σ = 60 S/cm).[176] The red trace in Figure 37 denotes the redox conductivity (S/cm) for the thiourea polymers before Pb(II) doping and the blue trace shows the conductivity measured for the same film after exposure to Pb(II) ions.

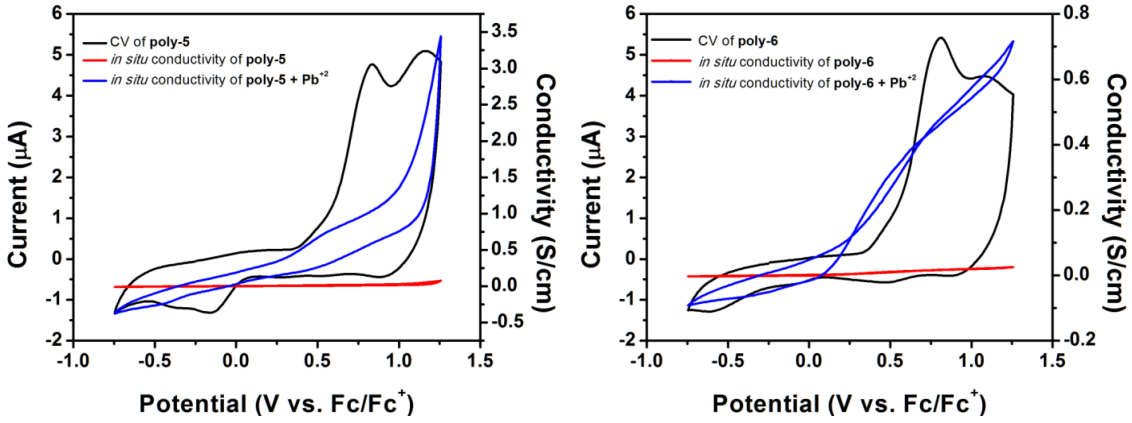

Figure 37. (left) Cyclic voltammogram of poly-**5** (black trace) and the *in situ* conductivity measurements for poly-**5** (red trace) and poly-**5** after Pb(II) ion exposure (blue trace). (right) Cyclic voltammogram of poly-**6** (black trace) and the *in situ* conductivity measurements for poly-**6** (red trace) and poly-**6** after Pb(II) ion exposure (blue trace).

Redox conductivities of the polymers were measured and the ranges of conductivity ranged between 9.36×10^{-3} to 7.75×10^{-2} S/cm. Following these measurements each polymer on the interdigitated electrode (IDE) substrate were scanned from -0.5 to +1.5 V in the presence of Pb(II) ions. The *in situ* redox conductivity measurements were performed again with significant increases in conductivity observed. The conductivity was increased several orders of magnitude in each Pb(II) exposed polymer. Table 11 outlines the redox conductivities before and after Pb(II) absorption.

Scheme 13 portrays the electropolymerization and post-polymerization metallation of the thiourea-based polymers.

Table 11. Redox conductivities of each polymer before and after Pb(II) exposure.

	Redox Conductivity (S • cm^{-1})	
ISEs	**Polymer**	**Polymer + Pb(II)**
poly-**5**	**7.75×10^{-2}**	**3.5**
poly-**6**	**9.36×10^{-3}**	**1.7**
poly-**7a**	**2.81×10^{-2}**	**0.7**
poly-**7b**	**1.87×10^{-2}**	**0.9**
poly-**8a**	**6.31×10^{-2}**	**2.7**
poly-**8b**	**4.67×10^{-2}**	**1.8**

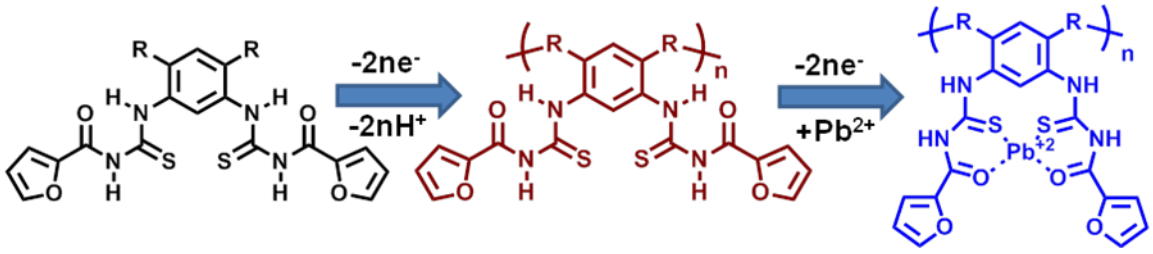

Scheme 13. Scheme outlining the electropolymerization and Pb(II) absorption process.

Mechanism of the Conductivity Enhancement

Possible explanations of the conductivity increase were studied from two mechanistic pathways. First the increase in conductivity was studied by virtue of the increase in ionic strength, as shown in Figure 38. Scan rate dependence studies were performed to study the rate of charge transfer through the polymers. The linearity of the current to the scan rate was then compared to the data gathered for polymers exposed to Pb(II) ions. A sharp increase in the slope of the linear dependence from the polymer to the Pb(II) exposed polymer would indicate the intercalation of Pb(II) ions into the polymer increased conductivity by virtue of the ionic strength. The increase would be related to the Pb(II) ions directly participating in charge diffusion in the polymers. In all cases, there was no significant increase observed in the scan rate dependence studies, see Figure 39, which shows no significant deviation in the slopes before and after Pb(II) ion exposure.

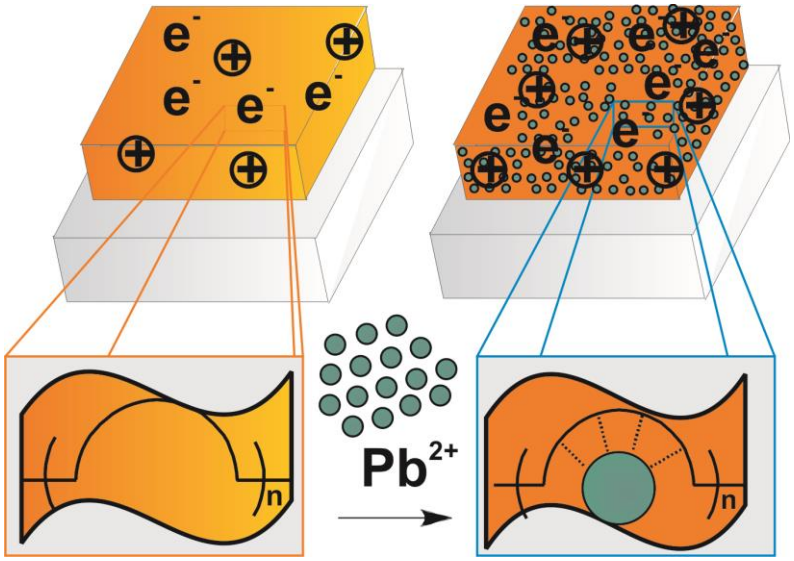

Figure 38. Depiction of the increase in charge production and flow from the ionic strength of the Pb(II) ions.

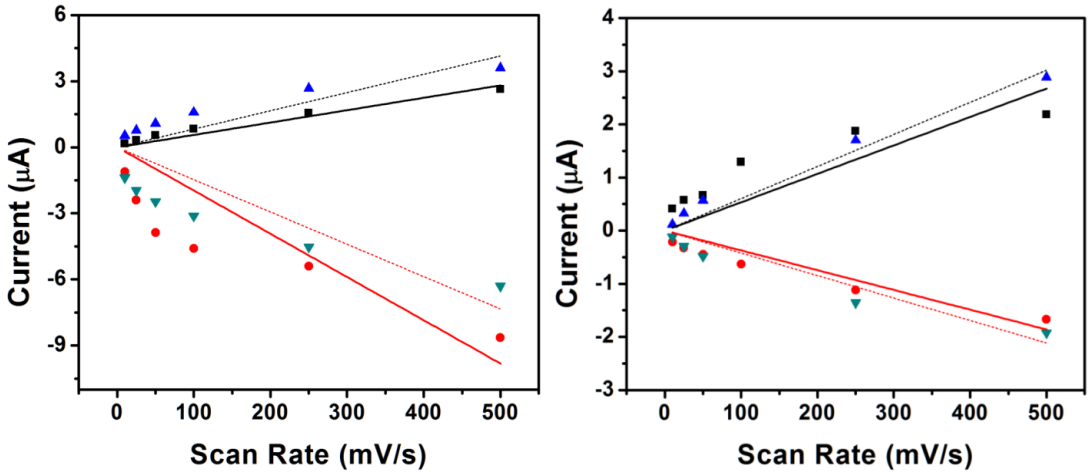

Figure 39. (left) Comparison of the oxidative and reductive scan rate vs. current in the mono(thiourea) poly - **8b** before and after Pb(II) exposure. (right) Comparison of the oxidative and reductive scan rate vs. current in the bisthiourea poly - **5** before and after Pb(II) exposure.

Scan rate dependence studies suggested that the ionic strength of the cations had little effect on the conductivity of the polymers. Another possible explanation for the sharp increase in redox conductivity is the Pb(II) metallation changes the planarity of the polymer chains. Crystal structures of the monomers indicated significant torsion and twisting in the aroylthiourea moieties. A similar lack of planarity could exist in the polymers, supported more so by only a small red shift observed in absorption spectra from the monomer (λ_{max} = 345 nm) to the polymer (λ_{max} = 357 nm) indicating only a slight increase in conjugation as a result of polymerization. Intercalation and binding of Pb(II) ions into the polymers may cause planarization of the polymer structure and therefore increased conjugation favoring formation of the highly conductive quinoidal form upon oxidation, as shown in Scheme 14.

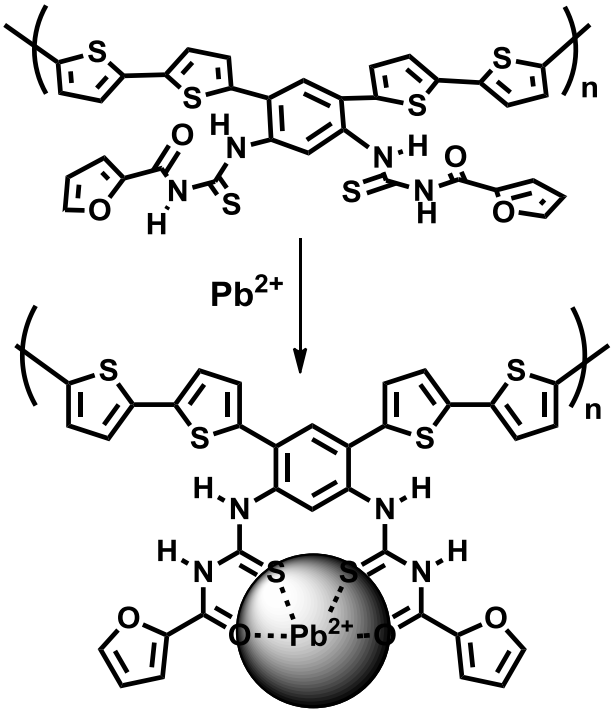

Scheme 14. Planarization of the thiourea polymers in the presence of Pb(II) ions.

Direct observation of a change in the polymer unit conformation was not possible through surface analysis techniques like TEM or STEM. Instead, spectroelectrochemistry of the polymers was performed to monitor the formation of polaron and bipolaron peaks. Figure 40 shows a plot of the absorption under increasing oxidation potential. Polaron and bipolaron peaks were observed at ~ 850 and 1200 nm, respectively. A distinct shift in the peaks should occur in the presence of Pb(II) if a templating effect is occurring. Spectroelectrochemical experiments were performed after Pb(II) exposure, however, gathering absorption spectra proved to be difficult. The dimethylformamide solvent used in the Pb(II) absorption process delaminated the polymer film from the ITO-coated glass substrate.

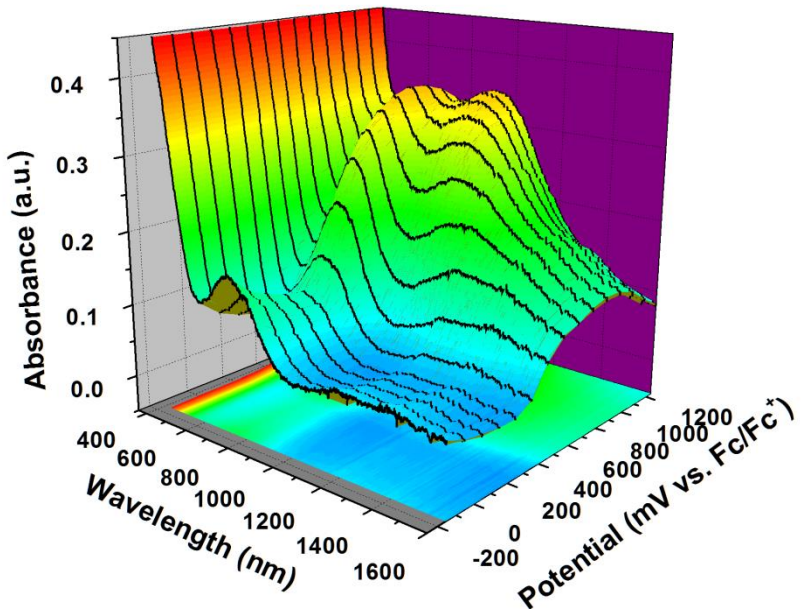

Figure 40. UV-Vis spectroelectrochemistry of poly-**5**.

Further attempts to understand any changes in conformation induced by Pb(II) ion binding focused on producing Pb(II) complexes from the monomers **5** – **8b**. A variety of Pb(II) salts were used as metal precursors and in each case, the reaction conditions yielded several different products by TLC. Initial purification attempts were attempted by recrystallization. X-ray quality crystals indicated that an alternate process to complexation occurred in the presence of Pb(II) ions. Figure 41 shows that the thioketone group in the thiourea portion of the molecules was replaced by methanol in the reaction. The thiourea-based materials in fact promoted the formation of PbS NPs instead of Pb(II) complexes.

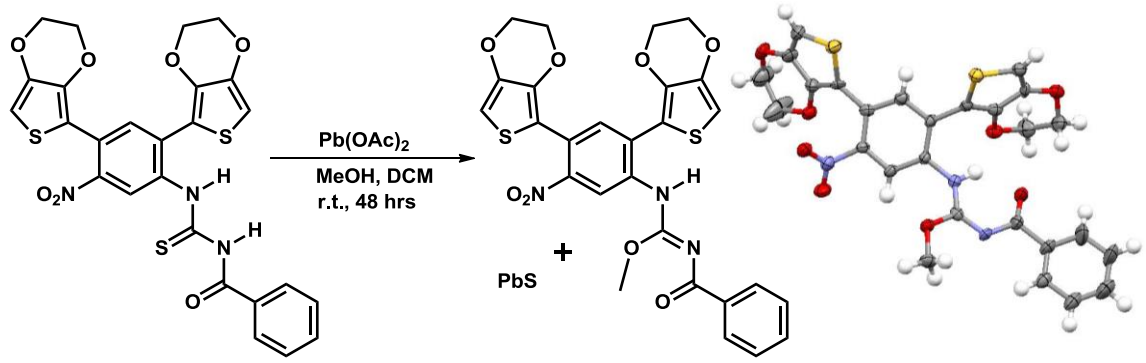

Figure 41. Scheme and crystal structure of the reaction of lead(II) acetate with monomer **8b**.

Other Electropolymerizable Ionophores for ISEs

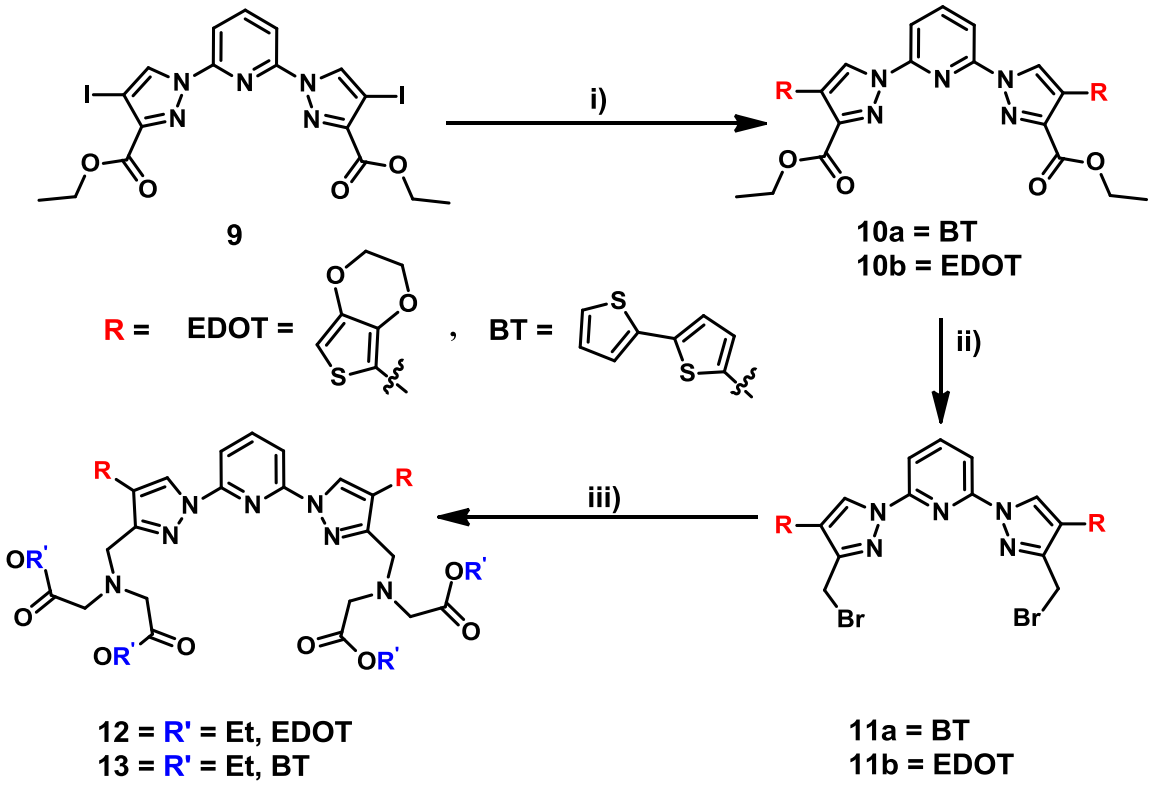

i) $Pd_2(dba)_3$, $^nBu_3PBF_4$, $(Bu)_3SnBT$, NMP, 100 ºC, 24 hrs. ii) a) $LiAlH_4$, THF, 0 ºC, 1 hr b) PBr_3, DMF, r. t., 18 hrs. iii) iminodi(ethyl)acetate, TFA, THF, r. t., 1 hr.

Scheme 15. Synthetic scheme to produce compounds **9** – **13.**

Before the aroylthiourea polymers became a main focus for solid state Pb(II) sensors, another electropolymerizable monomer was synthesized, as shown in Scheme 15.[181-188] Producing monomers **12** and **13** was synthetically tasking and overall yields in the reaction were approximately 4%. The monomer was effectively polymerized by scanning oxidative potential from -0.25 to +1.25V (Figure 42).

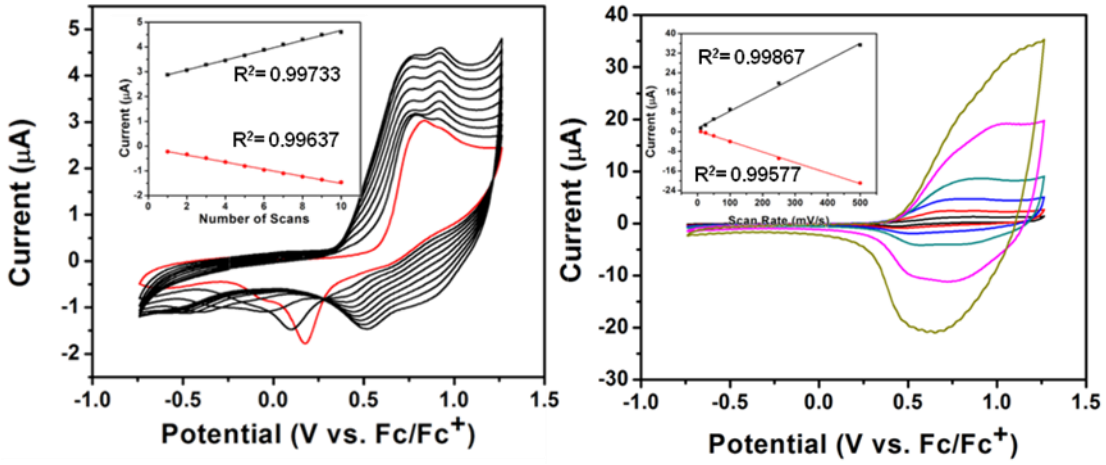

Figure 42. (Left) Electropolymerization of poly-**12** from 20 cycles of film growth under oxidative current. (inset) The film growth dependence showing linear growth of the polymer over the growth cycles. (Right) Cyclic voltammagrams at scan rates of 10-500 mV/s in monomer-free solution. (inset) linearity of scan rate for oxidative (black trace) and reductive (red trace) scans.

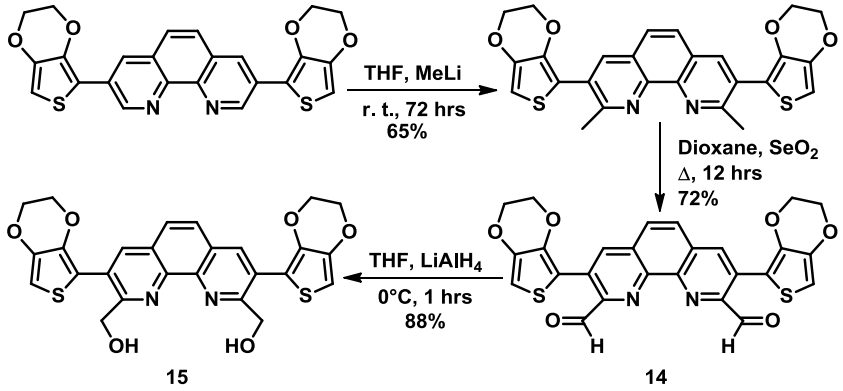

Scheme 16. Synthetic pathway used to produce the electropolymerizable phen(MeOH)$_2$ (**15**).

Structural differences correlated to selectivity measurements of the monomers, **5** - **8b**, and the conducting polymer ionophores, poly – **5** – poly – **8b**, indicated that the local geometry or "binding pocket" of the aroylthiourea moieties governed selectivity. Following this principle, effective polymeric ionophores would be produced from electropolymerizable monomer systems with discrete binding areas. As mentioned earlier, phenanthroline di(methanol) (phen$(MeOH)_2$) has shown superior affinity toward Pb(II) ions over other ions, such as Zn(II) and Ni(II). This high affinity was explained by geometry of the imine-dimethanol area being roughly equivalent in size to the ionic radius of a Pb(II) ion. Considering this work and some guidelines formed from studying the aroylthiourea systems, a synthetic route was developed to incorporate these ionophores into polymer systems.

Scheme 16 shows the synthetic route used to produce another electropolymerizable ionophore, 3,8-di(ethylenedioxythien-5-yl) neocuproine. 3,8-*bis*(ethylenedioxythien-5-yl)-1,10-phenanthroline ($EDOT_2$phen) was produced *via* a Stille cross coupling reaction between 3,8-dibromo-1,10-phenanthroline and tri(butyl)stannylethylenedioxy-thiophene with a ^{n}BuLi-activated $PdCl_2(PPh_3)_2$ catalyst.[177,178] $EDOT_2$phen was then saturated in dry THF, and MeLi was added to produce 3,8-*bis*(ethylenedioxythien-5-yl)-2,9-dimethyl-1,10-phenanthroline.[178] The methyl groups were oxidized using SeO_2 to render **14**, the dialdehyde precursor, and hydrogenation using $LiAlH_4$ yielded the target molecule **15**.

CONCLUSIONS

Incorporating ionophoric units into a conducting polymer backbone resulted in highly effective materials for solid state single piece ISEs. The aroylthiourea receptor units were first studied in the electropolymerizable monomers, and it was observed that the ancillary groups on the thiourea moieties and the type of thienyl-based electropolymerizable group changed selectivity. The bulkier EDOT groups directed more preferential sensing of the smaller Sn(II) ion, while the BT groups typically facilitated Pb(II) sensing. The mono(thiourea)-type ionophores demonstrated different selectivities, and may serve as effective Hg(II) ISE materials. Polymer selectivity studies indicated that the conducting polymer ionophores possessed similar selectivites to the parent monomers. Furthermore, these polymers were highly stable under the test conditions and in aqueous environments in the pH range of 2-10. The addition of the conducting polymer to the ionophore greatly increased sensitivity with LODs ranging from 10^{-8} – 10^{-9} M. The increased recognition can be directly related to the redox conductivity of these materials in the presence of Pb(II) ions. The redox conductivity in each conducting polymer increased significantly in the presence of the Pb(II) ions from ~10^{-3} – 10^{-2} S cm^{-1} to ~1 - 5 S cm^{-1}.

Chapter 4: Highly Conjugated Dual Emissive Ligands: Pathway to Effective Antennas for Both Visible and Near-IR Emitting Ln(III) Ions

INTRODUCTION

Background

There have been examples of extremely efficient transition metal systems demonstrating the effectiveness of incorporating metal centers into luminescent materials. For example, Pt(II), Ir(III) and Ru(II) cyclometallated complexes have been utilized to produce phosphorescent materials. In the case of cyclometallated and other types of transition metal complexes, the ligand can have a significant impact on emission color and efficiency. Furthermore, isomerism in the complexes can strongly effect luminescent properties, as seen in the case of *mer* – and *fac* – Ir(III)$(ppy)_3$ complexes. In the *fac*-Ir$(ppy)_3$ isomer luminescence quantum yield is an order of magnitude greater compared to the *mer*-Ir$(ppy)_3$ isomer.[189] The complex [Ir$(dfb\text{-}mb)_2(fptz)$] showed that using even stronger field ligands can greatly change emission color toward blue emission with quantum yields of 73%.[189] Heteroleptic ligand motifs using interligand charge transfer to decrease nonradiative decay have led to Ir(III) complexes approaching unity. Besides Ir-based complexes, Pt(II) complexes have shown effective color tuning and highly efficient phosphorescence. Similarly, emission tuning is performed by modulating the field strength of the ligand chromophore. In one particular case, 3-isoquinolinylindazolate derivatives tuned Pt(II) complex emission from 567 to 685 nm. Quantum yields vary wildly between the complexes, ranging from 24-83 %.[189] It is difficult to obtain sharp, pure color emission in transition metal phosphors due to ligand centered (LC) emission mixing with MLCT/LMCT emission states. Lanthanide-based emission pathways differ

greatly when compared to transition metal phosphors, and several differences in emission have made Ln(III) materials very attractive in LED applications.[190-194]

Ln(III) Sensitization

Lanthanide ions intercalated or introduced into emissive layers have improved device performance, but the free ions tend to crystallize within the material.[191] In turn, localized concentrations of Ln(III) ions can create a quenching effect and lower device efficiencies. The Ln(III)-Ln(III) quenching process can be avoided by introducing the ion in the form of a Ln(III) complex in a ligand phosphor. Complexation of the lanthanide ions to a ligand chromophore opens a pathway for sensitization of the *f** excited state, which otherwise cannot be directly excited.[190-192] A sensitization approach to producing luminescent lanthanide complexes must be used due to the shielded *f-f** orbitals, by the 5*s* and 5*p* orbitals. The sensitization of the lanthanide ion, or "the antenna effect" (Scheme 17), is achieved by first populating the singlet and triplet states of a luminescent ligand and then transferring the energy into the lanthanide excited state.[190-192] For effective energy transfer it is necessary for the triplet energy level of the ligand (T_1) to be higher in energy than the lanthanide excited state ($^{Ln}f^*$). Typically, an energy level difference of ~2000 - 4000 cm^{-1} is typically the most effective energy gap between the T_1 and $^{Ln}f^*$ energy states. Sensitization in this manner was first reported by Weissman using β-diketonates, but there are many examples of other ligands used as sensitizers.[195-206]

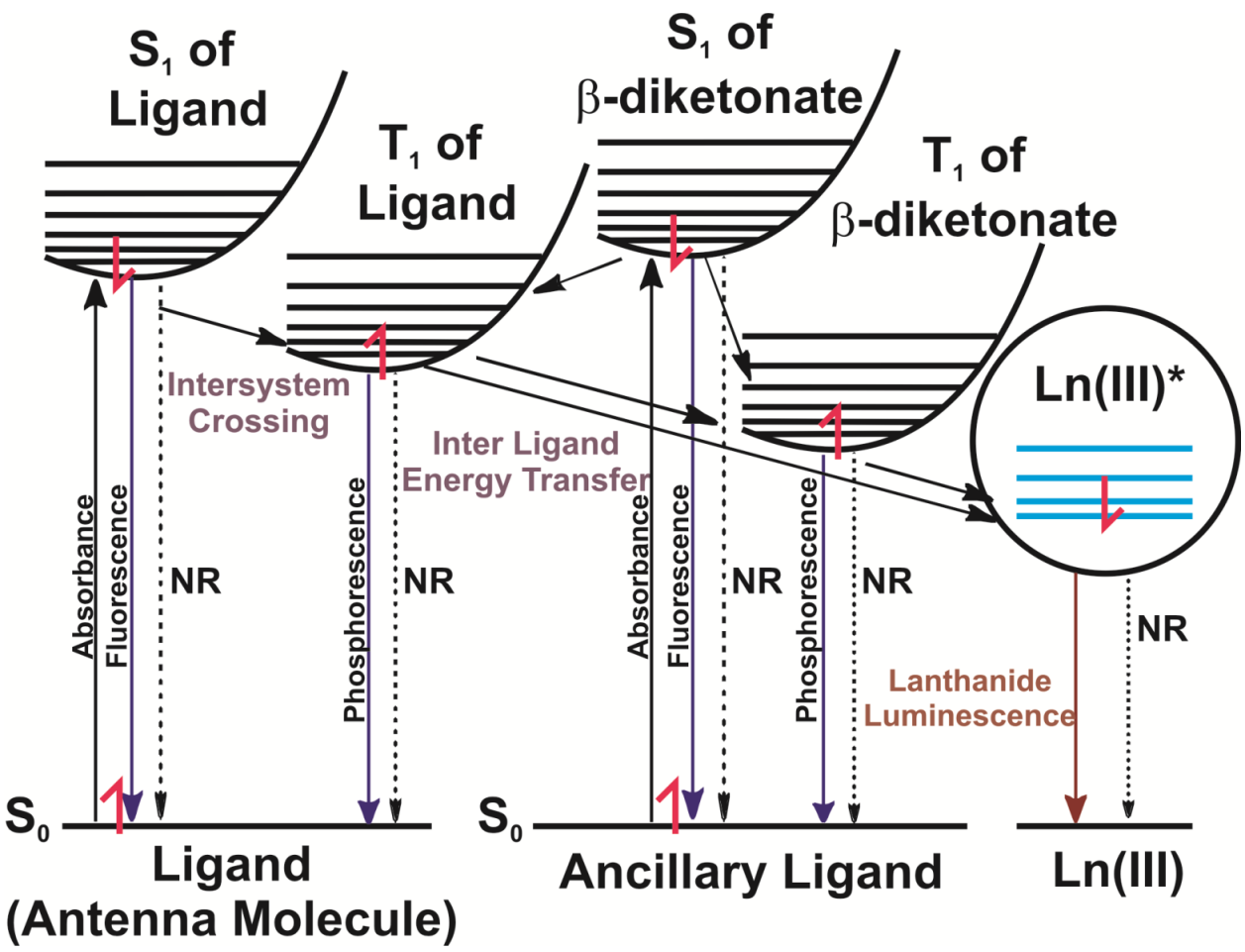

Scheme 17. Graphical representation of the possible energy pathways in sensitization of the Ln(III) excited state.

Ln(III) complexes produce sharp and pure color emission, and in the case of Eu(III) and Tb(III) complexes luminescence can be extremely efficient. Prior work in our group featured Eu(III) complexes bound to featuring *bis*(pyrazole)pyridine sensitizing ligands and β-diketonate ancillary ligands. The alignment of the triplet energy levels for the ligands facilitated highly efficient luminescence and photophysical characterization of the Eu(III) complexes showed quantum yields (Φ_{QY}) of 93%. These results especially demonstrate the necessity for proper triplet energy level control in complex design and

alignment. Similar results have been achieved in aqueous conditions by utilizing modified pyridine *bis*(oxazole) (pybox) ligands. De Bettincourt-Dias *et al.* produced Eu(III) $(pybox)_3$ complexes that achieved Φ_{QY} of 61%, and Tb(III)$(pybox)_3$ complexes with Φ_{QY} approaching 50%.[198]

As mentioned earlier challenges, such as Ln(III) complex phase segregation, leads to Ln(III) OLED devices with inconsistent emission across the active layer. Luminescent Ln(III) metallopolymers may serve as an alternative emissive layers in polymer light emitting diodes (PLED)s. Metallopolymers serve as scaffolds for constrained order of Ln(III) centers and homogeneity in emissive layers. Ln(III)$(\beta$-diketonate$)_3$ coupled to diimine and pyrazolylpyridine-type ligands have rendered highly luminescent polymeric materials.[198-200,208] Past work in our group showed that that Eu(III) β-diketonates could be bound into an electropolymerizable phenanthroline ligand, and these polymers generated luminescent Eu(III) metallopolymers. As an extension of that work, luminescent 3,4-ethylenedioxythiophenyl (EDOT) appended *bis*(pyrazole) pyridine Eu(III) and Tb(III)$(\beta$-diketonate$)_3$ complexes were synthesized, but the monomers were unable to be electropolymerized. Utilizing more soluble electropolymerizable sensitizers with more stable polaron formation during the monomer oxidation may lead to polymer formation.

Pathways to Broadly Usable Antenna Ligands

The broad range of energies (~9,000-34,000 cm^{-1}) associated to the Ln(III) excited states typically means that the sensitizing ligand is specifically engineered toward a specific Ln(III) ion. Antenna ligands are typically effective at either sensitizing visible

Ln(III) or near-IR Ln(III) ions. For example, ligands useful for near-IR Ln(III) sensitization usually possess triplet energy levels too low in energy for effective Tb(III) sensitization. Simple modification of the antenna has proven to be an effective way to sensitize the broad spectrum of lanthanides. Prior work in our group featured and exchange of the thienyl groups in the 3 and 8 position of phenanthroline to produce effective sensitizers for Eu(III) to IR-emitting Er(III) ions. Conjugation length was used to tune the triplet energy level, moving from thienyl to terthienyl moieties. This approach, while effective at lowering the triplet energy levels, was synthetically tasking. Effective Tb(III) sensitization was not achievable through these types of antenna ligands due to the low triplet energy levels.[198]

Beyond synthetic modification of the antenna ligand, tuning the triplet energy level can be approached by utilizing a sensitizing molecule with dual triplet emission. Phosphors with two distinct phosphorescent emission bands are uncommon, and can range from metal complexes to organic molecules. Dual emission states in metal complexes are typically facilitated simply be a mixture of ^{3}LC and ^{3}MLCT bands. For organic-based systems stimulating triplet emission is typically performed at 77 K in order to decrease vibrational relaxation. Dual triplet emission is atypical for organic chromophores and very few systems have indicated this behavior. Typical organic systems that possess multiple stable emission states consist of conjugated quinoxaline type systems.[209] Phenalenone has shown this behavior in which there are two distinct singlet states from the $n\pi^*$ (S_1) and $\pi\pi^*$ (S_2) and two distinct triplet states $\pi\pi^*$ (T_1) and $n\pi^*$ (T_2). Emission spectra and computational data support intersystem crossing rates $\approx 2 \times 10^{10}$ s^{-1} between the S_1 and T_1.[207] The T_2 state was found to be nearly degenerate with

the S_1 leading to ISC occurring rapidly between as well. In addition, dual phosphorescence has been observed in halogenated toluene and anthraquinone derivatives.[209]

Dual Emission in Highly Conjugated Phenazine and Quinaxoline Systems

Dipyrido[3,2-*a*:20,30-*c*] phenazine (dppz) and 2,3-di-2-pyridylquinaxoline (dpq), two diimine-type ligands with an extended π-network, create highly luminescent complexes when bound to transition and lanthanide ions.[210-213] These materials have shown promise not only in imaging but in LEDs, as well. Creating electropolymerizable derivatives of these two ligands would provide good sensitizers for lanthanide emission and good scaffolds to produce luminescent metallopolymers. There have been several reports of poly-$(EDOT)_2$dppz in the literature. Electrochromic and electrochemical deposition studies showed that uniform films could be easily electrodeposited from $TBAPF_6$/monomer solution.[214] The synthesis of $EDOT_2$dppz is straightforward, and the diamine precursor can be used to produce many ligands. There are no current reports of $(EDOT)_2$dpq in the literature.

$(EDOT)_2$dppz (**L1**) and $(EDOT)_2$dpq (**L2**) were synthesized and then complexed with Ln(III) β-diketonates to produce the metal complexes (Scheme 19). Initial absorption and photophysical characterization of **L1** and **L2** indicated two separate emission pathways present. Differing the excitation wavelength accessed $n\pi^*/\pi\pi^*$ singlet and triplet states or an ILCT singlet and triplet states. Characterization of the monomers using fluorimetry showed the Eu(III) and Tb(III) complexes produced luminescent lanthanide materials. Dy(III) complexes showed high quantum yields, up to 8.2% in solution, making these complexes some of the most efficient Dy(III)-based materials.

Metallopolymers were produced from every monomer and lanthanide luminescence was detectable for the Eu(III) and Tb(III) polymers. Visible emitting Dy(III), Eu(III), and Tb(III) were sensitized by the high energy $n\pi^*/\pi\pi^*$ singlet and triplet states. As shown in Scheme 18, excitation of the lower ILCT states led to effective sensitization of Yb(III) and Nd(III) ions. Yb(III) complexes emitted at 977 nm with a quantum yield upward of 5.3%. The resulting polymers also showed Yb(III) emission, attaining quantum yields of 0.011%.

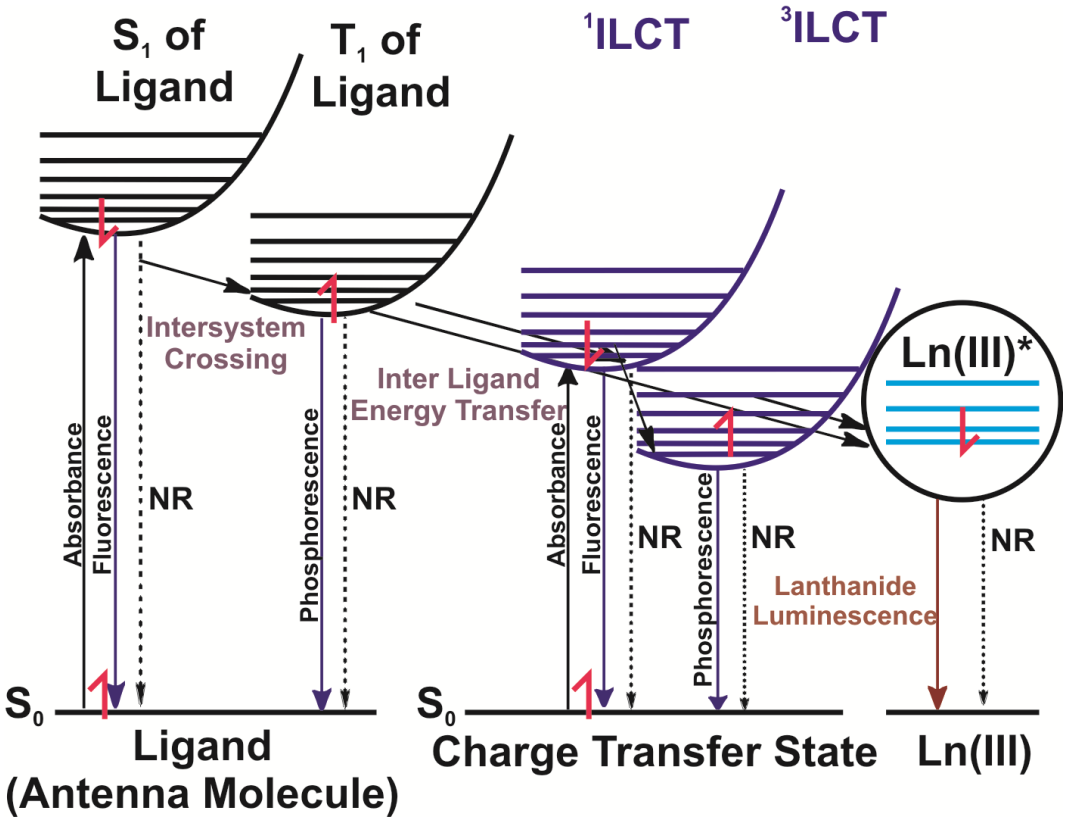

Scheme 18. The charge transfer centered triplet state allows for effective sensitization of near-IR emitting Ln(III) ions.

EXPERIMENTAL

General Methods

Air- and moisture-sensitive reactions were carried out in heat gun dried glassware using standard Schlenk techniques under an inert nitrogen atmosphere. Solvents were dried using an Innovative Technology, Pure Solv solvent purifier with double purifying column or using 4 Å activated molecular sieves. All other chemical were used as received from commercial suppliers. NMR spectra were recorded with a Varian Unity +300 (^{1}H, 300 MHz, ^{13}C{^{1}H} 75 MHz) and were referenced to residual solvent peaks. Chemical ionization (CI) mass spectra were collected on a Micromass Autospec Ultima mass spectrometer. X-ray photoelectron spectroscopy (XPS) was carried out on a PHI 5700 XPS system equipped with a dual Mg X-ray source and monochromatic Al X-ray source complete with depth profile and angle-resolved capabilities.

Synthesis

Synthesis of the Ligands

(L1). Synthesis of **1** followed a procedure adapted from literature.[214] To a 100 mL round-bottom flask, 1,2-diamino-3,6-di(3,4-ethylenedioxythienyl)benzene (0.39 g, 1 mmol) and 1,10-phenanthroline-5,6-dione (0.21 g, 1 mmol) were added. Ethanol (50 mL) was added and the resulting orange solution was refluxed and stirred for 48 hours. The resulting dark violet solution was filtered and washed with cold ethanol (2×25 mL) yielding a lustrous violet powder with no further purification necessary (0.515 g, 91.7%). ^{1}H NMR ($CDCl_3$): 9.6 (d, J = 2.0, 2H), 9.19 (d, J = 1.0, 2H), 8.51 (s, 2H), 7.71 (q, J = 2.0, 2H), 6.55 (s, 2H), 4.36-4.29 (dd, J = 1.0, J = 19.8, 8H). ^{13}C{^{1}H} NMR ($CDCl_3$): product was too insoluble in deuterated solvents to acquire a spectra. HRMS (CI) m/z

calculated for $C_{22}H_{12}N_2O_4S_2$ 563.63 $[M + H]^+$, found 563.59. Elemental analysis calculated (found): C, 64.04 (64.44); H, 3.22 (3.43).

(L2). Similar to **L1**, instead 2,2'-pyridil (0.212 g, 1 mmol) was added. The orange solution was refluxed over 72 hours, resulting in a dark red solution with a red precipitate. The red precipitate was filtered and washed with ethanol (2 × 25 mL), with no further purification necessary (0.401 g, 71.4%). ^{1}H NMR ($CDCl_3$): 8.7 (s, 2H), 8.52 (d, J = 7.8, 2H), 8.31 (d, J = 4.5, 2H), 7.97 (t, J = 6.0, 2H), 7.25 (d, J = 4.5, 2H), 6.6 (s, 4H), 4.43-4.39 (dd, J = 2.7, J = 26.9, 8H). ^{13}C{^{1}H} NMR ($CDCl_3$): 159.2, 151.8, 148.3, 137.1, 135.6, 128.9, 127.0, 125.1, 123.1, 103.4, 90.3, 65.9, 65.2. HRMS (CI) m/z calculated for $C_{22}H_{14}N_2O_4S_2$ 565.64 $[M + H]^+$, found 565.66. Elemental analysis calculated (found): C, 63.81 (63.84); H, 3.57 (3.56).

Synthesis of the Ln(III) Complexes

General Procedure for Ln(III)-1 or Ln(III)-2. The following procedure was adapted from literature.[198] **L1** or **L2** (1 equiv., 0.025 mmol) in 1:1 ethanol/DCM (4 mL) was added to a 25 mL round bottom flask. To this solution a solution of a Ln(III)(β-diketonate)$_3$ • $3H_2O$ (1 equiv., 0.025 mmol) in methanol was slowly added. The following violet solution rapidly turned dark blue and was further stirred at room temperature overnight. The blue solution was then filtered and crystals suitable for diffraction were produced by slow vapor diffusion of pentane into the filtrate.

Gd(hfac)$_3$-L1. Yield: 0.024 g (71.4%) HRMS (CI) m/z calculated for $C_{45}H_{21}F_{18}GdN_4O_{10}S_2$ 1342.02 $[M + H]^+$, found 1342.0411. Elemental analysis calculated (found): C, 40.30 (40.23); H, 1.58 (1.50).

Tb(hfac)$_3$-L1. Yield: 0.0255 g (75.9%) HRMS (CI) m/z calculated for $C_{45}H_{21}F_{18}N_4O_{10}S_2Tb$ 1343.69 $[M + H]^+$, found 1343.70. Elemental analysis calculated (found): C, 40.25 (41.23); H, 1.58 (1.70).

Tb(btfac)$_3$-L1. Yield: 0.0199 g (%) HRMS (CI) m/z calculated for $C_{60}H_{36}F_9N_4O_{10}S_2Tb$ 1367.998 $[M + H]^+$, found 1368.0550. Elemental analysis calculated (found): C, 52.72 (58.11); H, 2.65 (2.88).

Tb(tta)$_3$-L1. Yield: 0.0227 g (%) HRMS (CI) m/z calculated for $C_{54}H_{30}F_9N_4O_{10}S_5Tb$ 1386.078 $[M + H]^+$, found 1386.08. Elemental analysis calculated (found): C, 46.83 (47.01); H, 2.18 (2.09).

Eu(hfac)$_3$-L1. Yield: 0.0246 g (73.6%) HRMS (CI) m/z calculated for $C_{45}H_{21}F_{18}EuN_4O_{10}S_2$ 1336.73 $[M + H]^+$, found 1337.099. Elemental analysis calculated (found): C, 40.40 (40.88); H, 1.73 (1.98).

Eu(btfac)$_3$-L1. Yield: 0.0231 g (67.9%) HRMS (CI) m/z calculated for $C_{60}H_{36}EuF_9N_4O_{10}S_2$ 1361.038 $[M + H]^+$, found 1361.0350. Elemental analysis calculated (found): C, 52.99 (52.81); H, 2.67 (2.68).

Eu(tta)$_3$-L1. Yield: 0.0277 g (80.2%) HRMS (CI) m/z calculated for $C_{54}H_{30}EuF_9N_4O_{10}S_5$ 1381.138 $[M + H]^+$, found 1381.20. Elemental analysis calculated (found): C, 46.99 (47.14); H, 2.34 (2.48).

Yb(btfac)$_3$-L1. Yield: 0.030 g (86.9%) HRMS (CI) m/z calculated for $C_{60}H_{36}F_9N_4O_{10}S_2Yb$ 1382.128 $[M + H]^+$, found 1382.130. Elemental analysis calculated (found): C, 52.18 (52.56); H, 2.63 (3.03).

Yb(dbm)$_3$-L1. Yield: 0.015 g (44.4%) HRMS (CI) m/z calculated for $C_{75}H_{51}N_4O_{10}S_2Yb$ 1406.418 $[M + H]^+$, found 1406.433. Elemental analysis calculated (found): C, 64.10 (64.93); H, 3.66 (3.80).

Yb(tta)$_3$-L1 . Yield: 0.021 g (60.1%) HRMS (CI) m/z calculated for $C_{54}H_{30}F_9N_4O_{10}S_5Yb$ 1400.208 $[M + H]^+$, found 1400.2800. Elemental analysis calculated (found): C, 46.35 (46.70); H, 2.16 (2.22).

Gd(hfac)$_3$-L2. Yield: 0.031 g (91.2%) HRMS (CI) m/z calculated for $C_{45}H_{23}F_{18}GdN_4O_{10}S_2$ 1344.04 $[M + H]^+$, found 1344.0411. Elemental analysis calculated (found): C, 40.24(40.23); H, 1.73 (1.90).

Dy(hfac)$_3$-L2. Yield: 0.012 g (35.2%) HRMS (CI) m/z calculated for $C_{45}H_{23}F_{18}DyN_4O_{10}S_2$ 1349.2900 $[M + H]^+$, found 1349.2900. Elemental analysis calculated (found): C, 40.09 (40.63); H, 1.72 (1.86).

Dy(btfac)$_3$-L2. Yield: 0.026 g (74.7%) HRMS (CI) m/z calculated for $C_{60}H_{38}DyF_9N_4O_{10}S_2$ 1373.688 $[M + H]^+$, found 1373.6850. Elemental analysis calculated (found): C, 52.50 (53.14); H, 2.79 (2.83).

Dy(tta)$_3$-L2 . Yield: 0.022 g (63.0%) HRMS (CI) m/z calculated for $C_{54}H_{32}DyF_9N_4OS_5$ 1391.668 $[M + H]^+$, found 1391.670. Elemental analysis calculated (found): C, 46.64 (47.43); H, 2.32 (2.60).

Tb(hfac)$_3$-L2. Yield: 0.023 g (67.0%) HRMS (CI) m/z calculated for $C_{45}H_{23}F_{18}TbN_4O_{10}S_2$ 1345.71 $[M + H]^+$, found 1345.7100. Elemental analysis calculated (found): C, 40.19 (40.64); H, 1.72 (1.96).

Tb(btfac)$_3$-L2. Yield: 0.027 g (78.1%) HRMS (CI) m/z calculated for $C_{60}H_{38}F_9N_4O_{10}S_2Tb$ 1370.018 $[M + H]^+$, found 1370.0170. Elemental analysis calculated (found): C, 52.64 (57.18); H, 2.80 (2.94).

Tb(tta)$_3$-L2 . Yield: 0.014 g (40.3%) HRMS (CI) m/z calculated for $C_{54}H_{32}F_9N_4O_{10}S_5Tb$ 1388.098 $[M + H]^+$, found 1388.098. Elemental analysis calculated (found): C, 46.76 (47.36); H, 2.33 (2.59).

Eu(hfac)$_3$-L2. Yield: 0.021 g (59.7%) HRMS (CI) m/z calculated for $C_{45}H_{23}F_{18}EuN_4O_{10}S_2$ 1338.75 $[M + H]^+$, found 1338.757. Elemental analysis calculated (found): C, 40.40 (40.13); H, 1.73 (1.80).

Eu(btfac)$_3$-L2. Yield: 0.029 g (83.3%) HRMS (CI) m/z calculated for $C_{60}H_{38}EuF_9N_4O_{10}S_2$ 1363.048 $[M + H]^+$, found 1363.050. Elemental analysis calculated (found): C, 52.91 (53.36); H, 2.81 (2.84).

Eu(tta)$_3$-L2 . Yield: 0.024 g (68.9%) HRMS (CI) m/z calculated for $C_{54}H_{32}EuF_9N_4O_{10}S_5$ 1379.118 $[M + H]^+$, found 1379.114. Elemental analysis calculated (found): C, 47.06 (47.75); H, 2.19 (2.39).

Yb(btfac)$_3$-L2. Yield: 0.018 g (51.6%) HRMS (CI) m/z calculated for $C_{60}H_{38}F_9N_4O_{10}S_2Yb$ 1384.138 $[M + H]^+$, found 1384.1370. Elemental analysis calculated (found): C, 52.10 (52.28); H, 2.77 (3.04).

$Yb(dbm)_3$-L2. Yield: 0.020 g (57.1%) HRMS (CI) m/z calculated for $C_{75}H_{53}N_4O_{10}S_2Yb$ 1408.438 $[M + H]^+$, found 1408.44. Elemental analysis calculated (found): C, 64.00 (63.23); H, 3.80 (3.96).

$Yb(tta)_3$-L2. Yield: 0.015 g (42.9%) HRMS (CI) m/z calculated for $C_{54}H_{32}F_9N_4O_{10}S_5Yb$ 1402.228 $[M + H]^+$, found 1402.24. Elemental analysis calculated (found): C, 46.29 (46.55); H, 2.30 (2.39).

UV-Vis and Luminescent Measurements

Absorption spectra were recorded on a Varian Cary 6000i Spectrophotometer with Starna Quartz Fluorometer Cells with a pathlength of 10 mm for the ligand and complexes. All spectroscopic data were obtained in DCM solutions unless otherwise noted. The absorption spectra of polymer films were performed on films that were fully reduced. Luminescent measurements were recorded on a Photon Technology International QM 4 spectrophotometer equipped with a 6-inch diameter K Sphere-B integrating sphere. For quantum yield measurements, the integrating sphere was used. Quantum yield was calculated by dividing the area under the emission peak of the complex by the difference between the area under the excitation peak of the sample and that of a blank solution ($A_{em\ sample}$ / ($A_{ex\ blank}$ - $A_{ex\ sample}$), where A = area under peak).

Electochemistry

Electrochemical syntheses and studies were performed in a dry-box under a nitrogen atmosphere using a GPES system from Eco. Chemie B. V.. All the electrochemical experiments were carried out in a three-electrode cell with a $Ag/AgNO_3$ reference

electrode (silver wire dipped in a 0.01 M silver nitrate solution with 0.1 M [(*n*-Bu)$_4$N][PF$_6$] (TBAPF$_6$) in CH$_3$CN), a Pt button working electrode, and a Pt wire coil counter electrode. Potentials were relative to this 0.01 M Ag/AgNO$_3$ reference electrode. Ferrocene was used as an external reference to calibrate the reference electrode before and after experiments were performed and that value was used to correct the measured potentials. The supporting electrolyte was 0.1 M TBAPF$_6$ that was purified by recrystallization three times from hot ethanol before being dried for 3 days at 100 °C under active vacuum.

RESULTS AND DISCUSSION

Synthesis of Dual Emissive Ligands

Synthesis of the two ligand precursors began with the bromination of 2,1,3-benzothiadiazole to produce 5,6-dibromo-2,1,3-benzothiadiazole in an 88% yield, as shown in Scheme 19. The dibromo aryl precursor was then cross coupled to 2-tri(butyl)stannyl-3,4-ethylenedioxythiophene using Pd(PPh)$_2$Cl$_2$. The reaction produced a lustrous red solid in a 76% yield. The EDOT-precursor was then reacted with LiAlH$_4$ to produce the desired diamine precursor.[214] The diamine precursor precipitated as a pale red crystalline material, with ^{1}H NMR signals corresponding the amine appearing at δ 4.53 ppm. Although the synthesis scheme denotes the diamine synthesis step as separate from the condensation, the diamine can be produced *in situ*, and after removing solvent, used directly thereafter in the condensation with the desired diketone. **L1** and **L2** were produced by condensation reaction of the synthesized diamine precursor with an aromatic dione. The synthesis of **L1** yielded a purple lustrous solid in a 92% yield.[214] The

synthesis of **L2** yielded a bright red solid in a 71.4% yield. Crystals were grown for **L2** from slow evaporation of chloroform and X-ray diffraction crystal structure was obtained. The structure showed significant torsion of the bypyridyl groups, as shown in Figure 43. Ln(III) complexes were made by refluxing the ligand and Ln(III)(β-diketonate)$_3$(H_2O)$_2$ in toluene for two hours. Crystals were isolated from slow evaporation of benzene over several days.

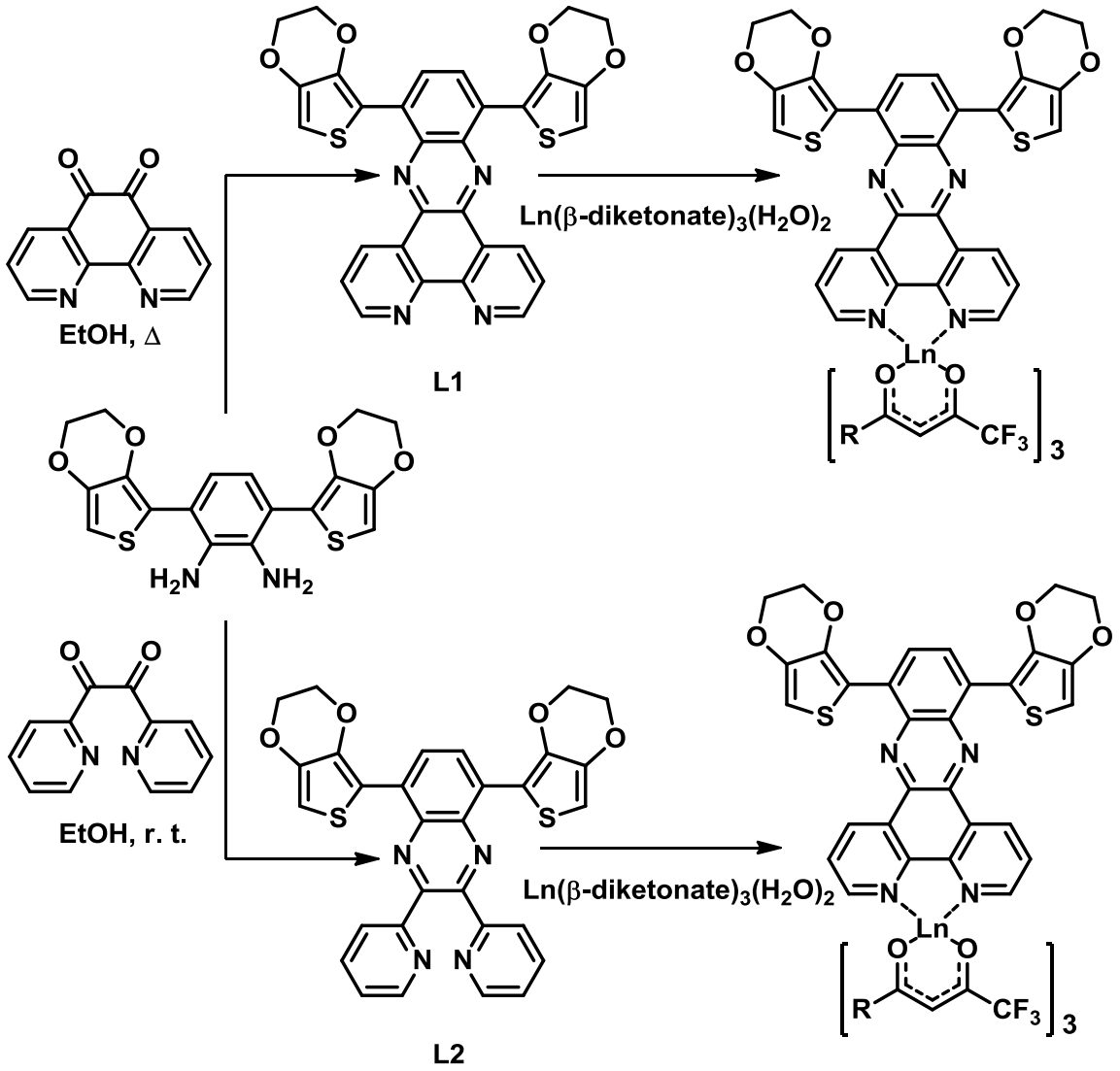

Scheme 19. Synthetic scheme of the ligand **L1** and **L2** and Ln(III) complexes.

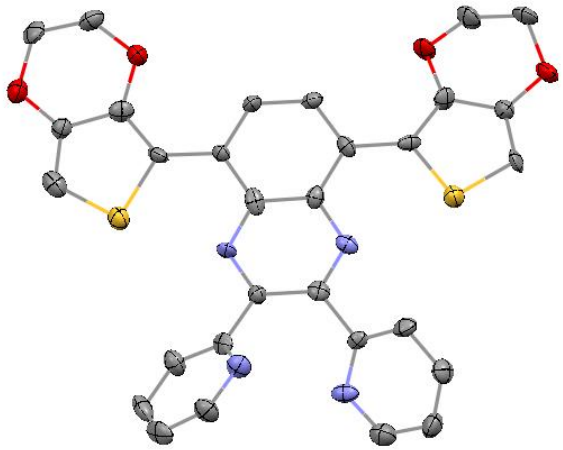

Figure 43. Crystal structure of **L2.**

UV-Vis and Near-IR Photophysical Properties of L1 and L2

Photophysics of L1

The photophysical properties of **L1** and **L2** were studied under a variety of conditions. The absorption spectra (Figure 44) for **L1** displayed broad peaks between 250-544 nm. The spectra featured a n-π^* transition band at 250 nm, a π- π^* transition band with a λ_{max} = 345 nm, and an inter-ligand charge transfer (ILCT) at 544 nm. Solvatochromism experiments supported the identification of the red broad band as the ILCT band, and the band showed a hypsochromic shift. Comparing **L1** to dppz (λ_{max} = 380 nm), there is a significant blue shift of absorption in the π-π^* band. Absorption spectra for **L2** exhibit peaks at 325 nm, corresponding to a π-π^* band. ILCT behavior was also observed, with a broad ILCT band at 475 nm, which further confirmed by studying the absorption using a solvatochromic conditions. **L2** also displays a blue shift relative to the π-π^* band of dpq (λ_{max} = 334 nm).

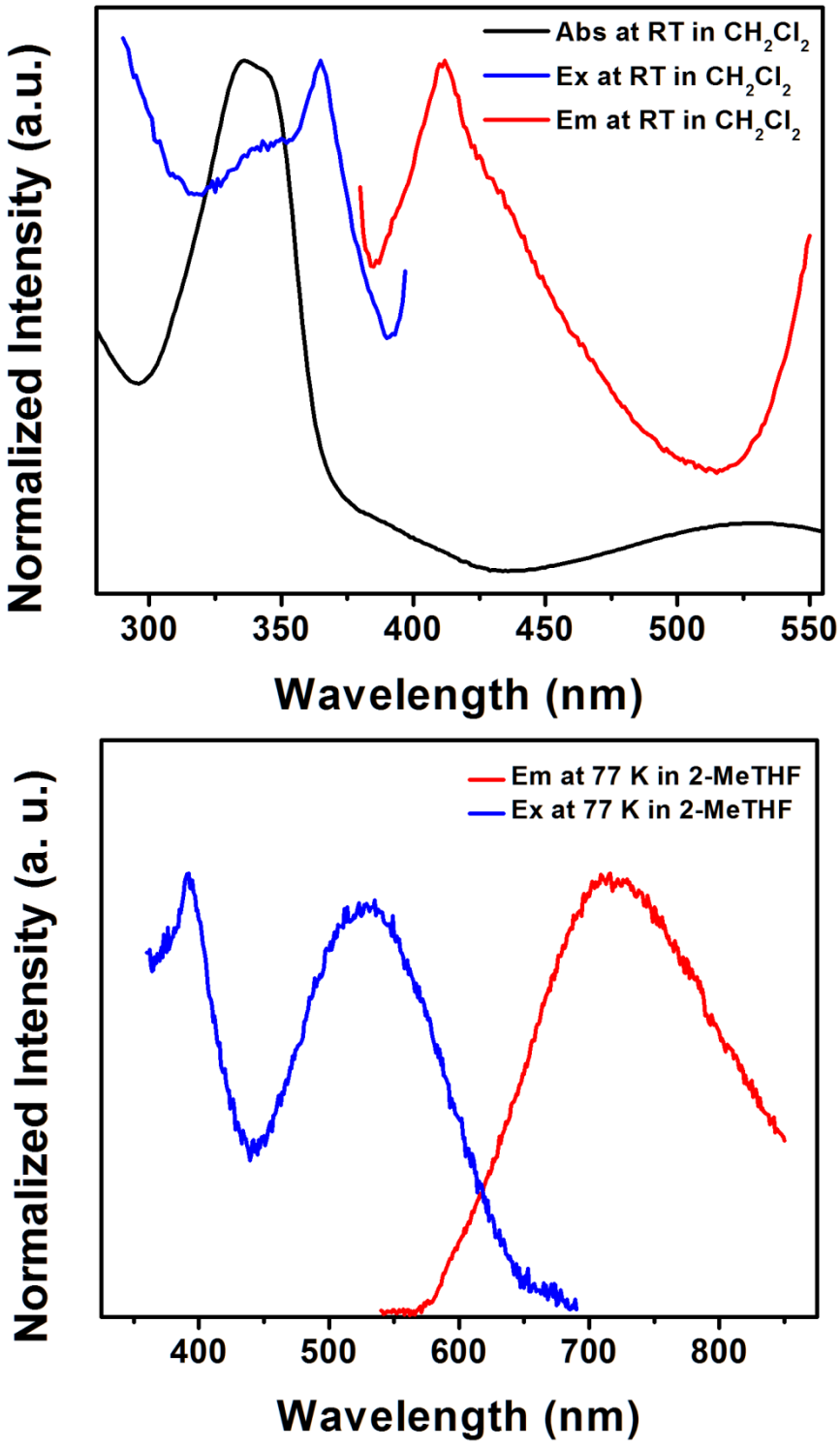

Figure 44. (top) Absorption and photophysical spectra for $EDOT_2dppz$ (**L1**) (bottom) NIR emission and excitation for **L1**.

Emission spectra (λ_{ex} = 360 nm) as shown in Figure 44, showed a peak at 405 nm and another red-shifted peak at 710 nm. At 77K, phosphorescent peaks appeared at 425 nm (τ = 7.3 μs) and 725 nm (τ = 47.5 μs). The difference in lifetimes supports two distinct phosphorescent transitions occurring in the ligand. The Gd(III) excited state lies above 33,100 cm^{-1}, allowing only bound ligand phosphorescence to be observed. Photophysical studies, as outlined in Table 12, of **L1** and **Gd-1** showed that lanthanide coordination shifted the measured T_1 levels significantly. The emission spectra (Figure 45,46) of **Gd-1**, in 2-MeTHF at 77K, showed the phosphorescent peaks shifted from 425 nm and 725 nm to 420 nm and 666 nm, respectively. The T_1 levels for both phosphorescent emission states, as shown in Figure 44 and 45, were 23,500 and 15000 cm^{-1}, respectively. Based on the position of the T_1 levels, Tb(III) and Yb(III) excited states could be sensitized by the T_1 and T_2 of **L1**.

Table 12. Photophysical data for the chromophores, **L1** and **L2**.

Ligand	λ_{abs} (nm) (ε)	λ_{ex} (nm)	λ_{em} (nm)	T_1 (Bound T_1) (cm^{-1})	τ (μs)	Φ_F
Dppz	**280, 370, 385**	**280**	**377**	**18,500**	**-**	**-**
$(EDOT)_2$dppz	**254 (38000), 345 (45000), 544(6000)**	**360**	**415**	**24,100 (23,500)**	**7.3±0.2**	**4**
nIR	**-**	**375, 525**	**715 (666)**	**13,800 (15,000)**	**47.5±4**	**-**
Dpq	**285, 360**	**360**	**435, 570**	**19,500**	**-**	**-**
$(EDOT)_2$dpq	**255 (12000), 335 (23000), 475 (5000)**	**367**	**425, 440,610**	**19,200 (23,900)**	**10.5±0.5**	**24**
nIR	**-**	**470 (500)**	**625 (645)**	**16,000 (15,500)**	**30.5±2**	**-**

Triplet Energy Level of the Bound L1

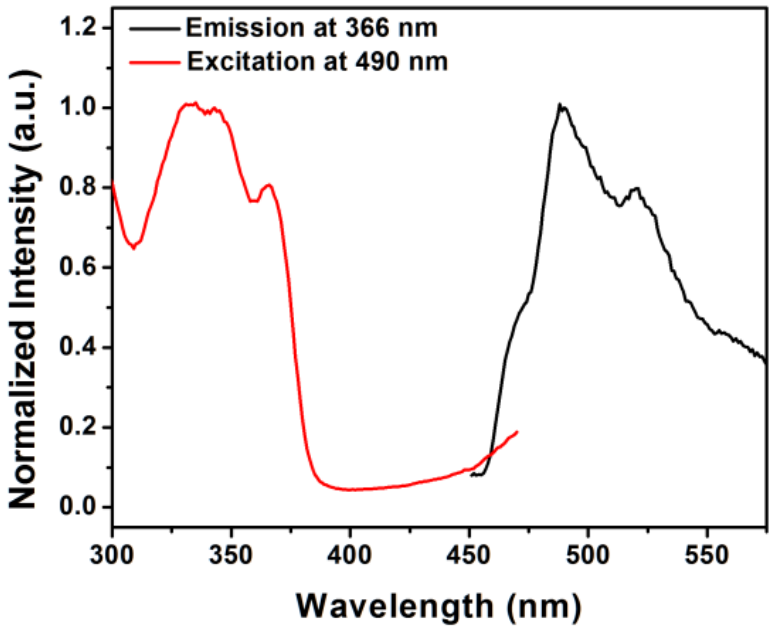

Figure 45. Emission and excitation spectra of $(hfac)_3Gd$-**L1** at 77 K in 2-MeTHF.

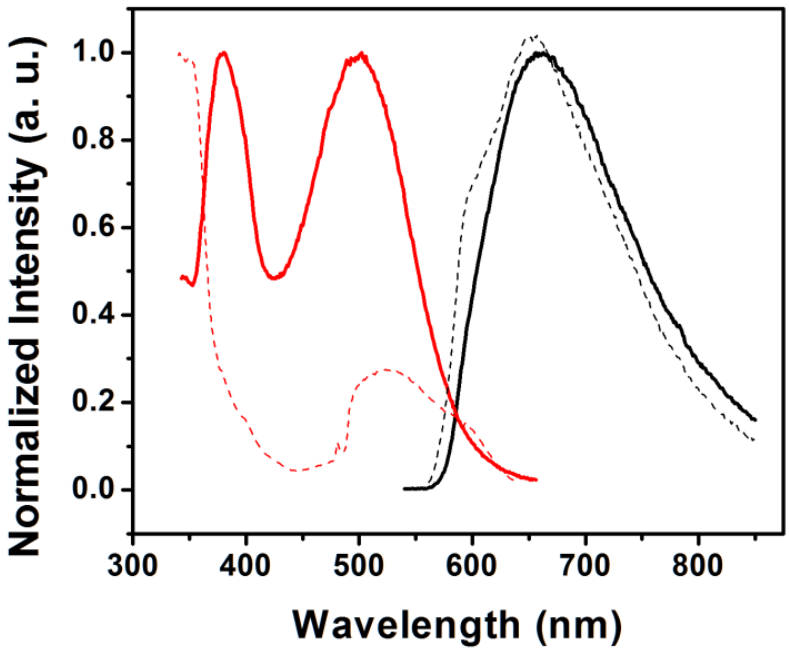

Figure 46. Near-IR emission and excitation spectra of $(hfac)_3Gd$-**L1** at 77 K in 2-MeTHF. The dotted traces represent the emission and excitation at room temperature.

Photophysics of L2

As shown in Figure 47, excitation of **L2** at 367 nm showed an emission peak at 425 nm with some vibronic structure. As shown in Figure 48, a large broad emission peak from 550-650 nm was observed, as well. Similar solvatochromism was observed with possible emission tuning in the orange-red region. Observation of the emission at 77 K showed a long-lived phosphorescent peak at 415 nm. The triplet energy level (23,900 cm^{-1}) for **L2** was taken as the blue edge of the phosphorescence peak.

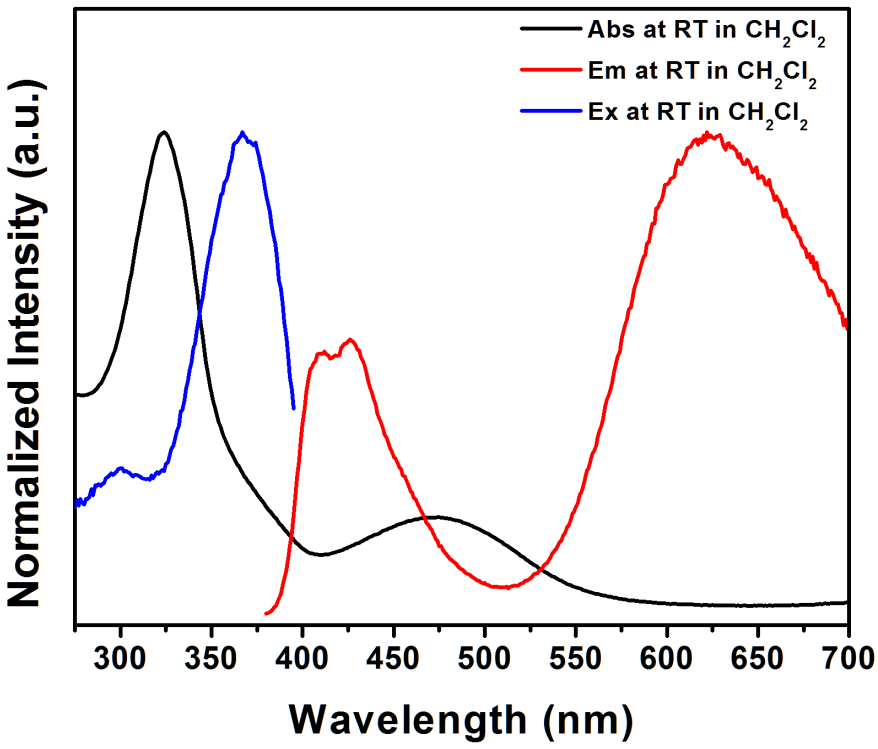

Figure 47. Absorption and photophysical spectra for $EDOT_2dpq$ (**L2**).

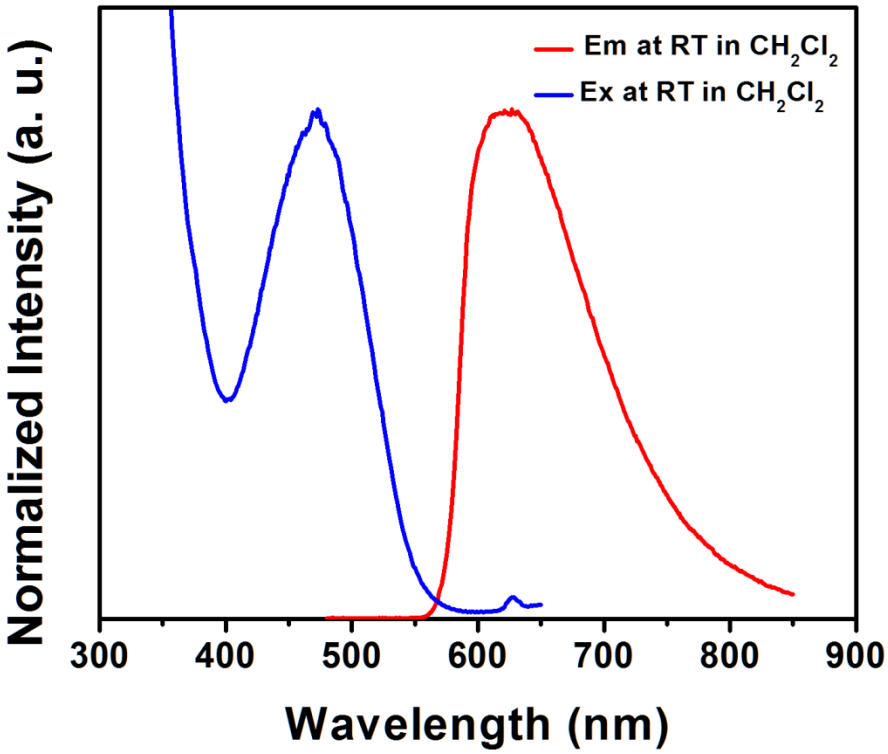

Figure 48. NIR emission and excitation spectra for **L2**.

Triplet Energy Level of the Bound L2

Gd(III)$(tta)_3$ complexes were made to probe the triplet energy levels of the ligands when bound to a lanthanide (III) ion. Emission spectra were gathered in 2-MeTHF at 77 K to promote phosphorescence emission. Emission from these complexes was dominated by the bound ligand and β-diketonates. Excitation of Gd-**L2** at 365 nm resulted in the formation of peaks with vibronic structure at 455 and 481 nm, as shown in Figure 49 and 50. Based on these bound triplet energy levels, the ligand may be effective at sensitization of Dy(III), Eu(III), Sm(III), and Tb(III) ions. NIR emission studies were also performed to explore the existence of a bound lower energy triplet state.

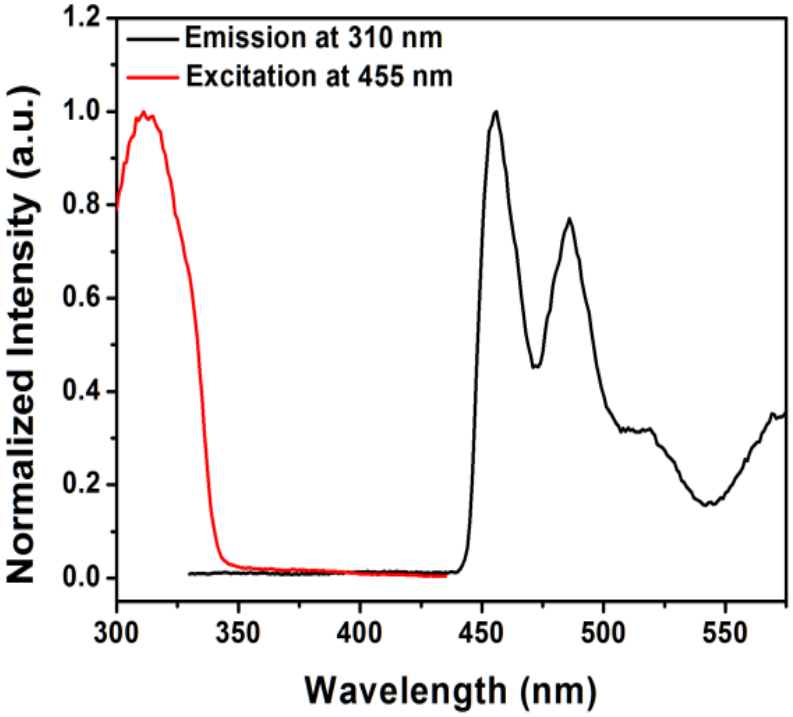

Figure 49. Emission and excitation spectra of $(tta)_3Gd$-**L2** at 77 K in 2-MeTHF.

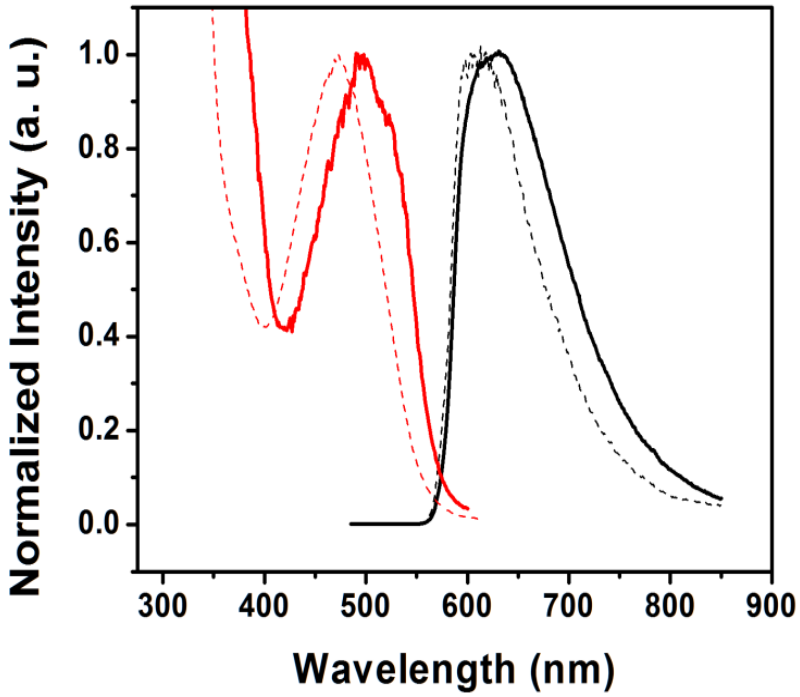

Figure 50. Near-IR emission and excitation spectra of $(tta)_3Gd$-**L2** at 77 K in 2-MeTHF. The dotted trace are spectra taken at room temperature in 2-MeTHF.

Blue Emission from Tm(III)(β-diketonate)$_3$ Complexes

Initial studies focused on producing Tm(β-diketonate)$_3$(**L**) complexes from ligands **L1** and **L2**. Complexes were produced primarily to examine the photophysics of the T_1 state in the antennas, probing the efficiency of energy transfer through the organic energy states into the lanthanide excited state. Producing the desired Tm(β-diketonate)$_3$ complexes was performed by refluxing **L1** and **L2** in toluene in a 1:1 ratio with Tm(β-diketonate)$_3$(H_2O)$_2$ complexes. Only Tm(hexafluoroacetylacetonate(hfac))$_3$ complexes **Tm-L1,L2** were studied, specifically due to the difficulty in producing a Tm(β-diketonate)$_3$(H_2O)$_2$ complex with a β-diketonate T_1 level high enough to properly sensitize the Tm(III) f^* state. The excited state level of Tm(III) lies at 21,500 cm^{-1} and the blue-emitting hfac ancillary ligand T_1 state lies at ~22,000 cm^{-1}.[215,216] Weak Tm(III) emission was observed using the highly conjugated ligands. The blue hypersensitive $^1G_4 \rightarrow {}^3H_6$ Tm(III) transition was observed at an excitation wavelength of 365 nm. Due to the weak emission of the Tm(III) complexes, lifetimes and quantum yields could not be measured. Further studies of the blue T_1 of the ligands were carried out by studying the luminescent properties of the green and yellow emitting Tb(III) and Dy(III) ions, with known Tb(III) and Dy(III) excited states, as shown in Figure 51, being 2000-4000 cm^{-1} from T_1 of **L1** and **L2**.

Highly Luminescent Dy(III)(β-diketonate)$_3$(L2) Complexes

Examples of ligand antennas for Dy(III) emission utilize chromophores with blue, high energy triplet state. This is due to the Dy(III) $^4F_{9/2}$ transition state lying at 21,100 cm^{-1}. Current examples of luminescent Dy(III) complexes possess variable quantum

yields between 0.0002 -19 %.[217] Several β-diketonate complexes were produced using each ligand type as the main sensitizing ligand. As mentioned before the ancillary ligand can greatly affect the energy transfer and the triplet energy level of the β-diketonate must be considered. β-diketonates used were hexafluoroacetylacetonate (22,000 cm^{-1}) , benzyltrifluoroacetylacetonate (btfac) (21,500 $cm^{-1)}$, and thienyltrifluoroacetone (tta) (20,800 cm^{-1}). In all complexes produced from **L1**, no Dy(III) emission was observed. The emission profile was very similar to the emission observed for the Gd(III) complexes. In the complexes featuring **L2** energy transfer was efficient and each complex displayed Dy(III) emission.

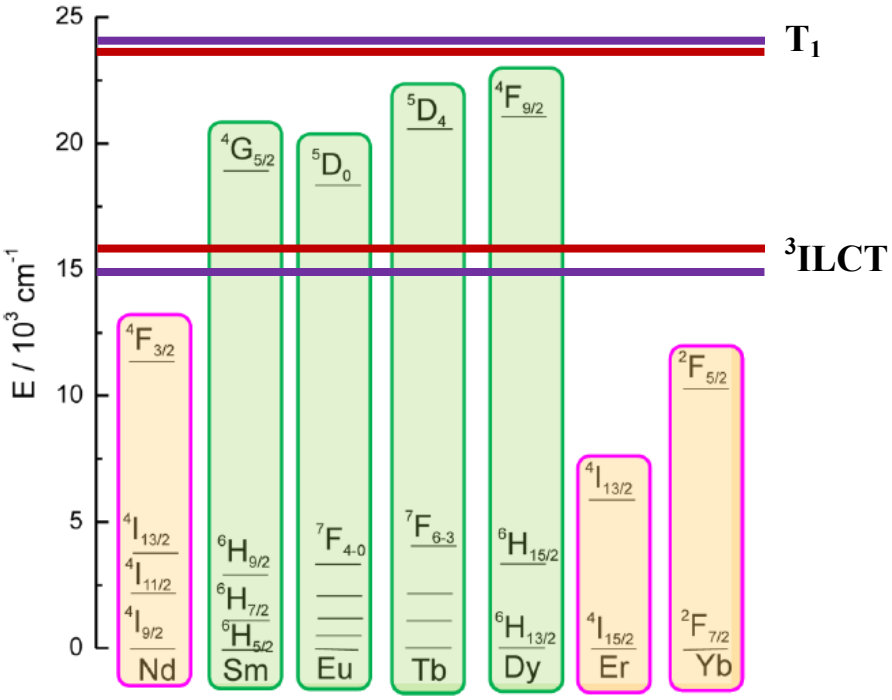

Figure 51. Excited state energy levels for visible and nIR-emitting Ln(III) ions. The lines represent the energy levels of the **L1** (purple) and **L2** (red).

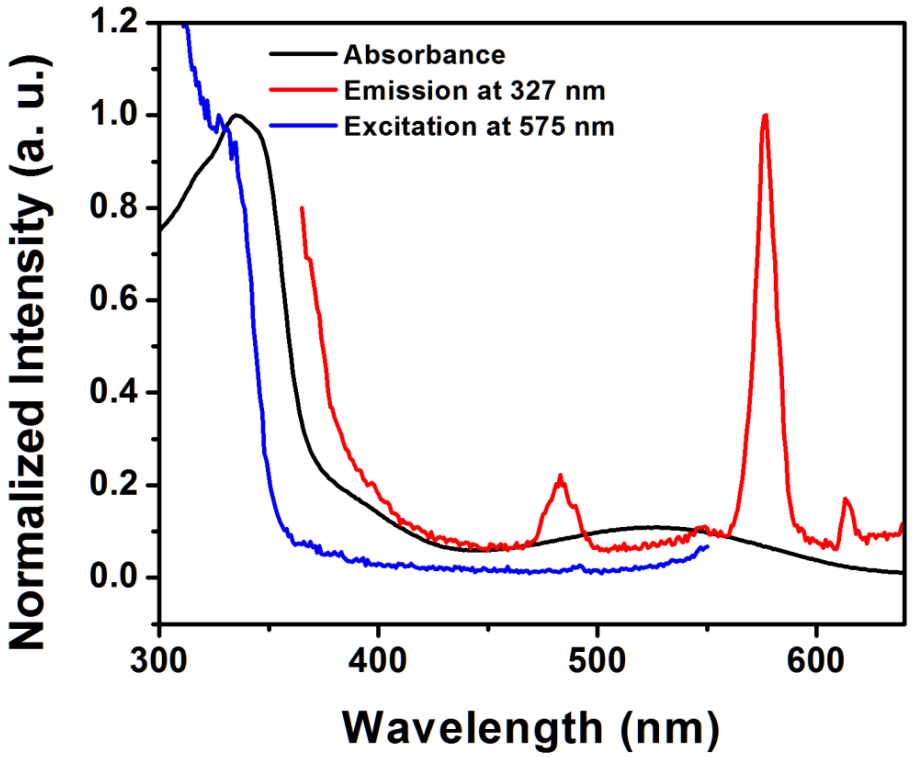

Figure 52. Representative emission, excitation, and absorption spectra of the $(EDOT_2dppz)$ Dy(III)$(tta)_3$.

Excitation at 327 nm showed Dy(III) emission for the (**L2**)Dy(III)(β-diketonate)$_3$ complexes with exceptionally high quantum efficiencies (2-8% solution, 1-5% solid state), as summarized in Table 13. Initial emission spectra showed characteristic emission bands ($^4F_{9/2} \rightarrow {}^6H_{15/2\text{-}9/2}$) for Dy(III), with a broad $^4F_{9/2} \rightarrow {}^6H_{15/2}$ transition dominating the spectrum, as shown in Figure 52.[217] Typical Dy(III) complexes possess quantum yields lower than 1%, with low lifetimes between 5-20 μs.[2] The $(EDOT_2dpq)$Dy(III)(β-diketonate)$_3$ emission peak at 575 nm showed relatively long lifetimes ranging from 22-29 μs. Furthermore, the quantum yields were found to be 2-8%, denoting efficient energy transfer for the complexes. Dy(III) metallopolymers have been synthesized as well, and there photophysics are currently being explored.

Table 13. Summary of photophysical data for the Dy(III) complexes.

Material	λ_{ex}(nm)	λ_{em}(nm)	τ (μs)	Φ_{Ln}	Φ_{Ln} (solid)
(EDOT$_2$dpq)Dy(hfac)$_3$	**327**	**575**	**29**	**8±1**	**2±1**
(EDOT$_2$dpq)Dy(btfac)$_3$	**327**	**575**	**24**	**2±1**	**1±0.2**
(EDOT$_2$dpq)Dy(tta)$_3$	**327**	**575**	**-**	**-**	**-**
(EDOT$_2$dppz)Dy(hfac)$_3$	**365**	**575**	**-**	**-**	**-**
(EDOT$_2$dppz)Dybtfac)$_3$	**367**	**575**	**-**	**-**	**-**
(EDOT$_2$dppz)Dy(tta)$_3$	**365**	**575**	**-**	**-**	**-**

Highly Luminescent Tb(III)(β-diketonate)$_3$(L1) Complexes

The ligand EDOT$_2$dppz (**L1**) T_1 bound energy level was measured to be at 23,500 cm^{-1}, and in the Tm(III) and Dy(III) complexes proper energy transfer did not occur. The energy level of **L1** was close enough to the Ln(III) excited states, and energy was likely lost through nonradiative processes. The excited state of Tb(III) lies at 20,500 cm^{-1}, suggesting more effective energy transfer would occur between **L1** and Tb(III) ions due to an energy gap of ~3000 cm^{-1}. A series of Tb(III)(β-diketonate)$_3$ complexes were synthesized from both **L1** and **L2**. Emission spectra (Figure 53) showed effective sensitization of Tb(III) ions for **L1**, and emissive sublevels appeared with the $^5D_4 \rightarrow {}^7F_5$ transition dominating the spectra. The quantum yield measurements, summarized in Table 14, of the (EDOT$_2$dppz)Tb(β-diketonate)$_3$ showed solid state yields from 25-36%, and solution quantum yields from 21-32%. Long-lived lifetime measurements were found, common to Tb(III) emission, ranging from 798-854 μs.

Table 14. Photophysical data for the Tb(III) complexes for ligands **L1** and **L2**.

Material	λ_{ex}(nm)	λ_{em}(nm)	τ (μs)	Φ_{Ln}	Φ_{Ln} (solid)
$(EDOT_2dpq)Tb(hfac)_3$	334	545	-	-	-
$(EDOT_2dpq)Tb(btfac)_3$	334	545	811	3±1	11.0 ±2
$(EDOT_2dpq)Tb(tta)_3$	367	545	-	-	-
$(EDOT_2dppz)Tb(hfac)_3$	353	545	829	32±2	36±1
$(EDOT_2dppz)Tbbtfac)_3$	325	545	798	21±4	25±5
$(EDOT_2dppz)Tb(tta)_3$	350	545	854	5±1	-

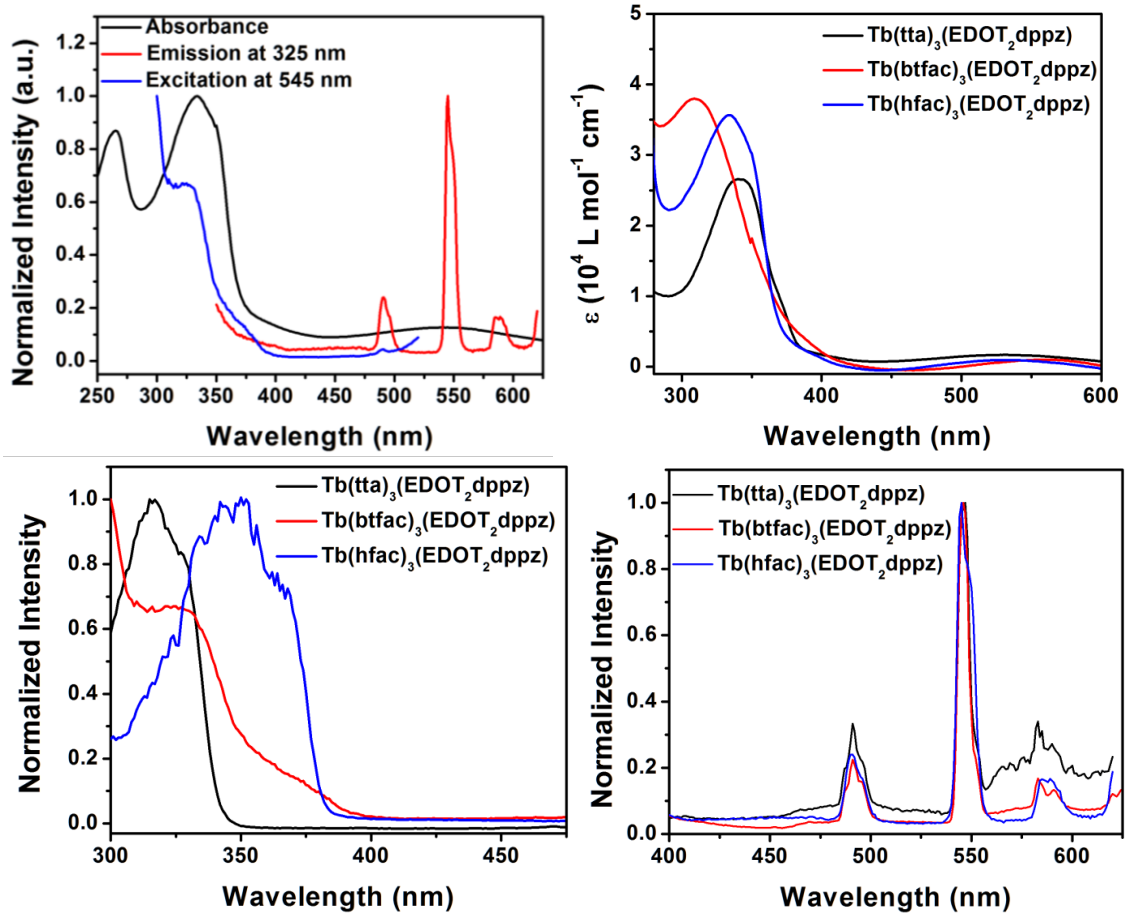

Figure 53. Photophysical spectra of the $(hfac)_3Tb$(**L1**) complex (top left). Absorption spectra for the Tb(**L1**) complexes (top right). Excitation spectra for the Tb(**L1**) complexes (bottom left). Emission spectra for the Tb(**L1**) complexes (bottom right).

Tb(III)(β-diketonate)$_3$(L2) and Eu(III)(β-diketonate)$_3$(L1, L2) Complexes: Ineffective Sensitization

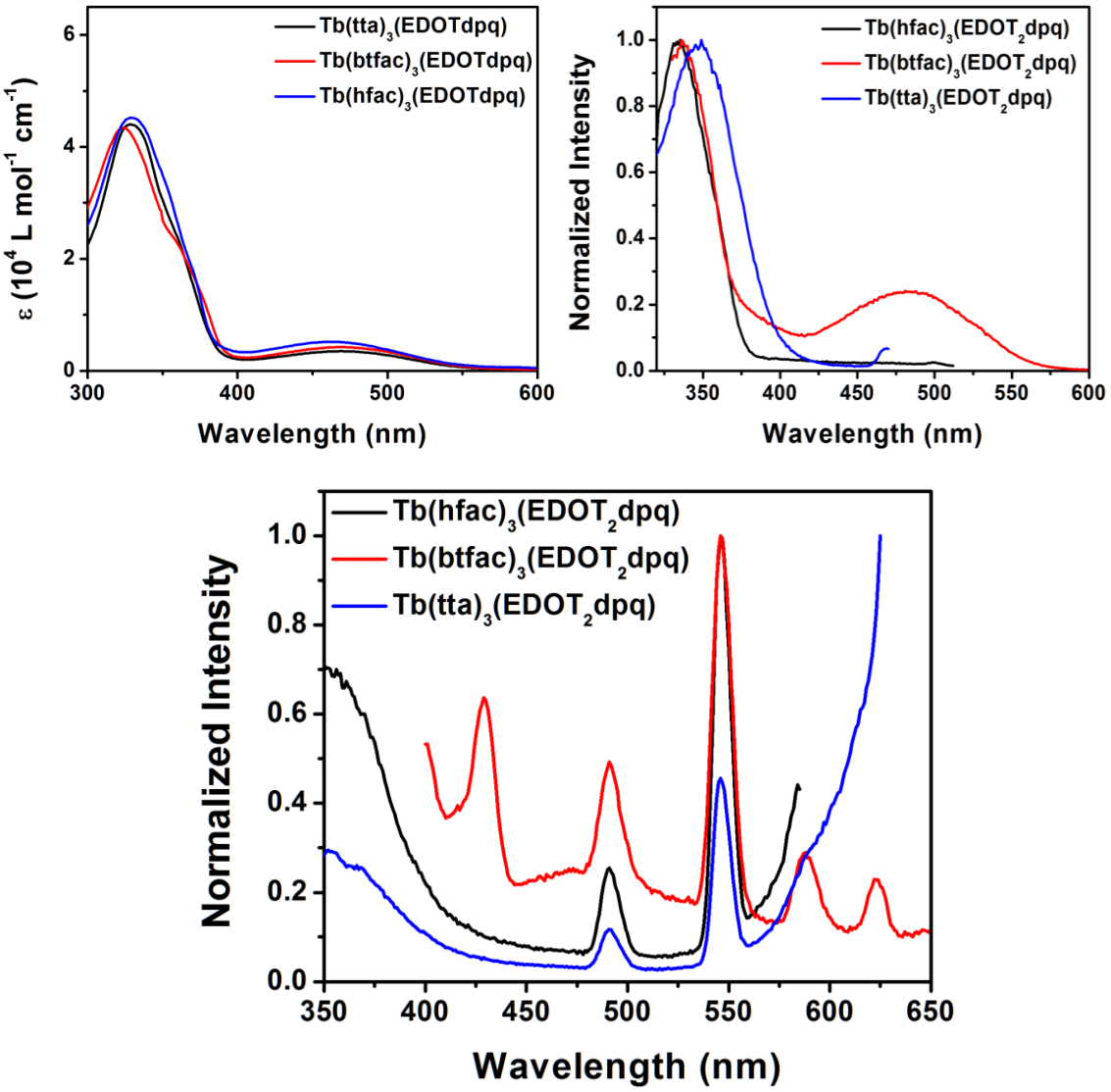

Figure 54. Absorption spectra for the Tb(**L2**) complexes (top left). Excitation spectra for the Tb(**L2**) complexes (top right). Emission spectra for the Tb(**L2**) complexes (center).

Emission from the Tb(III) complexes produced using the EDOT$_2$dpq ligand (**L2**) showed weak luminescence. Furthermore, similar to the **L1** - based systems, the

ancillary β – diketonate was important in sensitization. All complexes indicated ineffective energy transfer, with various ligand emission features present in the spectra. For the $(btfac)_3Tb$(**L2**) complex all characteristic emission peaks for Tb(III) emission were present, however, fluorescence from the ligand was present at 430 nm. While the dual triplet states open pathways for efficient sensitization of both visible and nIR-emitting lanthanides, the second ^{3}ILCT triplet state possibly serves as a deactivation pathway, as well. Significant emission from the ligand was observed along with Tb(III) emission. Figure 54 shows the mixture of emission bands present in the $Tb(hfac)_3$(**L2**) and $Tb(tta)_3$(**L2**) complexes.

Table 15. Photophysical data for the Eu(III) complexes.

Eu(β-diketonate)$_3$	**λ_{abs} (nm)**	**λ_{ex} (nm)**	**λ_{em} (nm)**	**τ (μs)**	**$\Phi_{Ln}(\Phi_{fl})$**	**Φ_{Ln}(solid)**
(EDOT$_2$dpq)Eu(hfac)$_3$	**309**	**355**	**615**	**-**	**-**	**-**
(EDOT$_2$dpq)Eu(tta)$_3$	**345**	**347**	**615**	**-**	**-**	**-**
(EDOT$_2$dpq)Eu(dbm)$_3$	**347**	**350**	**615**	**-**	**-**	**-**
(EDOT$_2$dppz)Eu(hfac)$_3$	**335**	**330**	**615**	**580**	**4 ± 2**	**7 ± 2**
(EDOT$_2$dppz)Eu(tta)$_3$	**333**	**350**	**615**	**675**	**3 ± 1**	**5 ± 3**
(EDOT$_2$dppz)Eu(dbm)$_3$	**340**	**339**	**615**	**633**	**7 ± 1**	**6 ± 1**

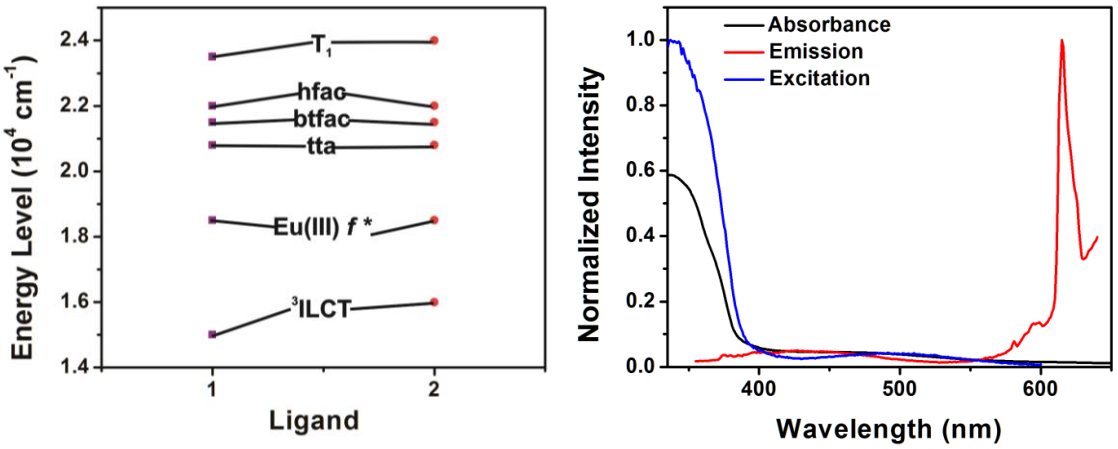

Figure 55. Energy level alignment of the triplet energy levels of **L1**, **L2**, and ancillary ligands to the Eu(III) excited state (left). Photophysical characterization of a selected Eu(III) complex, $(hfac)_3Eu(\mathbf{L2})$ (right).

This trend continued in the case of the Eu(III) complexes (Table 15) and can be explained by the alignment of ligand triplet energy levels and lanthanide excited states shown in Figure 55. The ^{3}ILCT level for both ligands is only ~2500 cm^{-1} from the Eu(III) excited state, and energy transfer from the T_1 energy level may degenerate to the ^{3}ILCT band instead of the Eu(III) excited state may be occurring. The dual triplet emission of the ligands allows for sensitization of the higher energy Ln(III) ions and possibly NIR Ln(III) ions, unfortunately at the cost of poor sensitization of Tb(III) and Eu(III) ions. After investigating the visible emitting Ln(III) ions, NIR emitting Ln(III) ions were studied using these highly conjugated ligands.

Sensitization of the NIR Emitting Ln(III) ions

Yb(III) ion sensitization in the literature has produced complexes with Φ_{Ln} greater than 0.15.[218] Furthermore, due to the proximity of the excited and ground states, potential vibrational relaxation is greatly increased. Ligands **L1** and **L2** were reacted with $Yb(III)(dbm)_3(H_2O)_2$ to test the ligands ability to sensitize NIR emitting lanthanides.

Both types of ligands rendered emissive Yb(III) materials with relatively high quantum yields (Table 16). Emission spectra, as shown in Figure 56, showed characterisitic Yb(III) emission peaks at 972 nm ($^2F_{5/2} \rightarrow {}^2F_{7/2}$). Stark splitting accounted for the multiple peaks at 1003 to 1033 nm.[219] Quantum yields, 5.3% for $(EDOT_2dppz)Yb(III)(dbm)_3$ and 1.8% for $(EDOT_2dpq)Yb(III)(dbm)_3$, were calculated by comparing lifetimes of the complexes to a $Yb(tta)_3(H_2O)_2$ reference ($\Phi = \tau/\tau_0$).[220] Initial results from Nd(III) and Er(III) complexes showed no identifiable emission spectra.

Table 16. Photophysical data for the Yb(III) complexes.

$Yb(dbm)_3$	λ_{ex} (nm)	λ_{em} (nm)	τ (μs)	Φ_{Ln}
$EDOT_2dppz$	535	977	22.3	5.3
$EDOT_2dpq$	485	977	16.8	1.8

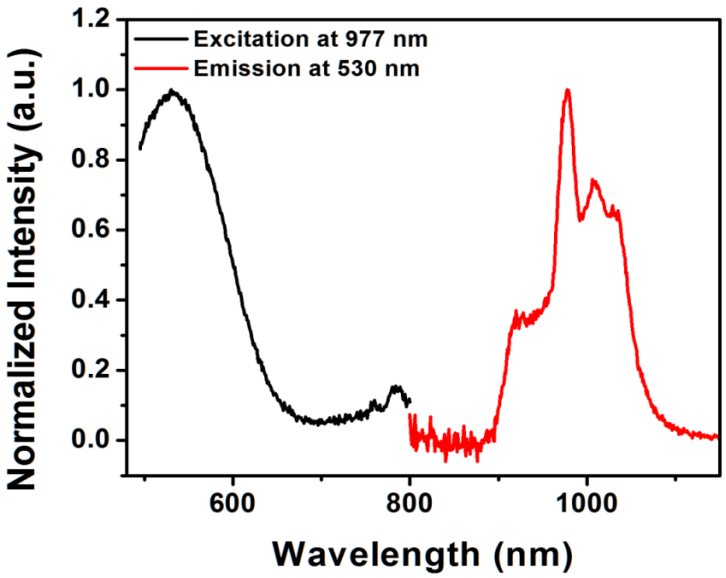

Figure 56. Excitation and emission spectra for the $(dbm)_3Yb$(**L1**) complex.

Electropolymerization of Ln(III) Complexes to Form Ln(III) Metallopolymers

Dy(III) Metallopolymers

After studying the luminescence of the Dy(III) complexes, the materials were tested as possible precursors for conducting metallopolymers. Under electrochemical conditions, metallopolymers were grown from four of the six Dy(III) monomers. The monomer featuring tta groups did not grow visible polymer on ITO/glass or any other substrate. This may be due, in part, to the polaron produced delocalizing into the ancillary ligand thienyl groups, destabilizing the monomer and inhibiting proper growth mechanisms. In all Ln(III)$(tta)_3$-based materials polymers did not form, and precipitate formed in solution. Precipitation suggests that the thienyltrifluoracetone complexes decomposed under oxidative conditions.

The other Dy(III)$(hfac/btfac)_3$(**L1/L2**) complexes when cycled from -0.5 to +1.5 V (vs. Fc/Fc^+) under oxidative conditions produce conducting metallopolymers. As shown in Figure 57, the polymers showed linear growth dependence over 20 scans indicating that each layer of polymer deposited is highly conductive. Furthermore, the scan rate dependence studies showed linear dependence further supporting highly conductive films were produced. The luminescence of the black Dy(III) films was then studied, but the films showed no detectable Dy(III) emission.

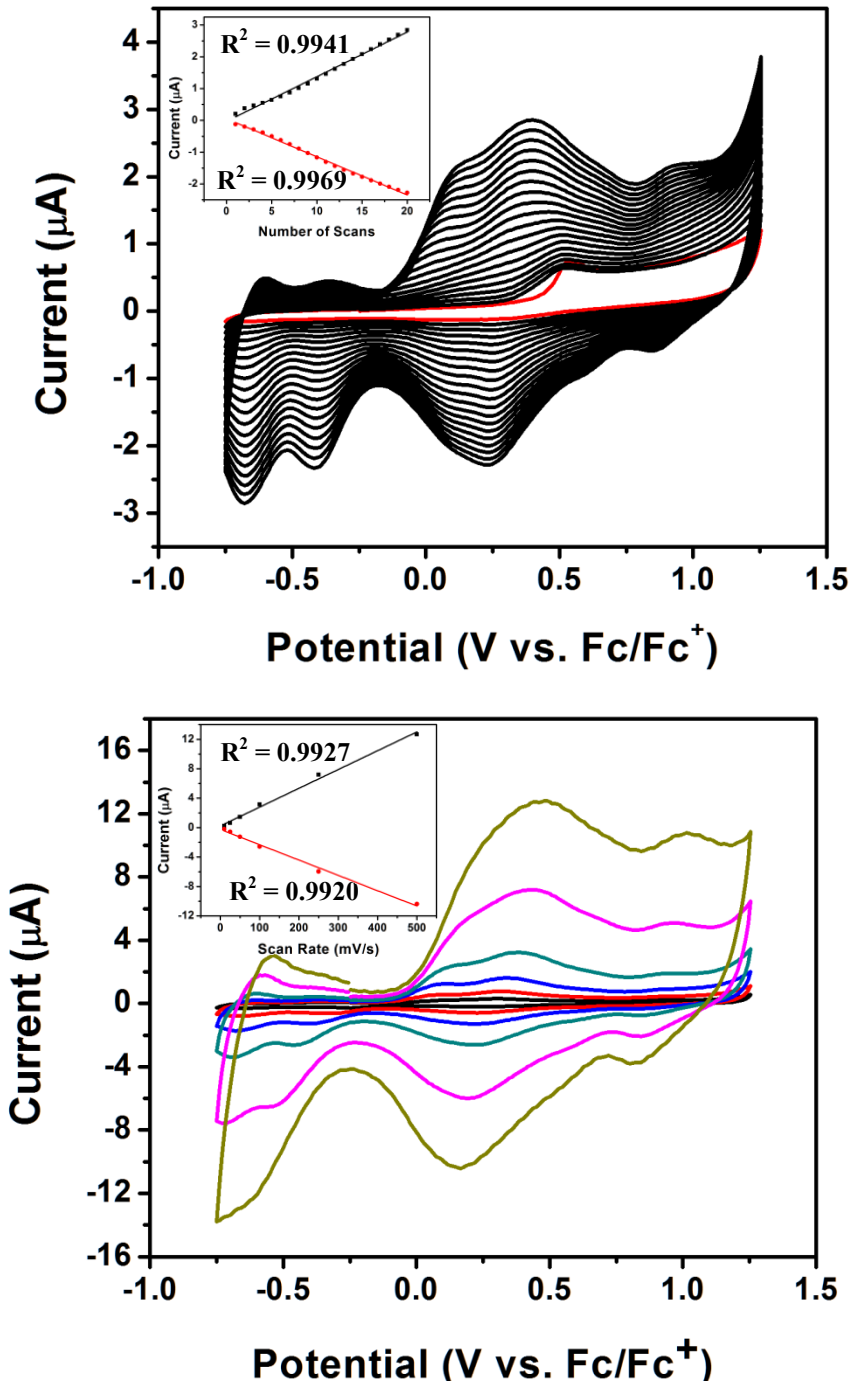

Figure 57. Film growth of poly-**Dy(L1)** over 20 scans at -0.5 V to +1.5V (top). Scan rate dependence of poly-**Dy(L2)** at -0.5 V to +1.5V from 10-500 mV/s in monomer-free solution (bottom).

Luminescent Tb(III) Metallopolymers

The Tb(III) luminescent monomers were then electropolymerized under oxidative potential from -0.5 V to 1.5 V, yielding conductive Tb(III) metallopolymer films. The metallopolymers formed readily, and electrochromic activity was present in the films. The metallopolymer deposition progressed from the clear ITO film to a yellow-orange film transient at ~0.25 V. A red-orange film was observed at 0.60 V, followed closely by the evolution of a blue-green color at 1.00 V. Further oxidative potential resulted in black films at 1.35 V. Reverse scans showed a progression back through the aforementioned chromism. However, after several deposition cycles the electrochromism was not observed any further.

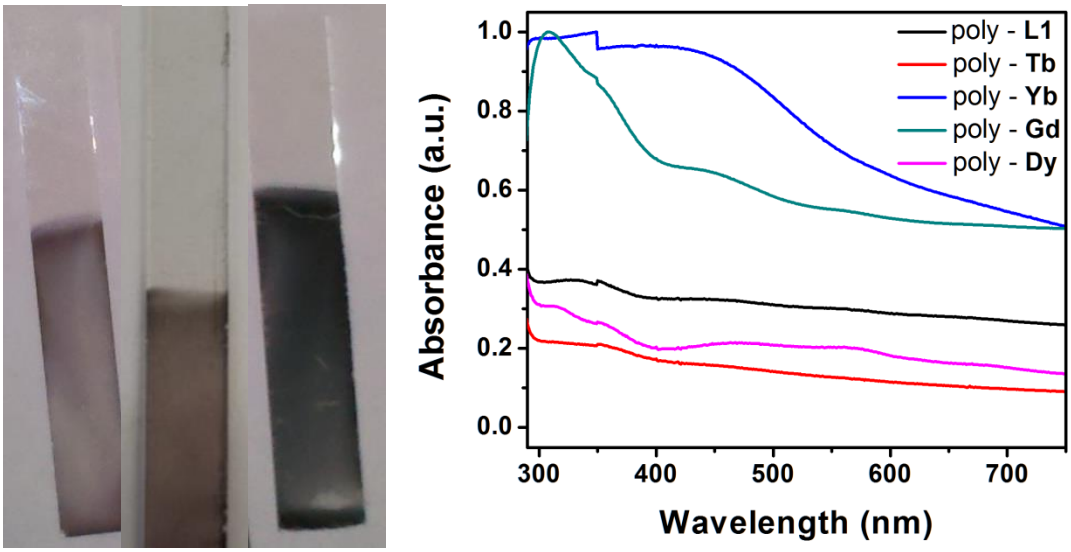

Figure 58. Pictures of the Ln(III) metallopolymer films after electropolymerization. Absorption spectra of the Ln(III) metallopolymers.

As mentioned earlier, the $EDOT_2dpq$ material was initially produced as an organic electrochromic material. Tarkuc *et al.* demonstrated that **L1** posessed a broad range of colors across oxidative potentials. Despite the coordination of the Ln(III)(β-diketonate)$_3$, the electrochromic behavior seems to be preserved in these samples. Further work may lead to a dual functioning material in which both the color and emission of the metallopolymer film can be fully controlled. UV-Vis absorption spectra for the Ln(III) metallopolymer films indicated strong absorption by the materials across the entire visible spectrum. While Yb(III)-based films showed recognizable maxima in the absorption, Tb(III) and Dy(III) metallopolymer spectra displayed very broad featureless absorption profiles, as shown in Figure 58.

Although films were easily formed (Figure 59), the resulting polymer films were poorly luminescent, with only very weak Tb(III) luminescence. Many deactivation pathways for luminescence could occur after electropolymerization. The packing of the metallopolymer on the substrate could facilitate luminescent quenching *via* a lanthanide-lanthanide deactivation pathway.[191] Furthermore, across all of the metallopolymers a significant change in absorption occurs with the polymers absorbing across the entire UV-Vis spectrum. Emission spectra for the Tb(III) containing metallopolymer film showed a very weak characteristic Tb(III) emission, with only the hypersensitive $^5D_4 \rightarrow {}^7F_5$ energy level at 545 nm observed in the emission profile.

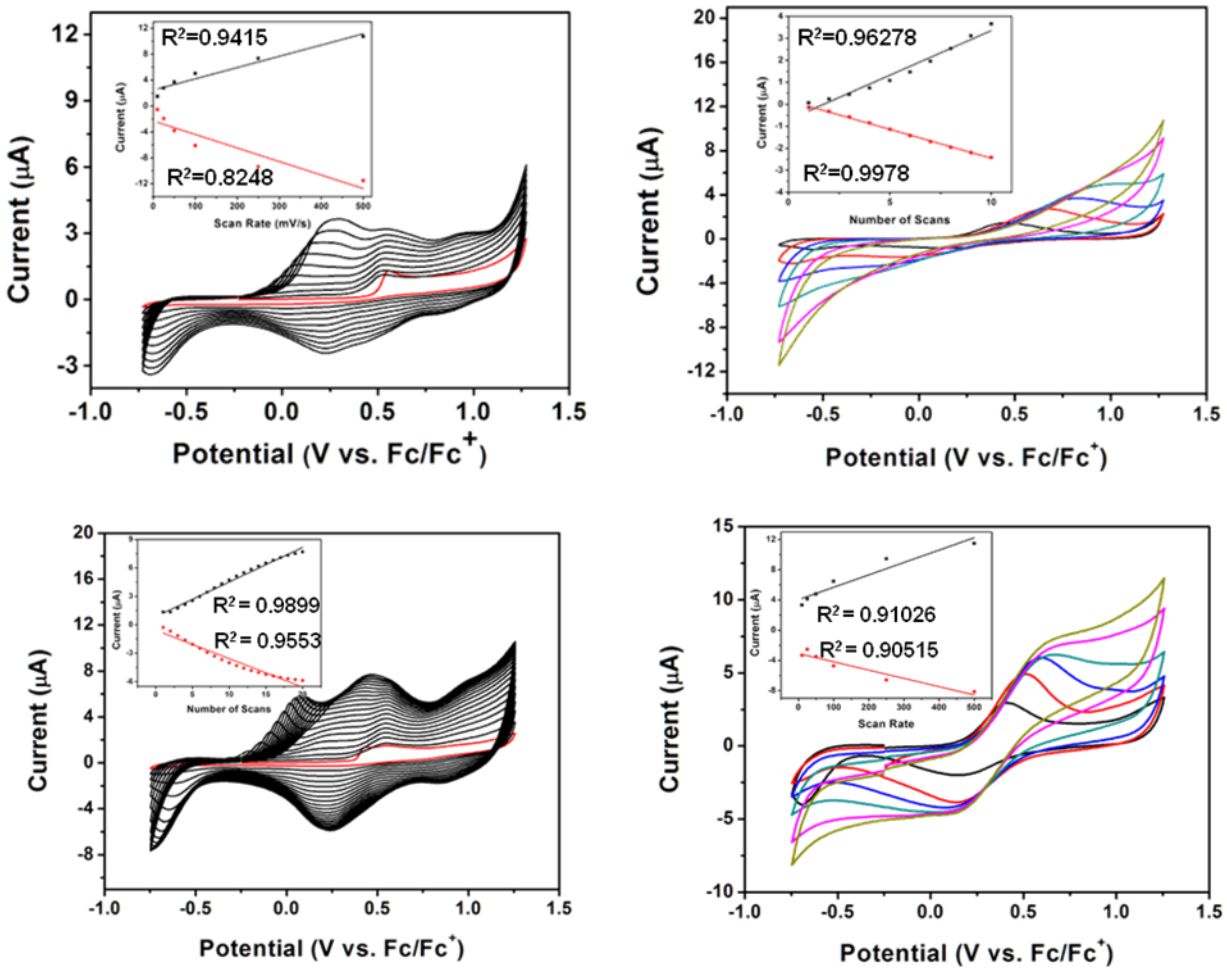

Figure 59. Film growth of poly-**Tb(L1)** over 20 scans at -0.5 V to +1.5V (top left). Scan rate dependence of poly-**Tb(L1)** at -0.5 V to +1.5V from 10-500 mV/s in monomer-free solution (top right). Film growth of poly-**Tb(L2)** over 20 scans at -0.5 V to +1.5V (bottom left). Scan rate dependence of poly-**Tb(L2)** at -0.5 V to +1.5V from 10-500 mV/s in monomer-free solution (bottom right).

Luminescent Yb(III) Metallopolymers

The visible-emitting Ln(III) monomers were electropolymerized without difficulty due to the advantageous stability, conductivity, and solubility afforded by ligands **L1** and **L2**. Resulting photophysical studies of the Dy(III), Tb(III), and Eu(III) metallopolymer films showed very poor luminescent properties. Poly-**Yb** films were also

studied, with broad Yb(III) emission present in the emission spectra of the metallopolymer. Yb(III) monomers were readily electropolymerized, as shown in Figure 60, and the Yb(III) metallopolymer films demonstrated measurable luminescence. Furthermore, compositional analysis of XPS peaks, as shown in Figure 61, showed a S to Yb ratio of 2.3:1 which is in good agreement with the 2:1 theoretical composition. Figure 62 show the photophysical spectra of the $Yb(dbm)_3$**L1**. The resulting dark grey films showed broad absorption across almost the entire visible spectrum. A large broad absoprtion band was observed from 350 – 750 nm. A broad emission peak at 977 nm, followed by broadened stark splitting, was observed by the films (157 nm thick). The emission intensity for the polymer film was significantly lower than the emission observed in the Yb(III) monomer, as shown in Figure 62. Yb(III) transition bands are broadened with less definition present in the peak centered at 977 nm. The emissive lifetime was measured to be 12.5 ± 0.7 μs. The quantum yield of lanthanide luminescence (Φ^{L}_{Ln}; ($\Phi = \tau/\tau_0$)) was found to be 0.088%.

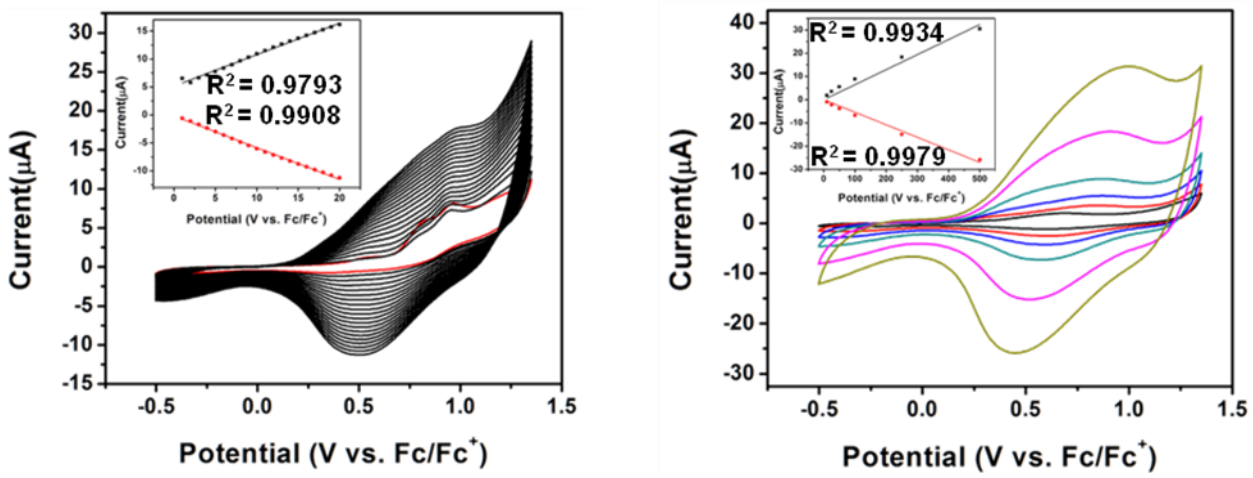

Figure 60. Film growth of poly-**Yb(L1)** over 20 scans at -0.5 V to +1.5V. (Inset) Linear growth of oxidative (black) and reductive (red) peaks (left). Scan rate scans from 10-500 mV/s of poly-**Yb(L1)** in monomer free solution (right). (Inset) Linear scan rate dependence of oxidative (black) and reductive (red) peaks

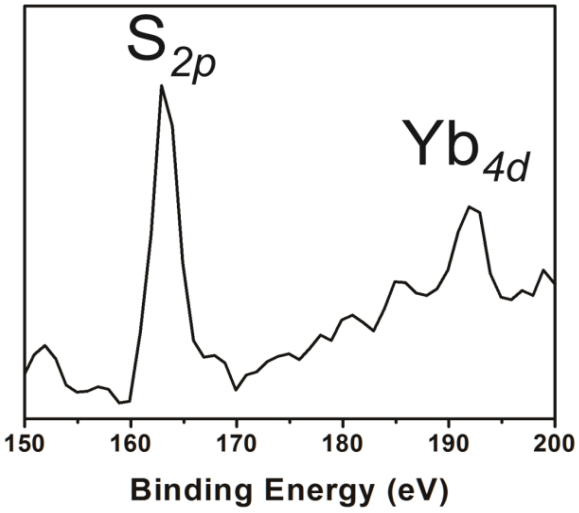

Figure 61. XPS spectra of poly-$(dbm)_3$Yb**L1**.

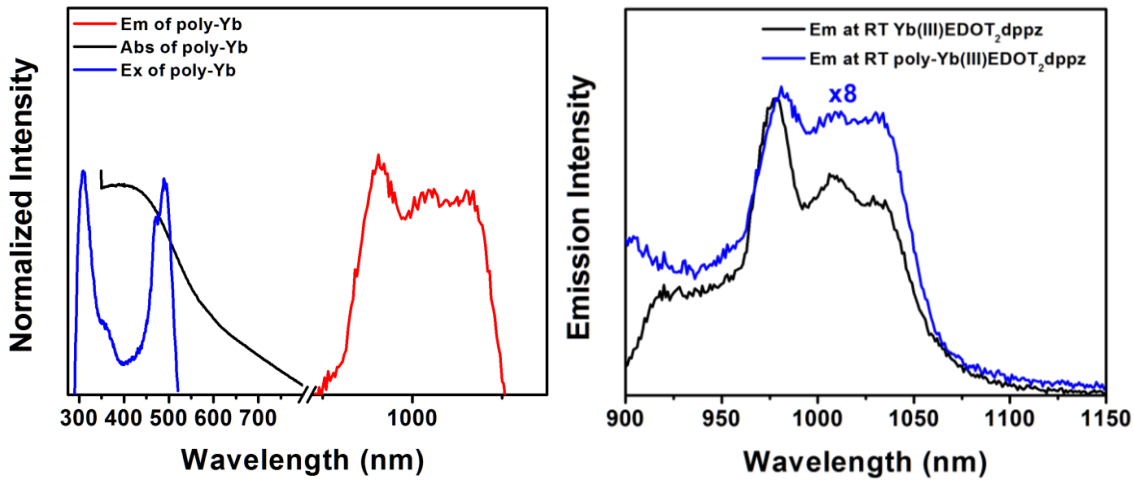

Figure 62. Photophysics of poly-$(dbm)_3$Yb**L1** and comparison of Yb(III) monomer and metallopolymer emission.

CONCLUSION

In summary, we report the synthesis of new types of antenna ligands for both visible and near IR emitting Ln(III) ions. Electrochemical studies supported high conductivity and effective polymerization of the highly conjugated ligands. Photophysical characterization of the antennas indicated that two separate triplet energy levels (T_1 and ^{3}ILCT) were accessible for excitation and emission. Synthesis of Dy(III), Tb(III), and Eu(III) β-diketonate complexes demonstrated the effective sensitization of lanthanide luminescence from the T_1 energy levels. These complexes were readily electropolymerized leading to not only a series of Ln(III) monomers, but many different metallopolymer materials. Excitation of the ^{3}ILCT effectively sensitized emission from Yb(III) monomer and metallopolymers, supporting the unusual electronic characteristics of the ligands could be harnessed appropriately (Figure 63).

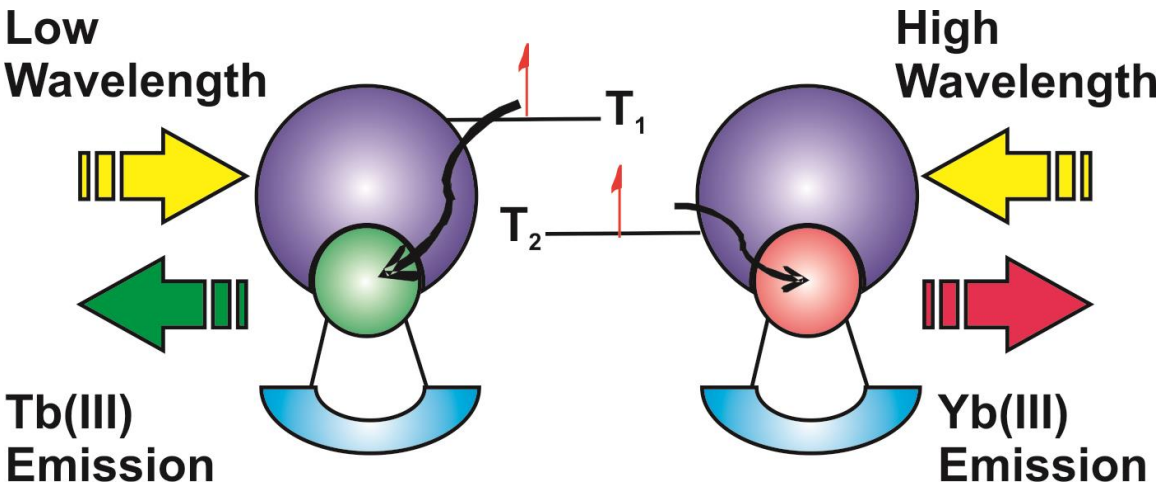

Figure 63. A depiction of the dual excitation pathways present in these ligand systems.

Chapter 5: Using Novel Electropolymerizable Redox-Active Pincer Ligands for Catalytic Rh(I,III) Complexes and Metallopolymers

INTRODUCTION

Redox-active ligands (RLs) are effective systems to modulate the oxidation state and electron density on metal centers. Electrochemical doping of RLs leads to easy tuning of the oxidation states in the ligand. Subsequently, doping leads to a change in the metal oxidation states gradually lengthening the metal-ancillary ligand bond distance.[221-225] A broad variety of systems have served as RLs, including ferrocene-based and thienyl-based compounds. Several examples of phosphine-ferrocene ligands have been developed, utilizing the one electron oxidation event of the redox-active metallocene as a RL. Terthienyl Wolf type I Rh(I) metallopolymers were developed by Mirkin *et al.* demonstrating that doping the backbone directly changed the Rh-L bond distance.[226] Analogous effects were observed in the ancillary isocyanide ligands attached to the Pt(II) center in an electropolymerizable Pt-[NCN] pincer metallopolymer.[227] Electrochemical doping of the backbone modulated the electron density on the Pt(II) center, increasing the metal-isocyanide bond distance in the polymers. These metallopolymers indicated conducting polymer systems could serve as effective RHLs and platforms for potential redox-active metallopolymer catalysts.

An alternative pincer to NCN-type ligands are resorcinol(phosphinite)-based or P^OC^OP systems. These pincers are directly analogous to PCP-type ligands in reactivity. First used as transition metal binding ligands by Kaska and coworkers, P^OC^OP ligands benefit greatly from the P-O bond present.[228] The P-O moiety adds rigidity and

stability, while maintaining the strong sigma donating and pi-accepting nature. Furthermore, C-H bond activation drove the formation of new types of M-C systems, and thus new organometallic reactivity. Highly active Ni(II), Ru(II), Pd(II), Rh(I,III) and Ir(I,III) catalysts have been produced using the tridentate PCP and $P^{O}C^{O}P$ pincer ligands. From these complexes, effective catalysts for hydroaminations, hydrogenations, aryl-aryl couplings, and other catalytically assisted reactions have been studied.[229-232] However, while reactivity and structural information has been gathered for Rh(I/III) $P^{O}C^{O}P$ complexes, further electrochemical and optical studies have not been performed.[230, 233-235]

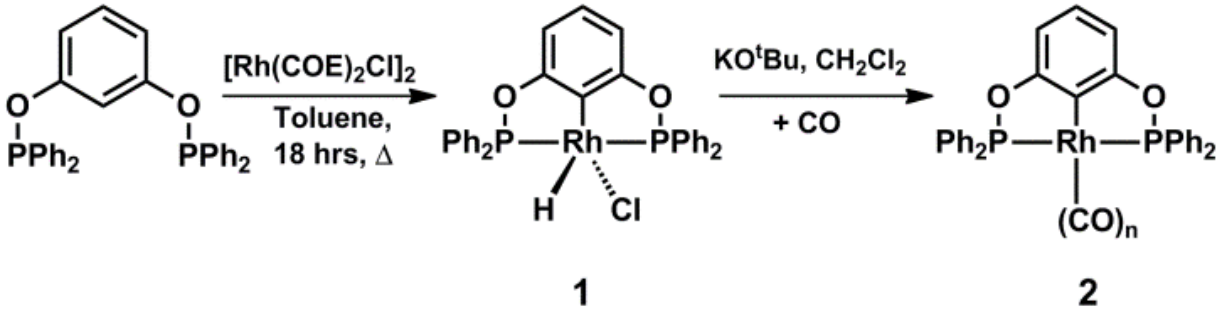

Scheme 21. Synthetic scheme of the model complexes **1** and **2**.

Rhodium complexes have served as effective homogeneous catalysts for hydrogenations and hydroformylations, amongst other catalytic transformations.[230,236] Theoretical and experimental information points to reductive elimination and catalytic activation rates as main limiting factors in catalytic performance.[236,237] Increasing the bond distance between the Rh center and ancillary ligands could directly impact the catalytic rates and kinetics in rate-determining steps. Including redox-active components in the catalyst may provide an electrochemical control of these crucial activation and dissociative processes. Incorporating active Rh(I) centers into a RL conducting polymer backbone could deliver hybrid catalysts systems capable of heightened activity under

oxidative potentials. Probing the change in the catalytic activity of a metallopolymer requires a ligand backbone that is in direct communication with the rhodium center, but is inert to the chemical and electrochemical conditions. Pincer ligands, such as P^OC^OP, serve as effective ligands in homogeneous catalysts. The ligand serves as a sigma donor and is appended with two-electron donating phosphine groups on either side. Furthermore, Rh P^OC^OP complexes have already proven to be effective hydrogenation and Kumade-Tamao-Corriu coupling catalysts. Incorporating known catalysts into polymers has also proven to be an effective method to produce catalytically active metallopolymers.[238-240]

Electropolymerizable 4,6-*bis*(2,2'-bithiophen-5-yl)resorcinol *bis*(diphenyl-phosphinite) (Scheme 22) and resorcinol(diphenylphosphinite) (Scheme 21) were synthesized to produce Rh(I,III) electropolymerizable monomer and model complexes, respectively. The model complexes, (P^OC^OP)Rh(H)(Cl) (**1**) and (P^OC^OP)Rh(CO) (**2**), were produced to gather spectral and electrochemical data on these types of systems. The (H)(Cl)Rh derivatives serve as stable Rh(III) intermediates to study the reactivity of the materials. Furthermore, Milstein *et al.* have utilized these types of Rh(III) pincer intermediates to produce carbonyl complexes. The carbonyl group serves as a good IR spectral handle. Electrochemical oxidation of the corresponding Rh-CO metallopolymer directly effects the Rh-CO bond distance. Utilzing electropolymerizable RHLs as backbones in catalytic systems opens avenues toward metallopolymer catalysts. The redox-active polymer backbone, in direct communication with the rhodium center, could then directly modulate electron density on the catalytic rhodium center and control catalytic activity. This chapter outlines the synthesis and electrochemical behavior of

electropolymerizable *bis*(bithienyl)di(phosphinato)resorcinol (P^OC^OP) ligands, **4**, and the resulting Rh(I,III) complexes, **5-7**. The Rh(III) monomers were synthesized as novel materials to probe the change in catalytic activity between Rh(I,III) monomers and metallopolymers.

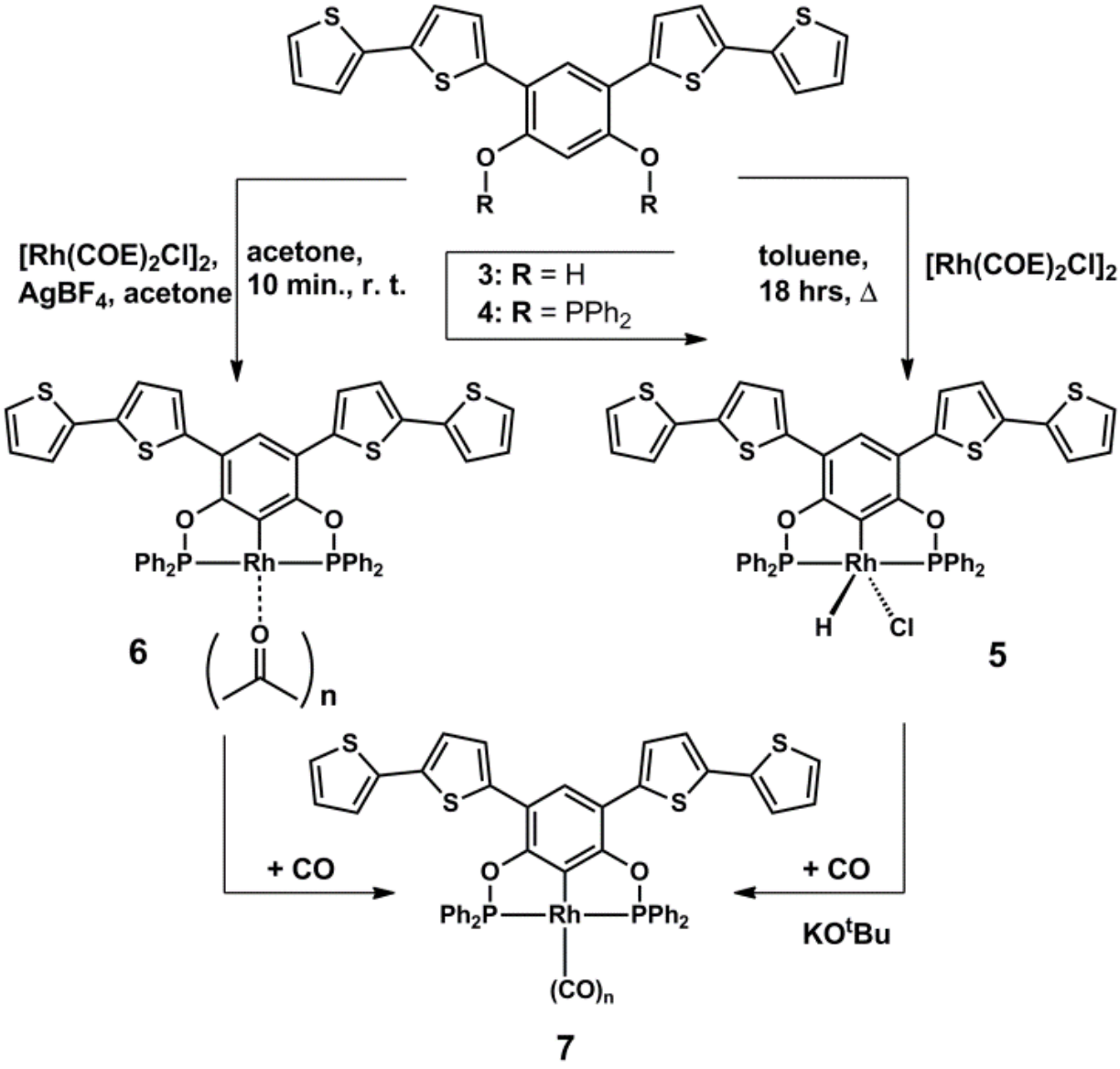

Scheme 22. Synthetic scheme for the electropolymerizable materials **3** - **7**.

EXPERIMENTAL

General Methods

Air- and moisture-sensitive reactions were carried out in heat gun dried glassware using standard Schlenk techniques under an inert nitrogen atmosphere. All solvents were dried using an Innovative Technology, Pure Solv solvent purifier with double purifying column. All other chemicals were used as received from commercial suppliers. NMR spectra were recorded with a Varian Unity +300 (^{1}H, 300 MHz, ^{13}C{^{1}H} 75 MHz) and were referenced to residual solvent peaks. Chemical ionization (CI) mass spectra were collected on a Micromass Autospec Ultima mass spectrometer. X-ray photoelectron spectroscopy (XPS) was carried out on a PHI 5700 XPS system equipped with a dual Mg X-ray source and monochromatic Al X-ray source complete with depth profile and angle-resolved capabilities. Infrared spectra were recorded using a Nicolet IR 200 FTIR spectrometer.

Electochemistry

Electrochemical syntheses and studies were performed in a dry-box under a nitrogen atmosphere using a GPES system from Eco. Chemie B. V.. All the electrochemical experiments were carried out in a three-electrode cell with a $Ag/AgNO_3$ reference electrode (silver wire dipped in a 0.01 M silver nitrate solution with 0.1 M [(*n*-$Bu)_4N][PF_6]$ ($TBAPF_6$) in CH_3CN), a Pt button working electrode, and a Pt wire coil counter electrode. Potentials were relative to this 0.01 M $Ag/AgNO_3$ reference electrode. Ferrocene was used as an external reference to calibrate the reference electrode before and after experiments were performed and that value was used to correct the measured

potentials. The supporting electrolyte was 0.1 M $TBAPF_6$ that was purified by recrystallization three times from hot ethanol before being dried for 3 days at 100 °C under active vacuum. Studies of complexes were performed at concentrations of 2×10^{-4} M.

Synthesis

Synthesis of the Ligands

1,5-Diacetoxy-2,4-*bis*(2,2'-bithiophen-5-yl)benzene[242,243], 5-tributylstannyl -2,2'-bithiophene[128], resorcinol(diphenylphosphinite)[233] were made according to literature procedure.

4,6-*Bis*(2,2'-bithiophen-5-yl)resorcinol (3). In a 200 mL Schlenk flask with a stir bar, 1,5-diacetoxy-2,4-*bis*(2,2'-bithiophen-5-yl)benzene (1.00 g, 1.91 mmol) was added under a nitrogen atmosphere. Dry THF (12 mL) was cannula transferred into the flask and the resulting yellow-orange solution was stirred for 10 minutes. $LiAlH_4$ (363 mg, 9.55 mmol) was added in small portions to the solution and stirred for two hours at room temperature. The resulting green solution was then heated at 60 ºC overnight. The yellow-green solution was quenched using dry ethanol (8 mL) and the solvent was then removed under vacuum at 40 ºC. The yellow green powder was then brought into a glovebox and dissolved in DCM (10 mL). The mixture was filtered through a celite-cotton plug and the filtrate was collected and the solvent removed under vacuum, yielding **1** (722 mg, 86.2 %) as a bright yellow powder. m.p. 184.6 ºC (decomp.) FTIR (solid): 3510 (s, O-H), ^{1}H NMR (CD_2Cl_2) δ: 9.49 (s, 2H), 7.87 (s, 1H), 7.54 (d, J = 4.0,

2H), 7.45 (dd, *J* = 4.2, 7.2, 2H), 7.27 (dd, *J* = 4.2, 7.6, 2H), 7.23 (d, *J* = 3.6, 2H), 7.06 (dd, *J* = 3.5, 5.1, 2H), 6.62 (s, 1H). $^{13}C\{^{1}H\}$ NMR ($CDCl_3$): product was too insoluble in deuterated solvents to acquire a spectra. HRMS (CI) m/z calculated for $C_{22}H_{14}O_2S_4$ 438.9900 $[M + H]^+$, found 438.944. Elemental analysis calculated (found): C, 53.21 (52.51); H, 2.44 (2.43).

4,6-*Bis*(2,2'-bithiophen-5-yl)resorcinol*bis*(diphenylphosphinite) (4). In a 100 mL Schlenk flask with a stir bar, **1** (200 mg, 0.45 mmol) and THF (15 mL) were added. After the solid dissolved, NaH (60% dispersion in oil, 38 mg, 0.95 mmol) was added in one portion and the solution was stirred for 10 minutes. To the resulting dark orange solution was added dropwise chlorodiphenylphosphine (200 mg, 0.91 mmol) dissolved in 10 mL THF. After the addition the solution slowly turned yellow, followed by the formation of a white solid. The suspension was refluxed overnight. After cooling, the solvent was removed under vacuum and the flask brought into a glovebox. The yellow-orange oily solid was dissolved in toluene and filtered through a celite-cotton plug. The toluene was removed under vacuum from the filtrate yielding crude yellow product. The solid was recrystallized using minimal DCM followed by slow addition of pentane. The resulting yellow powder was collected through filtration in an 84% yield (305 mg). m.p. 147.2 ºC (decomp.) ^{1}H NMR (CD_2Cl_2) δ: 7.87 (s, 1H), 7.84 (t, *J* = 1.5, 8H) 7.54 (d, *J* = 4.0, 2H), 7.52 (d, *J* = 3.6, 8H) 7.49-7.40 (m, 10H), 7.28 (dd, *J* = 1.2, 3.6, 2H), 7.23 (d, *J* = 3.6, 2H), 7.20 (s, 1H), 7.06 (dd, *J* = 3.6, *J* = 5.2, 2H). $^{13}C\{^{1}H\}$ NMR (CD_2Cl_2): 143.6, 135.7, 135.1, 134.2, 132.1, 131.7, 130.4, 130.0, 129.8, 129.5, 129.0, 128.9, 128.4, 124.4. $^{31}P\{^{1}H\}$ NMR (CD_2Cl_2): 111.1 HRMS (CI) m/z calculated for $C_{46}H_{32}P_2O_2S_4$ 806.0800

$[M + H]^+$, found 807.0944.

Synthesis of the Rh(I,III) Complexes

Synthesis of Model Complex (1). A 20 mL screw top pressure vessel with a stir bar was loaded with $[(COE)_2RhCl]_2$ (50 mg, 0.062 mmol) and resorcinol*bis*(diphenylphosphinite) (59.6 mg, 0.124 mmol) in toluene (2 mL) in a glovebox. The tube was sealed, brought out of the glovebox, and stirred at 150 ºC for 5 hours. The resulting dark red solution was filtered through a cotton pad in the glovebox and the solvent was concentrated to 0.5 mL and placed in a freezer at -30 ºC. The resulting red powder was gathered *via* filtration in a 78.3 % yield (48.6 mg). ^{1}H NMR (CD_2Cl_2) δ: 7.93 (t, J = 8.5, 1H), 7.87 (d, J = 4.0, 2H), 7.6-7.2 (m, 20H), 6.95 (s, 1H), -22.8 (d, J = 23.4, 1H). ^{13}C{^{1}H} NMR ($CDCl_3$): product was too insoluble in deuterated solvents to acquire a spectra. ^{31}P{^{1}H} NMR (CD_2Cl_2): 132.2 (d, J = 106.7) HRMS (CI) m/z calculated for $C_{30}H_{24}ClO_2P_2Rh$ 617.828 $[M + H]^+$, found 617.822.

Carbonylation of Complex 1 to form 2. In a Teflon-capped J. Young tube was added 50 mg of complex **3** in CD_2Cl_2 (1 mL). KO^{t}Bu (10 mg) was added and an atmosphere of CO gas was introduced to the tube. ^{1}H NMR (CD_2Cl_2) δ: 7.87 (d, J = 1.5, 2H), 7.84-7.26 (m, 21H) 6.85 (s, 1H). ^{13}C{^{1}H} NMR ($CDCl_3$): product was too insoluble in deuterated solvents to acquire a spectra. ^{31}P{^{1}H} NMR (CD_2Cl_2): 154.0 (dd, J = 122.5, J = 9.0).

Synthesis of Complex 5. A 20 mL screw top vial with a stir bar was loaded with $[(COE)_2RhCl]_2$ (23 mg, 0.031 mmol) and **2** (50 mg, 0.062 mmol) in toluene (2mL) in a glovebox for fifteen minutes. The dark suspension was then filtered and the solvent removed under vacuum. The crude product was recrystallized from methylene chloride and hexanes, yielding a red-brown solid (68.2%, 40 mg). ^{1}H NMR (CD_2Cl_2) δ: 8.01 (s, 1H), 7.84-7.26 (m, 27H) 6.85 (s, 1H). $^{13}C\{^1H\}$ NMR ($CDCl_3$): product was too insoluble in deuterated solvents to acquire a spectra. $^{31}P\{^1H\}$ NMR (CD_2Cl_2): 131.6 (d, J = 204.3) HRMS (CI) m/z calculated for $C_{48}H_{36}ClO_2P_2RhS_4$ 945.318 $[M + H]^+$, found 946.360

Carbonylation of Complex 5 to form 7. In a Teflon-capped J. Young tube was added 50 mg of complex **3** in CD_2Cl_2 (1 mL). KO^tBu (10 mg) was added and an atmosphere of CO gas was introduced to the tube. ^{1}H NMR (CD_2Cl_2) δ: 7.87 (d, J = 1.5, 2H), 7.84-7.26 (m, 21H) 6.85 (s, 1H). $^{13}C\{^1H\}$ NMR ($CDCl_3$): product was too insoluble in deuterated solvents to acquire a spectra. $^{31}P\{^1H\}$ NMR (CD_2Cl_2): 152.7 (dd, J = 155.0, J = 18.6).

$(BT_2P^OC^OP)Rh(acetone)_2$ carbonylation route. In a glovebox, to a suspension of $[(COE)_2RhCl]_2$ (0.14 mmol, 33 mg) in 10 mL acetone was added in one portion $AgBF_4$ (0.28 mmol, 17.6 mg). The color of the solution turned from orange to yellow, and the solution was stirred for 20 minutes at room temperature. The $[Rh(COE)_2(acetone)_2]BF_4$ was filtered through a cotton plug, and to the yellow solution was added dropwise a solution of **4** (0.28 mmol, 75 mg). The resulting dark red solution was filtered and the solvent removed under vacuum. A red-brown precipitate was gathered and dissolved in

minimal amounts of acetone and methylene chloride. Hexanes was added to the solution resulting in the precipitation of a red solid. The solution was filtered and washed with hexanes and no further purification was performed, yielding 80 mg of acetone precursor (73%). ^{1}H NMR (CD_2Cl_2) δ: 7.80 (s, 1H), 7.76 (t, *J* = 1.5, 8H) 7.54 (d, *J* = 4.0, 2H), 7.53 (d, *J* = 3.6, 8H) 7. 5-7.45 (m, 10H), 7.28 (dd, *J* = 1.2, *J* = 3.6, 2H), 7.23 (d, *J* = 3.6, 2H), 7.20 (s, 1H), 7.06 (dd, *J* = 3.6, *J* = 5.2, 2H), 6.67 (d, *J* = 22), 2.47 (m, 12H). ^{31}P{^{1}H} NMR (CD_2Cl_2): 133.1 The red solid was then dissolved in CD_2Cl_2 (1 mL) in Teflon-cap sealed J. Young tube. CO gas was introduced and the tube was kept under CO atmosphere for 30 min. at -10 ºC. The solution slowly turned lighter resulting in a light red solution. ^{1}H NMR (CD_2Cl_2) δ: 7.80 (s, 1H), 7.76 (t, *J* = 1.5, 8H) 7.54 (d, *J* = 4.0, 2H), 7.53 (d, *J* = 3.6, 8H) 7. 5-7.45 (m, 10H), 7.28 (dd, *J* = 1.2, *J* = 3.6, 2H), 7.23 (d, *J* = 3.6, 2H), 7.20(s, 1H), 7.06 (dd, *J* = 3.6, *J* = 5.2, 2H), 6.67 (d, *J* = 22), 2.47 (m, 12H).^{13}C{^{1}H} NMR ($CDCl_3$): product was too insoluble in deuterated solvents to acquire a spectra. ^{31}P{^{1}H} NMR (CD_2Cl_2): 152.2 (dd, *J* = 142.0, *J* = 18.6).

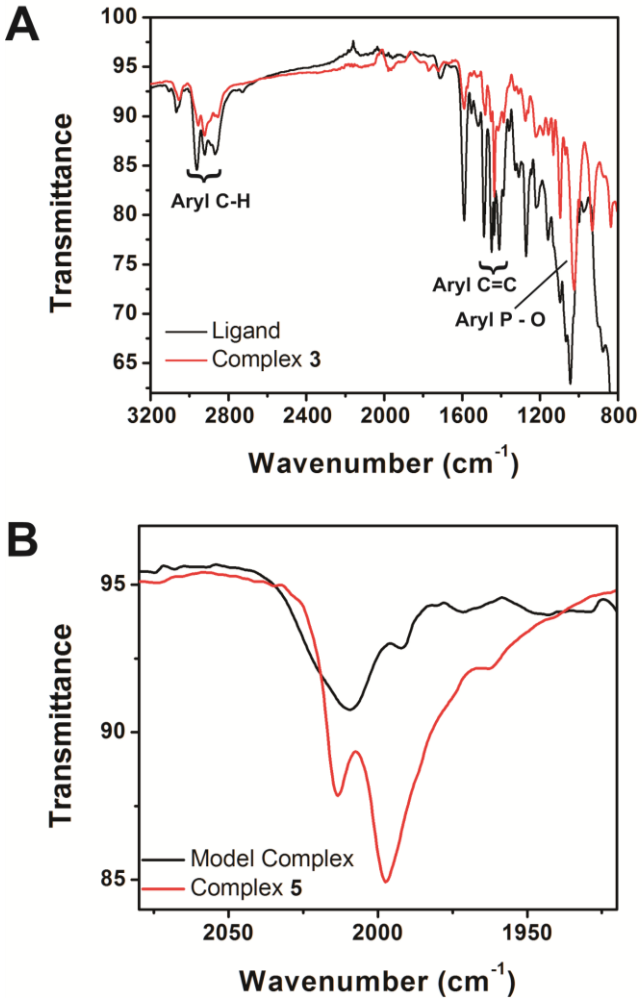

Figure. 64 (A)ATR-IR transmission spectra of ligand **3** and complex **4**. (B) Carbonyl IR bands present in complexes **3b** and **5**.

RESULTS AND DISCUSSION

Initial Pathways to Redox-Active Electropolymerizable Ligands

Initial attempts in producing redox-active electropolymerizable ligands focused on the synthesis of bithienyl appended PCP-type system. However, the later stages of the synthetic pathway utilized very unstable compounds that were insoluble. The synthetic problems lead to a focus on $P^{O}C^{O}P$ systems as the basis of the redox-active electropolymerizable ligands. Efforts to produce complexes **5** – **7** began by using an

alternate route (Scheme 23), and after difficulty with the metallation procedure the current synthetic procedure was adopted. The alternate route started with the phosphination of 4,6 – diiodoresorcinol. Isolation and purification of the 4,6 – *bis*(diphenylphosphinite)resorcinol was performed by filtering through an alumina plug and recrystallizing from a saturated toluene solution. A multiplet at δ = 111.77 ppm in the $^{31}P\{^{1}H\}$ NMR and supporting ^{1}H NMR confirmed that the product was synthesized. The 4,6–*bis*(diphenylphosphinite)resorcinol was a good intermediate for further modification. Several attempts to produce **4** directly from this precursor *via* a Stille coupling yielded a Pd(II) complex, as denoted by a singlet in $^{31}P\{^{1}H\}$ NMR at δ = 136.61 ppm and supporting ESI-MS mass spectrum. Following these results, a Rh(III) complex was produced directly from the pincer precursor as a alternative dihalide material to be used in a C-C cross coupling reaction. There are no current examples in the literature of a Rh $P^{O}C^{O}P$ complex with functionality in the 4 and 6 positions of the benzene core. Furthermore, the $^{31}P\{^{1}H\}$ NMR spectra showed a doublet at δ = 133.24 ppm (J = 157 Hz) corresponding to the spin-active product. Stille coupling reactions were peformed using the Rh(III) intermediate with tri(butyl)stannylbithiophene under a wide variety of reaction conditions and catalysts. The bithienyl appended product could not be produced using any reaction conditions that were attempted and only decomposition or products lacking the Rh-based coupling were isolated. The difficulty and complexity of this synthetic route, specifically due to the inability to produce an electropolymerizable redox-active rhodium monomer, resulted in exploration of alternative synthetic pathways.

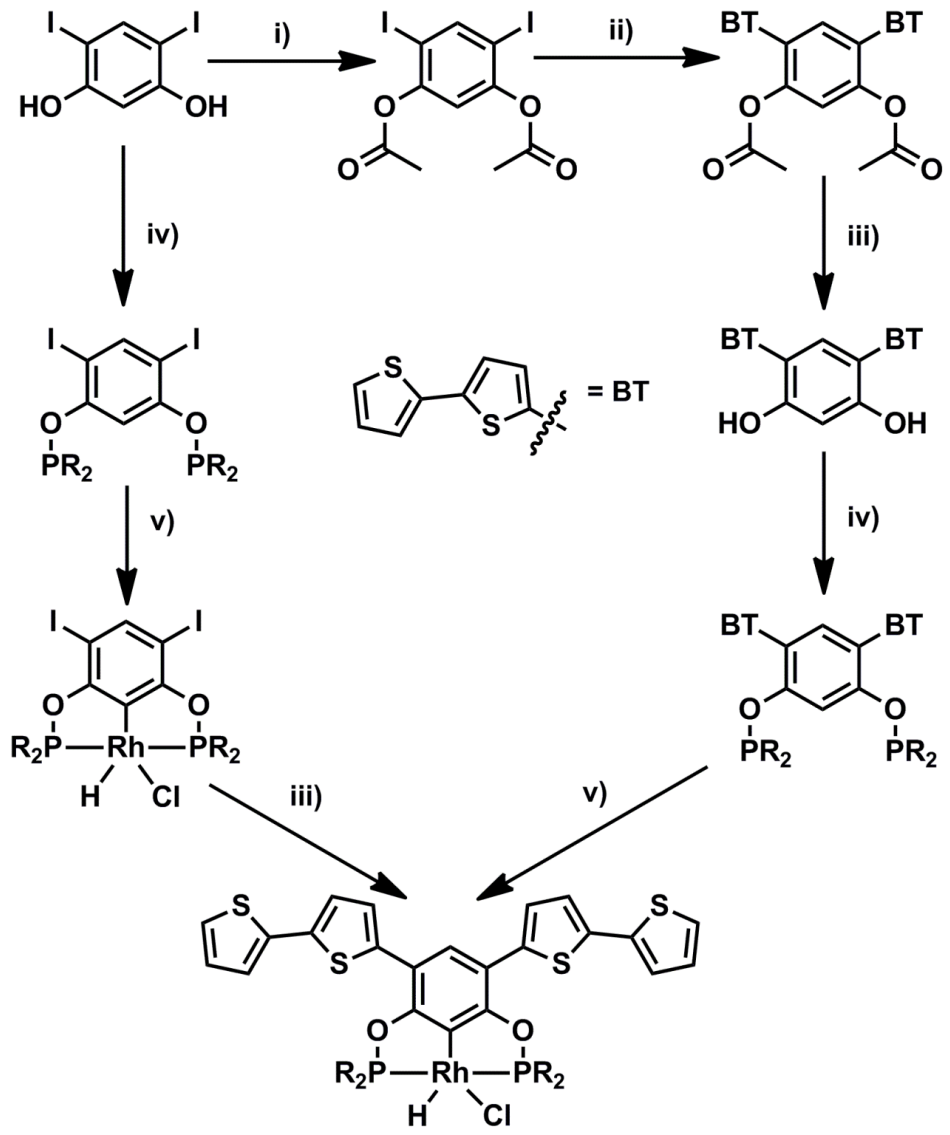

Scheme 23. The different synthetic pathways explored to produce complex **5**.

Producing an Electropolymerizable Redox-Active Ligand

Synthesis of the ligands began by producing diacetoxydiiodobenzene following literature procedure.[242,243] Tri(butyl)stannyl bithiophene was then Stille coupled with the di(acetoxy)diiodobenzene to render the desired protected precursor. The resorcinol precursor was produced by deprotection of the acyl group using $LiAlH_4$ in THF. The

4,6-di(2,2'-bithien-5-yl)resorcinol, **3**, was unstable in the presence of light and oxygen. The instability of these types of thienyl-appended systems is related to the *meta*-phenylene linkages promoting oxidation and dearomatization of the benzene core.[243] The bithienyl appended resorcinol was then reacted with NaH and chlorodiphenylphosphine to produce ligand **4** as a pale yellow solid. Formation of ligand **4** was observed by $^{31}P\{^{1}H\}$ NMR as a singlet resonance at δ 111.1 ppm. Other resorcinol(diphenylphosphinite) ligands bear similar resonance patterns, typically near 111 ppm for diphenylphosphine type POCOP ligands.[229,241,242] IR spectra of the ligand, as shown in Figure 64, showed bands from 2800-2920 cm^{-1} (aryl C-H stretch), multiple bands at 1480-1550 cm^{-1} (aryl C=C stretch), and sharp broad band at 1035 cm^{-1} assigned to an aryl P-O stretch.

Rh(I,III) Metallation Routes

$[Rh(COE)_2Cl]_2$ was used to produce the metal complex, model-**1**, using resorcinol (diphenylphosphinite) in a pressure vessel at 150 ºC. The method was adapted from procedures performed by Milstein *et al.* to produce the analogous $(H)(Cl)Rh(^{i}Pr_2POCOP^{i}Pr_2)$ complex in 90% purity.[228] ^{1}H NMR spectroscopy indicated highly pure isolation (~98%) of **1** as a dark red solid. Attempts to synthesize complex **7** began using the same conditions applied in the synthesis of model-**2**. The pressure vessel reaction produced a product in modest yields (30-40%). Unfortunately, purification was difficult from the crude mixture. Another synthetic route was utilized instead, by simply mixing ligand **4** with $[Rh(COE)_2Cl]_2$ for 10 minutes. The resulting pale orange complex was characterized by $^{31}P\{^{1}H\}$, $^{13}C\{^{1}H\}$, ^{1}H NMR with a

characteristic doublet (δ 131.6 (J_{Rh-P} = 204.3 Hz)) observed in the $^{31}P\{^{1}H\}$ NMR. The coupling constant in the model and Rh(III) monomers correspond to known trigonal bipyramid $(POPh)_3Rh(H)(CO)$ complexes.[245] The Rh(CO) complex **7** was synthesized initially by abstracting the chloride using potassium *tert*-butoxide. This approach yielded the desired carbonyl complex, but purification methods resulted in **7** (91% purity by ^{1}H NMR). An alternate route utilizing $[Rh(acetone)_2(COE)_2]BF_4$ with the $BT_2P^OC^OP$ ligand produced the intermediate complex shown in Scheme 22.

Electropolymerization of the Rh(III) Monomer

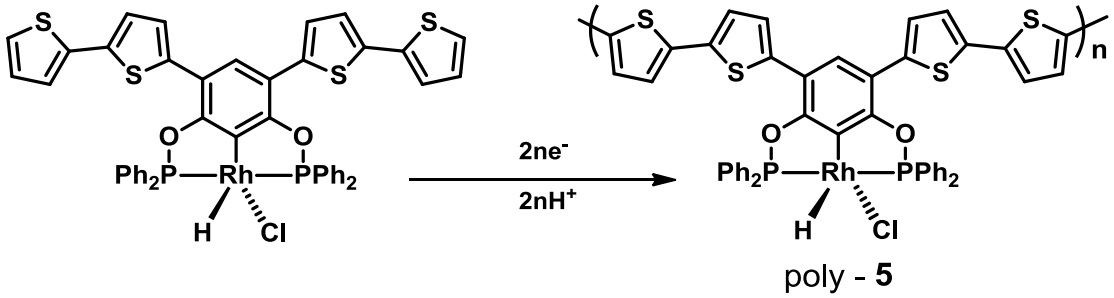

Scheme 24. Electrochemical polymerization of **5** to poly-5.

The Rh(III) monomer, **5**, was then electropolymerized (Scheme 24) in 0.1 M $TBAPF_6$/DCM under oxidative conditions from -0.5 V to 1.5 V (Fc/Fc^+). The linearity of the polymer growth scans suggests the polymers films are highly conductive and potential can pass easily through the entire film. Further evidence of high conductivity is the linear relationship of current to scan rate as shown in Figure 66. The scan rate dependence denotes the formation of a material that facilitates charge transfer even at high scan rates. Polymers were grown onto stainless steel, and XPS spectroscopy was

performed to probe the composition. Compositional analysis indicated that the ratio of Rh: P: S was 1: 1.77: 3.55, in good agreement with the theoretical composition of 1:2:4.

Spectroelectrochemistry of poly-5

Electrochemically "doping" the polymer backbone results in the formation of polaron and bipolaron states, which each have characteristic peaks in the UV-Vis-NIR absorption spectrum. In Figure 65, polaron and bipolaron formation was observed in poly-**5** by monitoring the absorption under increasing oxidative potential. The formation of the radical cations supports that electrons move freely through the material. The Wolf-Type II metallopolymer consists of redox-active backbone in direct communication with the rhodium center. Oxidation of poly-**5** results in modulation of the electron density of the rhodium metal center, lengthening the bonds of the bound hydride and chloride ancillary ligands.

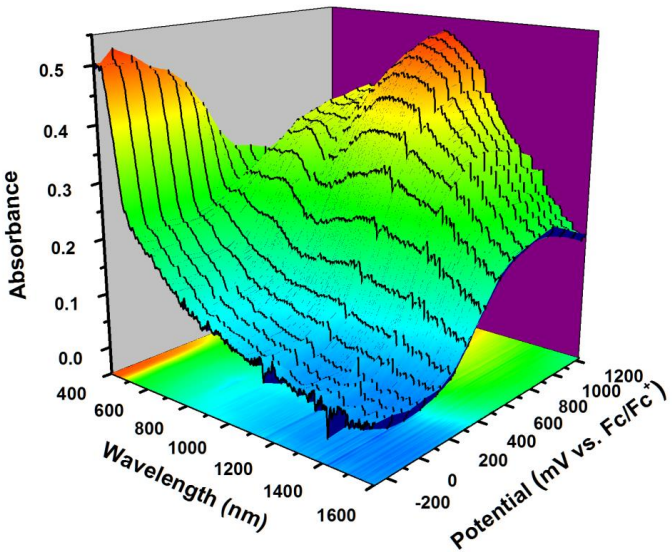

Figure 65. UV-vis-NIR spectroelectrochemistry spectra of poly - **5**. Bipolaron formation was observed as a broad peak at ~1250 nm.

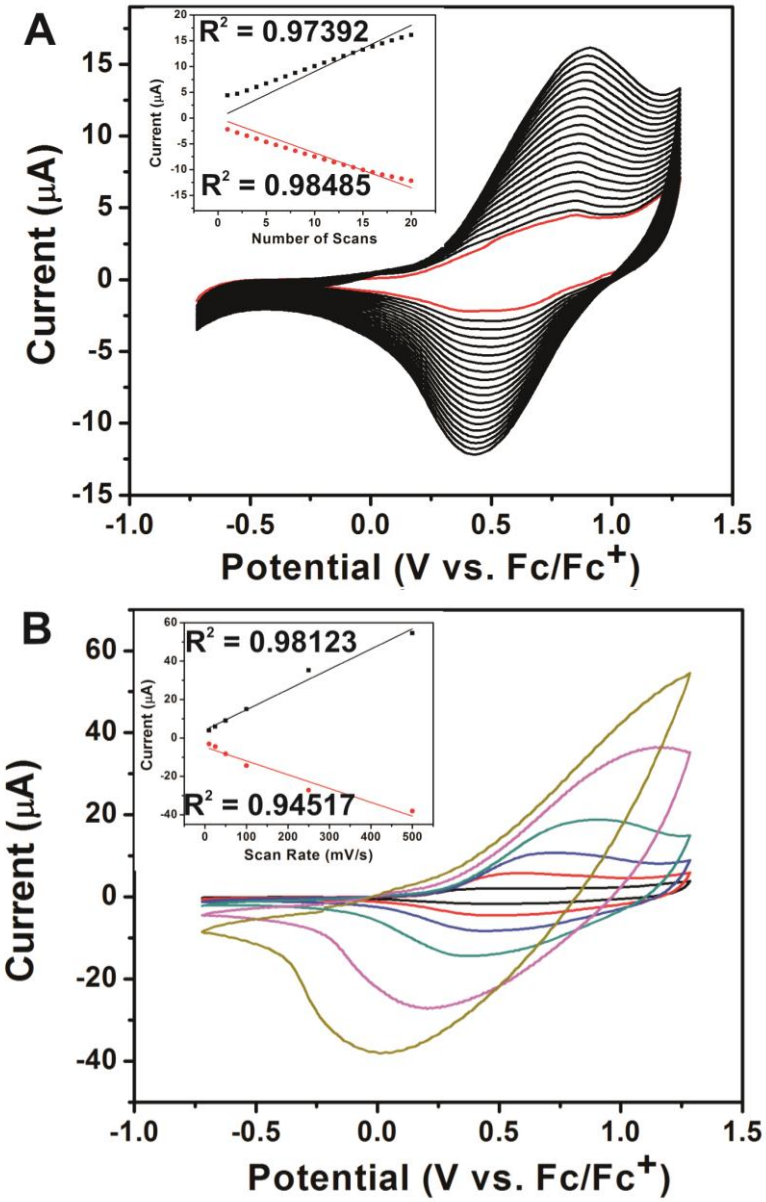

Figure 66. (A) Electropolymerization of **5** from 20 cycles of film growth under oxidative current (top). The film growth dependence showing linear growth of the polymer over the growth cycles (top inset). (B) Cyclic voltammagrams at scan rates of 10-500 mV/s in monomer free solution (bottom). Scan rate vs. current for oxidative (black trace) and reductive (red trace) scans(bottom inset).

Catalysis of the Monomers and Metallopolymers

Catalysis using 1 and 5

Rh-CO absorption bands were observed from transmission IR spectra of the model Rh(CO) complex (ν = 2008 cm^{-1}) and complex 7 (ν = 1998, 2015 cm^{-1}). Poly-**7** IR spectra were gathered on ITO substrates using IR reflectance spectroscopy. After studying the neutral metallopolymers, the film was doped under an oxidative potential in electrochemical conditions. The C-O stretch shifted significantly in the doped state to a broad, ill-defined peak at ν = 1983 cm^{-1}. Obtaining more resolved data for the polymer materials proved to be very difficult, with poor resolution in the CO IR bands.

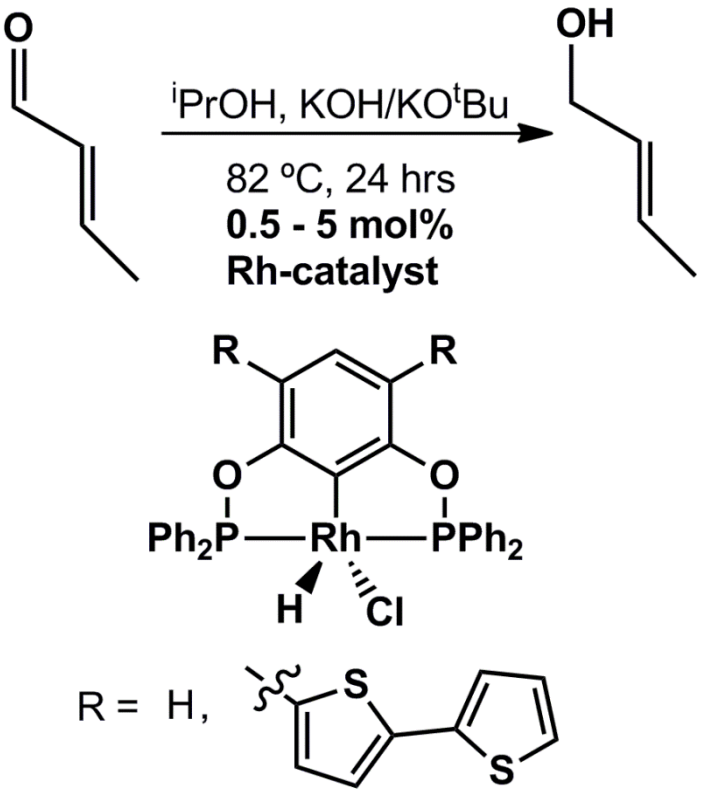

Scheme 25. Selective hydrogenation of crotonaldehyde to crotyl alcohol by complexes **1** and **5**.

Rh(I,III) pincer catalysts have been utilized for hydrosilylations, hydrogen-transfer hydrogenations, enantioselective allylations, alkane dehydrogenations, and other catalytic reactions.[246-250] The extent of catalytic studies with Rh-P^{O}C^{O}P systems has dealt with producing Kumada coupling intermediate complexes and alkane dehydrogenations/hydrogenations. Complexes **1** and **5** were used initially as catalysts in the hydrogenation of *cis*-cyclooctene and 1-octene. The reaction conditions ranged from 25 – 40 ºC under 1 bar H_2 atmosphere with KO^{t}Bu as a catalytic activator. Reactions were monitored by tracking the olefin peaks using ^{1}H and ^{13}C {^{1}H} NMR spectroscopy. For both substrates the olefin hydrogen resonance at δ 5.23 and δ 4.67 ppm showed only nominal decreases in the olefin resonance peaks. Following the poor activity toward cyclic and acylic alkenes, selective hydrogenation of α,β-unsaturated aldehydes was attempted. Initial catalytic studies studied the conversion of cyclohexanone to the cyclohexanol. Catalyst **3** (0.5 mol%) at 82 ºC showed near complete conversion (91%) as evident in NMR spectra. The conversion was tracked by ^{1}H and ^{13}C {^{1}H} NMR, with disappearance of the keto-carbon at δ 212.4 ppm and appearance of hydroxyl peak in cyclohexanol at δ 3.66 ppm. Similar results were observed for the 2,2'-bithienyl appended complex **5**, with conversion at 90%. Following successful conversion to cyclohexanol, the conversion of butanal to butanol was studied. Similar percent conversion was observed. Finally, selectivity was studied through catalytic hydrogenation studies of the α,β-unsaturated crotonaldehyde, *via* a scheme shown in Scheme 25. Both catalysts showed high selectivity for hydrogenation of the aldehyde oxygen. The large steric bulk around the catalysts, **1** and **5**, allows coordination of the

oxygen in the aldehdye but not the olefin group. Table 17 summarizes the conversion and selectivity of the catalysis experiments.

Table 17. Summary of catalytic data for different hydrogenation reactions using complexes **1** and **5**.

Substrate[a,b]	Complex **1**		Complex **5**	
	Conversion[c]	Yield[d]	Conversion[c]	Yield[d]
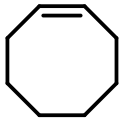	< 1	-	< 1	-
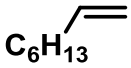	< 1	-	< 1	-
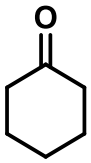	91	71	90	80
	94	74	99	70
	91(99)	88	99(99)	90

[a] *Cis*-cyclooctene and 1-octene hydrogenation reactions were performed at 1 bar H_2, 25 ^oC, 5 mol% catalyst loading.
[b] Cyclohexanone, butanal, and crotonaldehyde reactions were performed at 0.5 mol% catalyst loading.
[c] Found based on integration of ^1H NMR peaks
[d] Isolated yield.

Catalysis using poly-5

Special consideration was taken to create an accurate comparison between monomer and metallopomyer catalytic experiments. Typical electropolymerization experiments deposit polymer as thin films with film thicknesses between 100 - 300 nm. This leads to microgram amounts of polymer gathered on a stainless steel and ITO substrate. The mass of metallopolymer deposited is directly related to the Q_+, the charge deposited in the oxidative half wave for the polymer film.[240] Deposition across a 2.5 cm^2 area would produce similar amounts of catalytic metallopolymer. Hydrogen-transfer hydrogenation transformations with poly-**5** on stainless steel were performed using the same conditions for the molecular experiments. Cyclohexanone was used as the substrate due to the ease of tracking the transformation by monitoring ^1H and $^{13}C\{^1H\}$ NMR resonances. Along with the Rh(III) metallopolymer experiments, a control experiment was conducted using pure stainless steel electrode in analogous conditions. Approximately 22% conversion of cyclohexanone to cyclohexanol was measured after 24 hours at 82 ºC. Extending the time to 48 hours resulted in 49% conversion. Near complete conversion of 94% was observed after four days, and conversion rates were slower relative to the molecular catalysts achieving complete conversion after 24 hours. After investigating the catalytic activity of the neutral poly-**5**, electrochemically doped metallopolymers films were studied to investigate the change in catalytic activity. The metallopolymer system may greatly accelerate the activation of the catalyst due to facilitated ancillary ligand dissociation. Also the degeneration of electron density in the system may greatly decrease the conversion rate, as depicted in Scheme 26.

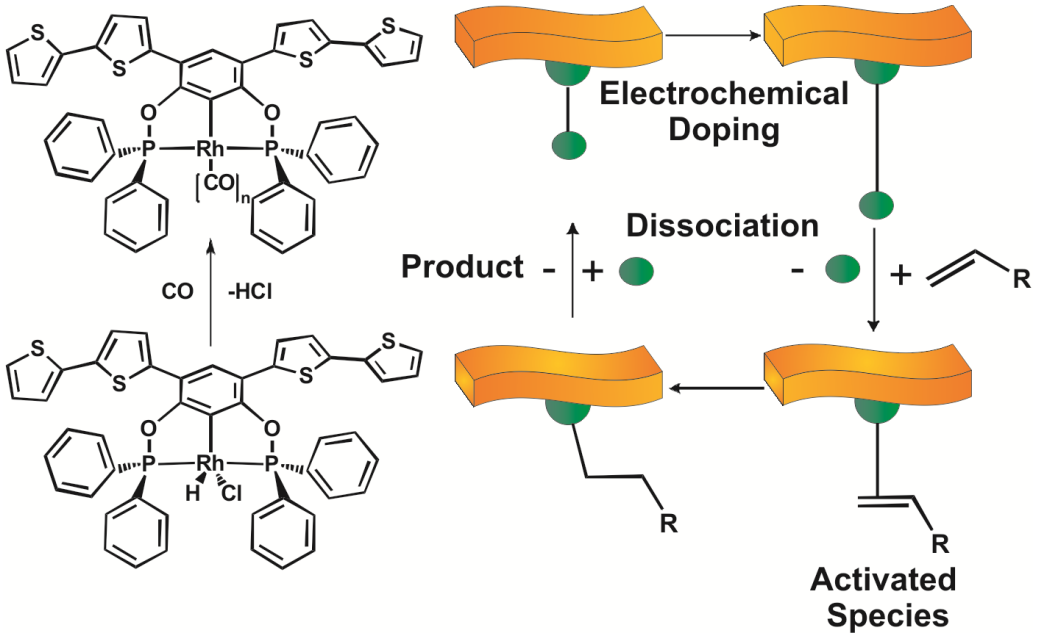

Scheme 26. Graphical representation of the facilitated activation in the Rh(III) metallopolymer catalysts.

Electrochemical oxidation of the redox-active metallopolymer backbone results in different accessible oxidation states, as indicated by the polaron and bipolaron formation in the spectroelectrochemical spectra. The change in the backbone would then lead to a modulation of the electron density on the Rh(III) center, as studied in the IR spectra of the poly-**7**. To study the effect of this attenuation on catalytic performance the conversion rates of the oxidized and doped metallopolymer, poly-**5**, was investigated. Two identical catalytic hydrogenation experiments using cyclohexanone were performed using the same conditions in a glovebox at room temperature. For one of the films an electrochemical potential was applied at +1.00 V, where strong bipolaron formation was observed in these films. Aliquots of the reactions were taken every hour for ten hours. ^{1}H NMR spectra of the aliquots indicated that the conversion rates were different for the doped and neutral metallopolymer films. Figure 67 shows the conversion for the metallopolymer, with the conversion rate for the doped film 56.7% less than the neutral poly-**5**. The percent conversion of the neutral film possessed similar conversion rates

(1.28 h^{-1}) when compared to conversation rates measured for the hydrogenation of cyclohexanone over 86 hours (1.16 h^{-1}). The conversion rate measured for poly-**5** under the 1.00 V potential was 0.51 h^{-1}. The significant decrease in the conversion rate can be explained by the electron withdrawing nature of the oxidized 2,2-bithienyl groups in the metallopolymer. The resulting change in the electron density may inhibit the initial oxidative addition step in the hydrogen transfer reaction.[251,252] In other work, electron withdrawing fluorine groups on a (PNP) $Rh(III)(H)_2$ complex decreased the percent conversion in ^{n}Pr-appended alkyne dimerization transformations.[253]

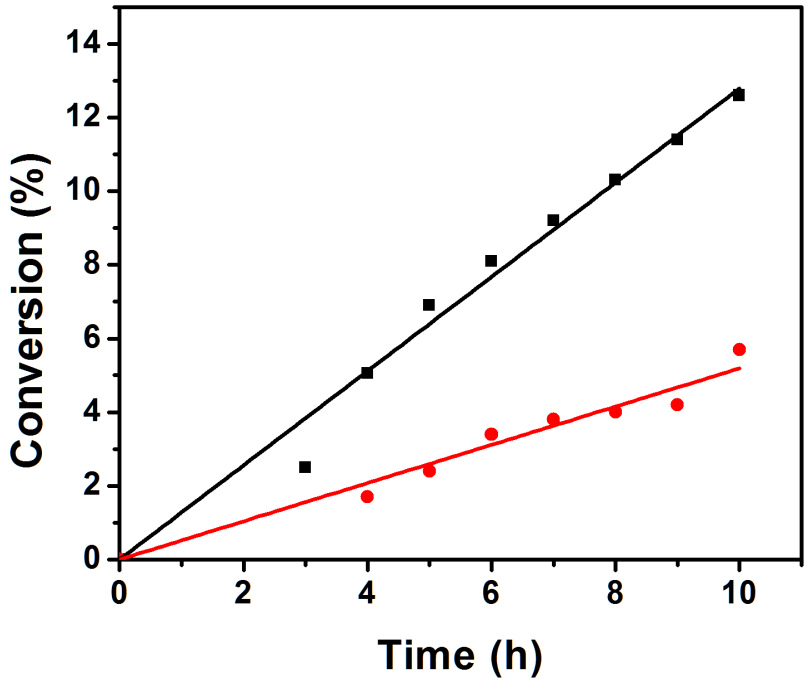

Figure 67. A comparison of the conversion rate of hydrogenation of cyclohexanone to cyclohexanol by the electrochemically oxidized poly-5 (red) and neutral poly-**5** (black).

Other Potential Catalytic Metallopolymers

The $BT_2P^OC^OP$ ligand system, while leading to an effective Rh(III) metallopolymer catalyst for hydrogen-transfer hydrogenation of aldehydes and ketones, is

unstable and difficult to produce. There are several other systems that may lead to effective metallpolymer catalysts, utilizing less sensitive and laborious synthetic routes. Prior work from the group focused on the synthesis of first an electropolymerizable $[NCN]^-$ system, leading into a well studied Pt(II)[NCN] metallopolymer system.[227] The same $[NCN]^-$ system could also be applied to a Rh(III) systems *via* the complexation route shown in Scheme 27. These type of Rh[NCN] complexes act effectively as hydrogen transfer hydrogenation and asymmetric aldol catalysts.[254]

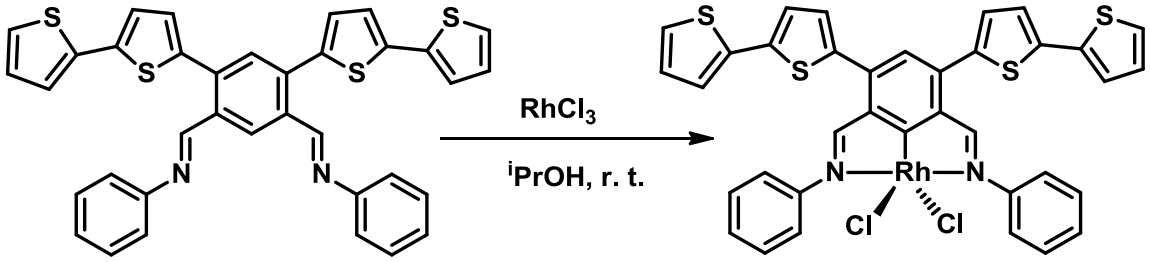

Scheme 27. The synthetic scheme for a electropolymerizable Rh[NCN] complex.

Apart from the pincer-type catalysts, other potential metallopolymer catalysts were produced using diimine-type ligands utilized originally as antennas for Ln(III) emission. Several electropolymerizable diamine precursors have been produced as highly accessible intermediates for further modification. Shown below in Scheme 28 are two diamine precursors in particular that can be used to access a family of potentially useful electropolymerizable non-innocent redox-active ligands to enhance transition metal catalysis. Condensation of these materials with an aryl diketone occurs readily, and a large number of diimine ligands can be produced quickly.

Several different terthienyl and *bis*(2-ethylenedioxythien-5-yl)benzene-based diiimines were produced using EDOT and terthienyl diamine precursors. Scheme 28 outlines the synthetic pathway used to create several new highly conjugated and electropolymerizable diimine ligands. It was observed with the Ln(III) complexes, that

thienyl-appended phenazine and quinoxaline-based systems can be easily polymerized. A family of easily electropolymerized catalysts could be produced from these diimine complexes. **L1**-**L4** were synthesized to study the resulting Pd(II) complexes, Pd-**L1-4**, as shown in Scheme 29. The Pd(II) complexes could be utilized as catalysts in a wide variety of reactions, such as C-C cross coupling reactions and oxidation reactions. Pd(II) metallopolymers (poly-**Pd1-4**) were produced, as well, to study the catalytic activity of the metallopolymers.

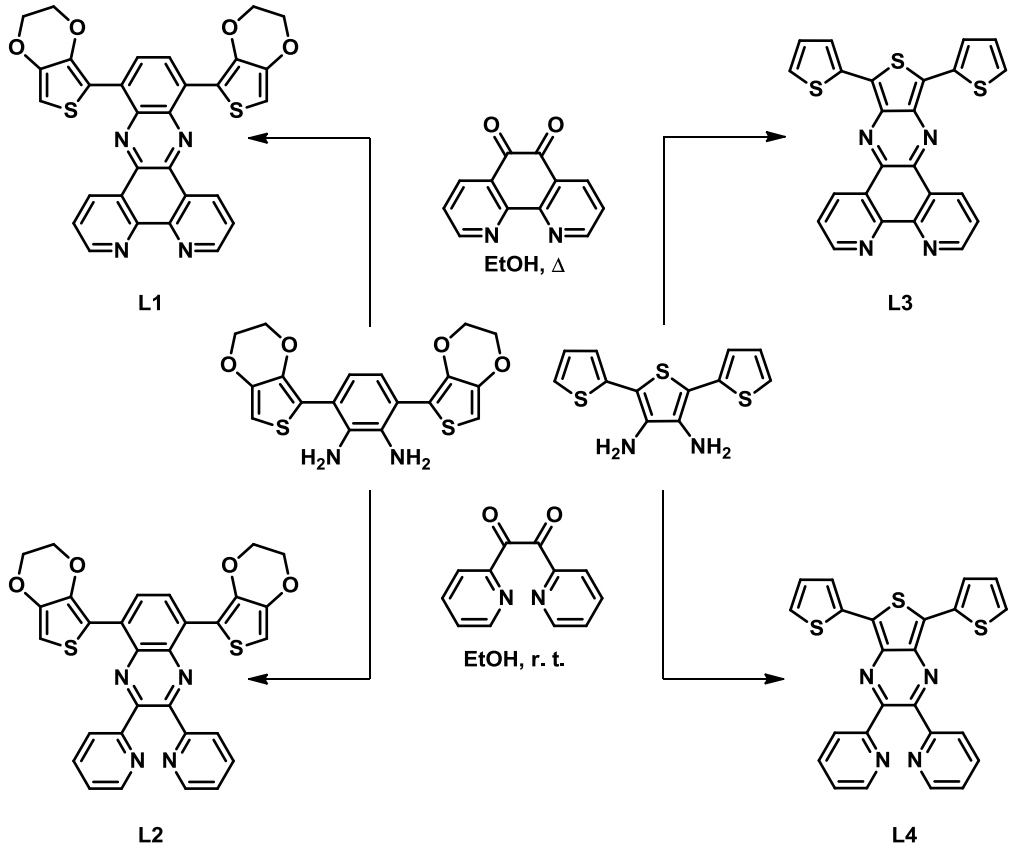

Scheme 28. Synthetic scheme for electropolymerizable ligands **L1-4**.

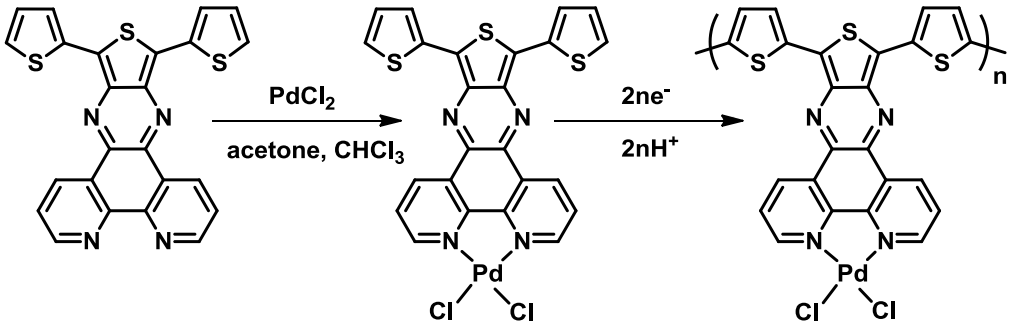

Scheme 29. The synthetic scheme to produce Pd-**L1-4** and poly-Pd-**L1-4**.

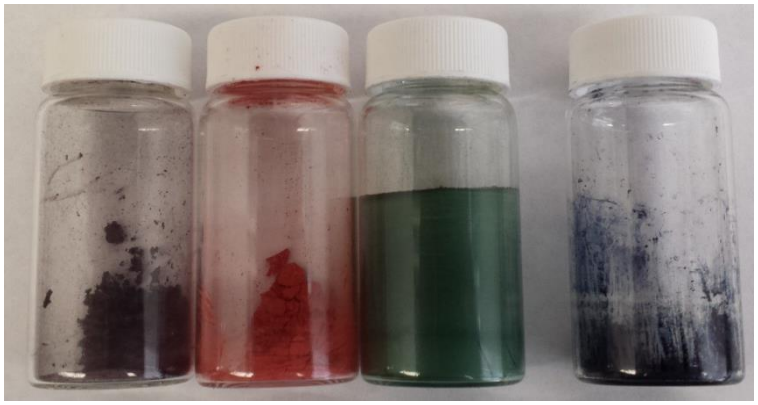

Figure 68. The compounds **L1**-**L4** (from left to right)**.**

The ligands were synthesized from the diamine precursors, with ^{1}H NMR and mass spectroscopy supporting ligand formation. The photophysical properties of the new ligands, **L3** and **L4**, indicated similar ILCT behavior to the previously studied **L1** and **L2**, as shown in Figure 69. Absorption spectra for **L3** showed a π-π* band at 355 nm and ILCT band at 660 nm. The above picture in Figure 68 shows each compound and the visible lustrous color produced by the charge transfer absorption. In the case of **L4**, a π-π* band at 345 nm and ILCT band at 570 nm. Strong emission bands were observed in **L3** and **L4** at 500 nm and 735 nm, respectively.

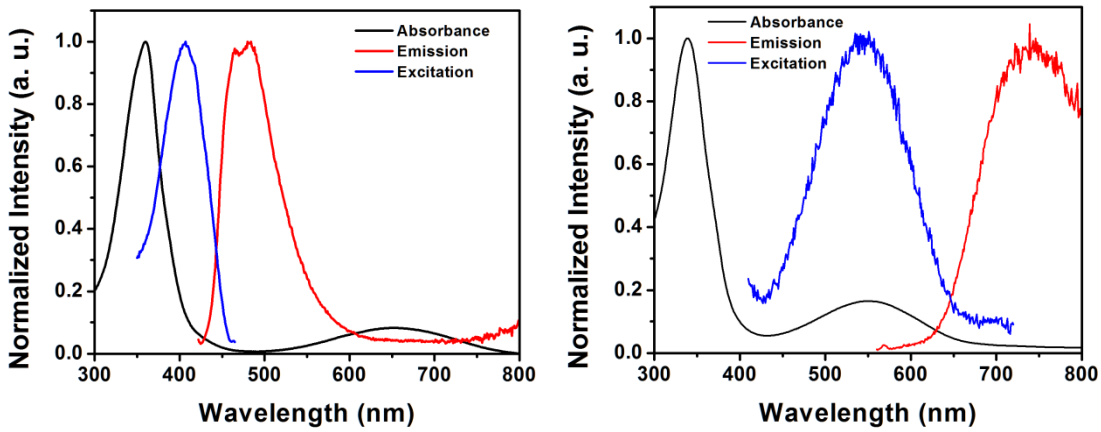

Figure 69. The photophysics for TerThdppz **L3** (right) and Terthdpq **L4** (left).

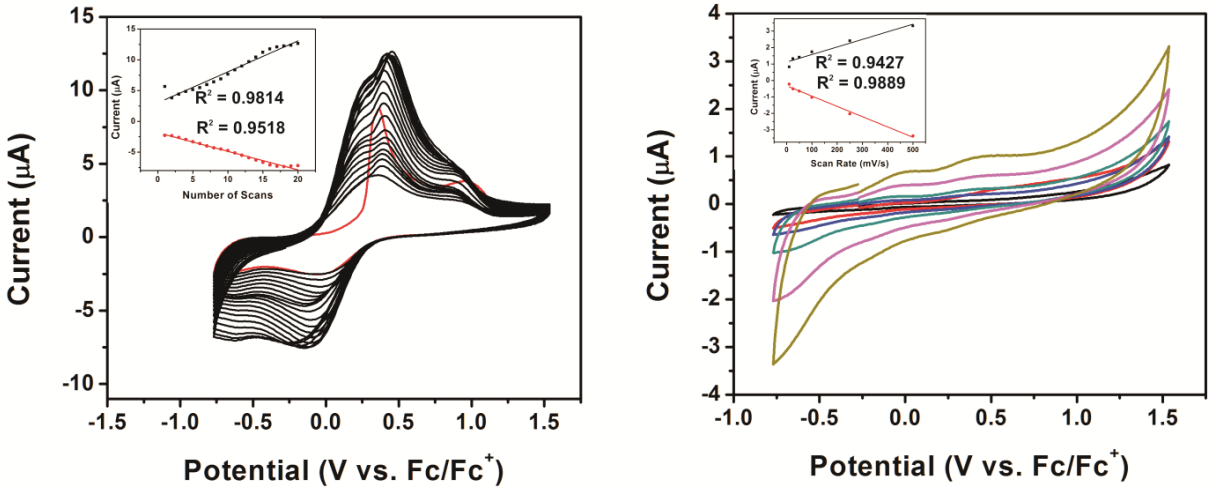

Figure 70. The polymerization and scan rate dependence studies of poly-Pd**L2.**

The Pd(II) monomers were electropolymerized by oxidative scanning from -0.5V to +1.5V. Pd-**L2** was electropolymerized, as shown in Figure 70, onto a Pt button electrode to study the film growth. The number of scan dependence was linear indicating that the polymer was conductive, and charges diffused through each layer of polymer easily allowing for further deposition. Also, scan rate dependence studies indicated that the films were conductive and charges moved freely through the material at any scan rate.

The monomers and metallopolymers were synthesized, and future work will focus on the catalytic performance of these materials in cross coupling reactions.

CONCLUSIONS

P^OC^OP-type ligands, due to the strong sigma donation of the benzene core and the easily modualted sterics and electronics on the phosphine groups, are attractive motifs for homogeneous catalysis. Incorporating 2,2'-bithienyl groups into these ligand systems resulted in an electropolymerizable redox-active ligand. The resulting model complexes and Rh(III) monomer were produced to study the electrochemical attenuation. IR reflectance spectroscopy indicated that electrochemical doping of the redox active ligand resulted in a change in the electron density of a Rh(CO) metallopolymer as observed by attenuation in carbonyl stretching frequency. A Rh(III)(H)(Cl) metallopolymer was produced to investigate the effect of ligand attenuation on catalytic performance. Initial catalytic studies with the monomers and model complexes demonstrated the effectiveness of these materials as selective hydrogenation catalysts. Electrocatalytic experiments indicated that doping the polymer backbone decreased the catalytic activity of the system relative to the neutral metallopolymer films.

Crystal Tables

Table S1. Crystal data and structure refinement for **5.**

Identification code	shelxl	
Empirical formula	C34 H22 N4 O4 S6	
Formula weight	742.92	
Temperature	293(2) K	
Wavelength	0.71075 Å	
Crystal system	Monoclinic	
Space group	P21/c	
Unit cell dimensions	a = 12.172(6) Å	α= 90°.
	b = 9.871(5) Å	β= 90.708(5)°.
	c = 27.492(13) Å	γ = 90°.
Volume	3303(3) $Å^3$	
Z	4	
Density (calculated)	1.494 Mg/m^3	
Absorption coefficient	0.461 mm^{-1}	
F(000)	1528	
Crystal size	0.339 x 0.068 x 0.030 mm^3	
Theta range for data collection	2.19 to 25.00°.	
Index ranges	-14<=h<=14, -11<=k<=11, -32<=l<=32	
Reflections collected	28352	
Independent reflections	5819 [R(int) = 0.1044]	
Completeness to theta = 25.00°	100.0 %	
Refinement method	Full-matrix least-squares on F^2	
Data / restraints / parameters	5819 / 0 / 448	
Goodness-of-fit on F^2	1.032	
Final R indices [I>2sigma(I)]	R1 = 0.0626, wR2 = 0.1145	
R indices (all data)	R1 = 0.1064, wR2 = 0.1381	
Largest diff. peak and hole	0.633 and -0.471 e.$Å^{-3}$	

Table S2. Crystal data and structure refinement for **7b**.

Identification code	shelxl	
Empirical formula	C24 H17 N3 O8 S3	
Formula weight	571.59	
Temperature	293(2) K	
Wavelength	0.71075 Å	
Crystal system	Triclinic	
Space group	P-1	
Unit cell dimensions	a = 8.778(2) Å	α= 101.619(7)°.
	b = 9.704(2) Å	β= 98.420(7)°.
	c = 16.708(4) Å	γ = 101.860(7)°.
Volume	1338.0(6) $Å^3$	
Z	2	
Density (calculated)	1.419 Mg/m^3	
Absorption coefficient	0.329 mm^{-1}	
F(000)	588	
Crystal size	0.9490 x 0.1160 x 0.0420 mm^3	
Theta range for data collection	3.10 to 27.48°.	
Index ranges	-11<=h<=11, -12<=k<=12, -21<=l<=21	
Reflections collected	14220	
Independent reflections	6105 [R(int) = 0.0437]	
Completeness to theta = 27.48°	99.4 %	
Absorption correction	Semi-empirical from equivalents	
Max. and min. transmission	1.0000 and 0.8200	
Refinement method	Full-matrix least-squares on F^2	
Data / restraints / parameters	6105 / 0 / 351	
Goodness-of-fit on F^2	1.051	
Final R indices [I>2sigma(I)]	R1 = 0.0569, wR2 = 0.1587	
R indices (all data)	R1 = 0.0746, wR2 = 0.1687	
Largest diff. peak and hole	0.960 and -0.370 $e.Å^{-3}$	

Table S3. Crystal data and structure refinement for **8b**.

Identification code	shelxl	
Empirical formula	C26 H19 N3 O7 S3	
Formula weight	581.62	
Temperature	293(2) K	
Wavelength	0.71075 Å	
Crystal system	Triclinic	
Space group	P-1	
Unit cell dimensions	a = 7.964(4) Å	α= 70.564(13)°.
	b = 13.412(8) Å	β= 81.69(2)°.
	c = 14.959(8) Å	γ = 88.63(3)°.
Volume	1490.5(14) $Å^3$	
Z	2	
Density (calculated)	1.296 Mg/m^3	
Absorption coefficient	0.294 mm^{-1}	
F(000)	600	
Crystal size	0.184 x 0.110 x 0.046 mm^3	
Theta range for data collection	1.46 to 25.00°.	
Index ranges	-9<=h<=9, -15<=k<=15, -17<=l<=17	
Reflections collected	25822	
Independent reflections	5159 [R(int) = 0.0624]	
Completeness to theta = 25.00°	98.2 %	
Refinement method	Full-matrix least-squares on F^2	
Data / restraints / parameters	5159 / 0 / 360	
Goodness-of-fit on F^2	1.086	
Final R indices [I>2sigma(I)]	R1 = 0.0610, wR2 = 0.1363	
R indices (all data)	R1 = 0.0785, wR2 = 0.1437	
Largest diff. peak and hole	0.346 and -0.350 e.$Å^{-3}$	

Table S4. Crystal data and structure refinement for **4b**.

Identification code	shelxl	
Empirical formula	C18 H14 N2 O6 S2	
Formula weight	418.43	
Temperature	293(2) K	
Wavelength	0.71075 Å	
Crystal system	Monoclinic	
Space group	P21/c	
Unit cell dimensions	a = 7.510(2) Å	α= 90°.
	b = 18.998(6) Å	β= 120.147(13)°.
	c = 13.878(4) Å	γ = 90°.
Volume	1712.2(9) $Å^3$	
Z	4	
Density (calculated)	1.623 Mg/m^3	
Absorption coefficient	0.354 mm^{-1}	
F(000)	864	
Crystal size	0.152 x 0.109 x 0.100 mm^3	
Theta range for data collection	2.92 to 25.00°.	
Index ranges	-8<=h<=8, -22<=k<=22, -15<=l<=16	
Reflections collected	12861	
Independent reflections	3008 [R(int) = 0.1525]	
Completeness to theta = 25.00°	99.8 %	
Refinement method	Full-matrix least-squares on F^2	
Data / restraints / parameters	3008 / 0 / 261	
Goodness-of-fit on F^2	1.080	
Final R indices [I>2sigma(I)]	R1 = 0.0857, wR2 = 0.1719	
R indices (all data)	R1 = 0.1410, wR2 = 0.2128	
Largest diff. peak and hole	0.469 and -0.672 $e.Å^{-3}$	

References

1. Shirakawa, H.; Louis, E. J.; MacDiarmid, A. G.; Chiang, C. K.; Heeger, A. J. *J. Chem. Soc., Chem. Commun.* **1977**, 579.

2. Chiang, C. K.; Druy, M. A.; Gau, S. C.; Heeger, A. J.; Louis, E. J.; MacDiarmid, A. G.; Park, Y. W.; Shirakawa, H. *J. Am. Chem. Soc.* **1978**, *100*, 1013.

3. Chiang, C. K.; Fischer, C. R.; Park, Y. W.; Heeger, A. J.; Shirakawa, H.; Louis, E. J.; Gau, S. C.; MacDiarmid, A. G. *Phys. Rev. Lett.* **1977**, *39*, 1098.

4. Turbiez, M.; Herguéz, N.; Leriche, P.; Frére, P. *Tetrahedron Lett.* **2009**, *30*, 7148.

5. Okamoto, K.; Housekeeper, J. B.; Michael, F. E.; Luscombe, C. K. *Polym. Chem.* **2013**, *4*, 3489.

6. González-Cano, R. C.; Saini, G.; Jacob, J.; Navarette, J. T.; Casado, J.; Delgado, M. C. *Chem. Eur. J.* **2013**, *19*, 17165.

7. Moorlag, C.; Sih, B. C.; Stott, T. L.; Wolf, M. O. *J. Mater. Chem.* **2005**, *15*, 2433.

8. Perepichka, I. F.; Perepichka, D. F.; Meng, H.; Wudl, F. *Adv. Mater.* **2005**, *17*, 2281.

9. Matsushima, T.; Matsuo, H.; Yamamoto, T.; Nakao, A.; Murata, H. *Sol. Energ. Mat. Sol. C.* **2014**, *123*, 81.

10. Eloi, J.-C.; Chabanne, L.; Whittell, G. R.; Manners, I. *Mater. Today* **2008**, *11*, 28.

11. Ho, C.-L.; Wong, W.-Y. *Coord. Chem. Rev.* **2011**, *256*, 2469.

12. Whittell, G. R.; Hager, M. D.; Schubert, U. S.; Manners, I. **2011**, *10*, 176.

13. Manners, I. *Science* **2001**, *294*, 1664.

14. Cameron, C. G.; Pickup, P. G. *Chem. Commun.* **1997**, 303.

15. Cameron, C. G.; Pickup, P. G. *J. Am. Chem. Soc.*, **1999**, *121*,7710.

16. Cameron, C. G.; Pittman, T. J.; Pickup, P. G. *J. Phys. Chem. B*, **2001**, *105*, 8838.

17. Milum, K. M.; Kim, Y. N.; Holliday, B. J. *Chem. Mater.* **2010**, *22*, 2414.

18. Wolf, M. O. *Adv. Mater.* **2001**, *13*, 545.

19. Wolf, M. O.; Wrighton, M. S. *Chem. Mater.* **1994**, *6*, 1526.

20. Holliday, B. J.; Swager, T. M. *Chem. Commun.* **2005**, 25.

21. Weinberger, D. A.; Higgins, T. B.; Mirkin, C. A.; Liable-Sands, L. M.; Rheingold, A. L. *Angew. Chem. Int. Ed.* **1999**, *38*, 2565.

22. Weinberger, D. A.; Higgins, T. B.; Mirkin, C. A.; Stern, C. L.; Liable-Sands, L. M.; Rheingold, A. L. *J. Am. Chem. Soc.* **2001**, *123*, 2503.

23. Higgins, T. B.; Mirkin, C. A. *Chem. Mater.* **1998**, *10*, 1589.

24. Gomez-Romero, P.; Sanchez, C. *Functional Hybrid Materials*; Wiley-WCH: Weinham, 2004.

25. Milliron, D. J.; Gur, I.; Alivisatos, A. P. *MRS Bulletin* **2005**, *30*, 41.

26. Coakley, K. M.; McGehee, M. D. *Chem. Mater.* **2004**, *16*, 4533.

27. *In Conjugated Polymers: Theory, Synthesis, Properties, And Characterization* 3rd ed.; Skotheim, T. A., Reynolds, J. R., Eds.; CRC Press: Boca Raton, 2007; Vol. 1.

28. Huynh, W. U.; Dittmer, J. J.; Alivisatos, A. P. *Science* **2002**, *295*, 2425-2427.

29. Lee, J.-Y.; Connor, S. T.; Cui, Y.; Peumans, P. *Nano Lett.* **2008**, *8*, 689.

30. Gaynor, W.; Lee, J. Y.; Peumans, P. *ACS Nano* **2010**, *4*, 30.

31. Huynh, W.; Dittmer, J. J.; Teclemariam, N.; Milliron, D. J.; Alivisatos, A. P. *Phys. Rev. B* **2003**, *67*, 115326.

32. Manna, L.; Milliron, D. J.; Meisel, A.; Scher, E. C.; Alivisatos, A. P. *Nat. Mater.* **2003**, *2*, 382.

33. Huynh, W.; Peng, X.; Alivisatos, A. P. *Adv. Mater.* **1999**, *11*, 923.

34. Gur, I.; Former, N. A.; Chen, C.-P.; Kanaras, A. G.; Alivisatos, A. P. *Nano Lett.* **2007**, *7*, 409.

35. Shallcross, C.; D'Ambruoso, G.; Korth, B.; Hall, H. K.; Zheng, Z.; Pyun, J.; Armstrong, N. *J. Am. Chem. Soc.* **2007**, *129*, 11310.

36. Campos, L. M.; Mozer, A. J.; Gunes, S.; Winder, C.; Neugebauer, H.; Sariciftci, N. S.; Thompson, B. C.; Reeves, B. D.; Grenier, C. R. G.; Reynolds, J. R. *Sol. Energy Mater. Sol. Cells* **2006**, *90*, 3531.

37. Kang, Y.; Kim, D. *Sol. Energy Mater. Sol. Cells* **2006**, *90*, 166.

38. Wang, Q.; He, Z.; Wild, A.; Wu, H.; Cao, Y.; Schubert, U. S. ; Chin, C.-H.; Wong, W.-Y.; *Chem. Asia. J.* **2011**, *6*, 1766.

39. Wong, W.-Y.; Chow, W.-C.; Cheung, K.-Y.; Fung, M.-K.; Djurisic, A. B.; Chan, W.-K. *J. Organomet. Chem.* **2009**, *694*, 2717.

40. Qin, C.; Fu, Y.; Chui, C.-H.; Kan, C.-W.; Xie, Z.; Wang, L.; Wong, W.-Y. *Macromol. Rapid Commun.* **2011**, *32*, 3472.

41. Zhan, H.; Lamara, S.; Ng, A.; Kenny, T.; Guernon, H.; Chan, W.-K.; Djurisic, A. B.; Harvey, P. D.; Wong, W.-Y. *Macromolecules* **2011**, *44*, 5155.

42. Zhan, H.; Wong, W.-Y.; Ng, A.; Djurisic, A. B.; Chan, W.-K. *J. Organomet. Chem.* **2011**, *696*, 4112.

43. Mak, C. S.; Leung, Q.-Y.; Li, C. H.; Chan, W. K. *Macromol. Rapid Commun.* **2010**, *31*, 875.

44. Liu, L.; Ho, C.-L.; Wong, W.-Y.; Cheung, K-Y.; Fung, M.-K.; Lam, W.-T.; Djurisic, A. B.; Chan, W.-K. *Adv. Funct. Mater.* **2008**, *18*, 2824.

45. Friebe, C.; Wild, A.; Perelaer, J.; Schubert, U. S. *Macromol. Rapid Commun.* **2012**, *33*, 503.

46. Lin, S.; Zhang, K.; Lu, J.; Zhang, J.; Yip, H.-L.; Huang, F.; Cao, Y. *J. Am. Chem. Soc.* **2013**, *135*, 15326.

47. Wong, W.-Y.; Wang, X.-Z.; He, Z.; Chan, K.-K.; Djurisic, A. B.; Cheung, K.-Y.; Yip, C.-T.; Ng, A. M.; Xi, Y. Y.; Mak, C. S.; Chan, W.-K. *J. Am. Chem. Soc.* **2007**, *129*, 14372.

48. Rawashdeh-Omary, M. A.; López-de-Luzuriaga, J. M.; Rashdan, M. D.; Elbjeirami, O.; Monge, M.; Rodriguez-Castillo, M.; Laguna, A. *J. Am. Chem. Soc.* **2009**, *131*, 3824.

49. Tennyson, E. G.; Smith, R. C. *Inorg. Chem.* **2009**, *48*, 11483.

50. Chen, X.-Y.; Yang, X.; Holliday, B. J. *J. Am. Chem. Soc.* **2008**, *130*, 1546.

51. Koga, Y.; Matsubara, K. *J. Polym. Sci. A. Polymer. Chem.* **2009**, *47*, 4358.

52. Chen, X.; Liao, J.-L.; Liang, Y.; Ahmed, M. O.; Tseng, H.-E.; Chen, S.-A. *J. Am. Chem. Soc.* **2002**, *125*, 636.

53. Masetti, F.; Mazzucato, U.; Galiazzo, G. *J. Lumin.* **1971**, *4*, 8.

54. Lakowicz, J. R. *Principles of Fluorescence Spectroscopy*, 3nd ed.;

Springer: Baltimore, MD, 2006.

55. Tennyson, A. G.; Kamplain, J. W.; Bielawski, C. W. *Chem. Commun*.

2009, 2124.

56. Wittmann, H. F.; Friend, R. H.; Khan, M. S.; Lewis, J. *J. Chem.*

Phys. **1994**, *101*, 2693.

57. Zaman, S.; Zainelabdin, A.; Amin, G.; Nur, O.; Willander, M. *Appl. Phys. A* **2011**, *104*, 1203.

58. Hussain, I.; Bano, N.; Hussain, S.; Nur, O.; Willander, M. *J. Mater. Sci.* **2011**, *46*, 7437.

59. Ryan, J. W.; Palomares, E.; Martínez-Ferrero, E.; *J. Mater. Chem.* **2011**, *21*, 4774.

60. Yuan, Y.; Riehle, F.-S.; Nitschke, R.; Krüger, M. *Mater. Sci. Eng., B* **2012**, *177*, 245.

61. Bolink, H. J.; Coronado, E.; Sessolo, M. *Chem. Mater.* **2009**, *21*, 439.

62. Duan, J.-P.; Sun, P.-P.; Cheng, C.-H. *Ad*v. *Mater.* **2003**, *15*, 224.

63. Schwartz, G.; Fehse, K.; Pfeiffer, M.; Walzer, K.; Leo, K. *Appl. Phys. Lett.* **2006**, *89*, 083509.

64. Wadeasa, A.; Beegum, S. L.; Raja, S.; Nur, O.; Willander, M. *Appl. Phys. A* **2009**, *95*, 807.

65. Bolink, H. J.; Brine, H.; Coronado, E.; Sessolo, M. *ACS Appl. Mat. & Inter.* **2010**, *2*, 2694.

66. Swager, T. M. *Acc. Chem. Res.* **1998**, *31*, 201.

67. McQuade, D.; Pullen, T.; Swager, T. M. *Chem. Rev.* **2000**, *100*, 2537.

68. Fegley, M. E.; Pinnock, S. S.; Malele, C. N.; Jones, W. E. *Inorg. Chim. Acta* **2012**, *381*, 78.

69. Holliday, B. J.; Stanford, T. B.; Swager, T. M. *Chem. Mater.* **2006**, *18*, 5649.

70. He, S.; Iacono, S. T.; Budy, S. M.; Dennis, A. E.; Smith, D. W.; Smith, R. C. *J. Mater. Chem.* **2008**, *18*, 1970.

71. Wild, A.; Winter, A.; Hager, M. D.; Schubert, U. S. *Analyst* **2012**, *137*, 2333.

72. Hu, Y.; Chen, Q.; Ding, Y.; Li, R.; Jiang, X.; Liu, B. *Adv. Mater.* **2009**, *21*, 3639.

73. Kumar, S. A.; Wang, S.-A.; Chang, Y.-T. *Thin Solid Films* **2010**, *518*, 5832.

74. Kumar, S. A.; Chen, S.-M. *Biosens. Bioelectron.* **2007**, *22*, 3042.

75. Alsawafta, M.; Badilescu, S.; Paneri, A.; Truong, V.-V. Packirisamy, M. *Polymers* **2011**, *3*, 1833.

76. Di Carlo, G.; Curulli, A.; Toro, G. R.; Bianchini, C.; De Caro, T.; Padeletti, G.; Zane, D.; Imgo, G. M. *Langmuir* **2012**, *28*, 5471.

77. Albano, V. G.; Bandini, M.; Moorlag, C.; Piccinelli, F.; Pietrangelo, A.; Tommasi, S.; Umani-Rochi, A.; Wolf, M. O. *Organometallics* **2007**, *26*, 4373.

78. Zulauf, A.; Mellah, M.; Hong, X.; Schulz, E. *Dalton Trans.* **2010**, *39*, 6911.

79. Kingsborough, R. P.; Swager, T. M. *Chem. Mater.* **2000**, *12*, 872.

80. Edelman, K. R.; Stevenson, K. J.; Holliday, B. J. *Macromol. Rapid. Commun.* **2012**, *33*, 610.

81. Scalzullo, S.; Mondal, K.; Witcomb, M.; Deshmukh, A.; Scurrell, M.; Mallick, K. *Nanotechnology* **2008**, *19*, 075708.

82. Islam R. U.; Witcomb, M. J.; Scurrell, M. S.; van der Lingon, E.; Mallick, K. *Synth. Commun.* **2011**, *41*, 3561.

83. Nagahara, H.; Konishi, M. US. Pat. 4734536 **1988**.

84. Long, S.; Zhang, A. Q.; Liu, H. F.; Li, L.; Ding, L. Q. Chin *J. Catal.* **2009**, *30*, 276.

85. Zhai, H.; Zhang, A.; Li, L.; Long, S. *J. Appl. Poly. Sci.* **2012**, *123*, 2140.

86. Janáky, C.; Endrődi, B.; Berkesi, O.; Visy, C. *J. Phys. Chem. C* **2010**, *114*, 19338.

87. Bencsik, G.; Lukacs, Z.; Visy, C. *Analyst* **2010**, *135*, 375.

88. Premkumar, J.; Ramaraj, J. *J. Mol. Catal. A: Chem.* **1999**, *142*,153.

89. Liu, G.; Hou, M.; Song, J.; Jiang, T.; Fan, H.; Zhang, Z.; Han, B. *Green Chem.* **2010**, *12*, 65.

90. Wang, J.; Song, G.; Peng, Y. *Tetrahedron Lett.* **2011**, *52*, 1477.

91. Wang, Y.; Liu, J.; Xia, C. *Tetrahedron Lett.* **2011**, *52*, 1587.

92. Coakley, K. M.; McGehee, M. D. *Chem. Mater.* **2004**, *16*, 4533.

93. *In Conjugated Polymers: Theory, Synthesis, Properties, and Characterization* 3rd ed.; Skotheim, T. A., Reynolds, J. R., Eds.; CRC Press: Boca Raton, 2007; Vol. 1.

94. Gaynor, W.; Burkhard, G. F.; McGehee, M. D.; Peumans, P. *Adv. Mater.* **2011**, *23*, 2905.

95. Lee, J.-Y.; Connor, S. T.; Cui, Y.; Peumans, P. *Nano Lett.* **2008**, *8*, 689.

96. Zhao, Y.; Thorkelsson, K.; Mastroianni, A. J.; Schilling, T.; Luther, J. M.; Rancatore, B. J.; Matsunaga, K.; Jinnai, H.; Wu, Y.; Poulsen, D.; Fréchet, J. M.; Alivisatos, A. P.; Xu, T. *Nature Mater.* **2009**, *8*, 979.

97. Mejia, M. L.; Agapiou, K.; Yang, X-P.; Holliday, B. J. *J. Am. Chem. Soc.* **2009**, *131*, 18196.

98. Mejia, M. L.; Reeske, G.; Holliday, B. J. *Chem. Commun.* **2010**, 5355.

99. Kamcev, J.; Germack, D. S.; Nykypanchuk, D.; Grubbs, R. B.; Nam, C.-Y.; Black, C. T. *ACS Nano,* **2013**, 7, 339.

100. Peng, Q.; Tseng, Y.-C.; Darling, S. B.; Elam, J. W. *ACS Nano*, **2011**, *5*, 4600.

101. Yin, J.; Xu, Q.; Wang, Z.; Yao, X.; Wang, Y. *J. Mater. Chem. C* **2013**, *1*, 1029.

102. Su, Z.; Sun, K.; Han, Z.; Liu, F.; Lai, Y.; Li, Y.; Liu, Y. *J. Mater. Chem.* **2012**, *22*, 16346.

103. Mali, S. S.; Shinde, P. S.; Betty, C. A.; Bhosale, P. N.; Oh, Y. W.; Patil, P. S. *J. Phys. Chem. Solids* **2012**, *73*, 735.

104. Kale, R. B.; Sartale, S. D.; Chougule, B. K.; Lokhande, C. D. *Semicond. Sci. Technol.* **2004**, *19*, 980.

105. Shen, Y.-J.; Lee, Y.-L. *Nanotechnology* **2008**, *19*, 045602.

106. Gao, X.-F.; Sun, W.-T.; Hu, Z.-D.; Ai, G.; Zhang, Y.-L.; Feng, S.; Li, F.; Peng, L.-M. *J. Phys. Chem. C* **2009**, *113*, 20481.

107. Lee, H.; Leventis, H. C.; Moon, S.-J.; Chen, P.; Ito, S.; Haque, S. A.; Torres, T.; Nuesch, F.; Geiger, T.; Zakeeruddin, S. M.; Gratzel, M.; Nazeeruddin, M. K. *Adv. Funct. Mater.* **2009**, *19*, 2735.

108. Ren, S.; Chang, L.-Y.; Lim, S.-K.; Zhao, J.; Smith, M.; Zhao, N.; Bulović, V.; Bawendi, M.; Gradečak, S. *Nano Lett.* **2011**, *11*, 3998.

109. Qian, L.; Yang, J.; Zhou, R.; Tang, A.; Zheng, Y.; Tseng, T.-K.; Bera, D.; Xue, J.; Holloway, P. H. *J. Mater. Chem.* **2011**, *21*, 3814.

110. Yu, Y.-Y.; Chien, W.-C.; Ciou, C.-Y.; Wu, H.-C. *Thin Solid Films* **2011**, *519*, 4721.

111. Maier, E.; Rath, T.; Haas, W.; Werzer, O.; Saf, R.; Hofer, F.; Meissner, D.; Volobujeva, O.; Bereznev, S.; Mellikov, E.; Amenitsch, H.; Resel, R.; Trimmel, G. *Sol. Energ. Mat. Sol. C.* **2011**, *95*, 1354.

112. Yang. Y.; Zhong, Z.; Bai, Z.; Zou, B.; Li, Y.; Scholes, G. D. *J. Phys. Chem. C* **2012**, *116*, 7280.

113. Corrado, C.; Jiang, Y.; Oba, F.; Kozina, M.; Bridges, F.; Zhang, J. Z. *J. Phys. Chem. A* **2009**, *113*, 3830.

114. Shi, L.; Pei, C.; Xu, Y.; Li, Q. *J. Am. Chem. Soc.* **2011**, *133*, 10328.

115. Riha, S. C.; Parkinson, B. A.; Prieto, A. L. *J. Am. Chem. Soc.* **2009**, *131*, 12054.

116. Steinhagen, C.; Panthani, M. G.; Akhavan, V.; Goodfellow, B.; Koo, B.; Korgel, B. A. *J. Am. Chem. Soc.* **2009**, *131*, 12554.

117. Guo, Q.; Hillhouse, H. W.; Agrawal, R. *J. Am. Chem. Soc.* **2009**, *131*, 11672.

118. Shavel, A.; Arbiol, J.; Cabot, A. *J. Am. Chem. Soc.* **2010**, *132*, 4514.

119. Dai, P.; Shen, X.; Lin, Z.; Feng, Z.; Xu, H.; Zhan, J. *Chem. Commun.* **2010**, *46*, 5749.

120. Zhou, Y.-L.; Zhou, W.-H.; Du, Y.-F.; S.-X., Wu. *Mater. Lett.* **2011**, *65*, 1535.

121. Tanaka, T.; Yoshida, A.; Saiki, D.; Saito, K.; Guo, Q.; Nishio, M.; Yamaguchi, T. *Thin Solid Films* **2010**, *518*, S29.

122. Riha, R. C.; Fredrick, S. J.; Sambur, J. B.; Liu, Y.; Prieto, A. L.; Parkinson, B. A. *ACS Appl. Mater. Interfaces* **2011**, *1*, 58.

123. Persson, C. *J. Appl. Phys.* **2010**, *107*, 053710.

124. Saunders, B. R.; Turner, M. L.; *Adv. Colloid Interface Sci.* **2008**, *138*, 1.

125. Ito, K.; Nakazawa, T. *Jpn. J. Appl. Phys., Part 1* **1988**, *27*, 2094.

126. Katagiri, H. *Thin Solid Films* **2005**, *480*, 426.

127. Fischereder, A.; Rath, T.; Haas, W.; Amenitsch, H.; Albering, J.; Meischler, D.; Larissegger, S.; Edler, M.; Saf, R.; Hofer, F.; Trimmel, G. *Chem. Mater.* **2010**, *22*, 3399.

128. Zhu, S. S.; Swager, T. M. *J. Am. Chem. Soc.* **1997**, *119*, 12568.

129. Agapiou, K.; Mejia, M. L.; Yang, X-P.; Holliday, B. J. *Dalton Trans.* **2009**, 4154.

130. Sheldrick, G. M. (1994) SHELXL97. *Program for the Refinement of Crystal Structures.* University of Göttingen, Germany.

131. Cromer, D. T.; Waber, J. T. International Tables for X-Ray Crystallography, Kynoch Press, Birmingham, vol. 4 (1974), Table 2.2A.

132. Dai, P.; Shen, X.; Lin, Z.; Feng, Z.; Xu, H.; Zhan, J. *Chem. Commun.* **2010**, *46*, 5749-5751.

133. Pankove, J. I. Optical Processes in Semiconductors, Prentice-Hall, New Jersey, 1971.

134. Adhikary, C.; Bera, R.; Dutta, B.; Jana, S. Bocelli, G.; Cantoni, A.; Chauduri, S.; Koner, S. *Polyhedron* **2008**, *27*, 1556.

135. Arici, C.; Ercan, F.; Kurtaran, R.; Atakol, O. *Acta Crystallogr C* **2001**, *C57*, 812.

136. Bilello, J. C. *J. Appl. Phys.* **1983**, *54*, 1821.

137. Sellers, M. S. *Appl. Surf. Sci.* **2010**, *256*, 4402.

138. Gurer, H. *Free Radic Biol. Med.* **2000**, *29*, 927.

139. Faridbod, F.; Norouzi, P.; Dinarvand, R.; Ganjali, M. R. *Sensors* **2008**, *8*, 2331.

140. Wenger, O. S. *Chem. Rev.* **2013**, *113*, 3686.

141. Gill, I. *Chem. Mater.* **2001**, *13*, 3404.

142. Yoon, J.; Chae, S. K.; Kim, J.-M. *J. Am. Chem. Soc.* **2007**, *129*, 3038.

143. Saadeh, S. M.; Abu Shawish, H. M.; Dalloul, H. M.; El-Halabi, N. M.; Daher, B. *Mater. Sci. Eng. C* **2012**, *32*, 619.

144. Fouskaki, M.; Chaniotakis, N. A. *Anal. Chem.* **2005**, *77*, 1780.

145. Ardakani, M. M.; Kashani, M. K.; Salavati-Niasari, M.; Ensafi, A. A. *Sens. Actuators B* **2005**, *107*, 438.

146. Gupta, V. K.; Jain, A. K.; Kumar, P. *Sens. Actuators B* **2006**, *120*, 259.

147. Ardakany, M. M.; Ensafi, A. A.; Naeimi, H.; Dastanpour, A.; Shamlli, A. *Sens. Actuators B* **2003**, *96*, 441.

148. Shim, J.; Jang, E.-J.; Chung, K.-C. *Anal. Lett.* **2007**, *40*, 3038.

149. Reeder, G. S.; Heineman, W. R. *Sens. Actuators B* **1998**, *52*, 58.

150. Bakker, E.; Bühlmann, P.; Pretsch, E. *Chem. Rev.* **1997**, *97*, 3083.

151. Bühlmann, P.; Pretsch, E.; Bakker, E. *Chem. Rev.* **1998**, *98*, 1593.

152. Bobacka, J.; Ivaska, A.; Lewenstam, A. *Chem. Rev.* **2008**, *108*, 329.

153. Ferreirós-Martinez, R.; Esteban-Gómez, D.; Platas-Iglesias, C.; de Blas, A.; Rodriguez-Bías, T. *Dalton Trans.* **2008**, 5754.

154. Mann, K. L. *J. Chem. Soc.* **1998**, 3029.

155. Lewis, J. A. *Inorg. Chem.* **2004**, *43*, 6534.

156. Ferreriós-Martinez, R.; Esteban-Gómez, D.; Platas-Iglesias, C.; de Blas, A.; Rodriguez-Bías, T. *Inorg. Chem.* **2009**, *48*, 10976.

157. Osipova, E. A.; Sladkov, V. E.; Shkinev, V. M. *Anal. Chem.* **2000**, *55*, 844.

158. Wilson, D.; Arada, M.; Alegret, S.; Valle, M. *J. Hazard. Mater.* **2010**, *181*, 140.

159. Otazo-Sánchez,E.; Pérez-Marin, L.; Estévez-Hernández, O.; Rojas-Lina, S.; Alonso-Chamarro, J. *J. Chem. Soc., Perkin Trans. 2* **2001**, 2211.

160. Otazo-Sanchez, E.; Ortiz-del-Toro, P.; Estevez-Hernandez, O.; Perez-Marin, L.; Beltran, A. C.; Villagomez-Ibarra, J. R. *Spectrochim Acta A* **2002**, *58*, 2281.

161. Gephart, R. T.; Williams, N. J.; Reibenspies, J. H.; De Sousa, A. S.; Hancock, R. D. *Inorg. Chem.* **2008**, *47*, 10342.

162. CrystalClear 1.40. **(2008)**, Rigaku Americas Corportion, The Woodlands, TX.

163. Altomare, A.; Burla, M. C.; Camalli, M.; Cascarano, G. L.; Giacovazzo, C.; Guagliardi, A.; Moliterni, A. G. G.; Polidori, G.; Spagna, R. *J. Appl. Crystallogr.* **1999**, *32*, 115.

164. Spek, A. L. *PLATON, A Multipurpose Crystallographic Tool*; Utrecht University: The Netherlands, 1998.

165. Farrugia, L. J. *WinGX an Integrated System of Windows Programs for the Solution, Refinement and Analysis of Single Crystal X-Ray Diffraction Data, version 1.64*; University of Glasgow: Glasgow, U.K., 1999-2003.

166. Farrugia, L. J. *J. Appl. Crystallogr.* **1999**, 32, 837.

167. *International Tables for X-ray Crystallography*; Wilson, A. J. C., Ed.; Kluwer Academic Press: Boston, 1992; Vol. C, Tables 4.2.6.8 and 6.1.1.4.

168. Estévez-Hernández, O.; Duque, J.; Pérez, H.; Santos Jr., S.; Mascarenhas, Y. *Acta Crystallogr. Sect. E: Struct. Rep. Online* **2009**, *E65*, o929.

169. Qin, C.; Wong, W.-Y.; Wang, L. *Macromolecules* **2011**, *44*, 483.

170. Hirose, K. *J. Inclusion Phenom. Mol. Recognit. Chem.* **2001**, *39*, 193.

171. Schwade, V. D. *Polyhedron* **2013**, *55*, 155.

172. Wang, J. *Talanta* **1994**, *41*, 857.

173. Kwan, P. H.; Swager, T. M. *Chem. Comm.* **2005**, 5211.

174. Kingsborough, K. P.; Swager, T. M. *Adv. Mater.* **1998**, *14*, 1100.

175. Sakamoto, M.; Wasserman, B.; Dresselhaus, M. S.; Wnek, G. E.; Elman, B. S.; Sandman, D. J. *J. Appl. Phys.* **1986**, *60*, 2789.

176. Yassar, A.; Roncali, J.; Garnier, F. *Macromolecules* **1989**, *22*, 804.

177. Saitoh, Y.; Koizumi, T.; Osakada, K.; Yamamoto, T. *Can. J. Chem.* **1997**, *75*, 1336.

178. Sauvage, J.-P.; Kern, J.-M.; Bidan, G.; Divisia-Blohorn, B.; Vidal, P.-L. *New J. Chem.* **2002**, *26*, 1287.

179. Chen, Q.; Zeng, M.-H.; Wei, L.-Q.; Kurmoo, M. *Chem. Mater.* **2010**, *22*, 4328.

180. Newkome, G. R.; Kiefer, G. E.; Puckett, W. E.; Vreeland, T. *J. Org. Chem.* **1983**, *48*, 5112.

181. Kadjane, P.; Stark, M.; Camerel, F.; Hill, D.; Hildebrandt, N.; Ziessel, R.; Charbonniére, L. J. *Inorg. Chem.* **2009**, *48*, 4601.

182. Li, G.; Kakarla, R.; Gerritz, S. W. *Tetrahedron Lett.* **2007**, 4595.

183. Zoppellaro, G.; Baumgarten, M. *Eur. J. Org. Chem.* **2005**, 2888.

184. Chen, M.S.; White, M. K. *Science* **2010**, *327*, 566.

185. Fiorentino, M.; Testaferri, L.; Tiecco, M.; Troisi, L. *J. Chem. Soc., Chem. Commun.* **1976**, *9*, 329.

186. Holliday, B. J.; Ulmann, P. A.; Mirkin, C. A.; Stern, C. L.; Zakharov, L. N.; Rheingold, A. L. *Organometallics*, **2004**, *23*, 1671.

187. Van Der Valk, P.; Potvin, P. G. *J. Org. Chem.* **1994**, *59*, 1766.

188. Zhou, Y.; Chen, W.; Wang, D. *Dalton Trans.* **2008**, 1444.

189. Chi, Y.; Chou, P. T. *Chem. Soc. Rev.* **2010**, *39*, 638.

190. Bünzli, J.-C. G.; Piguet, C. *Chem. Soc. Rev.* **2005**, *34*, 1048.

191. de Bettencourt-Dias, A. *Dalton Trans.* **2007**, *22*, 2229.

192. Kido, J.; Okamoto, Y. *Chem. Rev.* **2002**, *102*, 2357.

193. Latva, M.; Takalo, H.; Mukkala, V.-M.; Matachescu, C.; Rodriguez-Ubis, J. C.; Kankare, J. *J. Lumin.* **1997**, *75*, 149.

194. Moore, E. G.; Samuel, A. P.; Raymond, K. N. *Acc. Chem. Res.* **2009**, *42*, 542.

195. Petoud, S.; Cohen, S. M.; Bünzli, J.-C. G.; Raymond, K. N. *J. Am. Chem. Soc.* **2003**, *125*, 13324.

196. Quici, S.; Marzanni, G.; Cavazzini, M.; Anelli, P. L.; Botta, M.; Gianolio, E.; Accorsi, G.; Armaroli, N.; Barigelletti, F. *Inorg. Chem.* **2002**, *41*, 2777.

197. Petoud, S.; Muller, G.; Moore, E. G.; Xu, J.; Sokolnicki, J.; Riehl, J. P.; Le, U. N.; Cohen, S. M.; Raymond, K. N. *J. Am. Chem. Soc.* **2007**, *129*, 77.

198. De Bettencourt-Dias, A.; Viswanathan, S.; Rollett, A. *J. Am. Chem. Soc.* **2007**, *129*, 15436.

199. Ramya, A. R.; Reddy, M. L. P.; Cowley, A. H.; Vasudevan, K. V. *Inorg. Chem.* **2010**, *49*, 2407.

200. Chen, X.-Y.; Yang, X.; Holliday, B. J. *Inorg. Chem.* **2010**, *49*, 2583.

201. Deun, R. V.; Moors, D.; Fré, B. D.; Binnemand, K. *J. Mater. Chem.* **2003**, *13*, 1520.

202. Asano-Someda, M.; Kaizu, Y. *J. Photochem. Photobiol. A* **2001**, *139*, 161.

203. Tsvirko, M. P.; Stelmakh, G. F.; Pyatosin, V. E.; Solovyov, K. N.; Kachura, T. F. *Chem. Phys. Lett.* **1980**, *73*, 80.

204. Gonçalves Silva, F. R.; Malta, O. L.; Reinhard, C.; Güdel, H. U.; Piguet, C.; Moser, J. E.; Bünzli, J.-C. *J. Phys. Chem. A* **2002**, *106*, 1670.

205. Klink, S. I.; Hebbink, G. A.; Grave, L.; Van Veggel, F. C. J. M.; Reinhoudt, D. N.; Slooff, L. H.; Polman, A.; Hofstraat, J. W. *J. Appl. Phys.* **1999**, *86*, 1181.

206. Ziessel, R. F.; Ulrich, G.; Charbonniere, L.; Imbert, D.; Scopelliti, R.; Bünzli, J.-C. G. *Chem. Eur. J.* **2006**, *12*, 5060.

207. Daza, M. C.; Doerr, M.; Salzmann, S.; Marian, C. M.; Thiel, W. *Phys. Chem. Chem. Phys.* **2009**, *11*, 1688.

208. Stanley, J. M.; Zhu, X.; Holliday, B. J. *Inorg. Chem.* **2010**, *49*, 2035.

209. Allen, N. S.; Pullen, G.; Shah, M.; Edge, M.; Holdsworth, D.; Weddell, I.; Swart, R.; Catalina, F. *J. Photoch. Photobio. A* **1995**, *91*, 73.

210. Sun, P.-P.; Duan, J.-P.; Lih, J.-J.; Cheng, C.-H. *Adv. Funct. Mater.* **2003**, *13*, 683.

211. Chen, G.-J.; Guo, Y.-N.; Tian, J.-L.; Tang, J.; Gu, W.; Liu, X.; Yan, S.-P.; Cheng, P.; Liao, D.-Z. *Chem. Eur. J.* **2012**, *18*, 2484.

212. Chen, G.-J.; Qiao, X.; Tian, J.-L.; Xu, J.-Y.; Gu, W.; Yan, S.-P. *Dalton Trans.* **2010**, *39*, 10637.

213. Zhang, L.; Li, B.; Zhang, L.; Su, Z. *ACS Appl. Mater. Interfaces* **2009**, *1*, 1852.

214. Tarkuc, S.; Unver, E. K.; Udum, Y. A.; Toppare, L. *Eur. Polym. J.* **2010**, *46*, 2199.

215. Klink, S. I.; Hebbink, G. A.; Grave, L.; Oude Alink, P. G.; van Veggel, F. C.; Werts, M. H. *J. Phys. Chem. A* **2002**, *106*, 3681.

216. Meshkova, S. B.; Topilova, Z. M.; Bol'shoi, D. V.; Nazarenko, N. A. *J. Appl. Spec.* **2000**, *67*, 893.

217. Kang, J.-G.; Kim, T.-J.; Kang, H.-J.; Park, Y.; Nah, M.-N. *J. Lumin.* **2008**, *128*, 1867.

218. Hernández, I.; Zheng, Y.-X.; Motevalli, M.; Tan, R. H. C.; Gillin, W. P.; Wyatt, P. B. *Chem. Commun.* **2013**, *49*, 1933.

219. Kang, T. S.; Harrison, B. S.; Bouguettaya, M.; Foley, T. J.; Boncella, J. M.; Schanze, K. S.; Reynolds, J. R. *Adv. Funct. Mater.* **2003**, *13*, 205.

220. Meshkova, S. B.; Topilova, Z. M.; Bolshoy, D. V.; Beltyukova, S. V.; Tsvirko, M. P.; Venchikov, V. Y.; Ya, V. *Acta Phys. Pol. A* **1999**, *95*, 983.

221. Annibale, V. T.; Song, D. *RSC Adv.* **2013**, *3*, 11432.

222. Lindner, E.; Pautz, S. Haustein, M. *J. Organomet. Chem.* **1996**, *509*, 215.

223. Lindner, E.; Keppeler, B.; Mayer, H. A.; Gierling, K.; Fawzi, R.; Steimann, M. *J. Organomet. Chem.* **1996**, *526*, 175.

224. Allgeier, A. M.; Slone, C. S.; Mirkin, C. A.; Liable-Sands, L. M.; Yap, G. P.; Rheingold, A. L. *J. Am. Chem. Soc.* **1997**, *119*, 550.

225. Liu, X.; Eisenberg, A. H.; Stern, C. L.; Mirkin, C. A. *Inorg. Chem.* **2001**, *40*, 2940.

226. Zhu, S. S.; Swager, T. M. *J. Am. Chem. Soc.* 1997, **119**, 12568.

227. Milum, K. M.; Kim, Y. N.; Holliday, B. J. *Chem. Mater.* **2010**, *22*, 2414.

228. Montag, M.; Efremenko, I; Cohen, R.; Shimon, L. J.; Leitus, G.; Diskin-Posner, Y.; Ben-David, Y.; Salem, H.; Martin, J. M.; Milstein, D. *Chem. Eur. J.* **2010**, *16*, 328.

229. Castonguay, A.; Spasyuk, D. M.; Madern, N.; Beauchamp, A. L.; Zargarian, D.

Organometallics, **2009**, *28*, 2134.

230. Bedford, R. B.; Chang, Y.-N.; Haddow, M. F.; McMullin, C. L. *Dalton Trans.* **2011**, *40*, 9034.

231. Findlater, M.; Cartwright-Sykes, A.; White, P. S.; Schauer, C. K.; Brookhart, M. *J. Am. Chem. Soc.* **2011**, *133*, 12274.

232. Espinosa-Jalapa, N. A.; Hernandez-Ortega, S.; Le Goff, X.-F.; Morales-Morales, D.; Djukic, J.-P.; Le Lagadec, R. *Organometallics* **2013**, *32*, 2661.

233. Nawara-Hultzsch, A. J.; Hackenberg, J. D.; Punji, B.; Supplee, C.; Emge, T. J.; Bailey, B. C.; Schrock, R. R.; Brookhart, M.; Goldman, A. S. *ACS Catal.* **2013**, *3*, 2505.

234. Timpa, S. D.; Fafard, C. M.; Herbert, D. E.; Ozerov, O. V. *Dalton Trans.* **2011**, *40*, 5426.

235. Salem, H.; Ben-David, Y.; Shimon, L. J.; Milstein, D. *Organometallics*, **2006**, *25*, 2292.

236. Luo, J.; Oliver, A. G.; McIndoe, J. S. *Dalton Trans.* **2013**, *42*, 11312.

237. Nelson, D. J.; Li, R.; Brammer, C. *J. Org. Chem.* **2005**, *70*, 761.

238. Albano, V. G.; Bandini, M.; Moorlag, C.; Piccinelli, F.; Pietrangelo, A.; Tommasi, S.; Umani-Rochi, A.; Wolf, M. O. *Organometallics* **2007**, *26*, 4373.

239. Zulauf, A.; Mellah, M.; Hong, X.; Schulz, E. *Dalton Trans.* **2010**, *39*, 6911.

240. Kingsborough, R. P.; Swager, T. M. *Chem. Mater.* **2000**, *12*, 872.

241. Morales-Morales, D.; Grause, C.; Kasaoka, K.; Redón, R.; Cramer, R. E.; Jensen, C. M. *Inorg. Chim. Acta* **2000**, *300-302*, 958.

242. Liang, Z.; Ma, S.; Yu, J.;Xu, R. *Tetrahedron* **2007**, *63*, 977.

243. Song, C. Swager, T. M. *Macromolecules* **2005**, *38*, 4569.

244. Wallner, O. A.; Szabo, K. J. *Org. Lett.***2004**, *6*, 1829.

245. Bedford, R. B.; Draper, S. M.; Noelle Scully, P.; Welch, S. L. *New J. Chem.* **2000**, *24*, 745.

246. Trzeciak, A. M.; Ziólkowski, J. J. *J. Organomet. Chem.* **2000**, *597*, 69.

247. Weng, W. Guo, C.; Celenligil-Cetin, R.; Foxman, B. M.; Ozerov, O. V. *Chem. Commun.* **2006**, 197.

248. Andavan, G. T.; Bauer, E. B.; Letko, C. S.; Hollis, T. K.; Tham, F. S. *J. Organomet. Chem.* **2005**, *290*, 5938.

249. Bauer, E. B.; Andavan, G. T.; Hollis, T. K.; Rubio, R. J.; Cho, J.; Kuchenbeiser, G. R.; Helgert, T. R.; Letko, C. S.; Tham, F. S. *Org. Lett.* **2008**, *10*, 1175.

250. Gupta, M.; Hagen, C.; Flesher, R. J.; Kaska, W. C.; Jensen, C. M. *Chem. Commun.* **1996**, 2083.

251. Rosales, M.; Vallejo, R.; Soto, J. J.; Bastidas, L. J.; Molina, K.; Baricelli, P. J. *Catal. Lett.* **2010**, *134*, 56.

252. Lange, S.; Leitner, W. *J. Chem. Soc., Dalton Trans.* **2002**, 752.

253. Weng, W.; Guo, C.; Celenligil-Cetin, R.; Foxman, B. M.; Ozerov, O. V. *Chem. Commun.* **2006**, 197

254. Mathiyazhagan, R. U.; Ramesh, R.; Ahn, K. H. *Tetrahedron Lett.* **2009**, *50*, 7014.

email: matthewr1987@gmail.com

This dissertation was typed by Matthew Thomas Raiford.